NASA CONTRACTOR REPORT

NASA CR-1034

STUDY OF MINERAL STABILITY IN THE LUNAR ENVIRONMENT

Prepared by
THE BENDIX CORPORATION
Ann Arbor, Mich.
for Manned Spacecraft Center

NATIONAL AERONAUTICS AND SPACE ADMINISTRATION • WASHINGTON, D. C. • JUNE 1968

NASA CR-1034

STUDY OF MINERAL STABILITY IN THE LUNAR ENVIRONMENT

Issued by Originator as Report No. BSR 2022

Prepared under Contract No. NAS 9-3734 by
THE BENDIX CORPORATION
Ann Arbor, Mich.

for Manned Spacecraft Center

NATIONAL AERONAUTICS AND SPACE ADMINISTRATION

For sale by the Clearinghouse for Federal Scientific and Technical Information
Springfield, Virginia 22151 – CFSTI price $3.00

PREFACE

This volume represents the final report on Bendix Aerospace Systems Division Project No. 82911, sponsored by the National Aeronautics and Space Administration under Contract No. NAS 9-3734. The award was based on the evaluation of Bendix Aerospace Systems Division's Technical Proposal BSD 965, August 1964, supplemented by Bendix Letter 64-520-13919, dated 30 September 1964, which were submitted in response to RFP No. BG 751-41-5-22 P, issued by the NASA Manned Spacecraft Center on 24 July 1964. The study was initiated 16 November 1964 and was reviewed periodically by Mr. U. S. Clanton, NASA Technical Representative for the project.

The highly specialized disciplines required to carry out several of the mineralogical experiments were provided by a team of consulting geologists from The University of Michigan. Technical management of the entire program was the responsibility of Mr. Milton Schloss, while certain administrative functions were performed by Dr. O. Lyle Tiffany during the first part of the investigation and by Dr. J. Rutkowski during the latter part.

The aforementioned persons and others who contributed materially to this project are acknowledged below together with a brief description of their assigned tasks:

Mr. Clarence W. Ahlstrom, Bendix Aerospace Systems Division
Design Engineer—responsible for the design, fabrication, and installation of test equipment during Phase I of the project.

Mr. Ted R. Brouillette, Bendix Aerospace Systems Division
Physicist—responsible for monitoring all tests and experiments during Phase II.

Dr. Paul L. Cloke, The University of Michigan
Associate Professor of Geology—responsible for the synthesis of ammonium feldspar, basalt glass fusion, and mass spectrometer analysis.

Mr. Thomas C. Cunningham, Jr., Bendix Aerospace Systems Division
Test Engineer—responsible for thermal simulation and measurement during Phase II.

Dr. Reynold M. Denning, The University of Michigan
Professor of Mineralogy—responsible for the differential thermal analysis (DTA), thermogravimetric analysis (TGA), and optical microscopic analysis.

Mr. Franklin, F. Foit, The University of Michigan
Ph. D. Candidate in Geochemistry—responsible for sample preparation and monitoring tests and experiments during Phase I.

Mr. Jerome Katz, Bendix Aerospace Systems Division
Photoscientist—responsible for perfecting a high-speed X-ray photographic technique for making powder diffraction patterns.

Dr. William C. Kelly, The University of Michigan
Associate Professor of Geology—responsible for the purity analysis of ammonium feldspar, basalt glass, and other test specimens.

Mr. Richard R. Lannin, Bendix Aerospace Systems Division
Environmental Lab Technician—responsible for the assembly and operation of test equipment during Phase II.

Dr. Eleanora C. Liu, Bendix Aerospace Systems Division
Senior Scientist—responsible for coordinating the chemical analyses of the pre-exposed and test samples.

Mr. Edwin E. Metevia, Bendix Aerospace Systems Division
Manager, Systems Test Department—responsible for providing technical assistance in the thermal vacuum field to achieve the prescribed lunar and spacecraft environments.

Mr. Herbert J. Mummery, Bendix Aerospace Systems Division
Environmental Lab Technician—responsible for the assembly and operation of test equipment during Phase I.

Mr. Lloyd L. Paus, Bendix Aerospace Systems Division
Design Engineer—responsible for the design, fabrication, and installation of test equipment during Phase II.

Dr. Donald R. Peacor, The University of Michigan
Assistant Professor of Geology—responsible for the X-ray photographic investigations in ambient and in vacuum.

Dr. J. Rutkowski, Bendix Aerospace Systems Division
Manager, Flight Sciences Department—responsible for the administrative management during Phase II.

Mr. Milton Schloss, Bendix Aerospace Systems Division
Project Manager—responsible for the technical direction and coordination of the study program, the plagioclase irradiation at The University of Michigan, and the preparation of progress and final reports.

Mr. Charles F. Sheppy, Bendix Aerospace Systems Division
Supervisor, Thermal Vacuum Section—responsible for maintenance, troubleshooting, repair, and checkout of test equipment.

Dr. O. Lyle Tiffany, Bendix Aerospace Systems Division
Chief Scientist—responsible for the administrative management during Phase I.

CONTENTS

	Page
1. INTRODUCTION	1-1
2. TEST MATERIALS	2-1
2.1 MINERAL SPECIMENS	2-1
2.2 SELECTION OF MINERALS	2-1
2.3 AMMONIUM FELDSPAR	2-3
2.3.1 Optical Microscopic Analysis of Anorthoclase	2-4
2.3.2 Differential Thermal Analysis	2-4
2.3.3 Thermogravimetric Analysis	2-4
2.3.4 Preliminary Experiment	2-4
2.3.5 Intermediate Experiments	2-7
2.3.6 Ammoniated Anorthoclase	2-11
2.3.7 Ammoniated Orthoclase	2-13
2.4 FUSION OF BASALT GLASS	2-14
2.4.1 Optical Microscopic Analysis of Basalt	2-14
2.4.2 Preliminary Experiments	2-14
2.4.3 Basalt Glass Production	2-16
2.5 IRRADIATION OF PLAGIOCLASE	2-16
2.5.1 Preliminary Tests	2-16
2.5.2 Sample Exposure	2-17
2.5.3 Radiation Hazards	2-17
2.6 SAMPLE PREPARATION	2-18
2.6.1 Rock Trimmer	2-18
2.6.2 Mica Books	2-18
2.6.3 Mortar and Pestle	2-18
2.6.4 Ball Mill	2-22
2.6.5 Sieving	2-24

CONTENTS (CONT.)

		Page
3.	EQUIPMENT AND TEST PROCEDURES	3-1
	3.1 OPTICAL MICROSCOPIC ANALYSIS	3-1
	3.2 DIFFERENTIAL THERMAL ANALYSIS (DTA)	3-2
	3.3 THERMOGRAVIMETRIC ANALYSIS (TGA)	3-6
	3.4 MASS SPECTROMETER ANALYSIS	3-8
	3.4.1 Bendix TOF Mass Spectrometer	3-11
	3.4.2 Test Procedure	3-12
	3.5 X-RAY DIFFRACTION ANALYSIS	3-13
	3.5.1 Ultrahigh Vacuum System	3-14
	3.5.2 Bendix X-Ray Camera	3-14
	3.5.3 Debye-Scherrer Camera	3-19
	3.6 PHASE II EXPERIMENTS	3-20
4.	ACTINOLITE	4-1
5.	AMMONIUM FELDSPAR	5-1
6.	ANTIGORITE	6-1
7.	BASALT GLASS	7-1
8.	CALCITE	8-1
9.	CALCIUM MONTMORILLONITE	9-1
10.	GOETHITE	10-1
11.	GYPSUM	11-1
12.	HEMATITE	12-1
13.	IRRADIATED PLAGIOCLASE	13-1
14.	MUSCOVITE	14-1
15.	NATROLITE	15-1
16.	TALC	16-1

CONTENTS (CONT.)

	Page
17. TEKTITE	17-1
18. SUMMARY AND CONCLUSIONS	18-1
18.1 TEST MINERALS	18-1
18.2 EXPERIMENTS	18-1
18.3 STABILITY CURVES	18-2
18.4 THEORETICAL VS. EXPERIMENTAL RESULTS	18-2
18.5 CONCLUSIONS	18-5
APPENDIX I CONTRACT SUMMARY	I-1

ILLUSTRATIONS

Figure	Title	Page
2-1	Photomicrograph of Anorthoclase, 47X, Analcite Crystal at Center	2-5
2-2	Anorthoclase DTA	2-6
2-3	Anorthoclase TGA	2-6
2-4	Reactors and Copper Capsules Used for Producing Ammonium Feldspar	2-9
2-5	Experimental Apparatus Assembled and Ready to be Placed in Furnace	2-10
2-6	Photomicrograph of Basalt, Crossed Polars, 47X	2-15
2-7	Flow Chart of Mineral Processing	2-20
2-8	Equipment Used to Pulverize and Crush Samples	2-21
2-9	Sample Preparation in Dry N_2 Atmosphere	2-23
2-10	Interior of Dry Box	2-25
3-1	Nickel Block Loaded With Mineral and Reference Material	3-3
3-2	DTA Furnaces: #2 in Operating Position; #1 Open, Exposing Block	3-4
3-3	Temperature Recording System	3-5
3-4	Calibration for Measurement of ΔT Pt vs. Pt 10% Rh	3-7
3-5	Recording Balance and Furnace for TGA	3-9
3-6	General View of Bendix TOF Mass Spectrometer and Auxiliary Equipment	3-10
3-7	Bendix Ultrahigh Vacuum System	3-15
3-8	Mineral Stability Test Setup (Photos)	3-16
3-9	X-Ray Camera Unit Attached to Ultrahigh Vacuum System	3-17
3-10	Camera Housing and Sample Holder	3-18
3-11	Mineral Stability Test Setup (Schematic)	3-21
4-1	Photomicrograph of Actinolite, Crossed Polars, 47X Chlorite Crystals at Right Edge	4-2
4-2	Actinolite DTA	4-4
4-3	Actinolite TGA	4-4
4-4	Mass Spectrometer Curve of Actinolite-Scan With H_2O Peak Plotted	4-5

ILLUSTRATIONS (CONT.)

Figure	Title	Page
4-5	Actinolite X-Ray Pattern Taken With Debye-Scherrer Camera	4-7
4-6	Actinolite X-Ray Pattern Taken With Bendix Vacuum Camera (Magnification 2X)	4-7
4-7	Structure of Tremolite, Diopside, and Enstatite	4-11
4-8	Stability Curve of Actinolite	4-14
5-1	Mass Spectrometer Curve of Ammonium Feldspar—H_2O, NH_2, and NH_3 Peaks Plotted	5-3
5-2	NH_4 Feldspar Standard Bendix Camera X-Ray Pattern, Phase I (Magnification 2X)	5-4
5-3	NH_4 Feldspar Standard Bendix Vacuum Camera Pattern, Phase II (Magnification 2X)	5-4
5-4	Structure of Ammonium Feldspar—Sanidine	5 8
5-5	Stability Curves of Ammonium Feldspar	5-11
6-1	Photomicrograph of Antigonite, Crossed Polars, 47X, Veinlet of Chrysolite in Upper Right Quadrant	6-2
6-2	Antigorite DTA	6-3
6-3	Antigorite TGA	6-3
6-4	Mass Spectrometer Curve of Antigorite—Scan With H_2O Peak Plotted	6-5
6-5	Antigorite X-Ray Pattern Taken With Debye-Scherrer Camera	6-6
6-6	Antigorite X-Ray Pattern Taken With Bendix Vacuum Camera (Magnification 2X)	6-6
6-7	The Structures of Serpentine and Forsterite	6-10
6-8	Stability Curve of Serpentine	6-12
7-1	Photomicrograph of Basalt Glass, 47X, Gas Bubble at Left, Plagioclase Relic at Lower Right, Crystallites Scattered Over Field	7-2
7-2	Basalt Glass DTA-1	7-3
7-3	Basalt Glass DTA-2	7-3
7-4	Basalt Glass TGA	7-3
7-5	Mass Spectrometer Curve of Basalt Glass—Scan With H_2O Peak Plotted	7-6
7-6	Basalt Glass X-Ray Pattern Taken With the Debye-Scherrer Camera	7-7

ILLUSTRATIONS (CONT.)

Figure	Title	Page
8-1	Phitomicrograph of Calcite, 210X, DTA Sample in Medium Having Index of Refraction of 1. 56	8-2
8-2	Calcite DTA	8-3
8-3	Calcite TGA	8-3
8-4	Mass Spectrometer Curve of Calcite—Scan With CO_2 Peak Plotted	8-5
8-5	Mass Spectrometer Curve of Calcite—CO and H_2O Peaks	8-6
8-6	Mass Spectrometer Curve of Calcite—C Peak	8-8
8-7	Mass Spectrometer Curve of Calcite—O Peak	8-9
8-8	Calcite X-Ray Pattern Taken With the Debye-Scherrer Camera	8-11
8-9	Calcite X-Ray Pattern Taken With Bendix Vacuum Camera (Magnification 2X)	8-11
8-10	The Structure of Calcite and Lime	8-14
8-11	Stability Curve of Calcite	8-15
9-1	Photomicrograph of Ca-Montmorillonite, 210X; the Untreated Sample in Medium Having Index of Refraction of 1. 48	9-2
9-2	Ca-Montmorillonite DTA	9-3
9-3	Ca-Montmorillonite TGA	9-3
9-4	Mass Spectrometer Curve of Ca-Montmorillonite—H_2O Peak	9-5
9-5	Ca-Montmorillonite X-Ray Pattern Taken With Debye-Scherrer Camera	9-7
9-6	Ca-Montmorillonite X-Ray Pattern Taken With Bendix Vacuum Camera (Magnification 2X)	9-7
9-7	Ca-Montmorillonite Standard X-Ray Pattern Taken With Bendix Vacuum Camera, Phase II	9-9
9-8	The Structure of Calcium-Montmorillonite	9-11
9-9	Stability Curve of Calcium-Montmorillonite	9-14
10-1	Photomicrograph of Goethite, 47X	10-2
10-2	Goethite DTA	10-3
10-3	Goethite TGA	10-3
10-4	Mass Spectrometer Curve of Goethite—Scan With H_2O Peak Plotted	10-5

ILLUSTRATIONS (CONT.)

Figure	Title	Page
10-5	Mass Spectrometer Curve of Goethite $-H_2O$ Peak	10-6
10-6	Goethite X-Ray Pattern Taken With Debye-Scherrer Camera	10-7
10-7	Goethite X-Ray Pattern Taken With Bendix Vacuum Camera (Magnification 2X)	10-7
10-8	Transformed Goethite (Hematite) Photograph Obtained at 130°C and 3×10^{-10} Torr	10-9
10-9	Goethite X-Ray Pattern Taken as a Standard for Phase II (Magnification 2X)	10-11
10-10	Transformed Goethite (Hematite) X-Ray Pattern Obtained at 75°C and 5×10^{-10} Torr	10-11
10-11	The Structures of Goethite, Hematite, and Magnetite	10-12
10-12	Stability Curves of Goethite and Hematite	10-16
11-1	Photomicrograph of Gypsum, Crossed Polars, 210X; the DTA Sample in Liquid Having Index of Refraction of 1.56	11-2
11-2	Gypsum DTA	11-4
11-3	Gypsum TGA	11-4
11-4	Mass Spectrometer Curve of Gypsum $-H_2O$ Peak	11-5
11-5	Mass Spectrometer Curve of Gypsum $-H_2O$ Peaks	11-6
11-6	Gypsum X-Ray Pattern Taken with Debye-Scherrer Camera	11-8
11-7	Gypsum X-Ray Pattern Taken With Bendix Vacuum Camera (Magnification 2X)	11-8
11-8	X-Ray Pattern of $CaSO_4 \cdot 1/2\ H_2O$ Obtained at Room Temperature and a Vacuum of 5×10^{-10} Torr	11-11
11-9	Gypsum X-Ray Pattern Taken as Standard for Phase II Experiment	11-11
11-10	X-Ray Pattern of $CaSO_4 \cdot 1/2\ H_2O$ Obtained at 5.4×10^{-10} Torr and Liquid Nitrogen Temperature	11-11
11-11	The Structures of Gypsum and Anhydrite	11-15
11-12	Stability Curves of $CaSO_4 - nH_2$	11-19
12-1	Photomicrograph of Hematite, 100X; the DTA Sample in Liquid Having Index of Refraction of 1.68	12-2
12-2	Hematite DTA	12-4
12-3	Hematite TGA	12-4

ILLUSTRATIONS (CONT.)

Figure	Title	Page
12-4	Mass Spectrometer Curve of Hematite—Scan With H_2O Peak Plotted	12-5
12-5	Hematite X-Ray Pattern Taken With Debye-Scherrer Camera	12-7
12-6	Hematite X-Ray Pattern Taken With Bendix Vacuum Camera (Magnification 2X)	12-7
13-1	Photomicrograph of Labradorite, Crossed Polars, 47X, Showing Albite Twinning, Rutile Needles (Parallel With Twinning), and Pyroxene Crystals in Central Dark Twin Band	13-2
13-2	Irradiated Plagioclase DTA	13-4
13-3	Irradiated Plagioclase TGA	13-4
13-4	Mass Spectrometer Curve of Plagioclase (Irradiated Labradorite)—H_2O Peak	13-5
13-5	Mass Spectrometer Curve of Plagioclase (Nonirradiated Labradorite)—H_2O Peak	13-6
13-6	Plagioclase (Irradiated) X-Ray Pattern Taken With Debye-Scherrer Camera	13-7
13-7	Plagioclase (Nonirradiated) X-Ray Pattern Taken With Debye-Scherrer Camera	13-7
13-8	X-Ray Pattern Taken With Bendix Vacuum Camera (Magnification 2X)	13-8
14-1	Photomicrograph of Muscovite, 210X DTA Sample Immersed in Liquid Having Index of Refraction of 1.48	14-2
14-2	Muscovite DTA	14-3
14-3	Muscovite TGA	14-3
14-4	Mass Spectrometer Curve of Muscovite—H_2O Peak	14-5
14-5	Muscovite X-Ray Pattern Taken With Debye-Scherrer Camera	14-6
14-6	Muscovite X-Ray Pattern Taken With Bendix Vacuum Camera (Magnification 2X)	14-6
14-7	Muscovite X-Ray Pattern Taken at 180°C and a Vacuum of 8×10^{-10} Torr (Pattern Identical to That Taken at Room Temperature)	14-6
14-8	Muscovite X-Ray Pattery Taken as a Standard for Phase II	14-10
14-9	The Structure of Muscovite	14-13
14-10	Stability Curves of Muscovite	14-21

ILLUSTRATIONS (CONT.)

Figure	Title	Page
15-1	Photomicrograph of Natrolite, 47X, Coarse Needles of Natrolite and Fine Needles of Scolecite in Central Area, Analcite in Clear Right Area, Wall Rock in Lower Left Quadrant	15-3
15-2	Natrolite DTA	15-4
15-3	Natrolite TGA	15-4
15-4	Mass Spectrometer Curve of Natrolite $-H_2O$ Peak	15-6
15-5	Natrolite X-Ray Pattern Taken With Debye-Scherrer Camera	15-8
15-6	Natrolite X-Ray Pattern Taken With Bendix Vacuum Camera (Magnification 2X)	15-8
15-7	The Structure of Natrolite	15-10
15-8	Stability Curve of Natrolite	15-12
16-1	Photomicrograph of Talc, 47X	16-2
16-2	Talc DTA	16-3
16-3	Talc TGA	16-3
16-4	Mass Spectrometer Curve for Talc $-H_2O$ Peak Plotted	16-5
16-5	Talc X-Ray Pattern Taken With Debye-Scherrer Camera	16-6
16-6	Talc X-Ray Pattern Taken With Bendix Vacuum Camera (Magnification 2X)	16-6
16-7	The Structures of Talc and Cristobalite	16-9
16-8	Stability Curves of Talc	16-13
17-1	Photomicrograph of Tektite, 47X	17-2
17-2	Tektite DTA	17-3
17-3	Tektite TGA	17-3
17-4	Mass Spectrometer Curve of Tektite $-H_2O$ Peak Plotted	17-5
17-5	Tektite X-Ray Pattern Taken With Debye-Scherrer Camera	17-6

TABLES

Table	Title	Page
2-1	List of Mineral Specimens	2-2
2-2	Tabulation of Experiments to Synthesize Ammonium Feldspar	2-8
2-3	Mineral Samples and Associated Impurities	2-19
2-4	Distribution of Mineral Fractions by Grain Size and Use	2-24
4-1	A Comparison of Experimental and ASTM D-Values for Actinolite	4-8
4-2	Comparison of Observed D-Values and Relative Intensity Measurements for Actinolite	4-9
5-1	Comparison of Experimental D-Values with Those of ERD et al., 1964	5-5
5-2	Comparison of Observed D-Values and Relative Intensity Measurements for the NH_4 Feldspar	5-6
6-1	Comparison of Experimental and ASTM D-Values for Antigorite	6-7
6-2	Comparison of Observed D-Values and Relative Intensity Measurements for Antigorite	6-8
7-1	Comparison of Experimental and ASTM D-Values for Basalt Glass	7-7
7-2	Comparison of Observed D-Values and Relative Intensity Measurements for Basalt Glass	7-8
8-1	Comparison of Experimental and ASTM D-Values for Calcite	8-10
8-2	Comparison of Observed D-Values and Relative Intensity Measurements for Calcite	8-12
9-1	Comparison of Experimental and ASTM D-Values for Ca-Montmorillonite	9-6
9-2	Comparison of Observed D-Values and Relative Intensity Measurements for Ca-Montmorillonite	9-8
9-3	Comparison of Observed D-Values and Relative Intensity Measurements for Ca-Montmorillonite, Phase II	9-9
10-1	Comparison of Experimental and ASTM D-Values for Goethite	10-8

TABLES (CONT.)

Table	Title	Page
10-2	Comparison of Observed D-Values and Relative Intensity Measurements for Goethite	10-8
10-3	D-Values and Relative Intensities of the Transformed Goethite (Hematite)	10-9
10-4	D-Values and Relative Intensities of the Standard Goethite and Transformation Product (Hematite)	10-13
11-1	Comparison of Experimental and ASTM D-Values for Gypsum	11-7
11-2	Comparison of Observed D-Values and Relative Intensity Measurements for Gypsum	11-9
11-3	Comparison of D-Values of Transformed Gypsum and Values From the ASTM Pattern of $CaSO_4 \cdot 1/2H_2O$	11-10
11-4	Comparison of D-Values of Gypsum Standards for Phases I and II	11-12
11-5	Comparison of D-Values of Transformed Gypsum ($CaSO_4 \cdot 1/2H_2O$) From Phases I and II	11-13
12-1	Comparison of Experimental and ASTM D-Values for Hematite	12-6
12-2	Comparison of Observed D-Values and Relative Intensity Measurements for Hematite	12-8
13-1	Comparison of Experimental and ASTM D-Values for Plagioclase (Irradiated and Nonirradiated)	13-8
13-2	Comparison of Observed D-Values and Relative Intensity Measurements for Plagioclase (Irradiated and Nonirradiated)	13-9
14-1	Comparison of Experimental and ASTM D-Values for Muscovite	14-7
14-2	Comparison of Observed D-Values and Relative Intensity Measurements for Muscovite	14-8
14-3	Comparison of D-Values and Relative Intensity for the Standard Bendix Camera Photograph and the Photograph Obtained at Ultrahigh Vacuum	14-9
14-4	Comparison of D-Values and Relative Intensities of the Muscovite Standards in Phases I and II	14-11
15-1	Comparison of Experimental and ASTM D-Values for Natrolite	15-5

TABLES (CONT.)

Table	Title	Page
15-2	Comparison of Observed D-Values and Relative Intensity Measurements for Natrolite	15-7
16-1	Comparison of Experimental and ASTM D-Values for Talc	16-7
16-2	Comparison of Observed D-Values and Relative Intensity Measurements for Talc	16-8

SECTION 1

INTRODUCTION

The primary objective of this study was to investigate the stability of selected earth minerals in a simulated lunar environment. This was to be accomplished through certain laboratory experiments and analyses, and involved selection of earth minerals having interesting and pertinent characteristics, and performance of thorough analysis of their reactions to exposure to vacuum and thermal environments closely simulating lunar conditions, and of their chemical and/or structural stability when exposed to spacecraft and earth environments.

During the course of the project, certain technical difficulties were encountered with test apparatus which required a comprehensive revision to the test procedure in order to provide results in consonance with the general objectives of the original contract. A summary of the original contract requirements, the difficulties encountered, and the contract modification is contained in Appendix I. Throughout this report, the program which Bendix conducted from contract inception through the comprehensive test procedure revision is referred to as Phase I. The subsequent period associated with the modified program is referred to as Phase II.

The program conducted hereunder consisted of "short-term" and "long-term" activities. The short-term activities involved acquisition of 14 mineral types and included laboratory production of basalt glass, synthesis of ammonium feldspar, and reactor irradiation of plagioclase. Tests and analyses conducted on the 14 samples during the short-term activities included differential thermal analysis, thermogravimetric analysis, optical microscopic measurement, mass spectrometer investigation, and X-ray diffraction pattern study. The objectives of the short-term experiments included validation of mineral identification, provision of some insight into what reactions should be expected during the long-term experiments, and provision of a standard for comparison with results obtained from the long-term experiments. The long-term activities

included temperature cycling of the mineral samples while in a vacuum, closely simulating a lunar environment, with somewhat accelerated cycling. This was to be followed by a 4-day exposure to a simulated spacecraft environment and a 2-day exposure to earth environment. X-ray photos were to be taken during the various stages, and chemical analysis would be performed at the termination of the testing. The temperature cycling was expected to encompass several months, depending upon the time required for equipment setup and time available during the original contract period. The long-term activities were substantially affected by problems encountered with the test apparatus and were subsequently conducted, using only six selected minerals, in accordance with a revised test plan incorporated into the contract by modification. Briefly stated, the testing performed involved a single temperature cycle at simulated lunar vacuum environment, with X-ray photographs of each sample being taken at various stages of the temperature cycle, and ending with a 4-day simulation of spacecraft environment (X-ray photographs being taken at this final stage also). The entire contract duration originally scheduled for 12 months was extended to 24 months to allow for equipment modification necessary for the revised test plan.

Sections 2 and 3 of this report describe the minerals selected, their preparation, and the equipments and general procedures used in the various types of tests conducted. Sections 4 through 17 treat the specific findings for each of the minerals tested, while Section 18 sets forth the significant conclusions which were reached based on test results. Section 19 presents a bibliography.

SECTION 2

TEST MATERIALS

2.1 MINERAL SPECIMENS

A total of twelve minerals and two glasses were investigated in Phase I. They included twelve natural and two synthesized materials as follows:

Actinolite	Gypsum
Ammonium Feldspar	Hematite
Antigorite	Irradiated Plagioclase
Basalt Glass	Muscovite
Calcite	Natrolite
Calcium-Montmorillonite	Talc
Goethite	Tektite

These materials are listed in Table 2-1, together with the localities in which they were found and the companies or institutions from which they were obtained. The synthetic materials are the ammonium feldspar and the basalt glass. The irradiated plagioclase was artificially induced by exposing labradorite to the radiation of a high-energy source.

2.2 SELECTION OF MINERALS

The minerals selected for study were considered to be representative of several classes of materials most likely to exhibit changes under lunar environmental conditions. The various classes chosen include a carbonate (calcite), common rock-forming silicates containing volatile hydroxyl ion (e.g., talc, muscovite), a compound with water of hydration

TABLE 2-1

LIST OF MINERAL SPECIMENS

Mineral	Locality	Source
Actinolite	Brno, South Moravia, Czechoslovakia	Southwest Scientific Co.
Anorthoclase (for NH_4 feldspar)	Tanganyika	Ward's Natural Science Establishment, Inc.
Antigorite	Montville, New Jersey	The University of Michigan Mineralogical Museum
Basalt (for basalt glass)	Branchville, Conn.	Southwest Scientific Co.
Calcite, var. Iceland spar	Creel, Chihuahua, Mexico	Southwest Scientific Co.
Calcium - montmorillonite, Sample #G360 Fine Fractured Helms Clay	Gonzales, Texas	Southern Clay Products, P.O. Box 44 Gonzales, Texas
Goethite	Mesabi Range, Minn.	Ward's Natural Science Establishment, Inc.
Gypsum, var. Selenite	Girgenti, Sicily	Southwest Scientific Co.
Hematite, Pencil ore	Egremont, Cumberland, England	Southwest Scientific Co.
Labradorite (for irradiated plagioclase)	Androtsy, Madagascar	Southwest Scientific Co.
Muscovite	Effingham Township, Ontario	Ward's Natural Science Establishment, Inc.
Natrolite	Springfield Butte, Lane County, Oregon	Ward's Natural Science Establishment, Inc.
Orthoclase (for NH_4 feldspar)	Madagascar	The University of Michigan Mineralogical Museum
Talc, foliated	New Fane, Vermont	The University of Michigan Mineralogical Museum
Tektite (Indochinite)	Thailand	Ward's Natural Science Establishment, Inc.

(gypsum), a mineral with zeolitic water (natrolite), a clay with interlayer water known to be easily lost or gained reversibly (montmorillonite), and an oxide with hydrogen-bonding (goethite). Also chosen was a feldspar containing volatile NH_4. In addition to these minerals which are all known to lose a volatile at high temperature or low pressure, basalt glass, a tektite, and a neutron-irradiated plagioclase were studied in order to determine possible changes in disordered structures which may occur in the lunar environment. The following paragraphs describe the preparation of the test materials including detailed accounts of the synthesis of the ammonium feldspar, the basalt glass, and the irradiation of labradorite to produce an irradiated plagioclase.

2.3 AMMONIUM FELDSPAR

As indicated above, ammonium feldspar was selected as a test material, since it represents a different class of phases which might yield a volatile, and therefore represents a possible devolatilization different from others. Ammonium feldspar occurs naturally as buddingtonite, but was sythesized to obtain samples for these tests.

The ammonium feldspar was synthesized by Dr. Paul L. Cloke, Associate Professor of Geology, The University of Michigan. Mixing 72 gm of a Tanganyika anorthoclase with a solution of 43.5 gm of NH_4Cl, 91 ml of H_2O, and 3.8 ml of concentrated NH_4OH and subjecting it to a temperature of 350°C and a pressure of 10,000 psi continuously for seven days, Dr. Cloke produced a feldspar with a high NH_4^+ content. It also contained impurities, such as copper and iron oxides, so other attempts were made including using a Madagascar orthoclase. Two and one-half grams of 300 mesh iron-rich orthoclase were mixed with lesser amounts of the same constituents mentioned above and subjected to 475°C and 9900 psi for seven days. Two and one-half grams of a high-purity ammoniated feldspar were finally produced.

This section describes the synthesis of ammonium feldspar in detail. Many problems of a technical and mechanical nature had to be overcome, some of which have been described in earlier reports. This section presents both positive and negative results.

2.3.1 Optical Microscopic Analysis of Anorthoclase

Anorthoclase was used initially in the synthesis of ammonium feldspar. The specimen was in part very clear, but contained other phases that could not be removed readily (Figure 2-1). About 10% of the sample was composed of clay stained with iron, surrounding 1 to 2 mm ellipsoidal cavities: The cavities were lined with clear trapezohedrons of analcite having an index of refraction of 1.485. In addition, there were a few equidimensional black crystals which could not be identified by optical means.

The axial angle of the anorthoclase is rather low, a little under 40°. The material is optically positive with $\alpha = 1.533$ and $\gamma = 1.54$. Some very fine lamellar twinning with nearly parallel extinction occurred in the crushed fragments of the feldspar.

2.3.2 Differential Thermal Analysis (Figure 2-2)

2.3.2.1 Sensitivity: 5 μv/cm

2.3.2.2 Peak Values: None (slight endothermic drift)

2.3.3 Thermogravimetric Analysis

The TGA shows no significant weight loss to a maximum temperature of 1050°C (Figure 2-3).

2.3.4 Preliminary Experiment

Because of the large amount (135 gm) of ammonium feldspar needed for experimental material, Dr. Cloke initially tried a somewhat different procedure than that employed by Barker (Am. Min. 49, 851-858, 1964). Instead of using sealed capsules, Dr. Cloke attempted to synthesize the powdered anorthoclase directly within the pressure vessel itself. It was hoped that the steel walls would not corrode and react with the solution, but the initial attempt was unsuccessful. To avoid the expense of gold capsules, copper tubing fused shut at both ends was tried with satisfactory results. Small copper crystals formed with the charge, but they were easily removed by heavy-liquid separations.

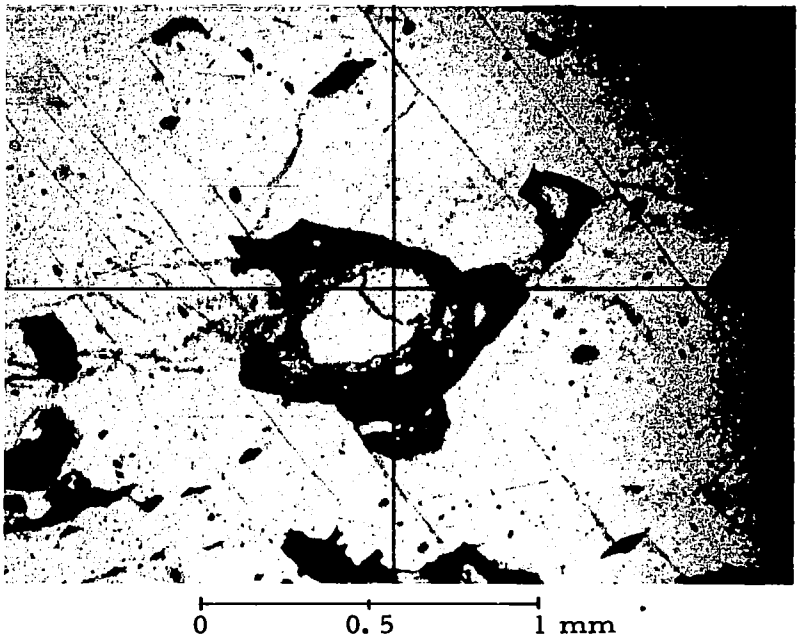

Figure 2-1 Photomicrograph of Anorthoclase, 47X, Analcite Crystal at Center

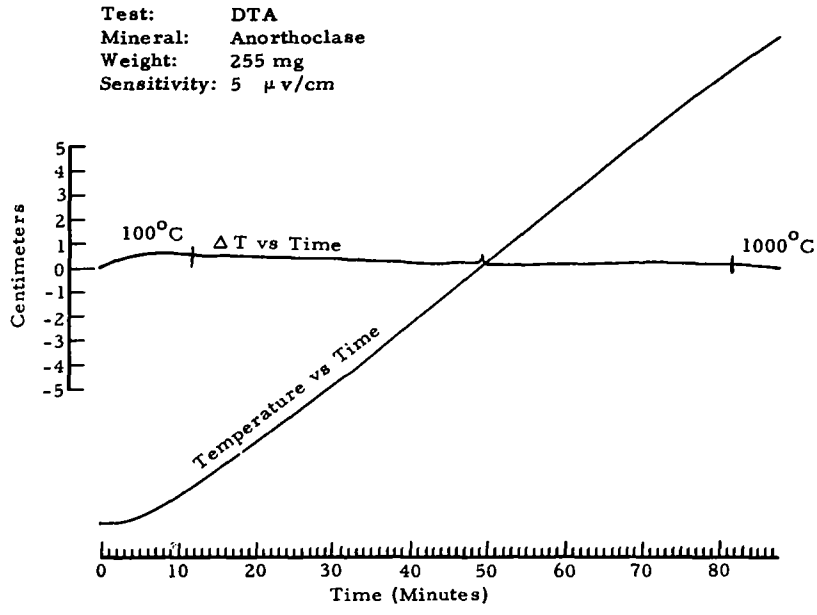

Figure 2-2 Anorthoclase DTA

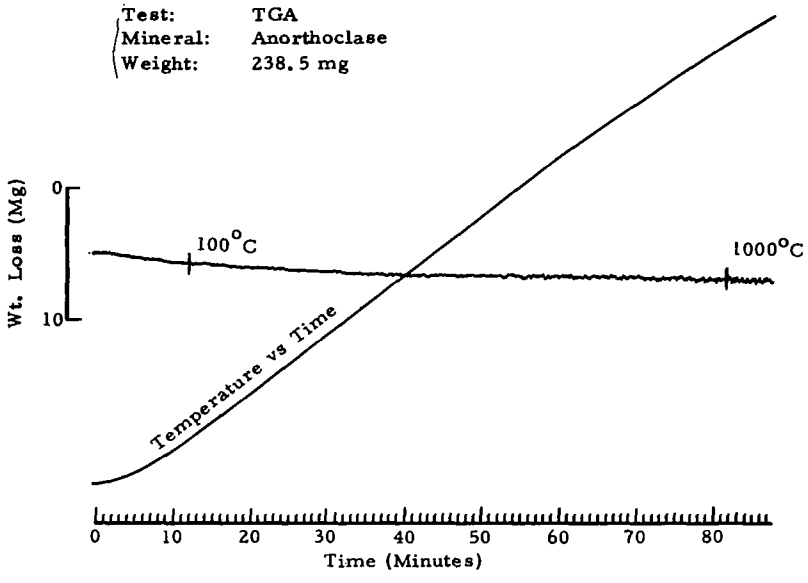

Figure 2-3 Anorthoclase TGA

Production of exchange reactions failed in the first attempts. The apparatus would not withstand the pressures used by Barker at the temperatures he cited in his report. Consequently, the experiments were carried out under less severe conditions. These experiments are summarized in Table 2-2. The last two runs, with the initial solutions made alkaline, successfully yielded ammonium feldspar. The exchange reaction took place between pressures of 8000 to 14,000 psi and at temperatures from 480 to 490°C.

2.3.5 Intermediate Experiments

The successful synthesis of 0.1 gm of anorthoclase described above established the conditions required for synthesizing a large quantity of ammonium feldspar at one time. One hundred and fifty grams of anorthoclase were sealed in a copper tube with an ammonium chloride solution containing 16-2/3% NH_4Cl and brought to pH9 with ammonium hydroxide. The copper capsule measured slightly smaller in outside diameter than the inside of the 500-ml reactor (Figure 2-4). When one end of the copper tube was flattened and fused shut, the tube would not fit in the reactor. In attempting to reshape the fused end so that it would fit inside the reactor, the seal was ruptured.

It was then attempted to make the 150 gm of ammonium feldspar in three lots. Two copper tubes of 1-in. OD, each containing 25 gm of powdered anorthoclase and an adequate amount of the pH9 NH_4Cl solution, were sealed. The two capsules were placed inside the 500-ml reactor with enough water to equalize the pressure inside and outside the capsules. When inserted into the furnace (Figure 2-5) and heated to 500°C, the reactor did not hold the pressure, allowing the solution to leak out of the copper capsules.

It was noted that the steel of the reactor was little affected by this solution. As the purpose of the copper capsules was to protect the steel from corrosion, further attempts to synthesize a large quantity of ammonium feldspar within the reactor itself were indicated. Before proceeding further, it was necessary to ensure that the 500-ml reactor would hold adequate pressure at a high enough temperature. The reactor was rated structurally adequate for 350°C and 12,000 psi, but careful consideration of the tensile strength of the steel at 500°C indicated that it was also safe for the

TABLE 2-2

TABULATION OF EXPERIMENTS TO SYNTHESIZE AMMONIUM FELDSPAR

Charge		Pressure (psi)	Temperature (°C)	Duration (hr)	Results
Solids	Solution				
0.67 gm sanidine from trachyte	2 ml 16-2/3% NH_4Cl	2,000 to 5,000 (very slow leak)	350	40	Sanidine plus a few unidentified extra lines in the diffraction pattern, no NH_4^+
Sanidine from welded tuff	16-2/3% NH_4Cl	2,000 to 5,000	350	40	Same as above
0.27 gm sanidine from trachyte	1.76 ml 16-2/3% NH_4Cl neutralized by NH_4OH	9,800	500	70	Essentially the same as above, fewer extra lines
0.1 gm $AlCl_3 \cdot 6 H_2O$, 0.075 gm ground SiO_2 glass	0.116 ml conc. NH_4OH, 1.2 ml H_2O	14,200 to 13,900	490	87.5	No determination attempted
Same as last plus 0.05 gm KCl and 0.05 gm NaCl	0.116 ml conc. NH_4OH, 1.1 ml H_2O	14,200 to 13,900	490	87.5	Not NH_4^+ feldspar
0.1 gm anorthoclase	1.4 ml 16-2/3% NH_4Cl	14,200 to 13,900	490	87.5	Essentially unchanged anorthoglase
0.1 gm anorthoclase	1.4 ml 16-2/3% NH_4Cl, neutralized by NH_4OH	14,200 to 13,900	490	87.5	White crystals, completely soluble in strong NH_4OH
0.1 gm anorthoclase	1.4 ml 16-2/3% NH_4Cl, brought to pH9 by NH_4OH	14,200 to 13,900	490	87.5	Ammonium feldspar

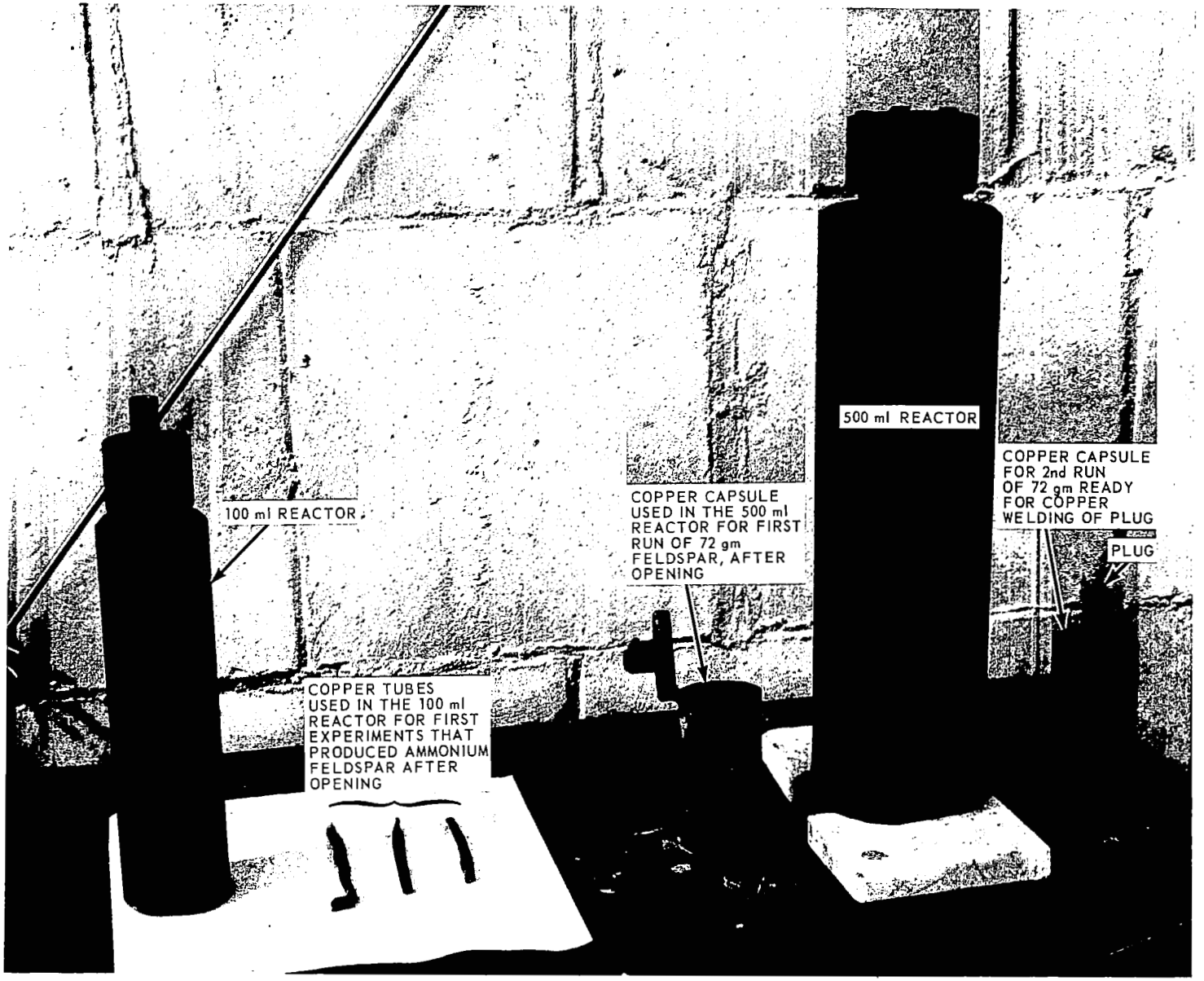

Figure 2-4 Reactors and Copper Capsules Used for Producing Ammonium Feldspar

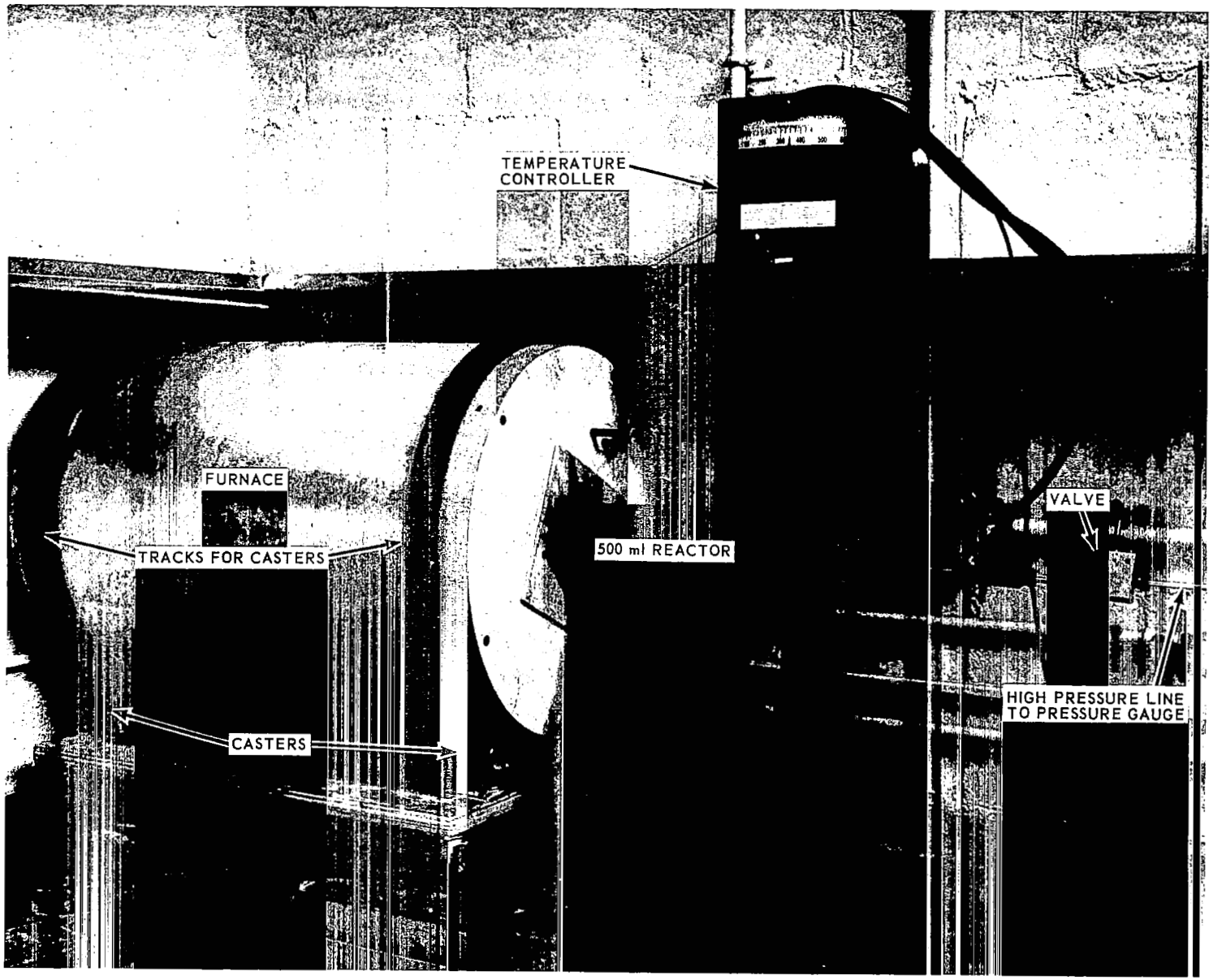

Figure 2-5 Experimental Apparatus Assembled and Ready to be Placed in Furnace

conditions contemplated. Several attempts to achieve a seal with only water in the reactor failed. It was concluded that the steel of the main nut, which is different from the steel of the body, was selected so that accidental overheating would cause enough differential expansion to provide a pressure relief, preventing an explosion from too great a buildup of pressure. This was confirmed by consultation with the manufacturer of the reactor. The sealing surfaces were refinished, and it was found that the reactor could maintain a pressure of at least 10,000 psi at 350°C.

Because of this appreciably lower temperature, it seemed likely that a longer time would be required to synthesize the ammoniated feldspar and/or that the nature of the solution would have to be changed. Investigations were then conducted in the 100-ml reactor to establish procedures.

Two samples were prepared. One sample contained anorthoclase in a pH9, 16-2/3%, NH_4Cl solution. The second contained anorthoclase, 1 gm of NH_4Cl, 2 m of H_2O, and sufficient NH_4OH to bring the pH to 8.5. In both cases, the NH_4Cl seemed to buffer the solution and prevent the attainment of a high pH, without diluting the solution too much. The samples were sealed in copper capsules, placed in the 100-ml reactor, and subjected to 350°C and 10,000 psi for 48 hr. Infrared spectrograms were made of the feldspar resulting from these tests.

The feldspar in the first sample was unchanged but that in the second had been converted to an ammonium feldspar.

Following this synthesis, a test of the 500-ml reactor was made. In this test, a mixture (which becomes a homogeneous solution at elevated temperatures) containing one part NH_4Cl to two parts H_2O brought to pH 8.5 with NH_4OH was placed in the reactor itself and heated at 350°C. The solution leaked out. It might have been due to rapid heating of the outside of the reactor, causing just enough expansion away from the cooler interior to open a minute hole. Once the leak started, the solution corroded the steel at two points, producing deeply etched pits. The leak might also have started from corrosion localized at the highest stress points on the sealing surfaces.

2.3.6 Ammoniated Anorthoclase

This failure necessitated extensive remachining and making a new sealing ring for the 500-ml reactor. To prevent a leak from reoccurring, a copper capsule was designed and fabricated. The capsule was filled with

72 gm of anorthoclase, 43.5 gm of NH_4Cl. 91 ml of H_2O, and 3.8 ml of concentrated NH_4OH. A copper screw was inserted in the hole forming part of the cover and copper welded in place. The capsule was placed in the reactor and heated to 350°C. Water was pumped in the reactor to maintain the required pressure.

Prior to this run, the furnace was fitted with encircling tracks and supported on casters to permit rotation of the furnace. This provided for adequate mixing of the anorthoclase with the solution and allowed the reaction to proceed at a reasonable rate.

The first morning, the reactor reached a pressure of 2400 psi at 350°C and was subsequently pumped to 10,000 psi. The pressure dropped slowly during the day but was pumped back to 10,000 psi. By the next morning, the pressure had dropped to 8500 psi. This procedure of pumping back to pressure was continued for seven days. On successive days, the pressure-drop gradually decreased, suggesting that the drop was due to deformation of the copper capsule and not to a leak. During the last five days, the pressure did not drop below 9400 psi. The reactor had been turned over one to three times daily during this week.

When the reactor and capsule were opened, it was found that appreciable conversion of the anorthoclase to ammonium feldspar had occurred. Samples of the feldspar were tested by X-ray diffraction and infrared spectrogram. Both indicated partial conversion to ammonium feldspar. Because of the variable grain size of the original anorthoclase, it was desirable to determine whether the replacement of the potassium ion by the ammonium ion was uniform, i.e., whether large grains contained the same percentage of ammonium as did the small grains. This was done by making diffraction and infrared patterns of some of the very fine ammoniated feldspar which remained in suspension during the washing of the feldspar to cleanse it from the NH_4Cl solution. This fine elutriated material was recovered by filtration. Their patterns showed markedly more ammonium than the sample containing all sizes, indicating a greater percentage of replacement of the fines. Since replacement proceeds from the grain surface, and all grains were equally affected, it is implied that only the surface layers of larger grains were affected.

For comparison, diffraction and infrared analyses were made of the untreated anorthoclase, including crushed bulk, elutriated fines, and coarse-sieved material. In addition samples of these materials were carefully weighed, heated, and reweighed to determine the combined percentages of NH_3 and H_2O lost. The results were as follows:

1. Elutriated fines lost 5.31% NH_3 and H_2O by weight

2. Crushed bulk lost 2.18% NH_3 and H_2O by weight

3. 120 to 240 mesh lost 1.15% NH_3 and H_2O by weight.

A fully ammoniated feldspar would lost 13.16% NH_3 and H_2O by weight during heating; therefore, these samples are 40%, 16-1/2%, and 8-3/4% ammoniated, respectively, based on the assumption that the ratio of ammonium ion to zeolitic water in the partially ammoniated feldspar is 2 to 1, as in the fully ammoniated feldspar.

The 72 gm of ammoniated feldspar were subsequently freed from copper and from some of the iron oxides by flotation with heavy liquids. Some material was lost during this treatment.

2.3.7 Ammoniated Orthoclase

Following the 17 June 1965 meeting in Houston, work began on the production of a small amount of high-purity ammoniated feldspar. This necessitated reconditioning the seals and replacing the seal ring on the 100-ml reactor. The highest purity feldspar available from The University of Michigan Mineralogical Museum was obtained for this purpose. The specimen, 2.5 gm of ferriferous orthoclase from Madagascar, was ground to pass through a 300-mesh nylon screen. Each of three gold capsules were then filled with 0.75 gm of orthoclase, 0.05 ml of concentrated NH_4OH, 0.40 ml of H_2O, and 0.18 ml of NH_4Cl. After the capsules were sealed, they were inserted into the 100-ml reactor, together with enough water to equalize the pressure inside the capsules. The reactor was heated for seven days at a temperature of 475°C and a pressure of 9900 psi. At the end of the reaction period, the capsules were opened and the samples removed for analysis. The absorption peaks of the infrared spectrogram and the X-ray diffraction peaks both confirmed the presence of a high percentage of ammonium ion in the resulting feldspar.

2.4 FUSION OF BASALT GLASS

The occurrence of a natural glass on the moon's surface is not unlikely. Such disordered material is very unstable and given extended time, even at the relatively low maximum lunar temperatures, ordering, with the formation and growth of crystallites of feldspar and SiO_2 polymorphs, is likely to occur. It was therefore decided to test a simulated natural glass (anhydrous).

The basalt glass was also produced in the laboratory by Dr. Cloke, assisted by Dr. William C. Kelly. Approximately 300 gm of a natural occurring basalt were crushed into 1/2-in. fragments, placed inside a large graphite crucible, and heated in a Globar furnace at a temperature of 1275°C. After 30 minutes, the basalt fragments had fused into a mass of basalt glass.

2.4.1 Optical Microscopic Analysis of Basalt

The composition of this basalt, as determined from a thin section (Figure 2-6) of the uniform sample, consists of:

1.	Labradorite laths to 0.4 mm in length	50%
2.	Labradorite zoned phenocrysts, 1 mm	5%
3.	Pigeonite ($2V = 30^{\circ}$, optically positive, birefringence about 0.025). Grains 0.05 to 0.2 mm	30%
4.	Opaque ground mass, devitrified glass	10%
5.	Serpentine, yellow stained after olivine	5%

2.4.2 Preliminary Experiments

A preliminary series of trials was made in which 10-gm samples of crushed basalt were melted in mullite, platinum, and graphite crucibles. The molten basalt reacted with the mullite crucible, and it was extremely difficult to remove the fused basalt from the platinum. The graphite, however, could be easily stripped from the basalt glass after fusion. Since there was no apparent reduction of the iron by the graphite, the graphite crucibles were selected for further production.

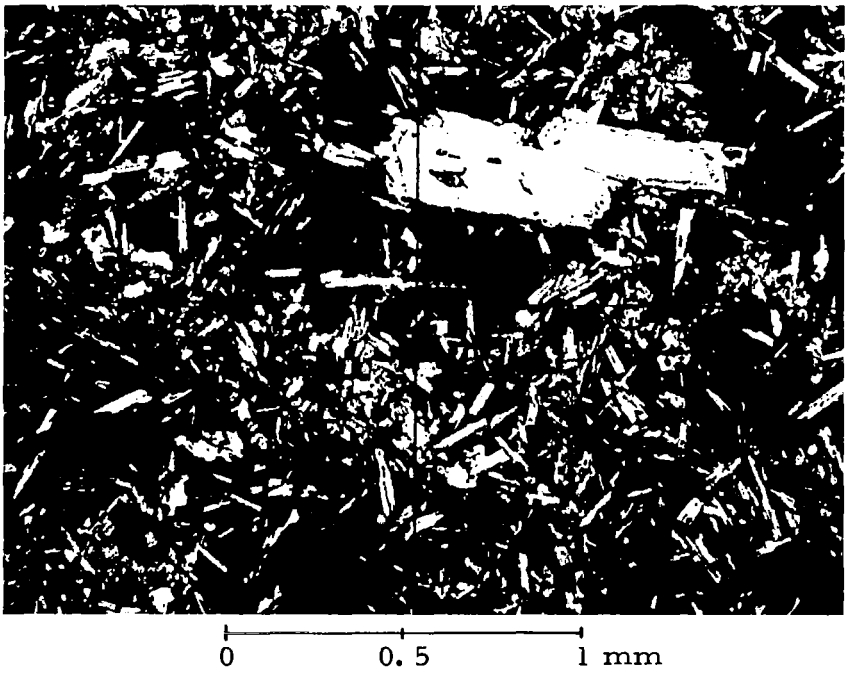

Figure 2-6 Photomicrograph of Basalt, Crossed Polars, 47X

2.4.3 Basalt Glass Production

Three hundred grams of the basalt were crushed into 1/2-in. fragments, and the sample was loaded into a large graphite crucible. The crucible was installed in a Globar furnace and heated at a temperature of 1275°C for 30 minutes. The crucible containing the molten basalt was removed from the furnace and air-cooled to room temperature. The resultant glass was subsequently ground in a dry nitrogen atmosphere.

2.5 IRRADIATION OF PLAGIOCLASE

The irradiated plagioclase was selected for testing in the simulated lunar environment, because it was hoped that the radiation would induce structural disorder which would be detectable in X-ray photographs. The long-term simulation (low pressure and temperature change) of the lunar environment might then have had one of two effects. It could promote reordering, or it could promote other structural changes, such as loss of Na or Ca, since the structure was in a disordered high-energy state.

A pure labradorite was selected for irradiation, ground to 100 mesh, and loaded into quartz tubes. The ends of the tubes were fused to make them watertight, and the samples were irradiated in the Ford Nuclear Reactor at The University of Michigan, a 2-Mw swimming-pool research reactor. A total neutron exposure of 10^{18} neutrons/cm^2 ($E > 0.1$ Mev) was used.

2.5.1 Preliminary Tests

The reactor personnel were wary of irradiating all the samples at one time as they had no previous knowledge of the thermal expansion properties and moisture content of labradorite. As a precaution, they exposed a small sample (64 mg) of 100-mesh labradorite at the core face for 1 hr to estimate the induced radioactivity. Sodium-24 was the main radioisotope produced, arising from two reactions:

$$Na^{23}\ (n, \gamma)\ Na^{24}$$

$$Al^{27}\ (n, \alpha)\ Na^{24}$$

Since Sodium-24 has a half-life of 15 hr, its radioactivity decayed in less than a week. No other prominent gamma-emitting isotopes were detected. A small amount of longer-lived β-activity was noted, however, and attributed to the presence of Calcium-45.

A 30-hr neutron exposure was then made of a tube containing a larger amount of powdered labradorite. Examination of this sample by reactor personnel indicated that all the remaining tubes of labradorite could be irradiated simultaneously for 30 hr with safety.

2. 5. 2 Sample Exposure

A total neutron exposure of 10^{18} neutrons/cm^2 (E > 0. 1 Mev) was used for the sample irradiations. Past studies have shown that 10^{18} neutrons/cm^2 or more are usually required to produce crystalline damage, which can be detected and studied by X-ray diffraction techniques.* The maximum fast-neutron flux in the Ford Nuclear Reactor is approximately 10^{13} neutrons/cm^2/sec (E > 0. 1 Mev). Thus, to achieve a higher total exposure (of 10^{19} to 10^{20} neutrons/cm^2) requires a considerably longer period of irradiation and, consequently, a much greater expense for rental of the reactor.

2. 5. 3 Radiation Hazards

After 30 hr at the core face, the tubes of labradorite were removed from the reactor and allowed to cool (14 days) until the short-lived (15 hr) Na^{24} had decayed to an undetectable level. A 22. 3-mg sample of the irradiated labradorite was counted in a windowless gas flow proportional counter. With an assumed efficiency of 50%, the gross beta activity was calculated at 2. 3 x 10^{-3} μc/mg.

This same sample was also placed on a spectrometer, where the only peaks that could be identified were from Fe^{59} (gamma energy 1. 09 and 1. 289 Mev). The quantity of Fe^{59} was appraised at about 8. 4 x 10^{-6} μc/mg. If it is assumed that all of the beta activity is due to Ca^{45} (half-life of 160 days) a person would have to ingest 12. 9 gm of the irradiated labradorite to consume an amount equal to the maximum permissible body burden, i. e., 30 μc. This assumes a specific gravity of 2. 3 x 10^{-3} μc/mg, as follows:

$$\frac{30\ \mu c}{2.33 \times 10^{-3}\ \mu c/mg} = 12.9\ gm.$$

As an aerosol, a dust load of 1. 2 mg/ft^3 of labradorite would be required to produce the maximum permissible concentration for insoluble Ca^{45}. To prevent the spread of troublesome contamination, it was recommended that the tubes of irradiated labradorite be opened in dead air space such as a glove box.

* A. Guinier, "Mise En Evidence Des DeFauts Cristallins Per Les Rayons X," Radiation Damage in Solids, ed. by D. S. Billington, Proceedings of the International School of Physics (Enrico Fermi), Academic Press, 1962.

2.6 SAMPLE PREPARATION

All mineral specimens, with the exception of calcium-montmorillonite, were received from suppliers in fragments ranging in size from 4 to 10 cm. The two pounds of calcium-montmorillonite arrived as finely powdered material.

2.6.1 Rock Trimmer

A rock trimmer was used to break the large fragments into more workable particles, on the order of 1 cm. Considerable care was taken not to introduce contaminating substances. The larger impurities were removed at this stage.

Samples were then further reduced to 1/2- to 1/4-cm particles. Except for the calcium-montmorillonite and the muscovite, all minerals were crushed to this size in a large porcelain mortar. After crushing, the fragments were screened to an 8-mesh sieve to remove the fines. This was done to prevent contamination of the mineral with abraded porcelain. The crushed material was then transferred to a large watch glass and microscopic (15X) and (in some cases) X-ray diffractometer analyses were performed to assure mineral purity. All fragments showing impurities were discarded. Table 2-3 shows the impurities associated with the minerals.

2.6.2 Mica Books

The preparation of muscovite differed somewhat, because its perfect cleavage and differential hardness make it extremely difficult to crush. Preparation of the muscovite samples entailed splitting the mica books, examining the sheets under a microscope, and reducing the sheets to the 1/4-cm size by cutting with a pair of scissors.

2.6.3 Mortar and Pestle

As shown in Figure 2-7, the processing described above applies to all of the minerals except the calcium-montmorillonite and muscovite. Since the porcelain ball mill (Figure 2-8) which was to be used for the final grinding was incapable of handling particles of a size greater than 8-mesh,

TABLE 2-3

MINERAL SAMPLES AND ASSOCIATED IMPURITIES

Mineral	Impurity
Actinolite	Talc
Anorthoclase	Oxidized Fe and a clayey material
Antigorite	Chrysotile
Basalt	None
Calcite	None
Calcium-Montmorillonite	None
Goethite	None
Gypsum	None
Hematite	None
Labradorite	Rutile
Muscovite	None
Natrolite	Analcite and clay
Talc	None
Tektite	None

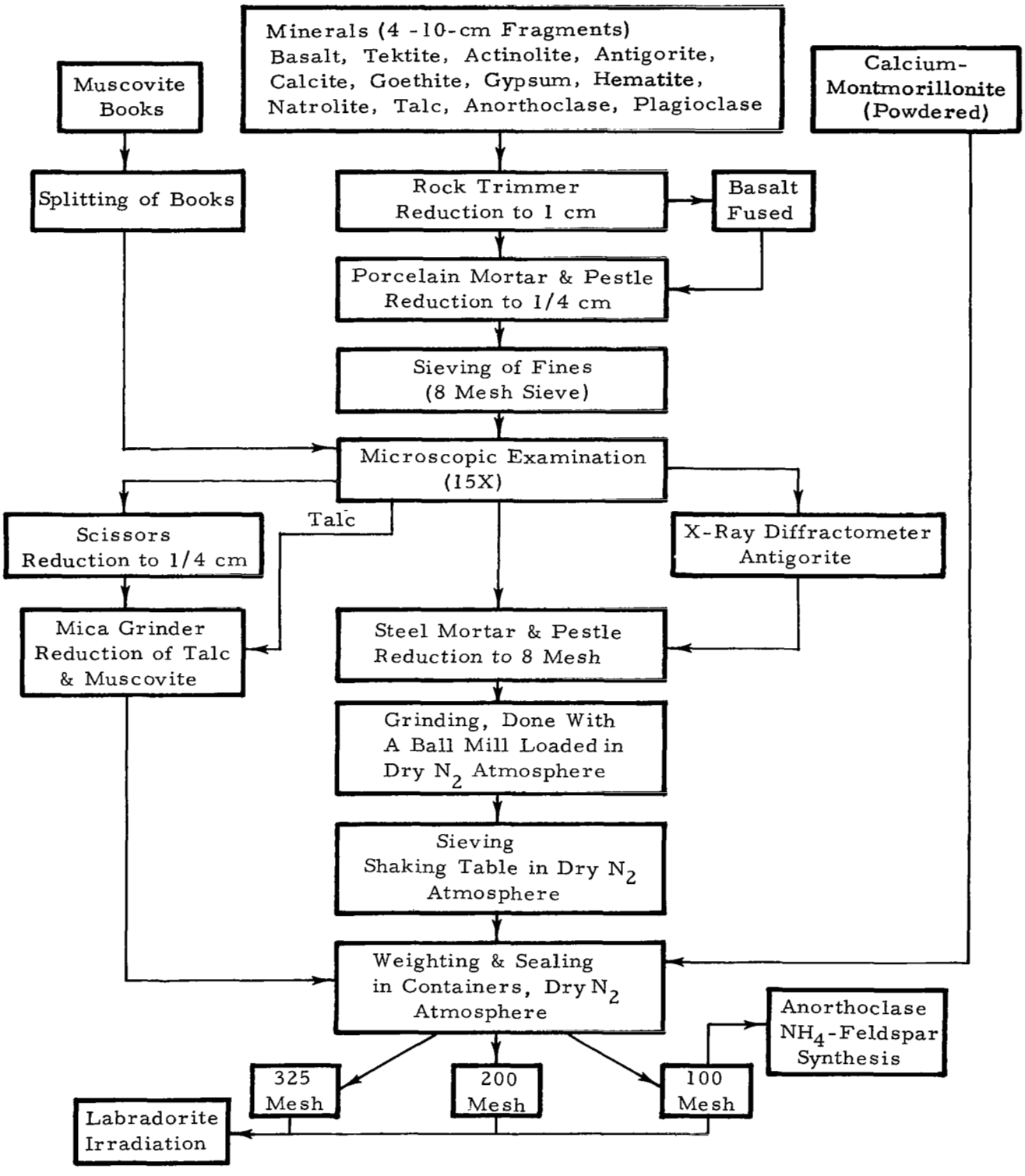

Figure 2-7 Flow Chart of Mineral Processing

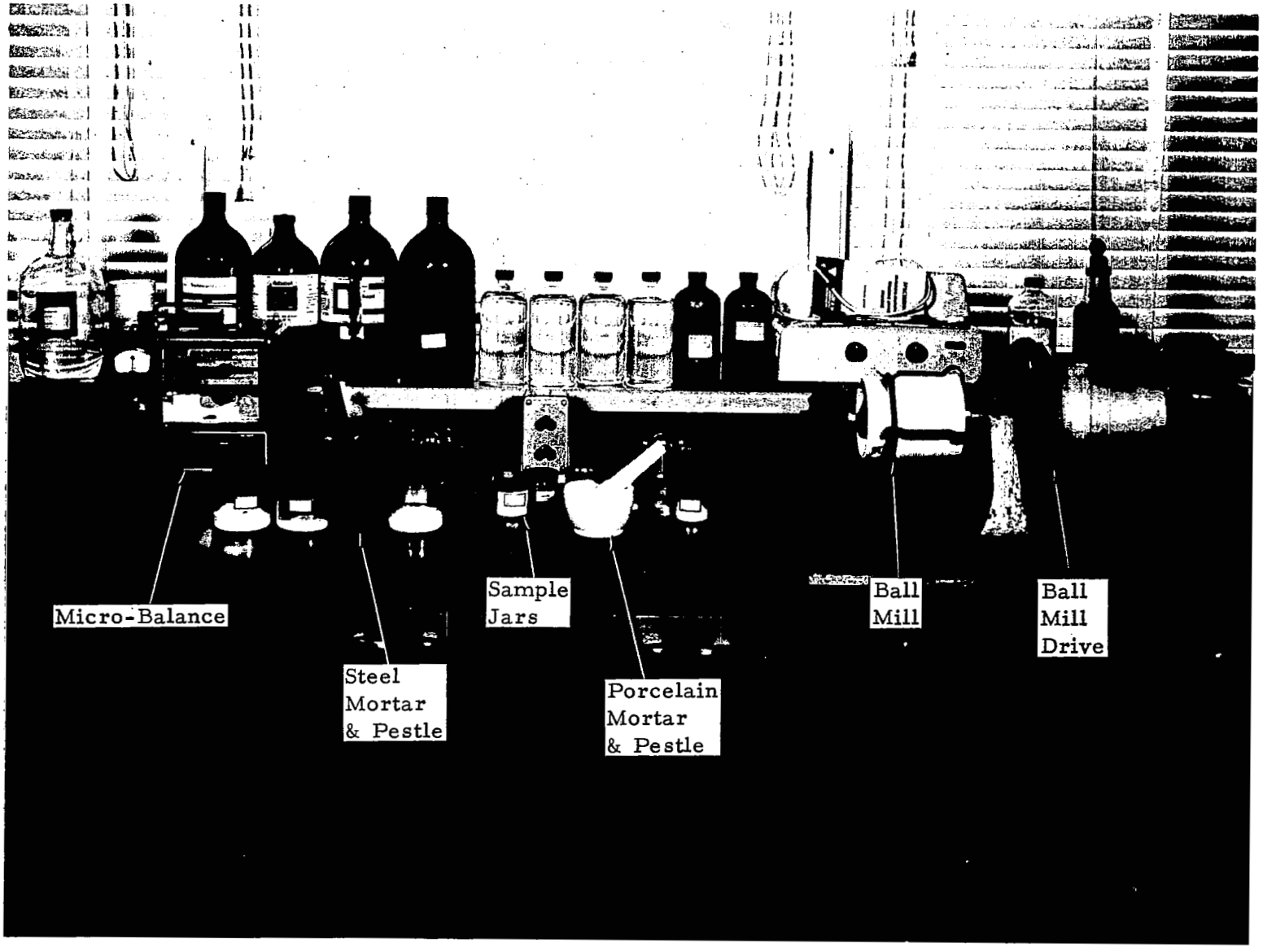

Figure 2-8 Equipment Used to Pulverize and Crush Samples

it was necessary to reduce the mineral fragments still further before final grinding could be initiated. Because abraded porcelain would pass through an 8-mesh sieve along with the mineral sample, comminution to this size was accomplished through the use of a small tool-steel mortar and pestle, thus precluding contamination. A silicon-carbide abrasive was used to clean oxidized Fe from the crushing surfaces of the steel mortar and pestle.

Particles of a size less than 8-mesh have a tendency to absorb water (this tendency increases inversely with particle size). Therefore, all further reduction was carried out in a dry nitrogen atmosphere within a dry box. See Figure 2-9.

Preparatory to final grinding, two minerals were placed in the dry box along with the two porcelain jars, a supply of porcelain balls, and two large watch glasses. The box was then sealed and dry nitrogen bled in at the rate of 1/2 ft^3/min. The box contains a volume of about 12 ft^3, so the inflow of dry nitrogen continued for about an hour until about 30 ft^3 of the gas had displaced the air and moisture in the box.

Thereafter, a 200-gm portion of each sample to be ground was spread out on a watch glass and continuously agitated for about five minutes. This reduced the amount of air and moisture which had already been adsorbed on the particles.

2.6.4 Ball Mill

The mineral fragments were then transferred to the porcelain jars, and charges of a 50/50 mixture of 1/2-in, and 1-in. porcelain balls were added. The size of the charge (generally proportional to the density of the substance being ground) was selected to prevent the porcelain balls from contacting and abrading one another.

The jars were sealed, removed from the dry box, attached to the ball mill drive assembly, and rotated at 75 rpm. Generally, the reduction to 100-, 200-, and 325-mesh fractions required 24 hr of grinding. For some of the harder minerals, the grinding process required 48 hr, interrupted by an occasional sieving of the fines.

Talc and muscovite cannot be properly ground in a ball mill unless an extended period of time is available. These minerals were therefore

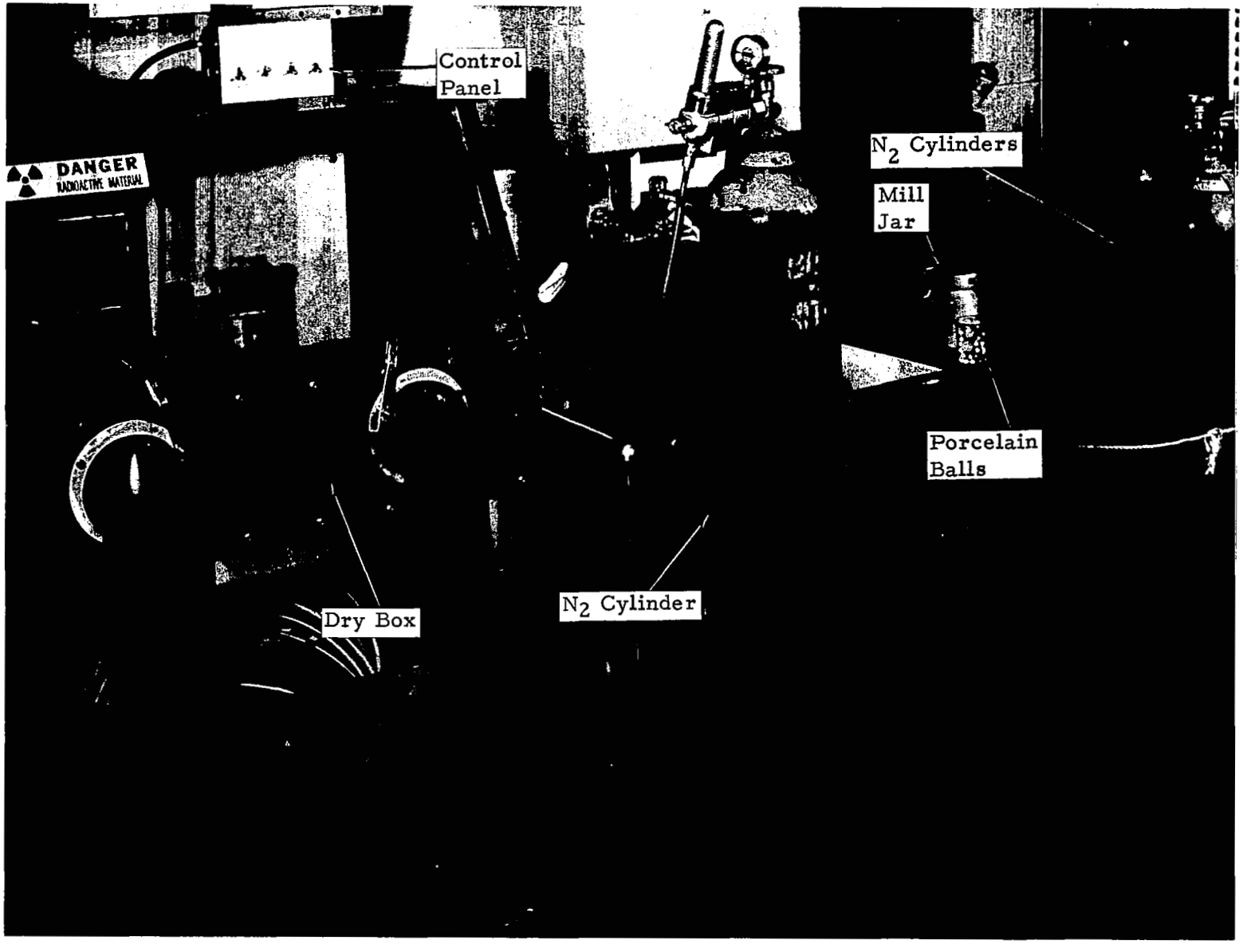

Figure 2-9 Sample Preparation in Dry N_2 Atmosphere

ground in a mica grinder. The grinding was done at ambient conditions, but subsequent sieving was performed in the dry box, where the presence of the dry nitrogen helped remove some of the water adsorbed during grinding.

2.6.5 Sieving

After 24 to 48 hr of grinding, one of the jars was removed from the drive assembly and sealed in the dry box with a set of Spex plastic sieves. After the nitrogen had been allowed to displace the air and moisture, the jar was opened. The sieves were then stacked in order from top to bottom (100-, 200-, 325-mesh), and a charge of the ground mineral was added to the top sieve. The stack of sieves was installed on the electric shaking take, and the charge was reduced to its various fractions. See Figure 2-10. After the sieving operation was completed, portions of the screened particles were weighed on a torsion balance and stored in glass jars and vials. Table 2-4 shows how the different fractions were used in this study.

The glass jars and vials containing the samples were removed from the dry box, and the spill was cleared away. The plastic sieves were dismantled and cleaned, and the nylon screens were replaced with new ones. This procedure helped eliminate the possibility of cross-sample contamination. The sieves were returned to the dry box with the second mineral; the box was sealed; and the sieving and weighing operation was repeated.

TABLE 2-4

DISTRIBUTION OF MINERAL FRACTIONS BY GRAIN SIZE AND USE

Mesh	Quantity (gm)	Use
100	100	NASA-MSC
	20	Index sample for chemical analysis
	5	Vacuum sample for chemical analysis
200	1-5	Mass-spectrometer analysis
	1-2	DTA and TGA
325	1	X-ray samples in ambient and vacuum

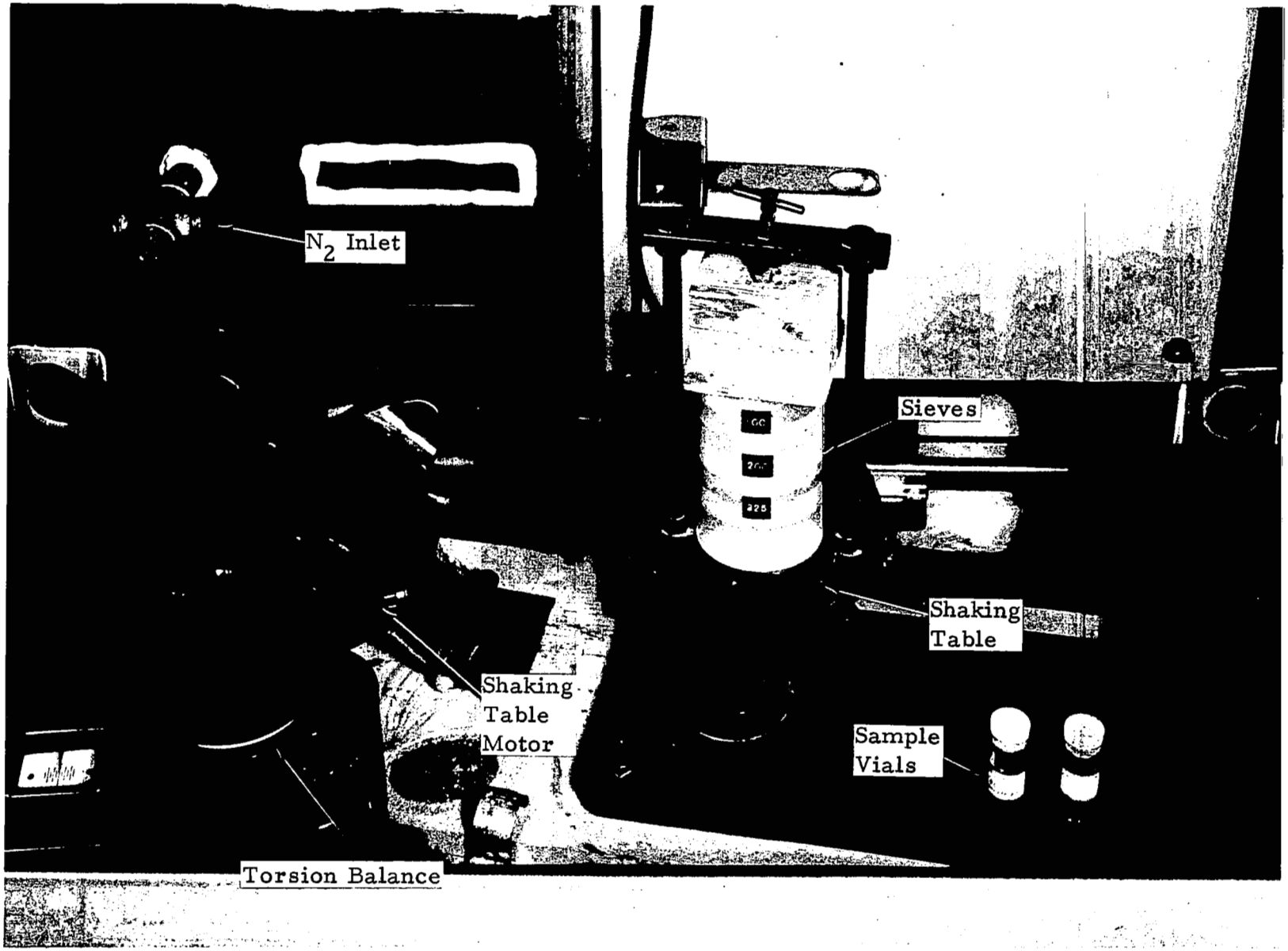

Figure 2-10 Interior of Dry Box

SECTION 3

EQUIPMENT AND TEST PROCEDURES

This section describes the equipment and procedures used in performing the test experiments on the 14 minerals. Test results are not included in this section. All test results are presented in the section having the appropriate mineral name heading.

3.1 OPTICAL MICROSCOPIC ANALYSIS

Thin sections of the following specimens had been prepared by Mrs. George Rev, Columbia University:

1. Actinolite
2. Anorthoclase - used in the synthesis of NH_4 feldspar
3. Antigorite
4. Basalt - used in the fusion of basalt glass
5. Basalt glass
6. Geothite
7. Hematite
8. Labradorite - used in the irradiation of plagioclase
9. Natrolite
10. Talc
11. Tektite.

No thin sections were prepared for calcite, calcium-montmorillonite, gypsum (selenite), and muscovite. All but the montmorillonite are clear single crystals. The montmorillonite specimen was received as finely powdered material. As thin sections of these specimens would provide no additional information, temporary grain mounts were made instead for refractive index determinations of these and certain other minerals. The refractive indexes are accurate to ±0.002 and were made with sodium light. Where refractive indexes were taken between crossed polars, a statement to that effect is made.

3.2 DIFFERENTIAL THERMAL ANALYSIS (DTA)

For the DTA run, the sample cavity in the furnace block was filled with nondiluted minerals. All minerals had been ground in dry nitrogen to pass 200 mesh except the muscovite and talc, which were ground in atmosphere, and the calcium montmorillonite, which was used as received. The reference material was 90% Al_2O_3 mixed with 10% quartz, so that the "inverted" quartz peak provided a temperature calibration on each record. Room temperatures ranged from 20 to 22°C, and the relative humidity was estimated at 40 to 50%.

As the nature of DTA curves depends to a large degree upon the physical details of instrumentation, and because there is no general agreement upon procedure for gathering and reporting the data, the pertinent aspects of the instrument used are described below.

A test sample, ranging in weight from 50 to 350 mg, was placed in the 1/4-in. cavity in a nickel block (Figure 3-1). The reference material was then placed next to it, in a similar cavity in the same block. The temperature difference between the reference material and the powdered mineral was measured by Pt vs. Pt 10% Rh thermocouples, 28 gauge. The furnaces (Figure 3-2) are wound with 77 turns of Chromel-A, 18 gauge, on 2-in. outside diameter (OD) McDanel AV 30 Alumina tubes. Armstrong bricks insulate the furnaces. The furnaces are operated in air with no scavenging other than that provided by thermal air currents.

Temperature measurements were recorded (Figure 3-3) by a galvanometer recording optically on a drum of photographic paper driven at a constant rate. Sensitivities of 100, 30, 10, and 5 μv/cm galvanometer deflection were available. The galvanometer was critically damped. Furnace temperatures were measured by means of a Chromel-Alumel couple in the

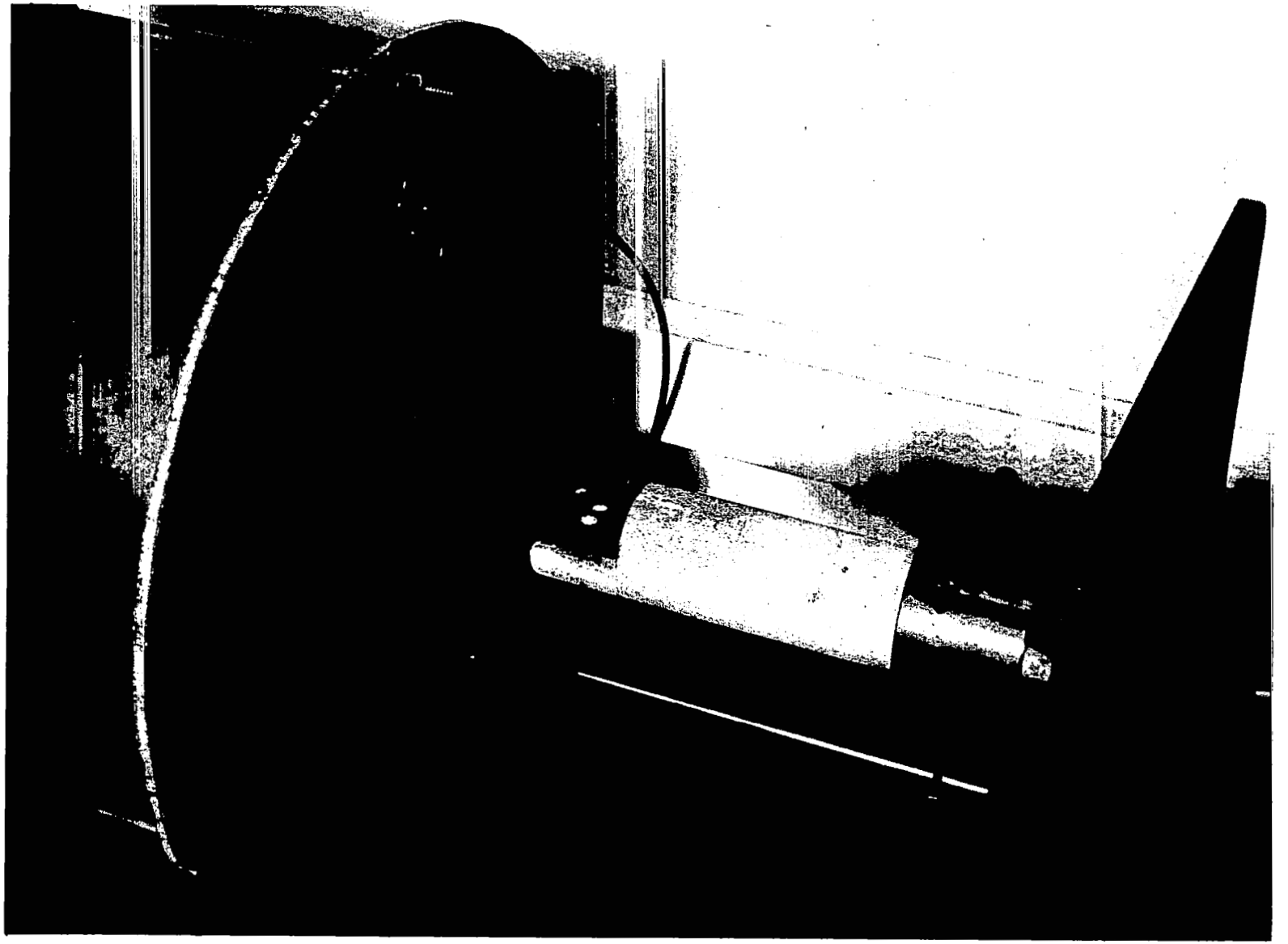

Figure 3-1 Nickel Block Loaded With Mineral and Reference Material

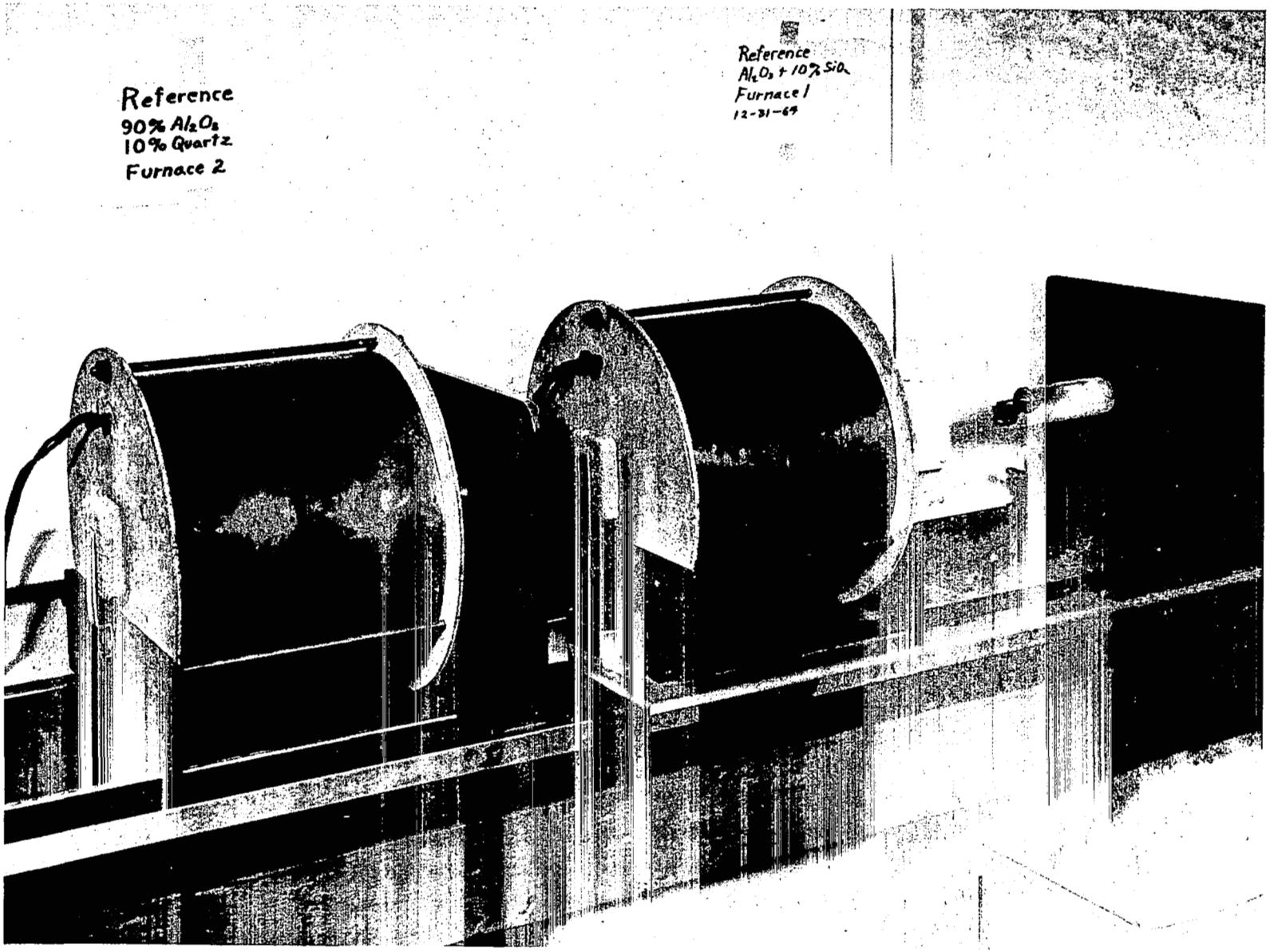

Figure 3-2 DTA Furnaces: #2 in Operating Position; #1 Open, Exposing Block

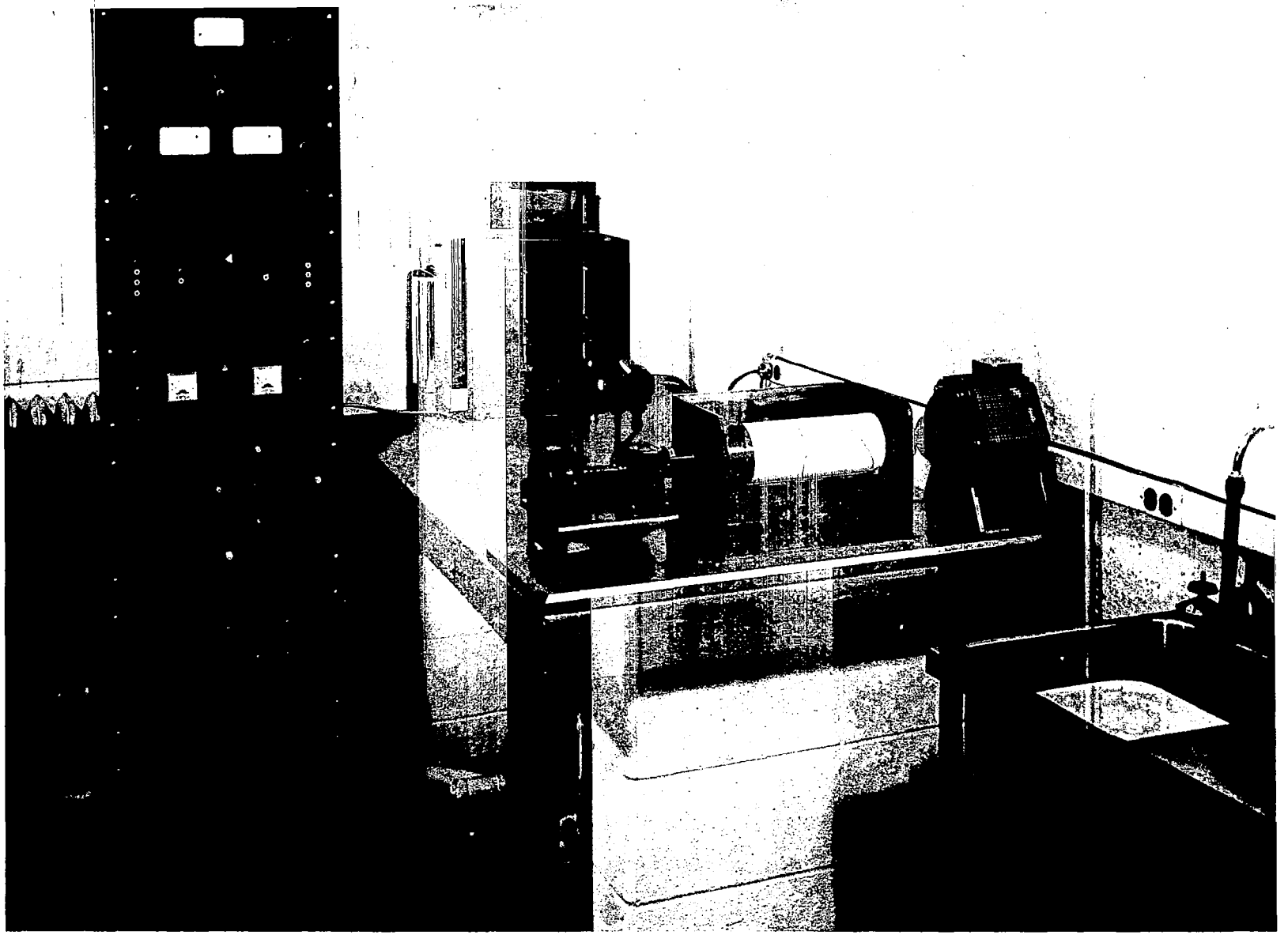

Figure 3-3 Temperature Recording System

nickel block. The cold-reference junction was placed in water in a thermos flask. The water temperature was read to 0.1°C with a mercury thermometer.

The furnace temperature was increased at about 13°C/minute over the temperature range of 100 to about 1000°C. Control was achieved by a synchronous motor-driven variable autotransformer which linearly increased the voltage from about 65 to about 130 v in 88 minutes. This produced a very nearly linear temperature increase as a function of time.

Furnace temperature calibration was accomplished essentially as described by Faust*. A temperature calibration point at 573°C of the reference sample, composed of 90% Al_2O_3 and 10% quartz by weight, is included on each DTA curve.

The recorded temperature was measured in the nickel block, and the calibration was within the reference material. The actual sample temperature during reaction may be obtained by adding the appropriate ΔT to the recorded T. In practice, reaction temperatures are reported at peak values, corrected for nonlinearity of couple response but not corrected for sample temperature. The accuracy of the data is ±5°C or better.

The temperature differences corresponding to 1-cm DTA galvanometer deflection for the sensitivities used may be obtained from the calibration curve shown in Figure 3-4. By way of comparison, the following peak heights are obtained from the low-high quartz inversion:

Scale (μv/cm)	Height (cm)
100	0.1
30	0.3
10	1.0
5	2.0

3.3 THERMOGRAVIMETRIC ANALYSIS (TGA)

Mineral samples, in about the same amounts as used in the DTA runs, were suspended in a vertical furnace similar to the DTA furnaces. A

*Am. Min., 1948, V. 33, pp. 337-345.

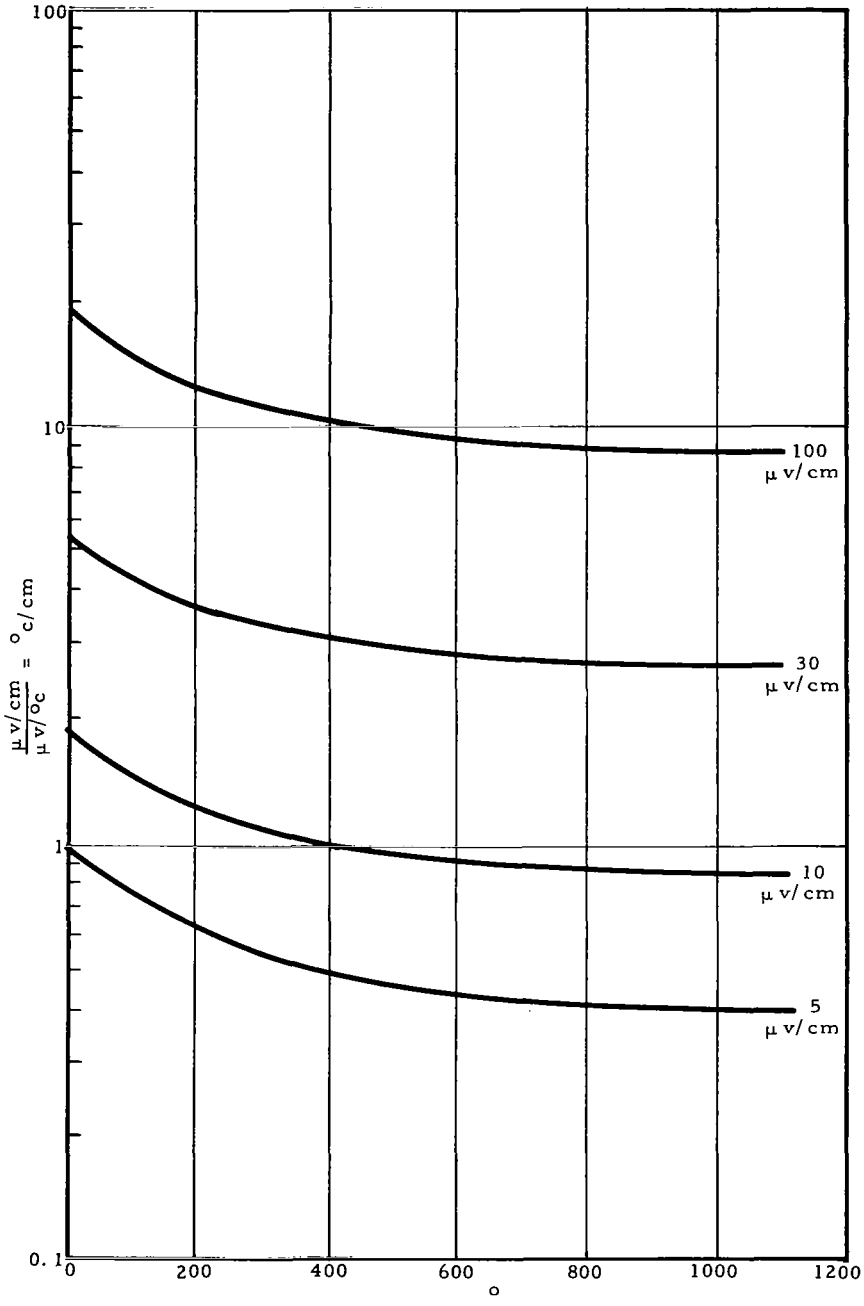

Figure 3-4 Calibration for Measurement of ΔT Pt vs. Pt 10% Rh

Chromel-Alumel thermocouple was placed about 5 mm below the platinum bucket which contained the sample. The heating rate and the temperature recording were the same as for the DTA.

Weight recording was accomplished through the same galvanometer that was used for the DTA recording. The thermogravimetric balance (Figure 3-5) used is a knife edge analytical balance. It is of deflecting-beam design with magnetic damping. A mirror controls the position of a light beam which illuminates a cadmium sulfide cell in a bridge circuit supplied by a pair of mercury cells.

The light source, a 6-v lamp operated at about 230 ma, was powered by an automobile storage battery which is charged through a silicon diode, resistance lamps, and a small variable autotransformer. Photocell monitoring of the blocked balance beam showed the light output to be free of long- and short-term drift.

During heating, a drift of about 1.65 mg apparent weight loss during a normal run was obtained which was due to air currents in the vertical system. Weight change was measured to an accuracy of ● 1 mg with a sample load of 100 mg.

Initial temperature calibration was done by placing a DTA couple in quartz in the sample bucket. The results were checked against the well-known calcium oxalate monohydrate pyrolysis curve. Accuracy is estimated at $\pm 10^{\circ}$C or better.

3.4 MASS SPECTROMETER ANALYSIS

The objectives of this analysis were: (1) to determine the stability characteristics of the 14 test samples under the extremes of high temperature and low pressure, and (2) to identify the constituents being volatilized. Moreover, in contrast to their calculated stability under equilibrium conditions, these experiments revealed the behavior of the specimens under dynamic conditions. The mass spectrometer used in this investigation was the Bendix Time-of-Flight (TOF) Mass Spectrometer (Figure 3-6).

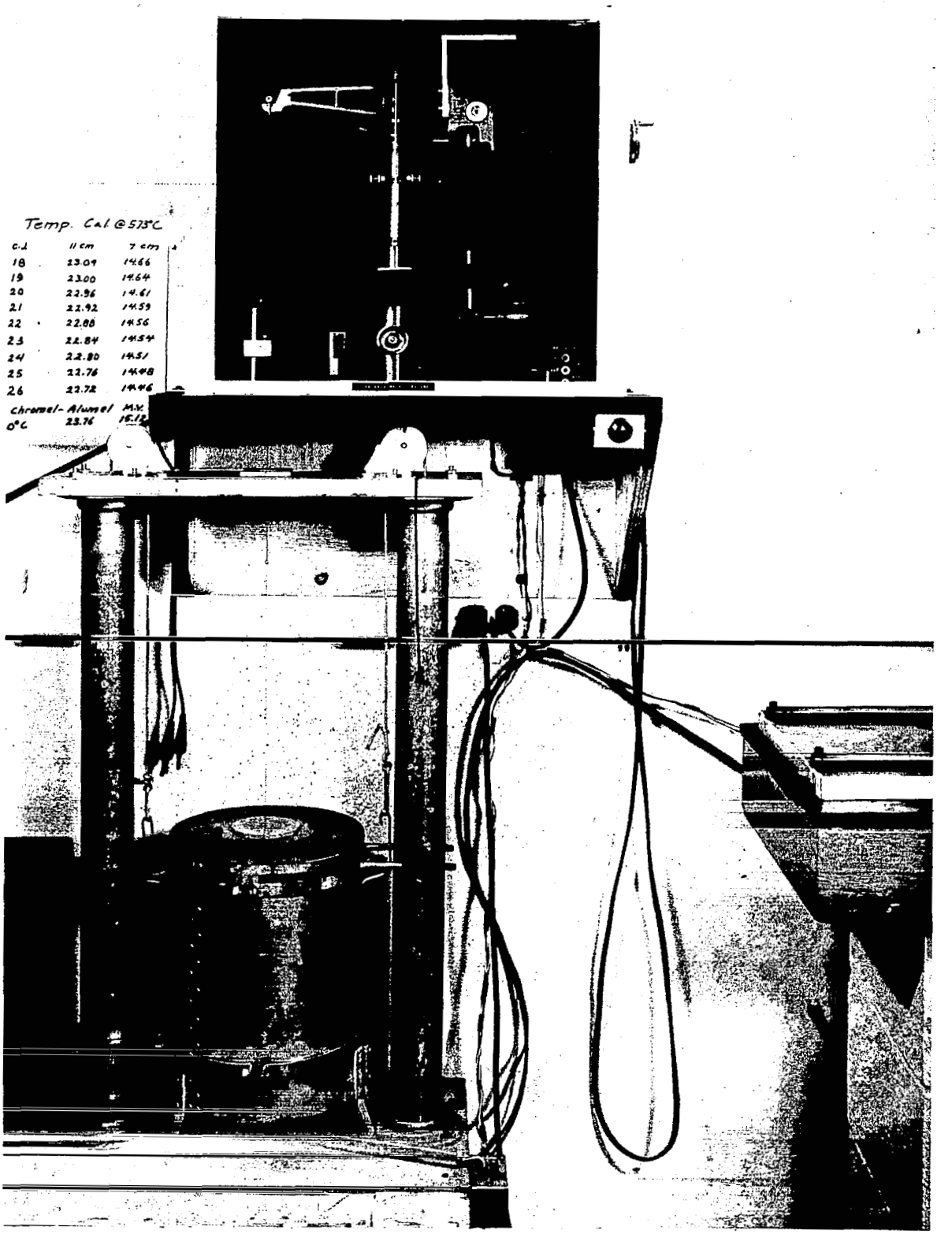

Figure 3-5 Recording Balance and Furnace for TGA

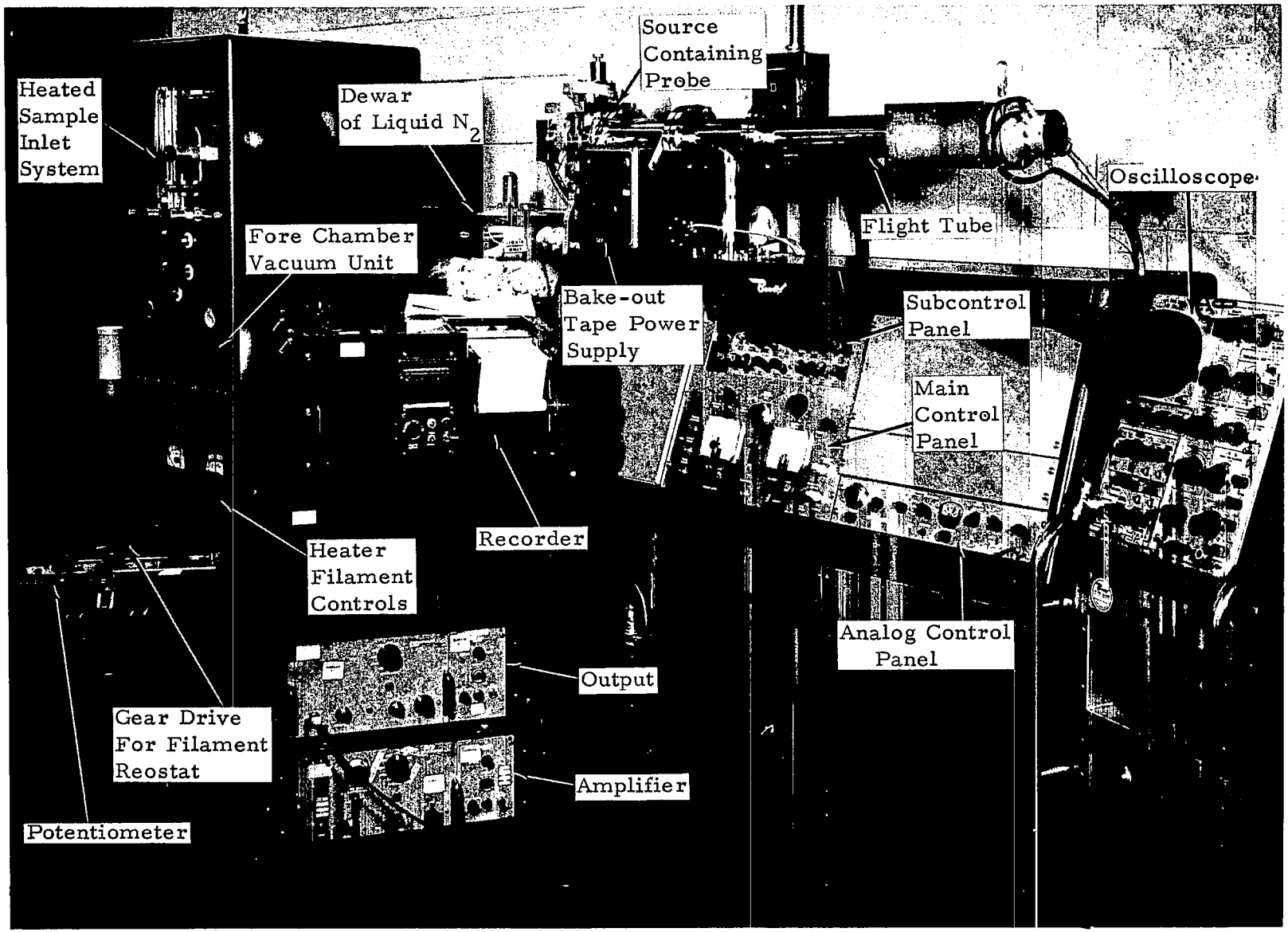

Figure 3-6 General View of Bendix TOF Mass Spectrometer and Auxiliary Equipment

3.4.1 Bendix TOF Mass Spectrometer

The Bendix TOF Mass Spectrometer consists of four basic elements: (1) an ion source to produce ions of the molecular species entering the ionization region, (2) a grid system that draws the ions from the ion source and accelerates the ions down the drift tube, (3) a drift tube for confining the ion "packet" and supplying the distance required to separate ions according to mass/charge ratio, and (4) an ion detector to collect the ions and measure their intensity.

The material to be analyzed is heated in a quartz crucible that rests in the coils of a tungsten filament. The center of the crucible is sealed, forming a lower section where a Chromel-Alumel thermocouple is inserted, and an upper section which contains the mineral sample. As the temperature rises, vapors are generated directly in the source region and rise into the path of an electron beam, which passes across the top of the crucible normal to the centerline. The electron beam, which lasts a fraction of a microsecond, ionizes the molecules. After this beam is turned off, the grid system is pulsed by a fixed potential of 2700 v to eject the resulting ionized molecules into the accelerating region.

It has been established that the time of flight for an ion is a function of its mass and charge. If the electron beam is energetic enough to singly ionize a molecule, the time of flight is reduced to a function of mass. That is, the time of flight is a function of the square root of twice the atomic weight: $T = K\sqrt{2M}$. If, however, the ion is multiply charged, the time flight is expressed as $T_n = K \frac{\sqrt{2M}}{n}$, where n represents the charge. K is a constant depending upon physical dimensions.

As a consequence, the ions reach the collector cathode at the end of the drift tube in ion groups of the same mass. As each of the ion groups strikes the collector cathode, a release of secondary electrons occurs. These secondary electrons are amplified by means of an electron multiplier. The amplified voltage pulse is then delivered to the vertical input of an oscilloscope in the correct mass-time sequence, resulting in a scope spectrum with the mass peaks of the lighter ions on the left and the peaks of the heavier ones on the right. The oscilloscope functions only as an aid in locating particular mass peaks. Quantitative measurements are achieved

through the use of an analog system, which permits the recording of mass spectra or mass ratios. The analog consists of an electrometer, a variable gate pulse, and a scan rate control circuit. This system allows the operator to monitor one mass peak or scan the entire spectrum at variable time rates.

3.4.2 Test Procedure

The procedure followed in analyzing the 14 samples is described below:

1. A new crucible was emplaced in the coils of the heating filament assembly mounted on the end of the probe. (The probe is not visible in Figure 3-6). The probe was then inserted in the fore vacuum chamber, and preliminary pumpdown was begun. After evacuating the forechamber to drift tube pressure (below 1×10^{-6} torr), the ball valve separating the forechamber from the drift tube was opened and the probe was pushed into the source region.

2. The filament power was turned on and the crucible baked out at 500°C for 10 minutes. This was necessary to drive off any volatiles contained in the crucible or adsorbed on the probe head.

3. After bakeout, the probe was withdrawn from the mass spectrometer, and then the crucible was removed and weighed on a Cahan Microbalance. A sample of the mineral (less than 200 mesh) was carefully deposited in the crucible, and both the crucible and sample were weighed. By taring, the sample weight was accurately established. It should be noted that sample weights ranged from 200 to 1200 micrograms (μg).

4. With the crucible returned to the probe and the probe reinserted into the source region, the mass spectrometer was reactivated. The analog system was adjusted to monitor mass peak 18 (water). Pumping continued until the 18-peak returned to a stable level. This indicated that, in general, the moisture accompanying the probe insertion had been pumped out of the drift tube and source region.

5. After the water level had stabilized, liquid nitrogen was added to the cold trap. The gear drive was then connected to the rheostat controlling the filament current, and the filament power was turned on. The gearing of the rheostat increased the temperature at a rate of 6 deg/min. As a result, the average run from ambient temperature (27°C) to 1000°C lasted approximately three hours. The pertinent portion of the spectrum was scanned at intervals of 15°C; temperatures were recorded manually by reading the output from the potentiometer, converting the reading to degrees centigrade, and noting it on the strip chart.

6. Upon completing a run, the crucible was again weighed to determine the weight loss of the sample, and the chart was examined for increases in certain mass peaks or the appearance of new peaks. If the latter occurred, the composition of the substance was identified and another run was made on the same mineral. However, in this run, the scanner was locked on the desired peak. The course of the reaction was followed throughout the temperature rise. This procedure provides the following information, namely, the temperature at which vaporization takes place and the amount of gas given off by the sample which is proportional to the area under a peak height-vs.-time curve.

3.5 X-RAY DIFFRACTION ANALYSIS

The primary objective of this analysis was to evaluate the stability of the 14 test samples while exposed to temperature and vacuum conditions simulating those of the lunar environment. The first part of the investigation was to determine the effects of temperature cycling on mineral stability, whereas the second part was to establish more precisely the temperatures at which changes took place. Phase I concerned all 14 samples; Phase II involved just 6 samples.

To conduct these experiments under thermal vacuum conditions simulating those of the moon, it was necessary to modify an ultrahigh vacuum system with an ultimate pressure of 5×10^{-11} torr, to design and build a thermal control system with a capability of providing the extremes of lunar temperature, and to design and build an X-ray camera that could monitor the samples while they were being subjected to the simulated lunar environment. Many problems were encountered in the vacuum technology, temperature instrumentation, and X-ray photography, but were successfully overcome in the course of the program.

3.5.1 Ultrahigh Vacuum System

X-ray patterns were made on the 14 samples while they were exposed to simulated lunar temperatures and pressure. The samples were installed in an ultrahigh vacuum system (Figure 3-7) manufactured by Varian Associates. The system consisted of a small cross-chamber and a 50 liters/sec ion pump coupled to a titanium sublimation pump of 500 liters/sec. All flanges and connections were copper-gasketed in the "Conflat" configuration. A zeolite trap was connected to the mechanical pump used for initial pumpdown or "roughing". A current meter installed on the base panel measured the ion pump current, which is proportional to the pressure. In addition, a magnetron-type ionization gauge (Redhead) was installed in the vacuum chamber. This gauge is capable of detecting pressures down to the 10^{-13} torr range. The test setup is shown in Figure 3-8.

3.5.2 Bendix X-Ray Camera

A special camera (Figure 3-9) was designed and built that could take X-ray diffraction patterns of the minerals while they were exposed to the vacuum environment of the cross-chamber.

The X-ray camera housing was specially devised to provide a thin beryllium window strip. The beryllium window was required to provide transparency for the X-ray diffraction beam to the film. The beryllium window was bonded to the 304 stainless steel housing with a silver-vacuum furnace braze. The housing configuration is depicted in Figure 3-10.

During Phase I, Ilford X-ray Film was used. It was enclosed in a light-tight envelope and was wrapped around the beryllium window. An 8 to 10 hour exposure time was required to obtain a good pattern. In Phase II, Kodak Royal Blue X-ray Film backed by an intensifying screen was used. A 1-1/2 hour exposure time was required for a photograph of quality equivalent to the Phase I photographs. The Phase II film was processed in a modified Kodak D-19 developer at a temperature of 75°F. More frequent monitoring of the samples was possible than in Phase I.

Photographs obtained using the material of less than 325 mesh were not always satisfactory for all specimens. Although samples were ground to a size usually prescribed for powder photographs, the distribution of sizes was such that there was a large fraction of crystallites with

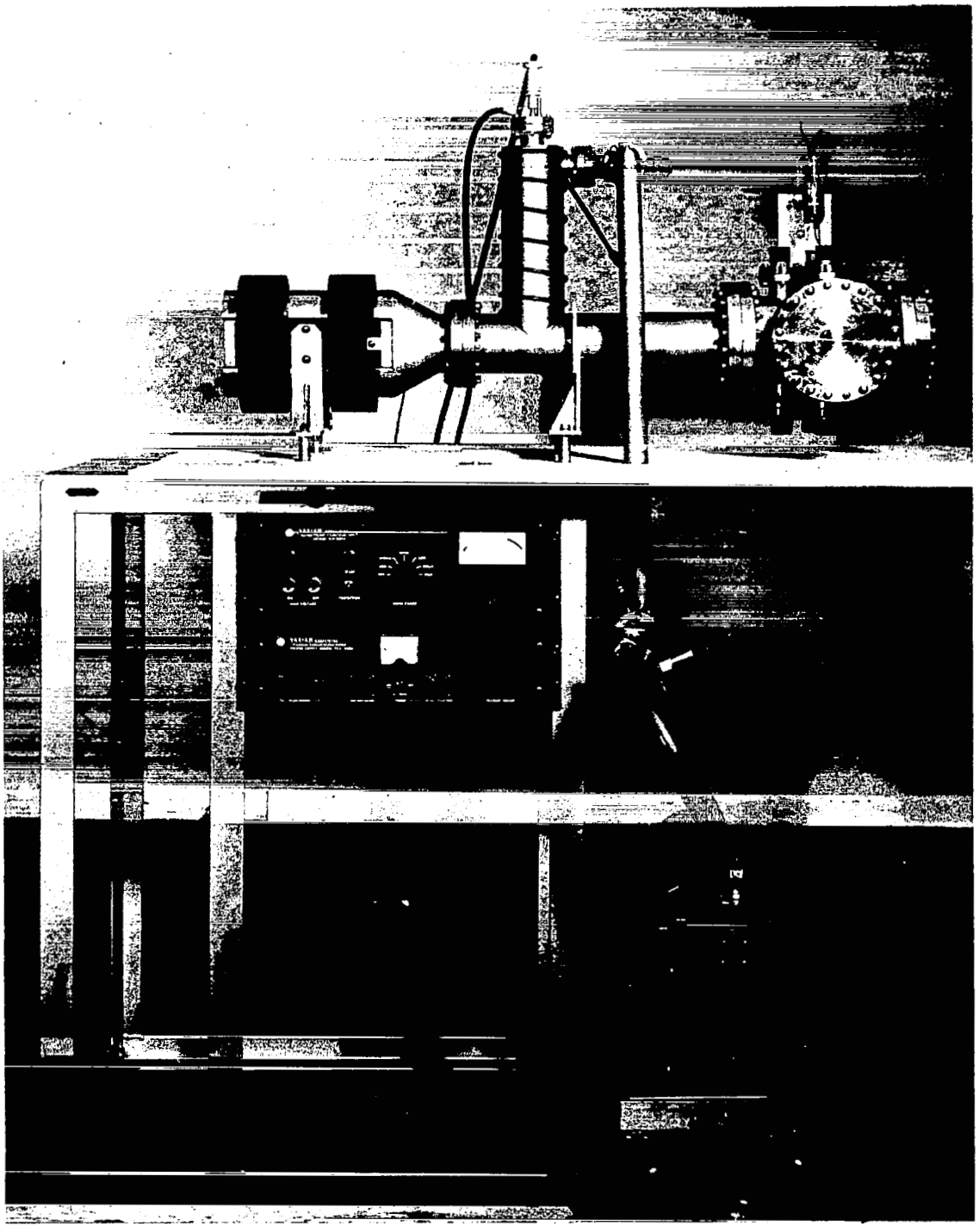

Figure 3-7 Bendix Ultrahigh Vacuum System

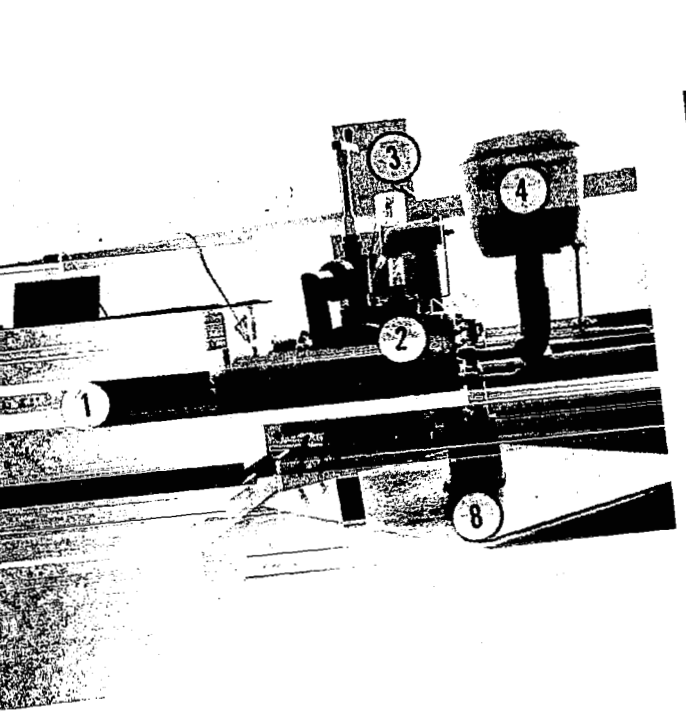

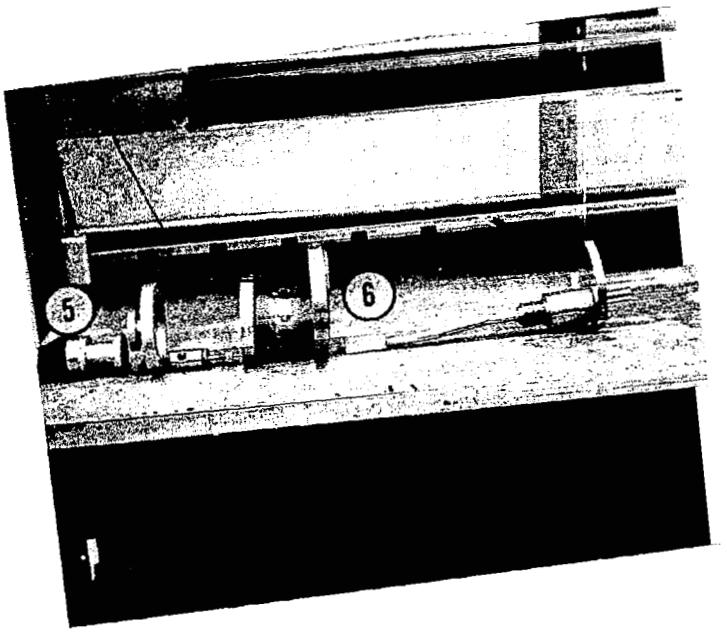

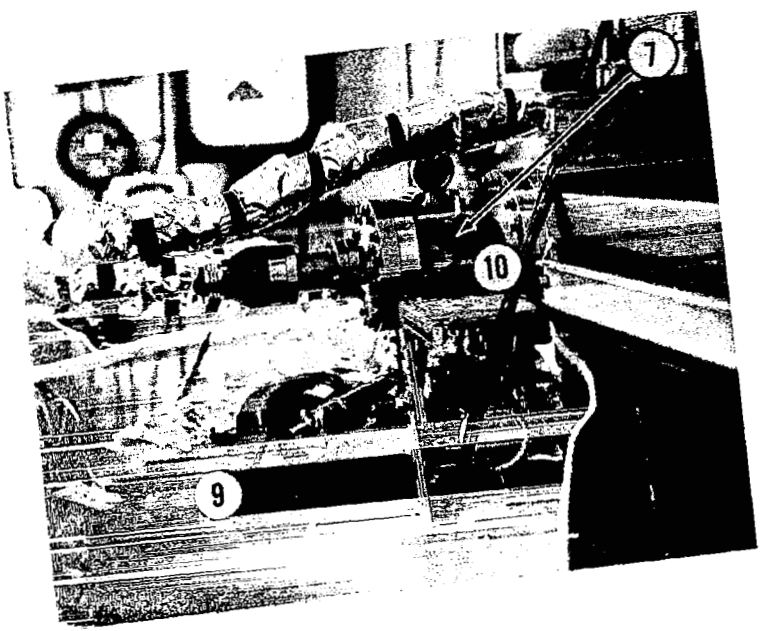

1. Varian Ion Pump, 500 l/sec
2. 6 in. D Vacuum Cross Chambe
3. Redhead Vacuum Tube Gage
4. LN_2 Gryopump Baffle Supply Su
5. Linear Motion Feedthrough
6. Sample Holder
7. Film Holder and Lead Shield
8. X-ray Source
9. Geiger Counter
10. Vacuum Camera

Figure 3-8 Mineral Stability Test Setup (Photos)

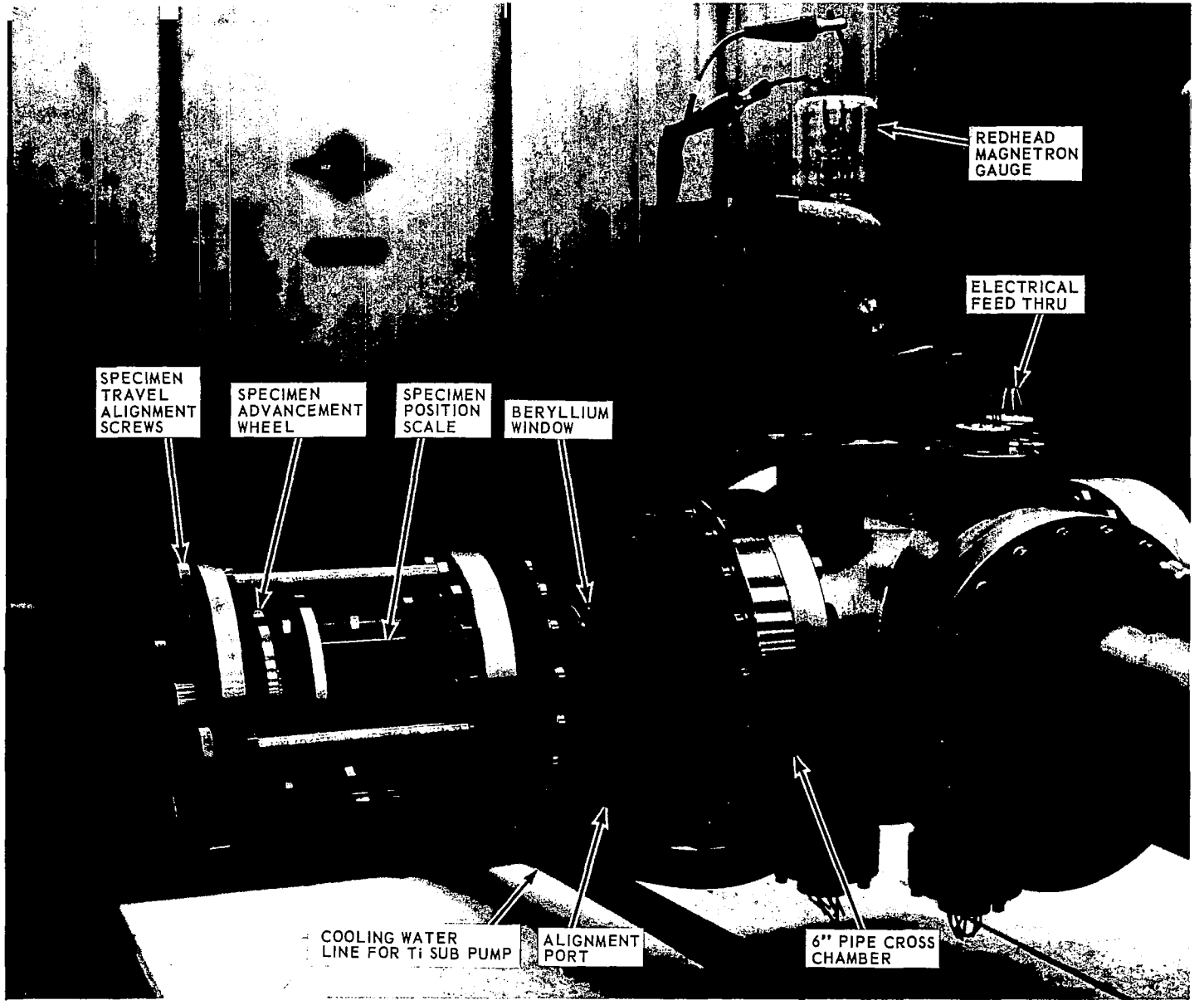

Figure 3-9 X-Ray Camera Unit Attached to Ultrahigh Vacuum System

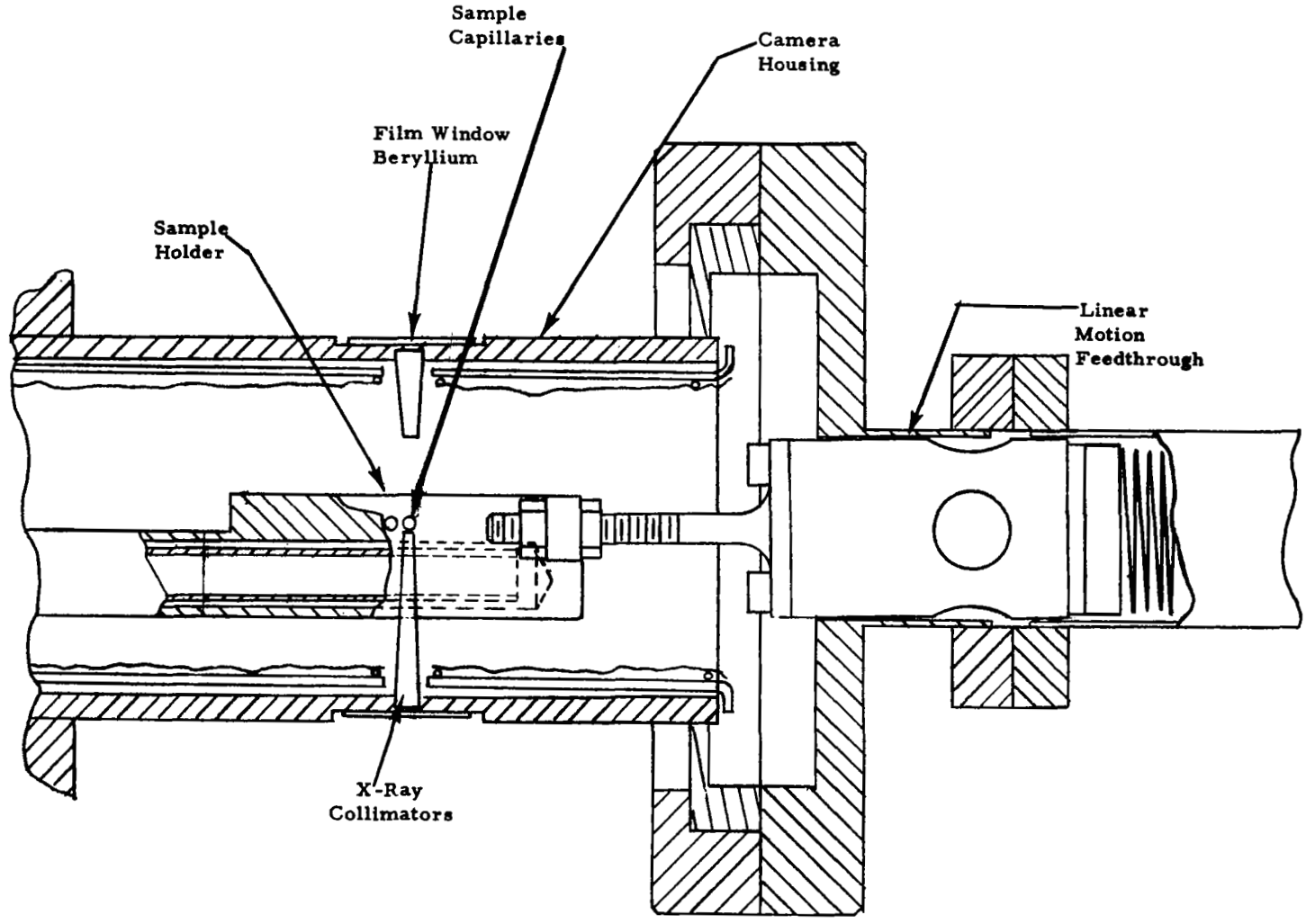

Figure 3-10 Camera Housing and Sample Holder

sizes only slightly less than 325 mesh. Photographs of some samples were very spotty; i. e., powder diffraction lines were very poorly defined. It was necessary, starting with the less than 325 mesh samples, to continue grinding. Grain size was estimated to be at least 500 mesh on the average.

Except for the geothite and hematite, all samples were mounted in 0. 2-mm-diameter glass capillaries. Experiments with various-sized capillaries showed that absorption of the X-ray beam was excessive for larger samples, but it was desirable to place as large a sample as possible in the beam path in order to obtain well-defined powder lines without spots of high intensity from large single crystallites. The 0. 2-mm size with Cu K_α radiation gave optimum conditions for all except the iron oxides, which are highly absorbing. Slightly smaller capillaries were chosen for the goethite and hematite, which were exposed to Mo K_α radiation.

The resulting patterns are all satisfactory with the following qualifications:

1. Because of the inability to rotate samples, a relatively large diameter X-ray beam collimator and large samples were required to obtain well-defined diffraction lines. This has resulted in lines being relatively broad. This effect has undoubtedly been augmented by line broadening as a function of small particle size. The results are entirely satisfactory, however, and well within the predicted limits of broadening.

2. A very few samples, despite the care taken in obtaining minimal grain size, produced some spotty character of the lines. This is particularly true of actinolite where the spots can be attributed to the excellent prismatic cleavages resulting in elongated crystallites, and partially to the preferred orientation of the crystallites. All photographs are readily interpretable, however.

3. 5. 3 Debye-Scherrer Camera

All test samples were photographed with a standard 57. 3-mm-diameter Debye-Scherrer camera. Exposures lasted for approximately 3 hr, except for the tektite and basalt glass. The two exceptions had longer exposures to facilitate the possible detection of small amounts of

crystalline phases. The hematite and goethite photographs were taken with Fe K_α radiation to obtain better line resolution and to avoid fluorescence with iron-containing samples; Cu K_α radiation was used with the other specimens.

The Debye-Scherrer photographs, taken at room temperature and pressure, served a dual purpose:

1. They provided standard patterns as obtained under normal operating conditions. This is particularly important for several of the mineral phases, which under natural conditions show wide ranges in solid solution. Their powder photographs, therefore, were likely to exhibit significant variations from those published in the literature as standard patterns. These variations would undoubtedly be significant in reference to the possible changes brought about by structural or chemical transformations in the simulated lunar environment.

2. They confirmed the identification of each test mineral. The X-ray data substantiated identifications by other methods, such as DTA and microscopic examination. The data also provided information on the nature of contaminating phases, if any occurred. Furthermore, diffraction patterns confirmed the compositional data in those phases which normally exhibit solid solution variations as a function of X-ray line position and relative intensity.

3.6 PHASE II EXPERIMENTS

The Phase II experiments were conducted in the Environmental Laboratory of the Bendix Aerospace Systems Division. The small cross-chamber and X-ray generator from The University of Michigan were used. The X-ray photographs were taken with the Bendix X-ray camera with a special sample holder.

The configuration of the temperature-controlled sample holder which was used in the testing is shown in Figures 3-10 and 3-11. Temperature control was accomplished with counter flowing fluid in the tubular members connected to the sample holder block. In this manner, intimate proximity of fluid and sample capillary was provided. To assure best heat conduction between the glass of the capillary holding the mineral and the stainless steel holder block, aluminum foil was installed around the capillary in the block.

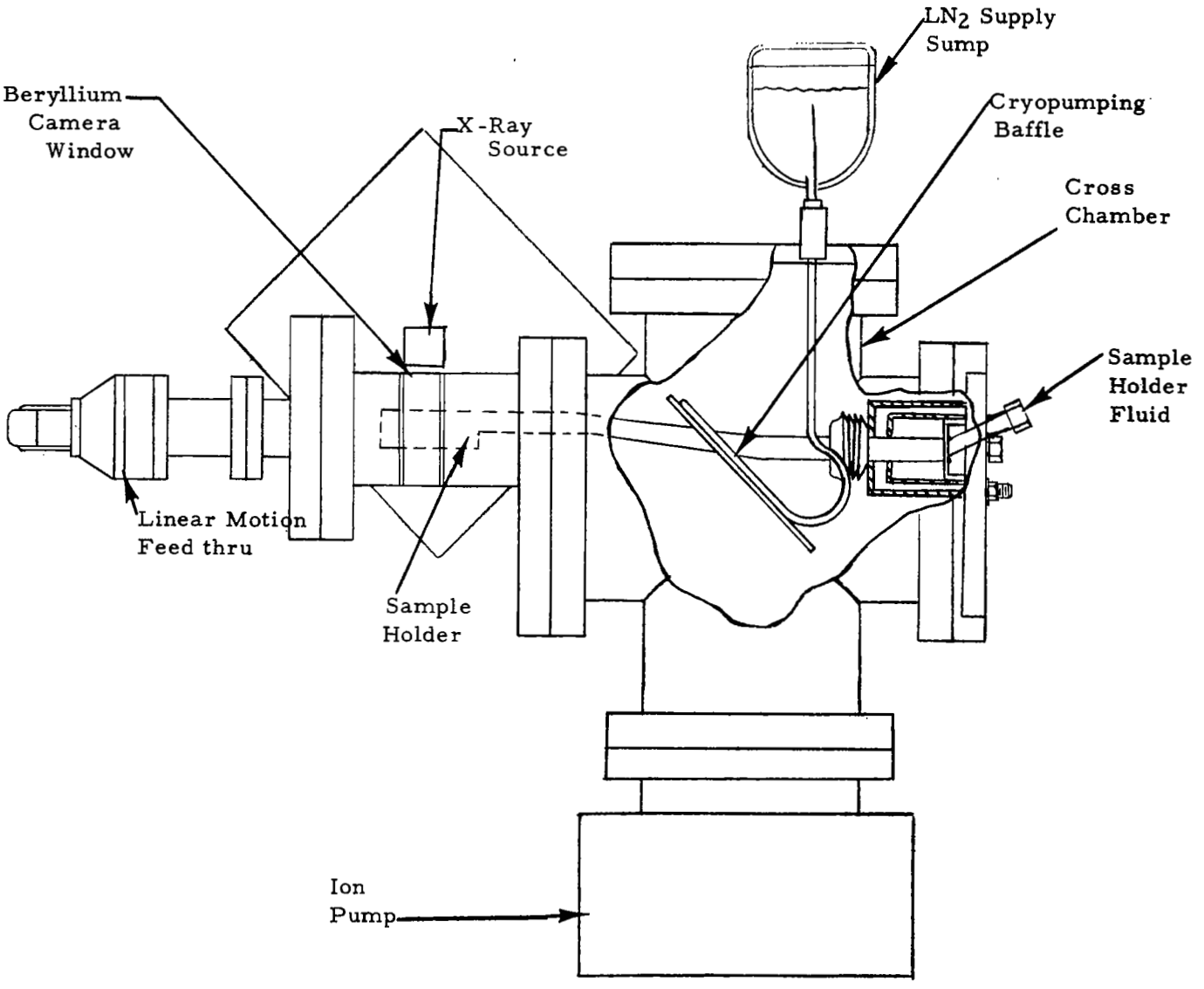

Figure 3-11 Mineral Stability Test Setup (Schematic)

The sample holder block attachment to the linear motion feedthrough shaft was designed for minimum heat conduction to prevent temperature error. Additionally, radiant heat transfer between the holder with samples and surrounding chamber walls was minimized by installation of specular reflectors.

The fluid conductive heat transfer method of sample temperature control necessitated use of a bellows seal for the fluid tubes. Three-fourths inch bellows movement was required for sample movement in front of the X-ray collimators. The combined bellows seal and tube guide design is shown in Figure 3-11. The intimate heat conduction sample holder was an outgrowth of knowledge gained during initial testing.

Alignment of the sample capillary for proper film exposure was found to be highly critical during testing. A Geiger counter in conjunction with the micrometer head feedthrough was used for alignment. The micrometer dial reading could be used for gross adjustment; however, due to varying thermal conditions, etc., precise final adjustment was required before each exposure.

Kodak Royal Blue X-ray film backed with an intensifying screen was used during the Phase II tests. The film was processed with modified Kodak D-19 developer at 75°F. Only 1-1/2 hour exposure time was required to obtain good quality photographs, so more frequent monitoring was possible than in Phase I.

Six mineral samples were tested in Phase II. These were the high purity ammonium feldspar (synthesized from the Fe-rich orthoclase from Madagascar), calcium montmorillonite, goethite, gypsum, muscovite, and natrolite. A molybdenum X-ray tube was used when photographing the goethite. The tests were conducted under the following nominal conditions:

1. Reference photographs - room temperature and pressure
2. 5×10^{-10} torr, liquid N_2
3. 5×10^{-10} torr, liquid CO_2
4. 5×10^{-10} torr, room temperature

5. 5×10^{-10} torr, 75°C

6. 5×10^{-10} torr, 130°C

7. 5-psia oxygen atmosphere, 100% relative humidity, 32°C, 4 days' exposure.

The tests were conducted during the period from 21 September to 15 November 1966. Difficulty was experienced in maintaining 5×10^{-10} torr in some of the tests. The first test with the liquid nitrogen required seven days to achieve the required vacuum. The initial pumpdown or "roughing" proceeded at a very slow rate to avoid the possibility of an explosive reaction of the sample powders. Liquid nitrogen was introduced with the pressure at 1.2×10^{-7} mm of Hg. After the required vacuum of 5×10^{-10} torr was maintained for a 24-hr stabilization period, the X-ray photographs were taken. During the installation of the CO_2 lines and introduction of the CO_2, a slight pressure rise occurred. The required vacuum was again attained and the X-ray photographs taken. A pressure rise to 1.7×10^{-8} torr occurred after the CO_2 lines were disconnected in preparation for the room temperature tests. A vacuum of 4.7×10^{-10} torr was attained, and X-ray photographs were taken. The photographs for the tests at 75°C were taken at 2.7×10^{-10} torr. The pressure rose from 4.9×10^{-10} to 9×10^{-9} torr when the hot silicone oil producing the 130°C temperature was introduced. The pressure was reduced to 7×10^{-10} torr and stabilized and the X-ray photographs taken. The very slightly increased pressure occurring during some of the tests should have had no effect on the phenomena observed.

The last series of X-ray photographs were made with the samples in a 5-psia oxygen environment, 100% humidity, at 32°C. After four days' exposure to these conditions, the samples were photographed.

All the sets of X-ray photographs were given to Dr. Peacor for analysis. Their evaluation has been included in the various sections describing the mineral specimens.

SECTION 4

ACTINOLITE

4.1 FORMULA

$Ca_2 (Mg, Fe)_5 Si_8 O_{22} (OH)_2$

4.2 MINERAL CLASSIFICATION AND VOLATILE

Silicate, Amphibole—hydroxyl ion.

4.3 SPECIMEN LOCALITY

Brno, South Moravia, Czechoslovakia.

4.4 PROCUREMENT SOURCE

Southwest Scientific Co., Scottsdale, Arizona.

4.5 OPTICAL MICROSCOPIC ANALYSIS

The thin section (Figure 4-1) discloses that the specimen is very pure. It is estimated that about 1% of nearly colorless chlorite is present, with a minute amount of finely divided magnetite associated with the actinolite.

The actinolite appears pale green and has a maximum birefringence of 0.025, extinction angle: $c \wedge \gamma = 17^{\circ}$, and negative optic sign: $2V = 85^{\circ}$.

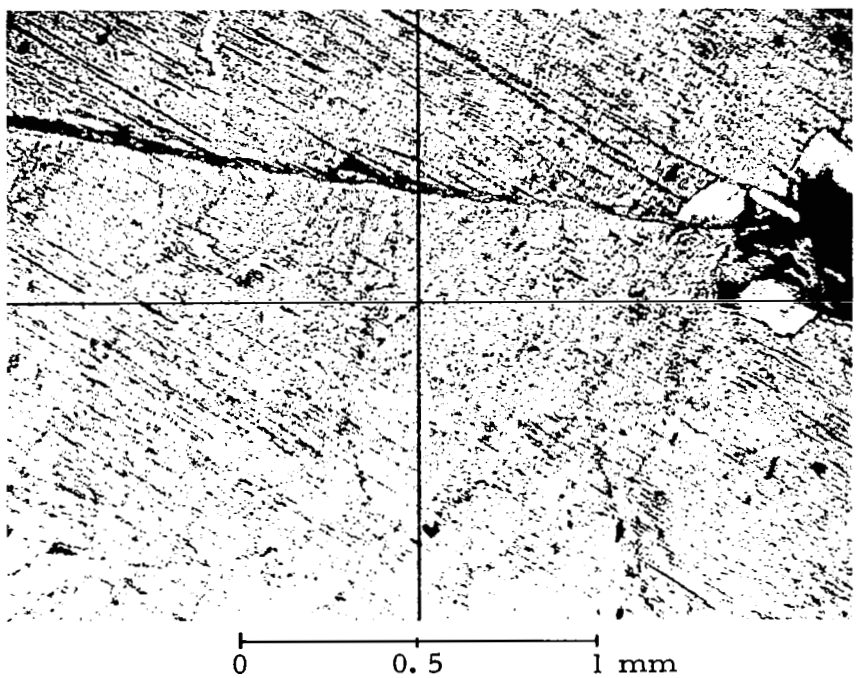

Figure 4-1 Photomicrograph of Actinolite, Crossed Polars, 47X, Chlorite Crystals at Right Edge

4.6 THERMAL ANALYSES

4.6.1 Differential Thermal Analysis

See Figure 4-2.

4.6.1.1 Sensitivity

The sensitivity is 10 μv/cm.

4.6.1.2 Peak Values

These are:

610°C(-) Perhaps chlorite

865°C(+)

1035°C(-) Reported values from 1002°C to 1160°C.

4.6.2 Thermogravimetric Analysis

The TGA (Figure 4-3) confirms the hydroxyl loss at 1035°C, although the reaction was not completed on the record. Not found is the 780°C to 890°C (-), which has been observed by many investigators.

4.6.3 Mass Spectrometer Analysis

The mass spectrometer curve (Figure 4-4) reveals a small adsorbed water loss. The two peaks in the curve, at 430° and 790°C, represent the loss of hydroxyl ion. These peaks correspond to the endothermic peaks at 610° and 1035°C on the DTA curve. The 430°C peak is probably due to the loss of OH^- from chlorite, a possible impurity in the sample. The other peak corresponding to the 790°C on the mass spectrometer curve and the 1035°C on the DTA curve is definitely due to the loss of OH^- from the actinolite.

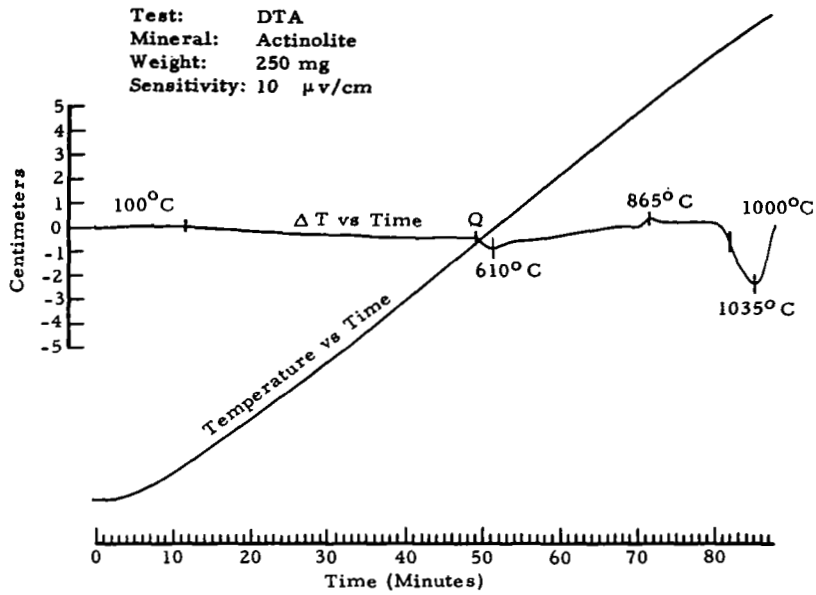

Figure 4-2 Actinolite DTA

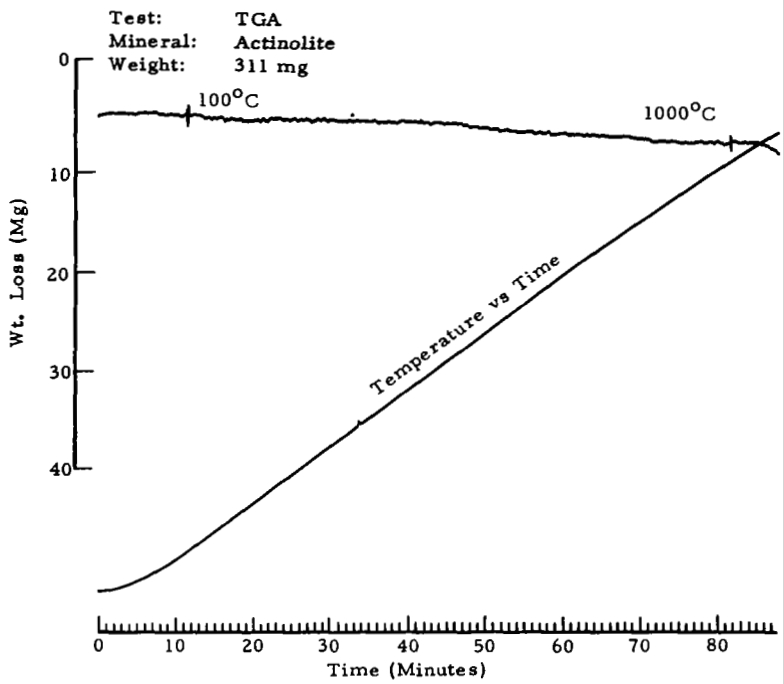

Figure 4-3 Actinolite TGA

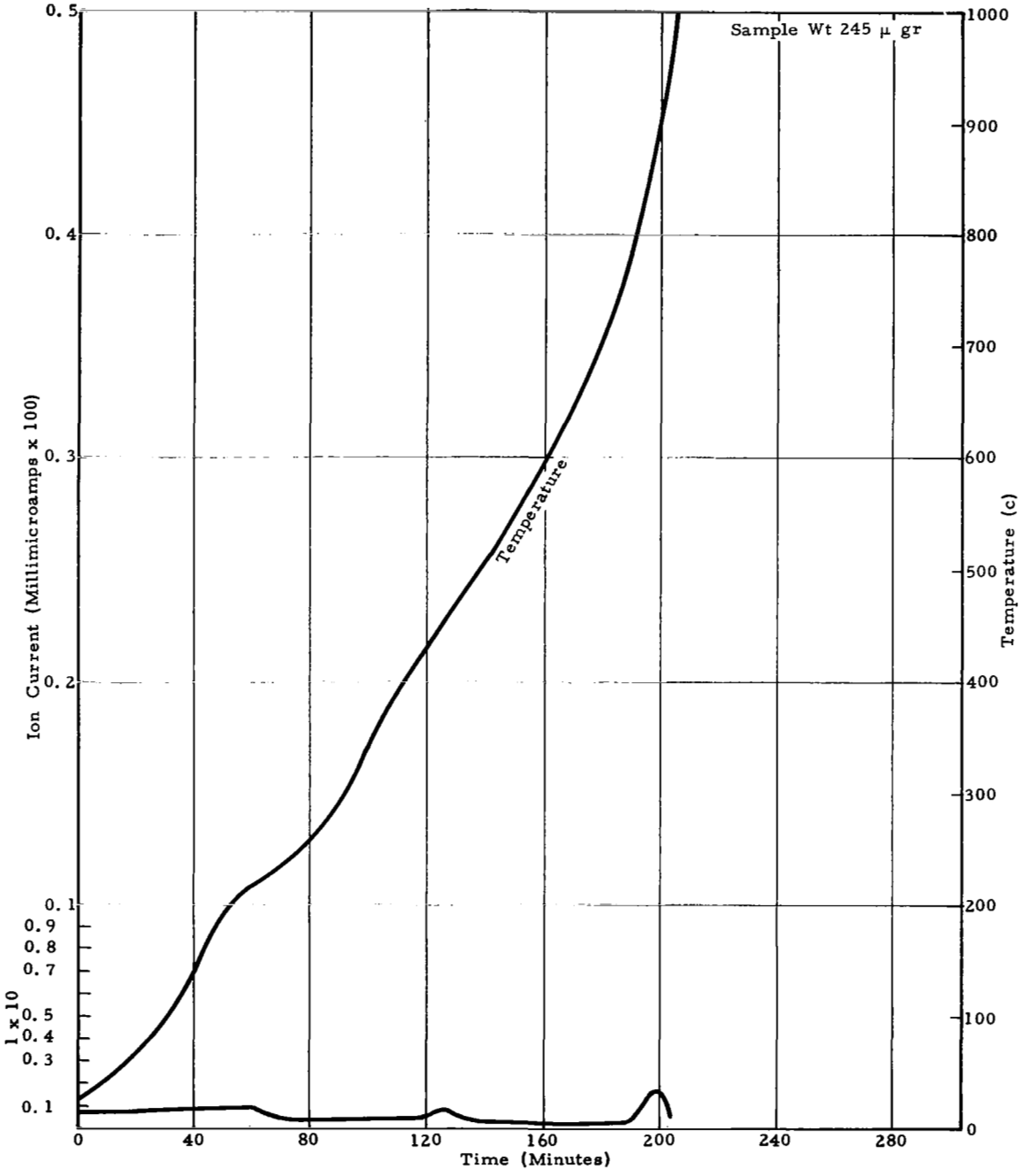

Figure 4-4 Mass Spectrometer Curve of Actinolite—Scan With H_2O Peak Plotted

4.7 X-RAY DIFFRACTION PATTERNS

4.7.1 Debye-Scherrer Standard

The actinolite pattern (Figure 4-5) contains a line with d = 4.2Å that does not appear in the ASTM standard list. However, this line is included in the ASTM pattern for tremolite, of which actinolite is a variety having a slightly different composition (Fe impurity). Thus, all lines are accounted for by actinolite alone. (Table 4-1.)

4.7.2 Bendix Vacuum Camera Standard

The lines of the Bendix camera standard, Figure 4-6, although spotty due to crystallite size, give good comparison with the Debye-Scherrer standard (see Table 4-2). Differences in part may be ascribed to preferred orientation due to the prismatic character of the crystallites. The list of lines for the Bendix standard is of course limited due to the poorer resolution obtainable with the diffraction geometry used.

4.7.3 Vacuum Patterns

All X-ray patterns of actinolite obtained under the conditions of Phase I duplicated the standard photograph. Therefore, no changes occurred for actinolite under these conditions, and the photographs are not included. Comparison with the standard photograph, for this example and for all others in this project, was most readily done by direct visual comparison. In this way, changes in the characteristics of the X-ray patterns are immediately evident, if present, and are free of differences due to the measurement error. Photographs, or data obtained by measurement from these photographs, are reproduced only in those cases where differences were evident on visual comparison. This mineral was not used in Phase II.

4.8 ANALYSIS OF THERMODYNAMIC AND CRYSTAL STRUCTURE PLAN

Actinolite, a chain silicate, is the intermediate member of the tremolite - actinolite - ferroactinolite series of the amphibole group. The composition of actinolite can be represented by the formula: $Ca_2(Mg, Fe^{+2})_5Si_8O_{22}(OH, F)_2$ in which the Fe^{+2} content ranges from 20-80% of the substitutional cations.

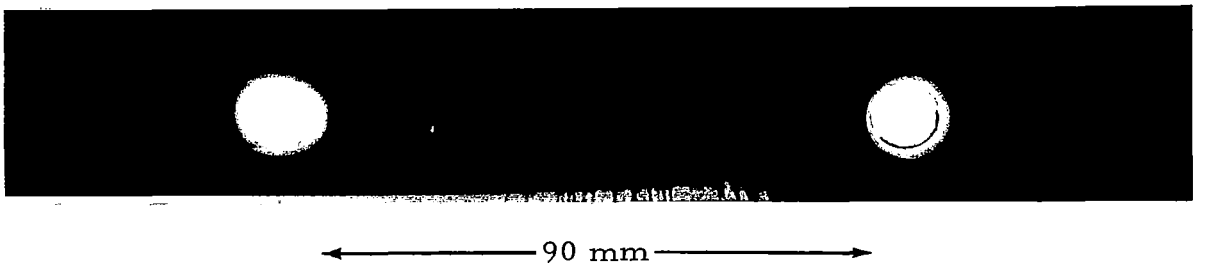

Figure 4-5 Actinolite X-Ray Pattern Taken with Debye-Scherrer Camera

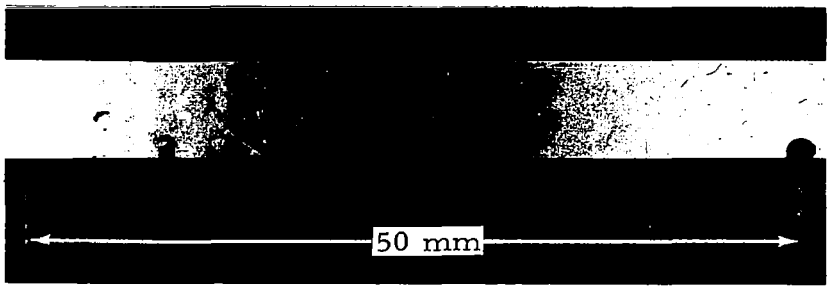

Figure 4-6 Actinolite X-Ray Pattern Taken with Bendix Vacuum Camera (Magnification 2X)

TABLE 4-1

COMPARISON OF EXPERIMENTAL AND ASTM D-VALUES FOR ACTINOLITE

EXP(Å)	ASTM(Å)	EXP(Å)	ASTM(Å)	EXP(Å)	ASTM(Å)	EXP(Å)	ASTM(Å)
9.0	9.06	3.23	3.27	2.15	2.16	1.29	1.29
8.4	8.42	3.10	3.11	2.02	2.04	1.195	
5.1	5.12	2.93	2.94 Only dense lines	2.00	2.01	1.160	
4.8	4.88	2.70	2.71	1.67	1.65	1.080	
4.5	4.52	2.58	2.59	1.57	1.58	1.070	End of List
4.2	4.20(Tremolite)	2.52	2.53	1.50	--	1.045	
3.82	3.81	2.32	2.33	1.43	1.43	1.027	
3.38	3.38	2.25	2.27	1.36	--	0.982	

TABLE 4-2

COMPARISON OF OBSERVED D-VALUES AND RELATIVE INTENSITY MEASUREMENTS FOR ACTINOLITE

Debye-Scherrer Standard, CuK_α		Bendix Camera Standard, CuK_α	
d_{obs}	$\frac{i}{i_o}$	d_{obs}	$\frac{i}{i_o}$
4.5	40	4.4	5
3.23	80	3.2	50
2.70	60	2.7	50
2.52	100	2.5	100
2.32	90	2.4	100
2.15	40	2.15	50
2.06	10	2.0	20
Not on original list		1.8	10
1.67	30	1.7	10
1.50	30	1.5	10
1.36	20	1.4	10

The structures of the amphiboles are based on the linking of $(Si, Al)O_4$ tetrahedra to form chains of the composition $((Si, Al)_4O_{11})$. (See Figure 4-7.) In all amphiboles, the chains have similar repeat distances (≈ 5.3 Å) and are bonded to neighboring chains by planes of cations, which in the case of actinolite are a limited proportion of Mg^{+2}, Fe^{+2}, and Ca^{+2} ions. Ideally, the Ca^{+2} ions occupy positions of 6-fold coordination.

The amphiboles exhibit extensive isomorphous substitution: F^- or Cl^- may replace OH^-: FE^{+2} or Mn^{+2} may replace Mg^{+2}; and Fe^{+2}, Mg^{+2}, Na^+ may replace Ca^{+2}. There is sufficient room between chains to permit entry of alkaline earth ions to balance a charge upset caused by the substitution of Al^{+3} for Si^{+4} in the silicon tetrahedra.

In actinolite, each oxygen of the OH^- ion is bound to three cations (Mg^{+2} or Fe^{+2}). Several investigators have reported 1-2% more water in their chemical analyses than is accountable for in structural water. Some researchers claim this is water adsorbed on the finely divided material prior to the H_2O determination, while others (Zussman, 1955, and Megaw, 1952) believe it reflects replacement of some of the oxygens of the $(Si_4O_{11})_n$ chains or the Na^+ or K^+ ions by OH ions. These hypotheses may explain the existence of a 3-stage water loss shown on many DTA curves.

The "dehydration" of actinolite is accompanied by the breakdown of the amphibole structure:

$$Ca_2Mg_xFe_{(5-x)}Si_8O_{22}(OH)_2 \rightarrow 2\ CaSiO_3 \cdot x\ MgSiO_3 \cdot (5-x)\ FeSiO_3 + SiO_2 + H_2O$$

actinolite

However, little or no work has been done on the stability of actinolite. Therefore, emphasis will be placed on the Mg-rich end member of the series, tremolite, for which there is a small amount of high temperature and high pressure data available. Due to their practically identical structures and similar heats of solution, 419,670 ± 1450 cal/mole (tremolite) and 433,040 ± 530 cal/mole (actinolite), their stabilities also should be quite similar.

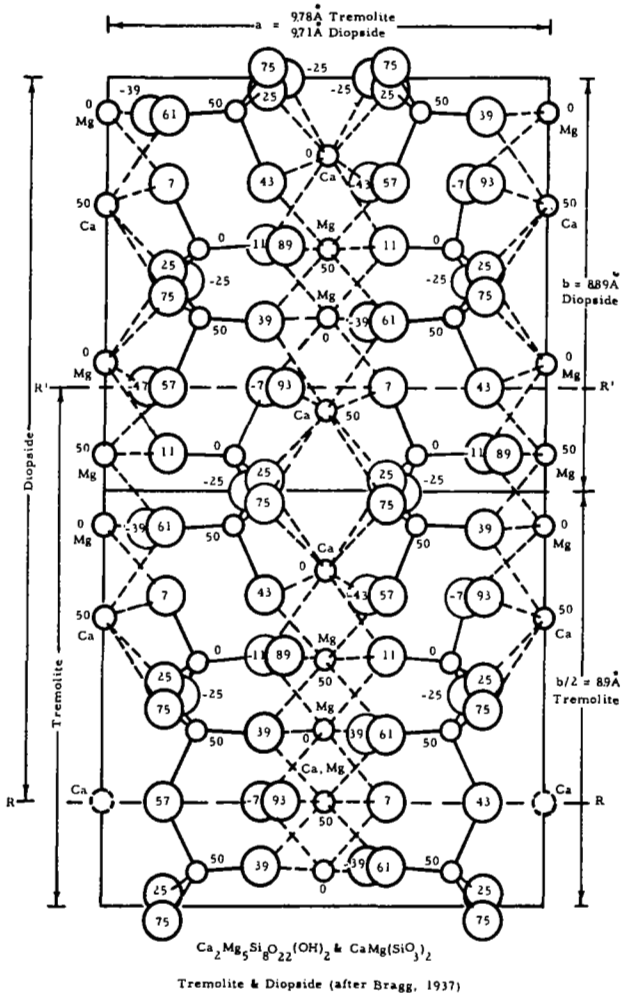

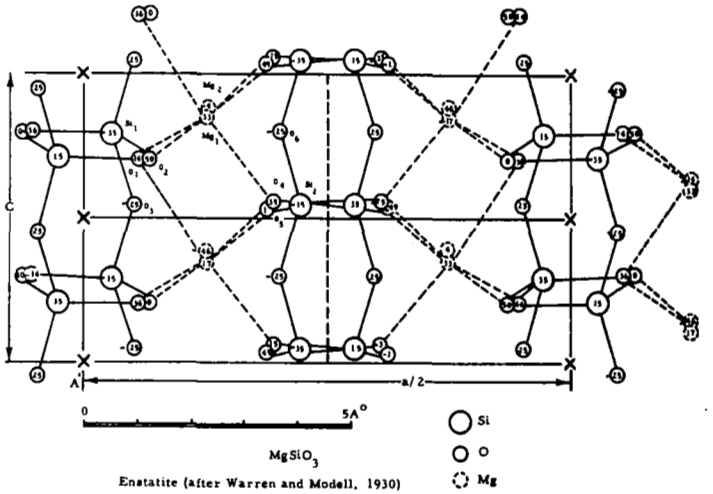

Figure 4-7 The Structure of Tremolite, Diopside, and Enstatite

Upon heating, tremolite decomposes to enstatite, diopside, quartz, and water vapor:

$$Ca_2Mg_5Si_8O_{22}(OH)_2 \rightarrow 3MgSiO_3 + 2CaMg(SiO_3)_2 + SiO_2 + H_2O$$

tremolite enstatite diopside quartz water

Diopside, a member of the pyroxene group, structurally resembles tremolite in that it is also based upon a chain structure. However, the pyroxene chains are formed by the linkage of successive SiO_4 tetrahedra by sharing two out of four of the tetrahedral oxygens (See Figure 4-7). This results in a chain of the general formula $(SiO_3)_n$. In the case of diopside, the chains are linked laterally by Ca^{+2} and Mg^{+2} ions. The Ca^{+2} ions lie principally between the bases of the tetrahedra in 8-fold coordination, whereas the Mg^{+2} ions lie principally between the apexes of the tetrahedra in 6-fold coordination. The chains are staggered in the c-axis direction (direction of elongation), producing monoclinic symmetry.

Enstatite, another pyroxene, has a chain structure $(SiO_3)_n$ similar to that found in diopside. The chains are linked laterally by Mg^{+} ions in a manner similar to the Ca^{+2} and Mg^{+2} linking in diopside. However, the smaller Mg^{+2} ions produce a different stacking of the chains, resulting in an orthorhombic cell with approximately double the dimensions of the diopside cell.

The last structure to be discussed in the decomposition of tremolite is that of quartz. The structure of quartz is based upon the sharing of all of the tetrahedral oxygen atoms with other SiO_4 tetrahedra to produce a 3-dimensional framework in which each silicon has four oxygens and each oxygen has two silicons as nearest neighbors. However, there are many polymorphic forms of this basic structure. Thilo (1939) reports the SiO_2 decomposition product to be cristobalite at 930-988°C.

The hydrothermal synthesis of tremolite has been studied by F. R. Boyd (1959). Data from his stability curve for the reaction tremolite→

enstatite + diopside + quartz + vapor have been reproduced in the following table:

T^oC	T^oK	P(bars-H_2O)	P mm Hg
740	1013	200	1.5×10^5
778	1051	400	3.0×10^5
808	1081	600	4.5×10^5
835	1108	1000	7.6×10^5
855	1128	1500	1.15×10^6

These data, with the exception of the last-mentioned temperature and pressure, conform to the Clausius-Clapeyron equation. Therefore, it is possible to evaluate the ΔH_T^o of the reaction and extrapolate this curve to lower temperatures and pressures. This extrapolation is represented in Figure 4-8. Also represented in this figure is the curve constructed from the following mass spectrometer and DTA data:

$$Ca_2Mg_xFe_{5-x}Si_8O_{22}(OH)_2 \rightarrow 2CaSiO_3 \cdot MgSiO_3 \cdot (5-x)\ FeSiO_3 + SiO_2 + H_2O$$

	P_{H_2O} mm Hg	T^oC
DTA	12.5	970 ± 20
Mass Spectrometer	5×10^{-6}	790 ± 5

Extrapolation of the data of Boyd (1959) to the lunar environment gives:

Lunar Temperature	T^oC	T^oK	P mm Hg
Minimum nighttime	-180	93	1.0×10^{-69}
Equilibrium at 1-m depth	- 55	218	4.0×10^{-22}

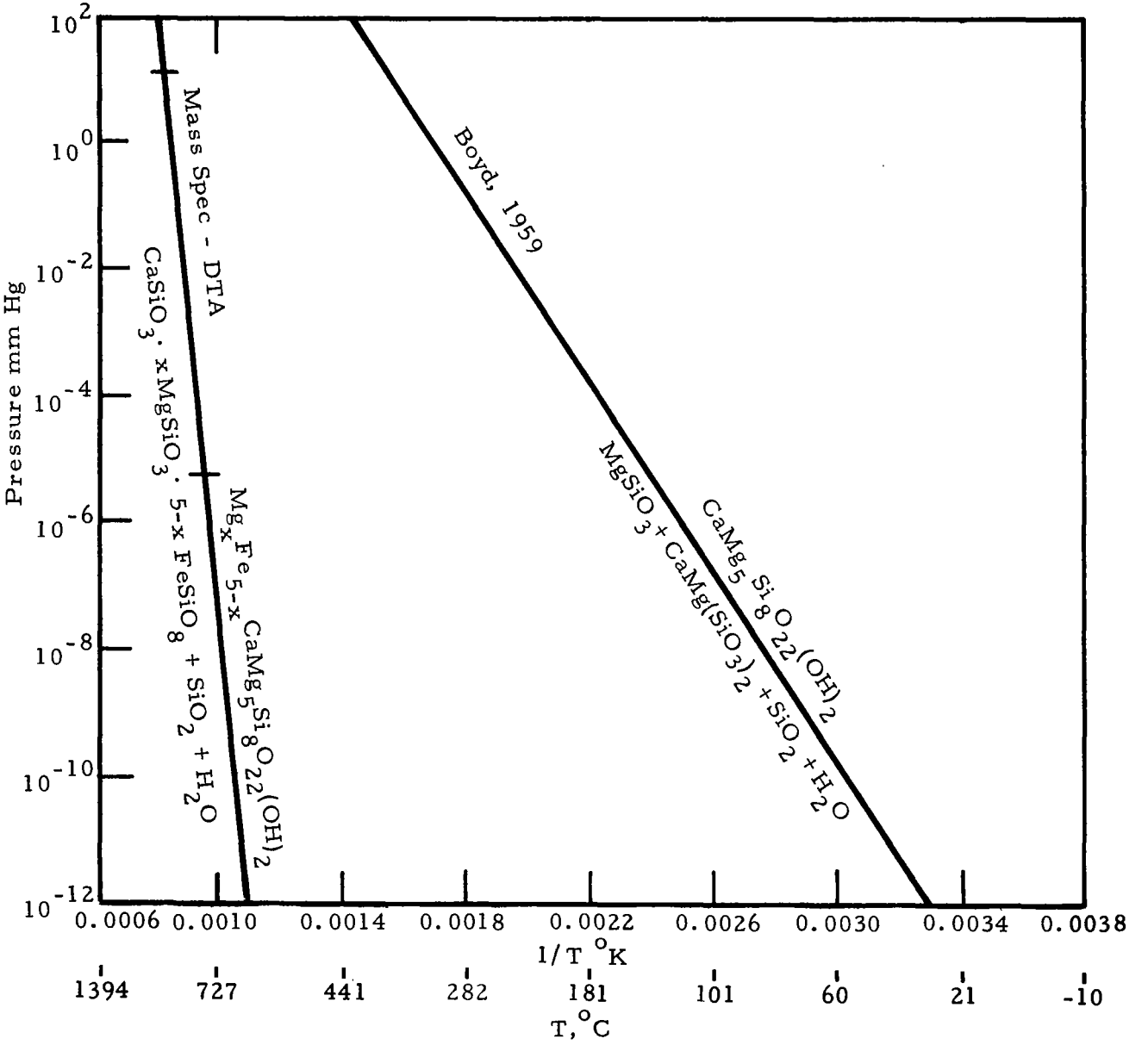

Figure 4-8 Stability Curve of Actinolite

Lunar Temperature	T°C	T°K	P mm Hg
Maximum daytime	+130	403	1.0×10^{-6}
At lunar pressure	+ 44	317	1.0×10^{-11}

If equilibrium is established, actinolite and tremolite should break down during the lunar day. However, they should be stable at the equilibrium temperature associated with a depth of 1 m. Reconstruction of the amphibole structure during the lunar night, while thermodynamically feasible given sufficient water vapor at the lunar pressure, is not probable. Boyd reported that quartz and pyroxene (decomposition products) tend to exist metastably with tremolite nuclei for great lengths of time.

SECTION 5

AMMONIUM FELDSPAR

5. 1 FORMULA

$NH_4 Al Si_3O_8 \cdot 1/2 H_2O$.

5. 2 MINERAL CLASSIFICATION AND VOLATILE

Silicate, feldspar group — NH_3, H_2O.

5. 3 SPECIMEN LOCALITY

Synthesized in the laboratory with the first 72 gm of ammoniated feldspar produced from a Tanganyika anorthoclase. Approximately 2. 5 gm of high purity ammoniated feldspar was produced from a Madagascar orthoclase.

5. 4 PROCUREMENT SOURCE

Anorthoclase obtained from Ward's Natural Science Establishment, Inc. . Rochester, New York; the orthoclase obtained from The University of Michigan Mineralogical Museum.

5. 5 OPTICAL MICROSCOPIC ANALYSIS

Since only the outer portions of the original feldspar were converted to ammonium feldspar, it is impossible to determine the optical properties of the ammonium feldspar phase.

5. 6 THERMAL ANALYSES

5. 6. 1 Differential Thermal Analysis

A sufficiently large sample was not obtained for the ammonium feldspar.

5.6.2 Thermogravimetric Analysis

A sufficiently large sample was not obtained for the ammonium feldspar.

5.6.3 Mass Spectrometer Analysis

The mass spectrometer analysis was run on the "pilot" batch of NH_4 feldspar produced from the Tanganyika anorthoclase. Because of the minute amount of sample synthesized at the time, the available material was sufficient for only the mass spectrometer analysis.

The three curves shown in Figure 5-1 depict the loss of H_2O, NH_3, and NH_2. The H_2O curve describes the combined loss of zeolitic water and water resulting from the complete structural breakdown. Zeolitic water begins to vaporize at 30°C. The NH_3 and associated structural water are lost at 52°C, and the appearance of NH_2 is due to the decomposition of NH_3 induced by the electron beam.

5.7 X-RAY DIFFRACTION PATTERNS

5.7.1 Diffractometer Standard

The diffraction patterns of different feldspars are very similar. Differences in specimen preparation or in diffraction instrumentation may produce pattern differences as great as those between the phases themselves. Therefore, standardization of methods is recommended. For this reason the standard X-ray photograph of this material was obtained with the powder diffractometer, since the standard pattern in the literature (Erd et al., 1964) was so obtained. A comparison of values is given in Table 5-1.

5.7.2 Bendix Vacuum Camera Standard

Refer to Figure 5-2 for the NH_4 feldspar standard Bendix camera X-ray pattern, Phase I.

Table 5-2 compares the Bendix Camera Standard with the Debye-Scherrer Standard.

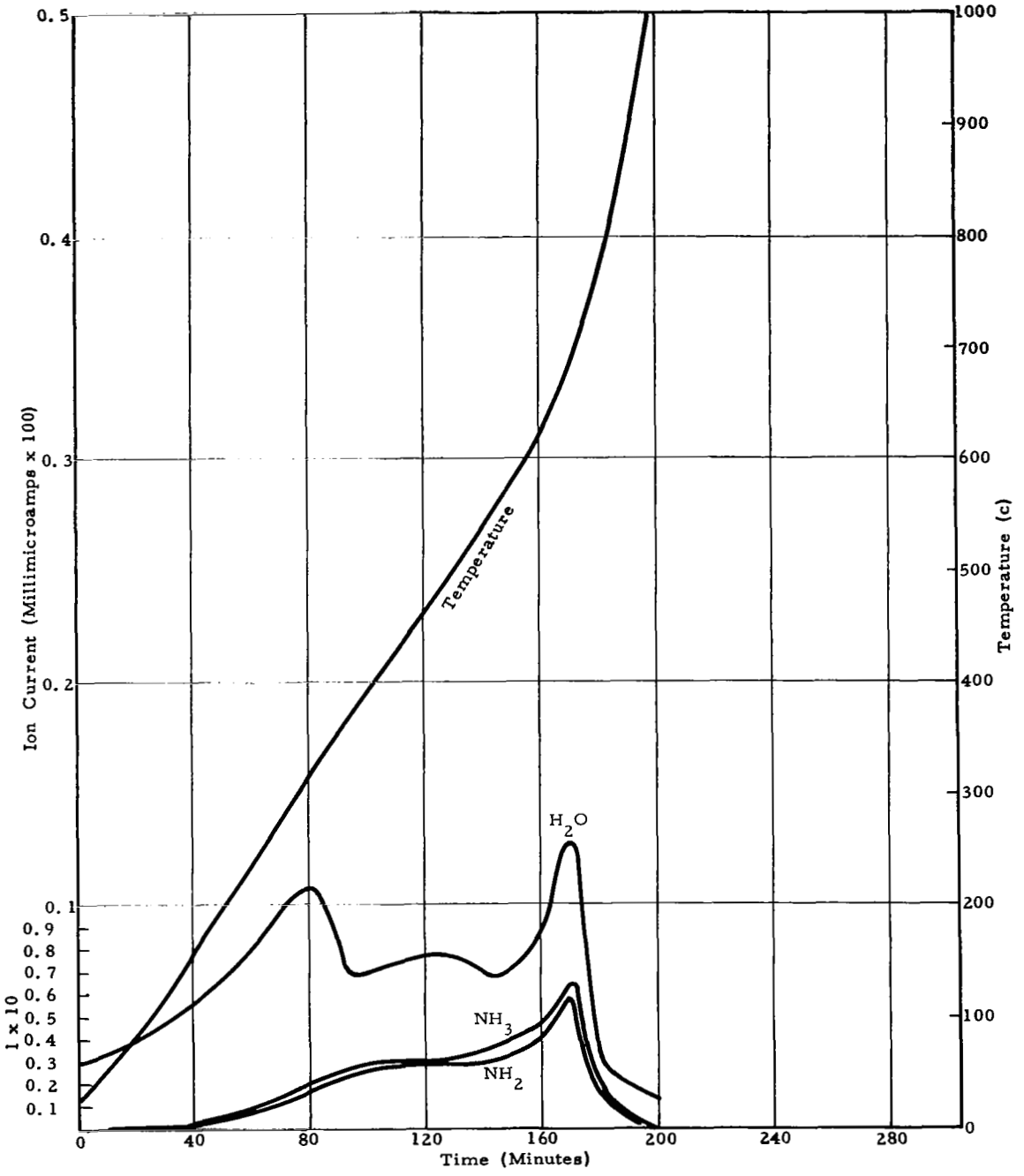

Figure 5-1 Mass Spectrometer Curve of Ammonium Feldspar—H_2O, NH_2, and NH_3 Peaks Plotted

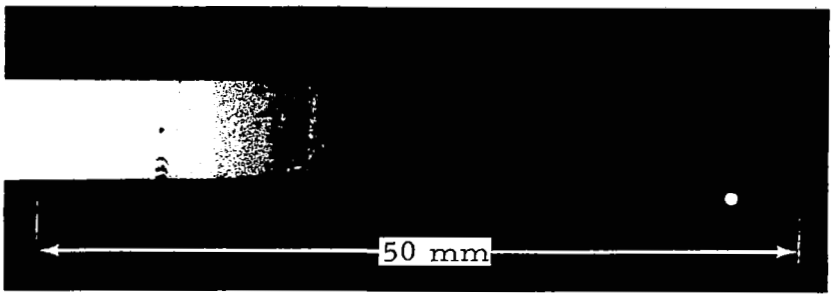

Figure 5-2 NH_4 Feldspar Standard Bendix Camera X-Ray Pattern, Phase I (Magnification 2X)

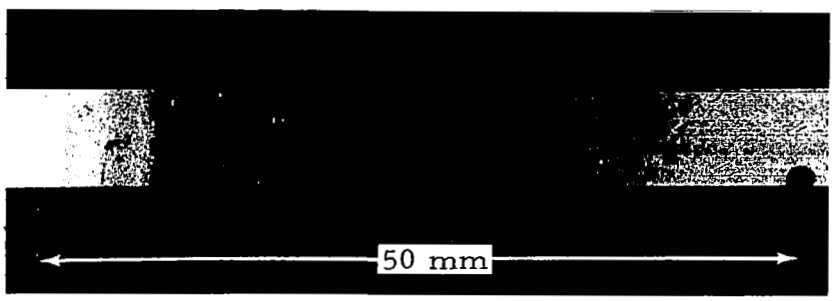

Figure 5-3 NH_4 Feldspar Standard Bendix Vacuum Camera Pattern, Phase II (Magnification 2X)

TABLE 5-1

COMPARISON OF EXPERIMENTAL D-VALUES WITH THOSE OF ERD et al., 1964

Experimental		Erd et al.	
d_{obs}	$\frac{i}{i_o}$	d_{obs}	$\frac{i}{i_o}$
6.52	96	6.46	18
5.91	33		
4.33	65	4.23	40
3.98	33	3.95	17
3.81	100	3.78	62
3.63	12	3.61	14
3.60	5		
3.462	23	3.46	55
3.381	72	3.320	70
3.314	34		
3.258	62	3.232	100
3.225	69		
3.129	3		
3.014	39	2.988	35
2.954	13		
2.910	20	2.895	25
2.894	15		
2.862	9		
2.767	9	2.763	13
2.650	12		
2.604	23	2.574	16

TABLE 5-2

COMPARISON OF OBSERVED D-VALUES AND RELATIVE INTENSITY MEASUREMENTS FOR NH_4 FELDSPAR

Debye-Scherrer Standard, CuK_α		Bendix Camera Standard, CuK_α	
d_{obs}	$\frac{i}{i_o}$	d_{obs}	$\frac{i}{i_o}$
4.23	40	4.2	20
2.78	62	3.8	30
3.32	70		
3.23	100	3.2	100
2.99	35	2.9	20
2.48	29	2.4	20
2.10	19	2.0	10
1.80	10	1.8	10
1.74	8	1.7	10

5.7.3 Vacuum Patterns

The patterns of NH_4 feldspar duplicated the standard photograph under all conditions of pressure and temperature. However, it is particularly difficult to observe the changes in structure attending NH_4 and H_2O loss, since the (Si, Al)-O framework remains unchanged. Stewart and others (unpublished) have shown that Na-K substitution is zeolitic in that it is readily achieved, but leaves the framework virtually unchanged. The lack of change in the X-ray patterns is not definite proof that the loss of volatiles has not therefore occurred.

5. 7. 4 Bendix Standard Pattern, Phase II

Refer to Figure 5-3 which shows the NH_4 feldspar standard Bendix vacuum camera pattern. This pattern duplicated, with the exception of two lines of weak intensity, that of the standard of Phase I.

5. 7. 5 Vacuum Pattersn, Phase II

Patterns obtained under all conditions of temperature and pressure duplicated that of the standard. As noted above, this does not necessarily prove that there has not been devolatilization since very high resolution is required to detect it.

5. 8 ANALYSIS OF THERMODYNAMIC AND CRYSTAL STRUCTURE DATA

The ammonium feldspar used in this stability study was synthesized from anorthoclase, an alkali feldspar near the sodium-rich end of the series $NaAlSi_3O_8-KAlSi_3O_8$. The synthesis was accomplished in a manner similar to that used by Barker (1964). Details of the synthesis are presented in Section 2. 2.

The alkali feldspar structure consists of Si - Al tetrahedra linked to one another tridimensionally. However, it is much easier to understand the nature of this structure if one considers the tetrahedra to be linked to form chains parallel to the a-axis direction (see Figure 5-4). The chains themselves are composed of horizontal rings of four tetrahedra with a repeat distance of approximately four times the height of one tetrahedron. Actually, the tetrahedra forming the chains do not lie in a plane but are twisted and distorted about the chain axis. Successive chains are linked to one another by the sharing of tetrahedral oxygen atoms to form a sheet of 4-membered and 8-membered rings of tetrahedra. Successive sheets are then stacked upon one another, resulting in a structure containing large interstices which may be occupied by Na^+ or K^+ ions, or by any other cation or radical of similar charge and size.

The exact symmetry of this general structure (triclinic or monoclinic) depends both upon which cation (Na^+ or K^+) predominates and the temperature. Furthermore, the amount of disorder in the (Si, Al) distribution is a function of the temperature of formation with the amount of disorder increasing with higher temperatures.

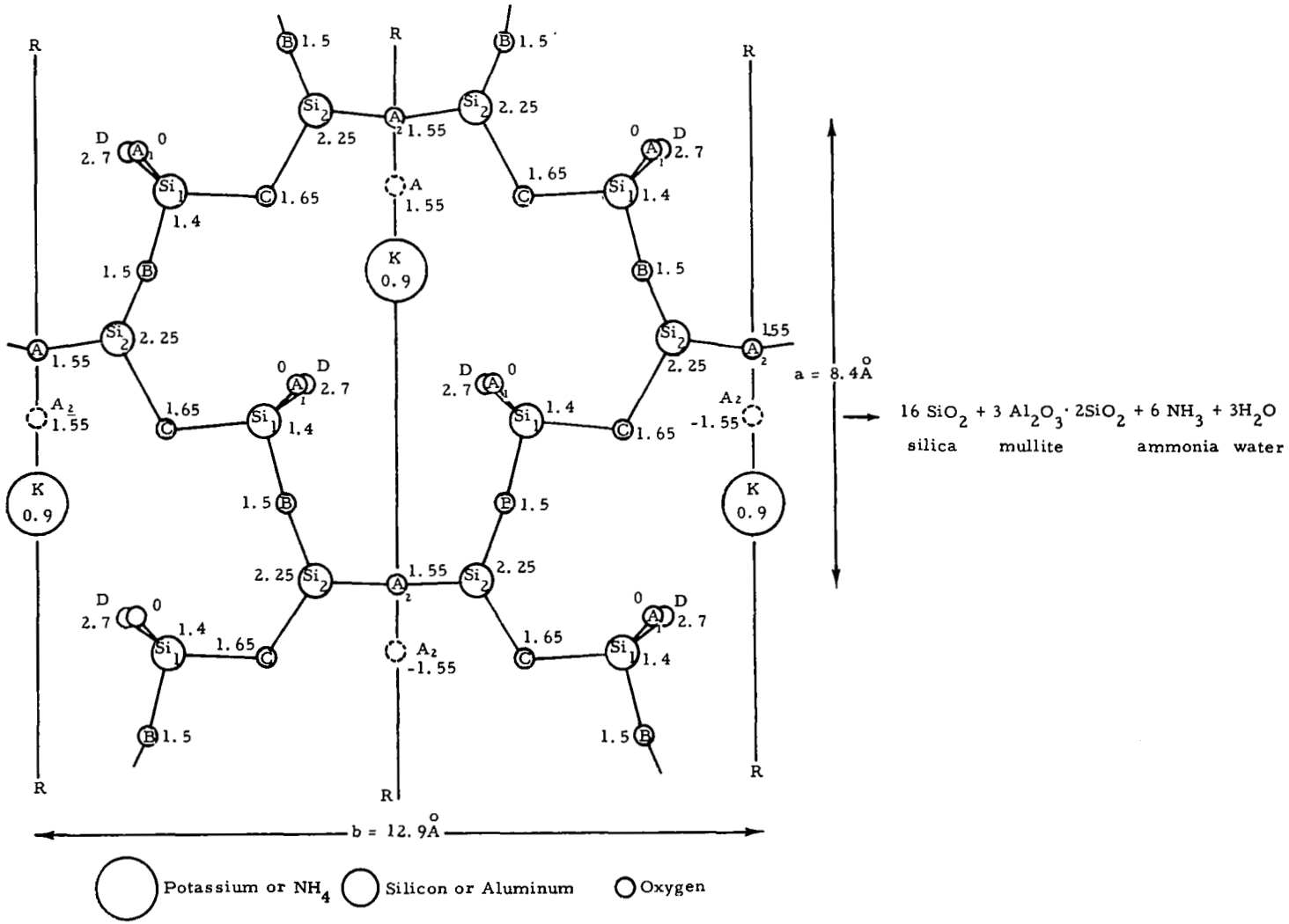

Figure 5-4 The Structure of Ammonium Feldspar–Sanidine

Barker in his exchange experiments noted that "sodium is replaced more readily by NH_4^+ than potassium, and in alkali feldspars containing both Na and K, the Na is almost entirely removed."* The end members of the series ($KAlSi_3O_8$ and $NaAlSi_3O_8$) undergo exchange with more difficulty than do the intermediate members. This is probably due to the fact that the structure of the end members is more stable because of the absence of solid solution.

Basically, ammonium feldspar can be synthesized in either anhydrous or hydrous systems. In the anhydrous system, ammonium feldspar is produced according to the reaction:

$$(K, Na)\ AlSi_3O_8 + NH_4Cl\ (dry) \rightarrow NH_4\ AlSi_3O_8 + (K, Na)\ Cl.$$

However, at temperatures only slightly higher than the temperature of formation, the ammonium feldspar breaks down, producing silica, mullite, ammonia, and water:

$$6\ NH_4AlSi_3O_8 \rightarrow 16\ SiO_2 + 3\ Al_2O_3\ \ 2\ SiO_2 + 6\ NH_3 + 3\ H_2O.$$

A hydrated ammonium feldspar is produced when synthesis takes place in a hydrous system. The production of the hydrated species can be represented by the equation:

$$(K, Na)\ AlSi_3O_8 + NH_4Cl + 1/2\ H_2O \rightarrow NH_4AlSi_3O_8 \cdot 1/2\ H_2O + (K, Na)\ Cl.$$

Solution

Hydrated ammonium feldspar has been experimentally demonstrated to be the most stable of the two types of ammoniated feldspar. Stability has been attributed to the incorporation of "zeolitic" water which appears to occupy random sites within the crystal structure.

---

* Barker, D. S., "Ammonium in Alkali Feldspars," Am. Min., V. 49, 1964, p. 854.

Hydrated ammonium feldspar has a natural counterpart, buddingtonite, which has been found in only one locality, Sulfur Bank, Lake County, California. It occurs as a low pressure and low temperature (120°C) replacement of albitic plagioclase. Buddingtonite contains "zeolitic" water in proportions comparable to that of the synthetically produced ammonium feldspar.

The ammonium feldspar used in the stability experiments was synthesized in a hydrous system. The presence of zeolitic water is evidenced by the mass spectrometer analysis.

The first increase in the water loss curve is due to the loss of the zeolitic water, while the second increase is due to the water liberated by the complete structural breakdown.

Due to the recent discovery, synthesis, and limited geologic importance of ammonium feldspar, no literature values for its thermodynamic properties are available. The breakdown curves in Figure 5-5 were plotted from the Differential Thermal Analysis data of Erd et al., 1964, and from the mass spectrometer analysis. These data are summarized as follows:

$$2\ NH_4\ AlSi_3O_8 \cdot \frac{1}{2} H_2O \rightarrow 2\ NH_4AlSi_3O_8 + H_2O$$

	P_{H_2O}, mm Hg	T°C
Mass Spectrometer	5×10^{-6}	30
DTA (Erd, 1964)	12.5	370

$$6\ NH_4Al\ Si_3O_8 \rightarrow 3\ Al_2O_3 \cdot SiO_2 + 16\ SiO_2 + NH_3 + 3\ H_2O$$

	P_{H_2O} mm Hg	T°C
Mass Spectrometer	5×10^{-6}	52
DTA (Erd, 1964)	12.5	498

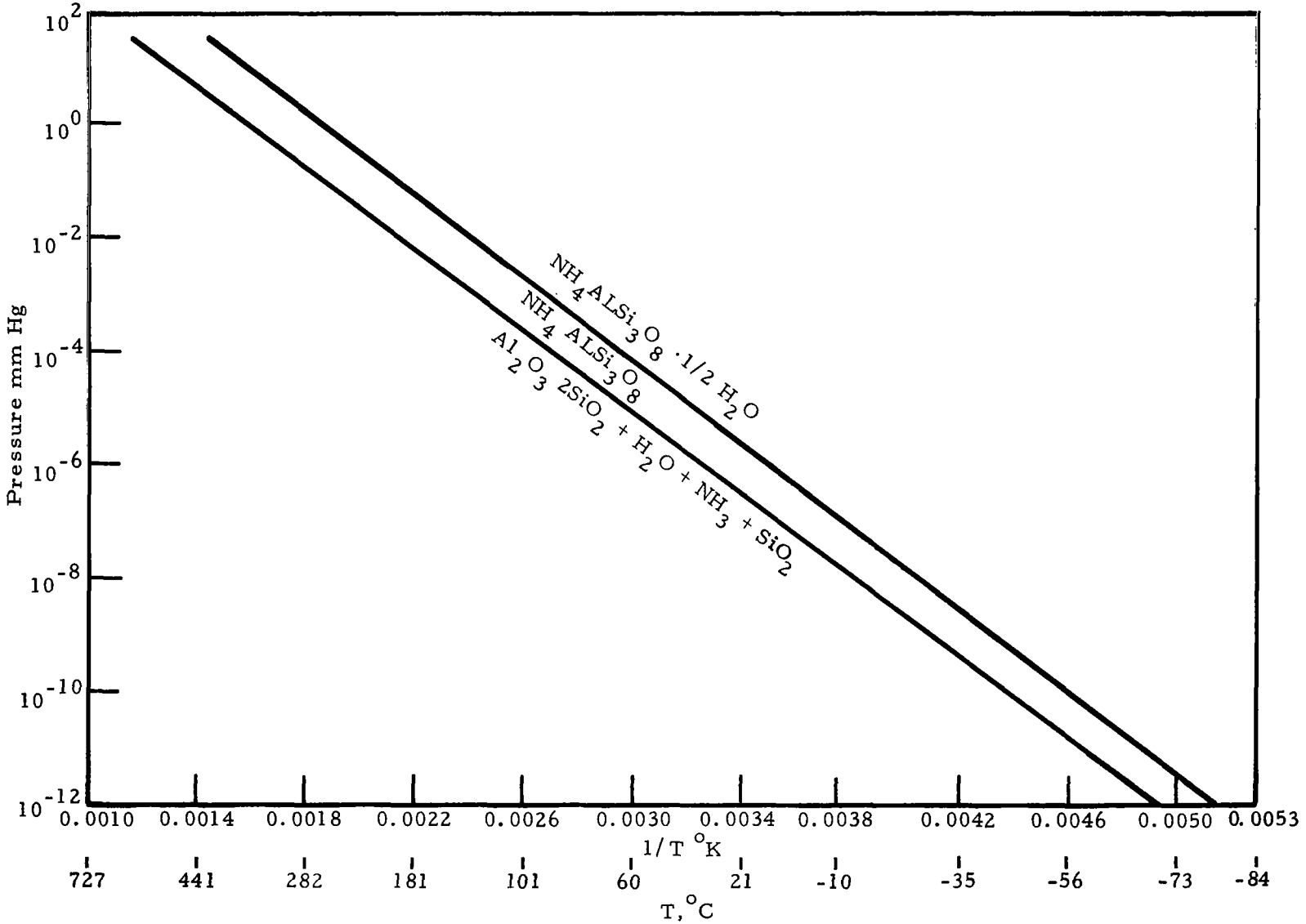

Figure 5-5 Stability Curves of Ammonium Feldspar

Note that there are two curves (NH_3 and NH_2) plotted in Figure 5-1. The appearance of the NH_2 is the result of decomposition by the electron beam of the NH_3 evolved from the sample:

$$NH_3 \xrightarrow{\Delta E} NH_2 + H.$$

From the stoichiometry of the equations, it is evident that the volume of NH_2 is equal to that of NH_3 from which it is produced. Therefore, the total amount of NH_3 produced is equal to the sum of the areas under each of the curves.

Extrapolation of data to the lunar environment results in:

$$NH_4AlSi_3O_8 \frac{1}{2} H_2O \rightarrow NH_4AlSi_3O_8 + \frac{1}{2} H_2O$$

Lunar Temperature	T^oC	T^oK	Pressure mm Hg
Minimum nighttime	-180	93	1.6×10^{-35}
Equilibrium at 1-m depth	- 55	218	7.6×10^{-11}
Maximum daytime	+130	403	4.6×10^{-3}
At lunar pressure	- 67	206	1.0×10^{-11}

$$6\ NH_4AlSi_3O_8 \rightarrow 3\ Al_2O_3 \cdot SiO_2 + 16\ SiO_2 + NH_3 + 3\ H_2O$$

Lunar Temperature	T^oC	T^oK	Pressure mm Hg
Minimum nighttime	-180	93	5.0×10^{-35}
Equilibrium at 1-m depth	- 55	218	1.8×10^{-11}
Maximum daytime	+130	403	5.6×10^{-4}
At lunar pressure	- 58	215	1.0×10^{-11}

and indicates that ammonium feldspar will completely decompose at the lunar daytime surface temperature and will not exist in a stable phase at the equilibrium temperature associated with a depth of 1 m. The formation of ammonium feldspar during the lunar night is highly unlikely due to the structural change accompanying the loss of water and ammonia. While only mullite, silica, ammonia, and water have been reported as decomposition products, there is the possible formation of intermediate structure types which will readily take up water and ammonia. Furthermore, the partial pressure of ammonia, if any is present in the lunar environment, is probably exceedingly low, much lower than the equilibrium vapor pressure of ammonium feldspar at these temperatures.

The curves pictured in Figure 5-5 are not meant to represent equilibrium stability boundaries due to the fact that they were constructed from nonequilibrium data. They merely represent the highest temperature and lowest pressure at which one would expect to find ammonium feldspar existing metastably under the heating rate conditions of these experiments. From previous experiments, it has been noted that the equilibrium values for these temperatures are generally several hundred degrees lower.

SECTION 6

ANTIGORITE

6.1 FORMULA

$Mg_3Si_2O_5(OH)_4$.

6.2 MINERAL CLASSIFICATION AND VOLATILE

Silicate, serpentine—hydroxyl..

6.3 SPECIMEN LOCALITY

Montville, New Jersey.

6.4 PROCUREMENT SOURCE

The University of Michigan Mineralogical Museum..

6.5 OPTICAL MICROSCOPIC ANALYSIS

About half the specimen in the thin section (Figure 6-1) is composed of veinlets of chrysotile a few millimeters wide. The cross fibers show high birefringence, parallel extinction, and are length slow. This chrysotile was easily separated from the host antigorite after the material had been coarsely crushed.

The antigorite appears very pale green, with low relief in Canada balsam. It is length fast, optically negative, with 2V about 20°. Except for a minute amount of opaque magnetite, the easily separated antigorite is of high purity.

6.6 THERMAL ANALYSES

6.6.1 Differential Thermal Analysis

Refer to Figure 6-2.

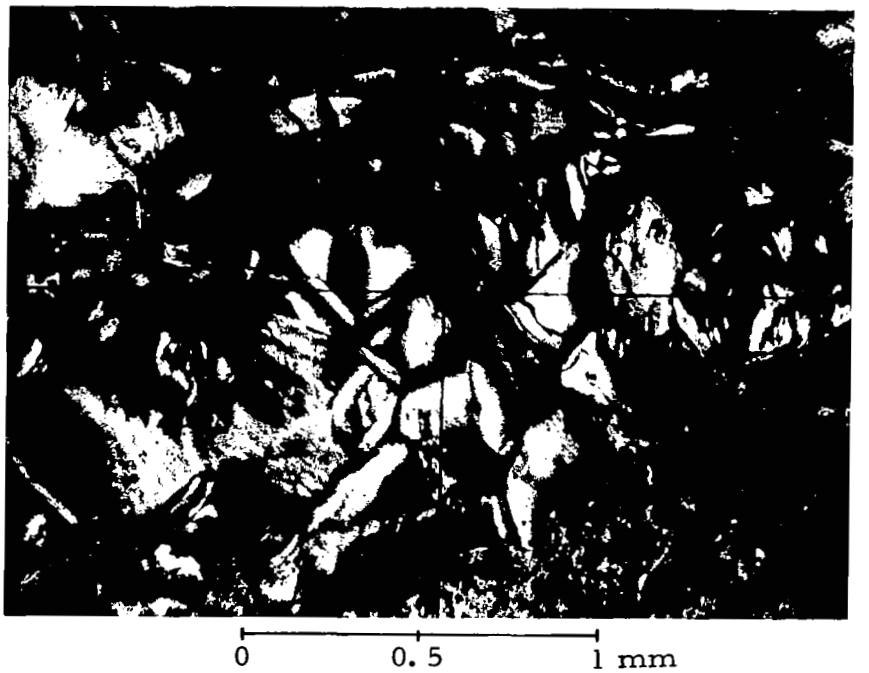

Figure 6-1 Photomicrograph of Antigonite, Crossed Polars, 47X, Veinlet of Chrysolite in Upper Right Quadrant

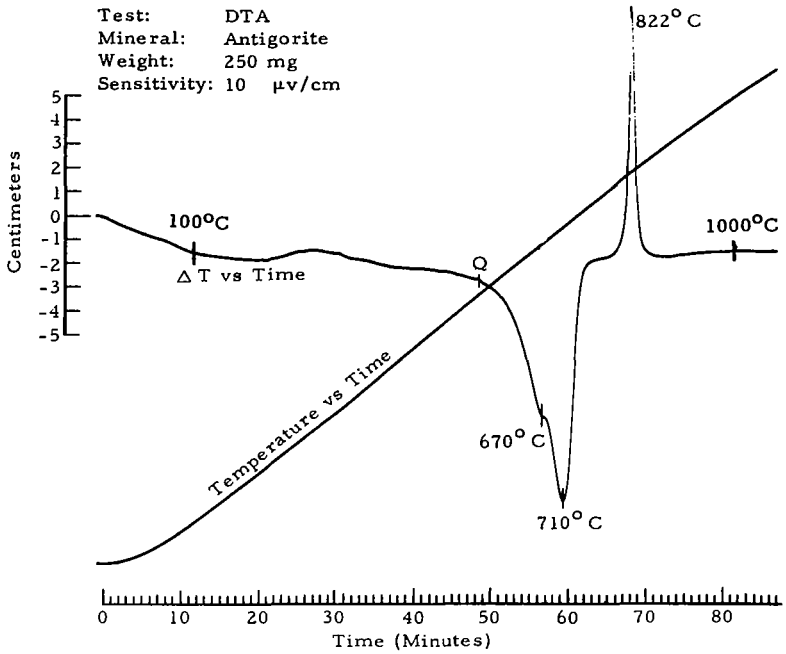

Figure 6-2 Antigorite DTA

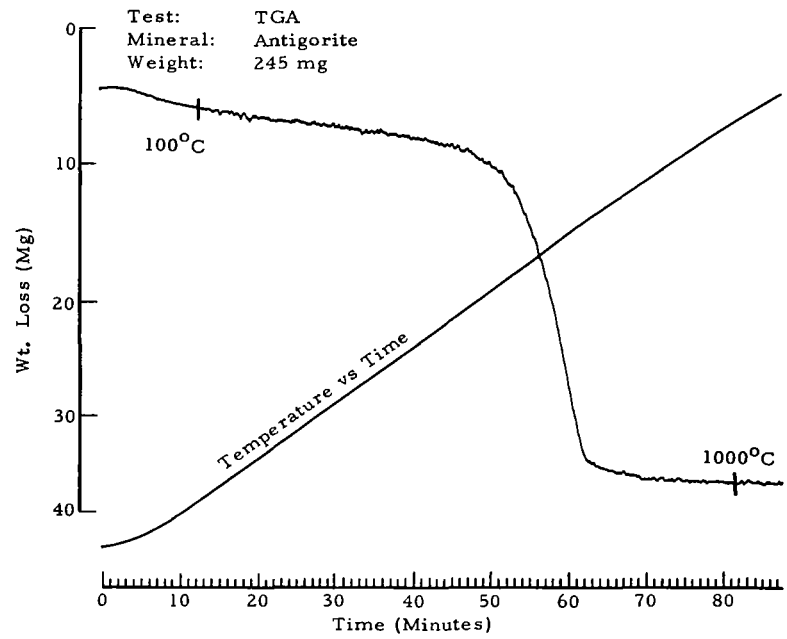

Figure 6-3 Antigorite TGA

6. 6. 1. 1 Sensitivity

The sensitivity is 10 μ / cm.

6. 6. 1. 2 Peak Values

These are: 670°C(-) First shoulder } Loss of OH
710°C(-) Major peak }

822°C(+) Sharp exorthermic peak. Phase transition.

The exorthermic peak is not found on the antigorite from the Antigore Valley, Italy. Nevertheless, this curve is similar to those published for serpentine, chrysotile, and antigorite.

6. 6. 2 Thermogravimetric Analysis

The TGA (Figure 6-3) shows a 4. 4-mg loss to 500°C, followed by a loss of 32. 5 mg during the major endothermic reaction. The latter weight loss amounts to 13. 0 % of the sample weight. It is in excellent agreement with the calculated OH loss which, based on the ideal formula, is 12. 9 %. The 4. 4-mg loss probably represents the loss of absorbed water.

6. 6. 3 Mass Spectrometer Analysis

The antigorite sample begins to decompose at 270°C under prevailing vacuum conditions in the mass spectrometer. The loss of OH is shown in the curve (Figure 6-4) as two large closely spaced peaks. This same reaction on the DTA curve is represented by the peak at 710°C and the minor shoulder at 670°C. However, the sharp endothermic peak at 822°C on the DTA curve, indicative of a phase transition, is not detectable in the mass spectrometer.

6. 7 X-RAY DIFFRACTION PATTERNS

6. 7. 1 Debye-Scherrer Standard

Refer to Figure 6-5 which shows the antigorite X-ray pattern taken with a Debye-Scherrer camera.

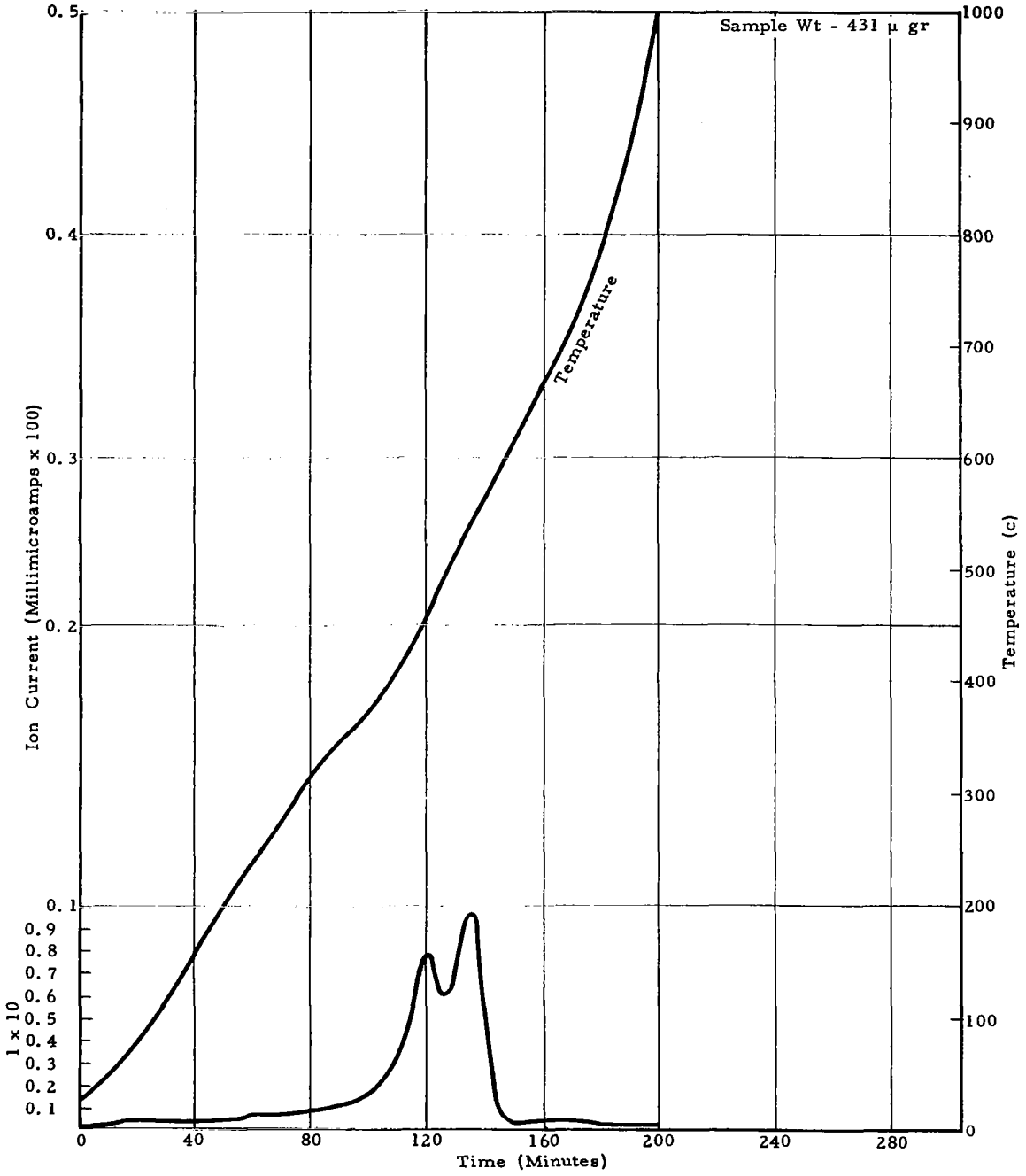

Figure 6-4 Mass Spectrometer Curve of Antigorite—
Scan With H_2O Peak Plotted

Figure 6-5 Antigorite X-Ray Pattern Taken With Debye-Scherrer Camera

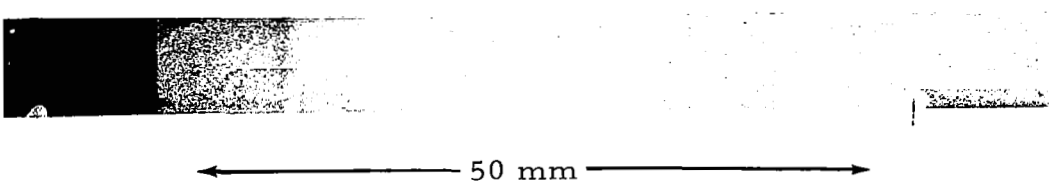

Figure 6-6 Antigorite X-Ray Pattern Taken With Bendix Vacuum Camera (Magnification 2X)

There is good agreement between the ASTM and Debye-Scherrer standard despite the fact that preferred orientation normally causes marked differences in some X-ray patterns of such layer-structure silicates. (See Table 6-1).

TABLE 6-1

COMPARISON OF EXPERIMENTAL AND ASTM D-VALUES FOR ANTIGORITE

Exp (Å)	ASTM (Å)	Exp (Å)	ASTM (Å)
7.2	7.28	2.15	2.15
4.6	4.64	2.09	2.12
3.83	3.91	1.53	1.53
2.79	2.798	1.49	1.49
2.50	2.51	1.31	1.315
2.45	2.45		

6.7.2 Bendix Vacuum Camera Standard

Figure 6-6 shows the antigorite X-ray pattern taken with the Bendix Vacuum Camera, Magnification 2X.

There is reasonable agreement between the Bendix and Debye-Scherrer patterns (see Table 6-2) with some differences ascribable to preferred orientation of the sample and poorer resolution of the Bendix Camera. However, the Bendix standard is adequate for comparison purposes relative to patterns obtained at high vacuum.

6.7.3 Vacuum Patterns

All diffraction patterns obtained under the conditions of Phase 1 precisely duplicated that of the standard. Devolatilization of the antigorite expressed through loss of hydroxyl ion as water should produce significant differences in X-ray patterns with a complete collapse of the octahedrally coordinated layer. Thus, devolatilization did not occur. This mineral was not used in Phase II.

TABLE 6-2

COMPARISON OF OBSERVED D-VALUES AND RELATIVE INTENSITY MEASUREMENTS FOR ANTIGORITE

Debye-Scherrer Standard, CuK_α		Bendix Camera Standard, CuK_α	
d_{obs}	$\frac{i}{i_o}$	d_{obs}	$\frac{i}{i_o}$
4.6	30	4.4	60
3.83	80	3.5	100
2.45	100	2.3	40
2.09	20	1.9	3
1.53	5	1.5	2
1.31	80	1.4	5

6.8 ANALYSIS OF THERMODYNAMIC AND CRYSTAL STRUCTURE DATA

Antigorite is one of three principal members of the serpentine group (antigorite, chrysotile, and lizardite) which have the approximate composition $Mg_3Si_2O_5(OH)_4$. The structure of these members is composed of polymorphic forms of a layer-type structure characteristic of the kaolinite group of minerals. Each layer consists of one sheet of pseudo-hexagonally linked SiO_4 tetrahedra joined to a brucite sheet of Mg - O(OH) octahedra. The tetrahedra in the Si-O sheet are unidirectional and are linked to the brucite sheet in such a manner as to replace two out of every three hydroxyls. The different dimensions of the SiO_4 and brucite sheets give rise to a layer distortion and consequent stacking adjustments and additional polymorphic forms.

The appearance of the polymorphic forms, chrysotile and antigorite, are the result of the tetrahedral SiO_4 and brucite sheets accommodating themselves to one another. In both cases, the accommodation takes the form of a bending of the layers concave to the SiO_4 sheets. In chrysotile, the repetition and bending of the two layers forming the unit cell result in a cylindrical structure with an outside diameter of 260 Å and a wall thickness

of ten layers. The structure of antigorite (See Figure 6-7) consists of periodic reversals of the layer curvature, resulting in corrugations perpendicular to the a-axis. The magnitude of the a-cell parameter is equal to the period of the corrugation or some multiple thereof. The now compact structure of antigorite as compared to the other members of the group accounts for its increased density and thermal stability.

Many products have been observed for the decomposition of serpentine. Bowen and Tuttle (1949) have reported the reaction

A) $Mg_3Si_2O_5(OH)_4 \rightarrow Mg_2SiO_4 + Mg_3Si_4O_{10}(OH)_2 + H_2O$

serpentine — forsterite — talc — water

for the decomposition of serpentine under hydrothermal conditions. Brindley and Zussman (1957) have reported

B) $2Mg_3Si_2O_5(OH)_4 \rightarrow 3Mg_2SiO_4 + SiO_2 + H_2O$

serpentine — forsterite — amorphous silica — water

for the decomposition of serpentine under conditions of high temperature and atmospheric pressure. It is important to note that under atmospheric conditions and probably also under vacuum conditions, the decomposition of antigorite proceeds in two steps with the formation of an intermediate phase, "dehydrated serpentine." DTA records show an endothermic peak at about 680 - 780°C corresponding to the loss of OH^- and an exothermic peak at 800 - 820°C for the structural breakdown. These reactions can be represented as follows:

C) $Mg_3Si_2O_5(OH)_4 \rightarrow Mg_3Si_2O_7 + 2H_2O$

serpentine — "dehydrated serpentine" — water

D) $2Mg_3Si_2O_7 \rightarrow 3Mg_2Si_2O_4 + SiO_2$

"dehydrated serpentine" — forsterite — amorphous silica

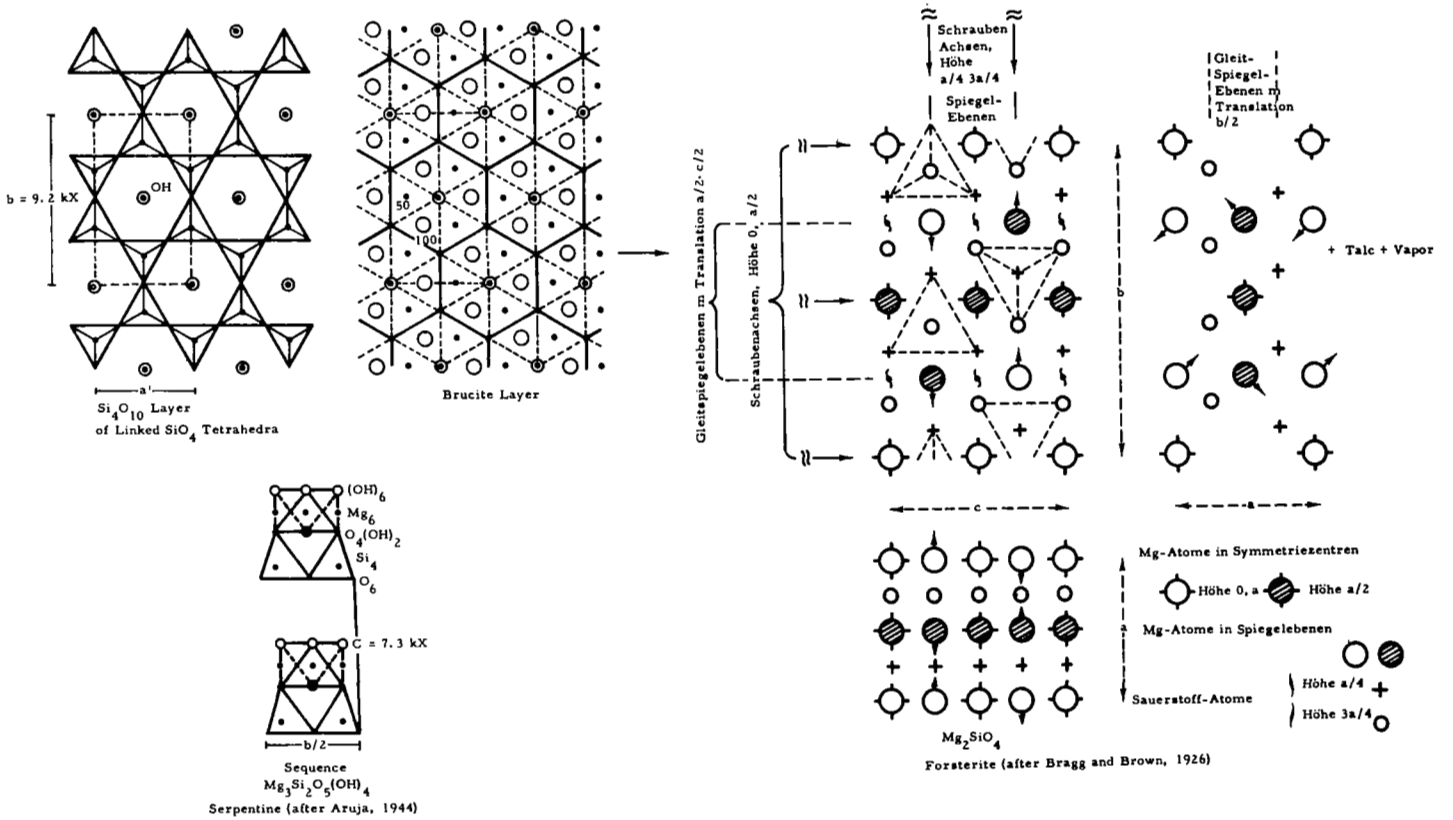

Figure 6-7 The Structures of Serpentine and Forsterite

In both A & B, one of the reaction products is forsterite. According to the X-ray data of Brindley and Zussman (1957), the cell dimensions of serpentine and forsterite are related in the following manner: $2a_s = b_f$ and $2b_s = 3c_f$ (see Figure 6-7). The loss of OH^-, while leaving the SiO_4 sheet largely intact, causes considerable disruption of the Mg - O(OH), brucite sheet. Consequently, the layer structure partially collapses to the three dimensionally bonded structure of forsterite. This transformation requires only a slight rotation of the SiO_4 tetrahedra in the tetrahedral sheet.

The stability curve for serpentine as determined from the data of Bowen and Tuttle (1949) is represented in Figure 6-8. Due to the lack of heat capacity information for serpentine, it was necessary to assume that the enthalpy of the reaction remained constant in extrapolating this curve to lower temperatures and pressures. Another assumption inherent in this type of analysis is that water vapor behaves as an ideal gas in the temperature and pressure ranges of hydrothermal synthesis. While both of these assumptions lead to a certain amount of deviation from equilibrium results, this is the best that can be done with the limited amount of thermodynamic information available at this time.

The mass spectrometer data are represented in Figure 6-4. However, this curve represents only the dehydration of serpentine due to the fact that reactions involving only solid phases cannot be observed in the mass spectrometer.

$$Mg_3Si_2O_5(OH)_4 \rightarrow Mg_3Si_2O_7 + 2H_2O$$

serpentine — "dehydrated serpentine" — water

	P_{H_2O} (mm H_g)	T^oC
DTA	12.5	490 ± 20
Mass Spectrometer	5×10^{-6}	270 ± 5

Extrapolation of the mass spectrometer and DTA data and the data of Bowen and Tuttle (1942) to the lunar environment gives:

serpentine → "dehydrated serpentine" + vapor

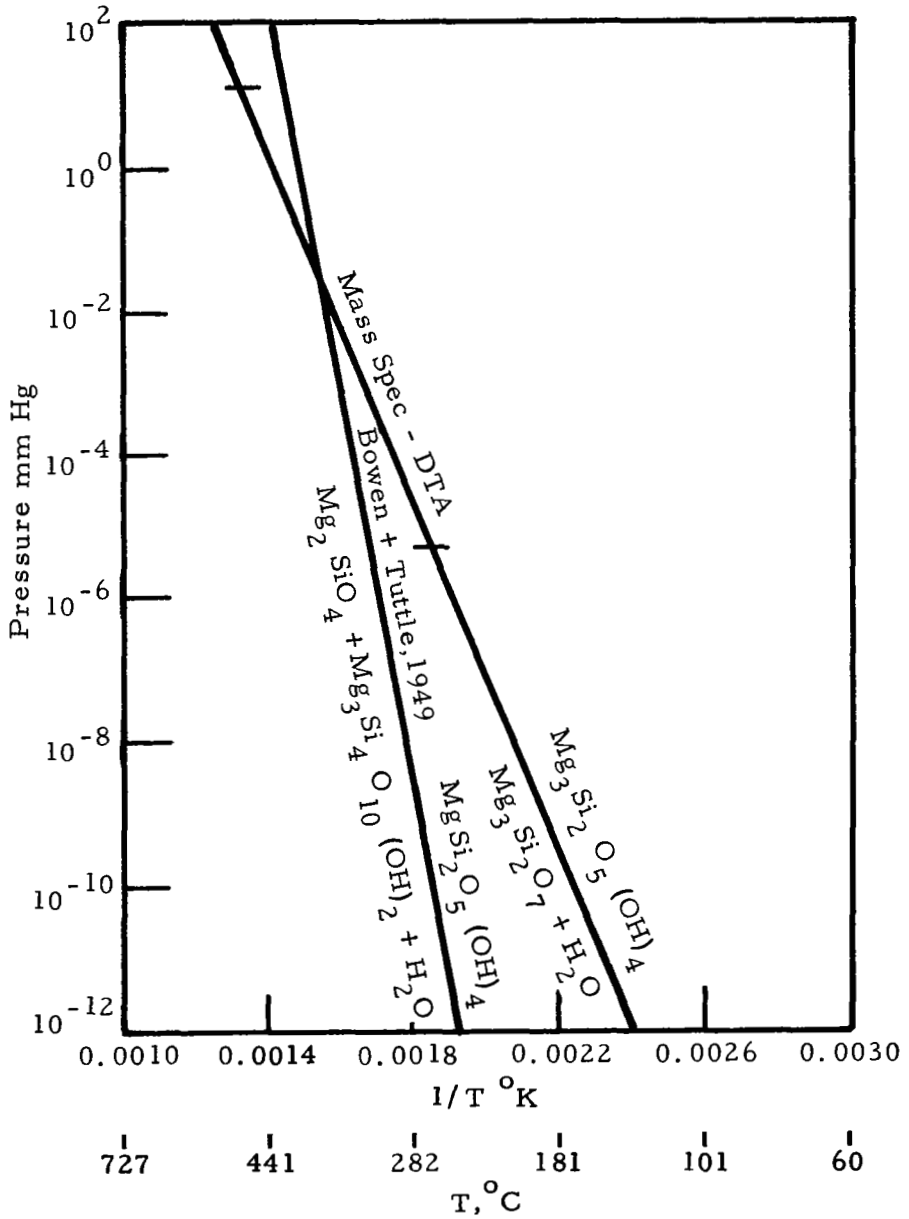

Figure 6-8 Stability Curve of Serpentine

Lunar Temperature	$T^{\circ}D$	$T^{\circ}K$	P_{H_2O} mm Hg
Minimum nighttime	-180	93	1.0×10^{-108}
Equilibrium at 1-m depth	- 55	218	1.0×10^{-37}
Maximum daytime	+130	403	2.2×10^{-12}
At lunar pressure	+152	452	1.0×10^{-11}

serpentine → forsterite + talc + vapor

Lunar Temperature	$T^{\circ}C$	$T^{\circ}K$	P_{H_2O} mm Hg
Minimum nighttime	-180	93	1.6×10^{-241}
Equilibrium at 1-m depth	- 55	218	1.0×10^{-80}
Maximum daytime	+130	403	6.3×10^{-27}
At lunar pressure	+258	531	1.0×10^{-11}

It has been shown experimentally that the curves plotted from the mass spectrometer and DTA data generally lie 200 - 300°C higher than the corresponding equilibrium curves. Based upon this consideration, serpentine should dehydrate during the lunar day but should be stable at a depth of 1 m. Rehydration during the lunar night is not probable due to the partial collapse of the serpentine structure. The reaction serpentine → forsterite + talc + vapor should not occur under lunar conditions.

SECTION 7

BASALT GLASS

7.1 FORMULA

7.2 MINERAL CLASSIFICATION

A simulated natural glass (anhydrous).

7.3 SPECIMEN LOCALITY

Produced in the laboratory from a pure basalt specimen originating from Branchville, Connecticut.

7.4 PROCUREMENT SOURCE

Southwest Scientific Co., Scottsdale, Arizona.

7.5 OPTICAL MICROSCOPIC ANALYSIS

The fusing of this pure basalt in the laboratory resulted in a brown scoriaceous glass with many gas bubbles (Figure 7-1). Fine crystallites, comprising about 2% of the mass, impart a cloudy appearance to the glass. These are no doubt the products of devitrification during cooling. Another 6% of unmelted labradorite crystals (relics of the larger phenocrysts) are scattered throughout the glass. The index of refraction of the basalt glass is 1.595.

7.6 THERMAL ANALYSIS

7.6.1 Differential Thermal Analysis

See Figure 7-2.

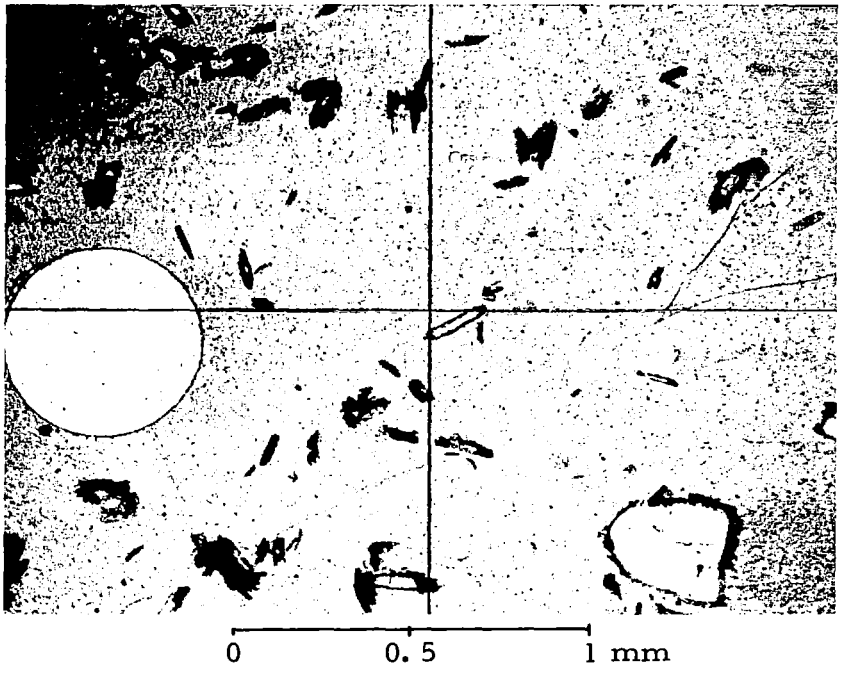

Figure 7-1 Photomicrograph of Basalt Glass, 47X, Gas Bubble at Left, Plagioclase Relic at Lower Right, Crystallite Scattered Over Field

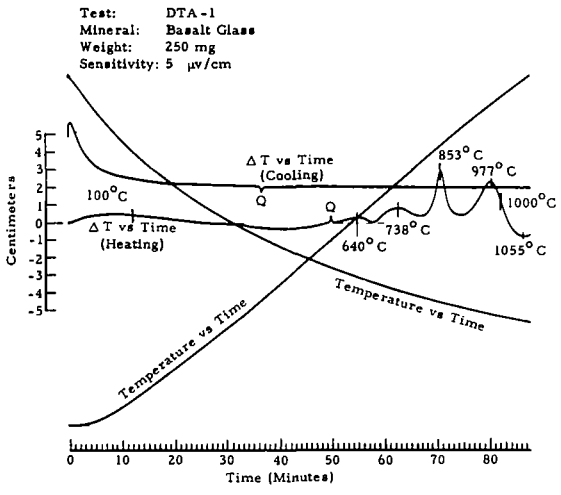

Figure 7-2 Basalt Glass DTA-1

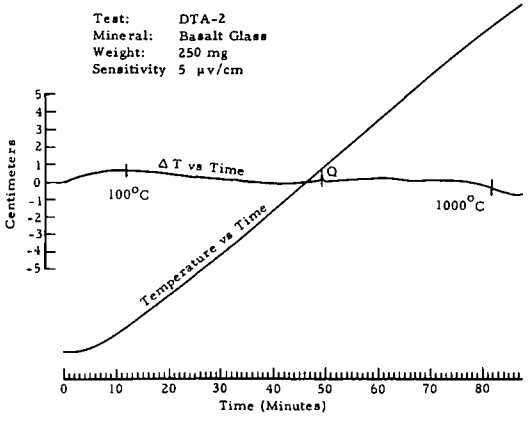

Figure 7-3 Basalt Glass DTA-2

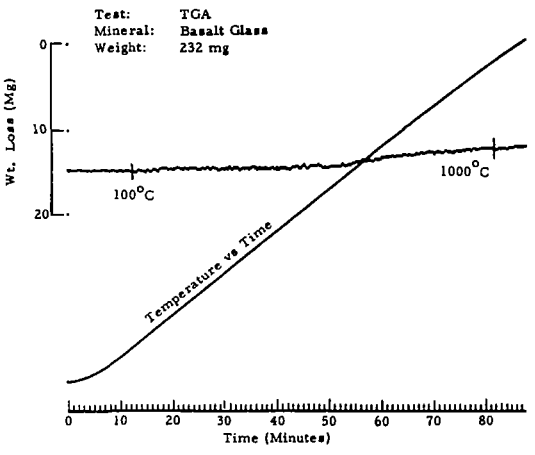

Figure 7-4 Basalt Glass TGA

7. 6. 1. 1 Sensitivity

The sensitivity is 5 μv/cm.

7. 6. 1. 2 Peak values

These are:

640°C (+) Broad

738°C (+)

853°C (+) Fairly sharp

977°C (+)

1055°C (-)

Upon cooling, these peaks are absent. The initial upward swing of the cooling DTA curve is instrumental. A second heating shows no such peaks (Figure 7-3). Perhaps the crystallites are responsible for some of the peaks.

7. 6. 2 Thermogravimetric Analysis

The TGA curve (Figure 7-4) records a 3-mg weight gain from 600 to 1050°C. Such a gain amounts to 1. 3% by weight. In view of the unexpected behavior of the basalt glass, additional tests were run, but identical results were obtained.

A possible explanation for this reaction is that the basalt glass (melted at 1300°C in a graphite crucible for 30 minutes and then air cooled) may contain elemental iron reduced by the graphite. The weight gain could then be accounted for by 9. 3 mg of iron oxidizing to Fe_2O_3. Whether the basalt glass contains the 3% uncombined iron is not known.

7. 6. 3 Mass Spectrometer Analysis

Except for a very small amount of absorbed water (Figure 7-5), the mass spectrometer does not detect the presence of any other volatile. As mentioned above, the DTA curve is quite complex, showing exothermic peaks at 640°C, 738°C, 853°C, and 977°C, and an endothermic peak at

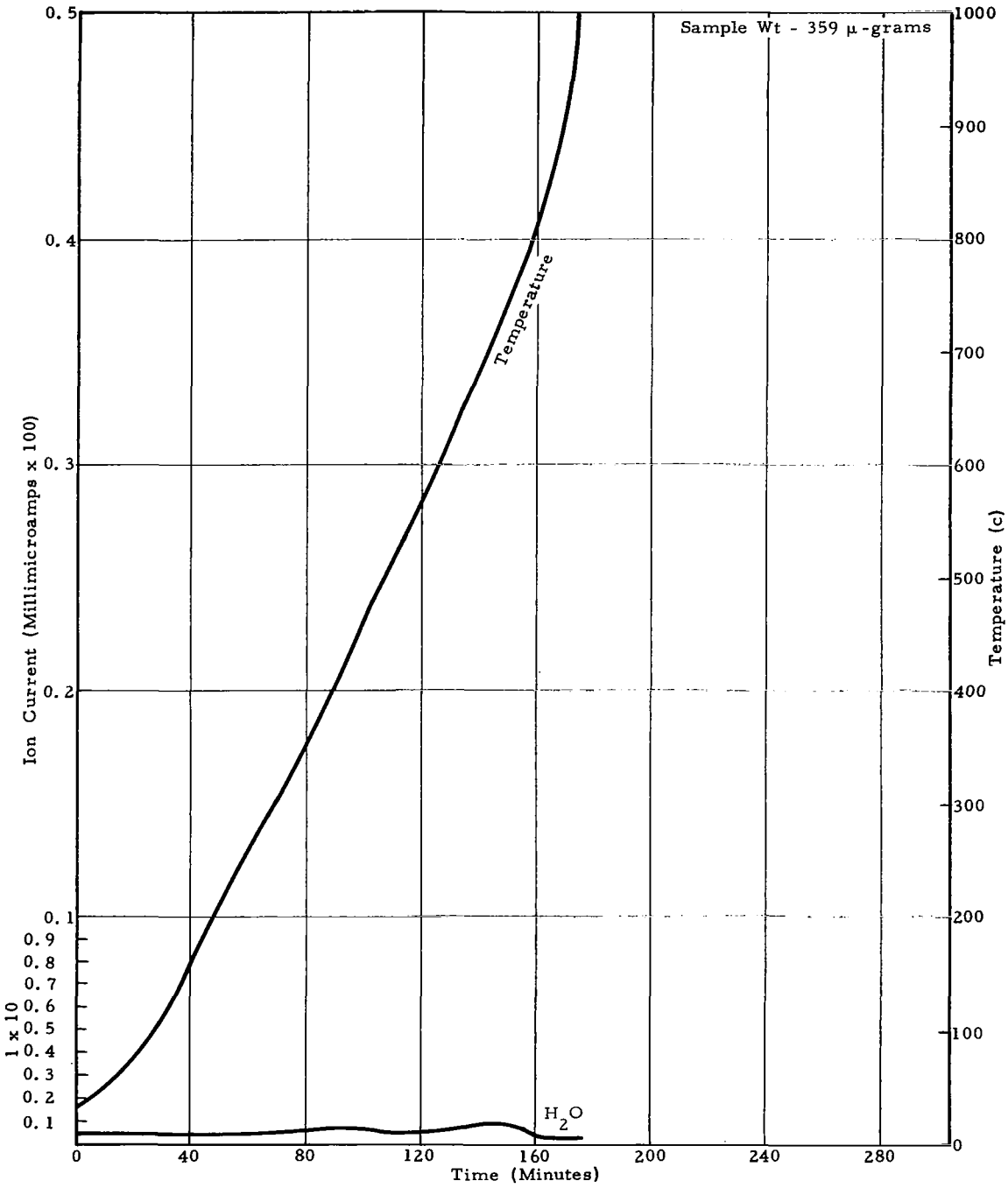

Figure 7-5 Mass Spectrometer Curve of Basalt Glass—Scan With H_2O Peak Plotted

1055°C. There is no corresponding reaction in the mass spectrometer. Moreover, the TGA sample gains weight during the course of the experiment, while the mass spectrometer sample does not. Presumably, the gain in weight may be the result of Fe oxidation. Since oxygen is absent in the mass spectrometer, this would account for no increase in weight in the mass spectrometer sample.

7.7 X-RAY DIFFRACTION PATTERNS

7.7.1 Debye-Scherrer Standard

The X-ray photograph (Figure 7-6) of the basalt glass shows no lines, confirming its noncrystalline nature. There is, however, one well-defined but very weak line with its d-value equal to 2.5Å (Table 7-1), corresponding to a strong plagioclase line. This confirms the results of a previous optical examination, which disclosed the presence of a small amount of unfused plagioclase. It may be explained by the fact that this X-ray

TABLE 7-1

COMPARISON OF EXPERIMENTAL AND ASTM D-VALUES FOR BASALT GLASS

Exp (Å)	ASTM (Å)
3.1	-
2.5	2.51 (plagioclase)
2.3	-

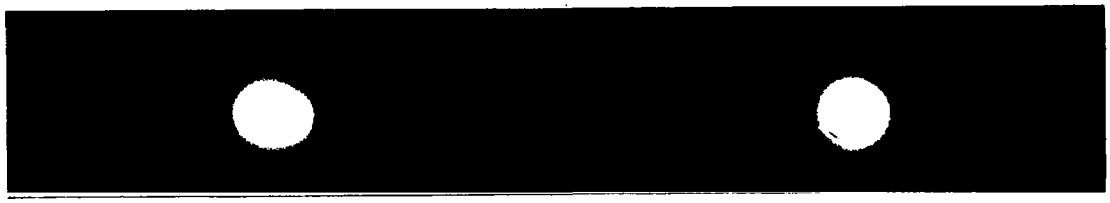

90 mm

Figure 7-6 Basalt Glass X-Ray Pattern Taken with the Debye-Scherrer Camera

film had an exposure time longer than normal. Since the line is weak, only a very small amount of plagioclase could be present. Two other very weak lines are discernible on the X-ray film. These too correspond to plagioclase lines.

7. 7. 2 Bendix Vacuum Camera Standard

Table 7-2 compares the Bendix Camera Standard with the Debye-Scherrer Standard.

TABLE 7-2

COMPARISON OF OBSERVED D-VALUES AND RELATIVE INTENSITY MEASUREMENTS FOR BASALT GLASS

Debye-Scherrer Standard, Cu K_α		Bendix Camera Standard, Cu K_α	
d_{obs}	$\frac{i}{i_o}$	d_{obs}	$\frac{i}{i_o}$
3. 1	20	The quantity of crystalline plagioclase in the sample is too small to cause observable diffraction lines on the Bendix Camera Standard.	
2. 5	100		
2. 3	20		

7. 7. 3 Vacuum Patterns

All diffraction patterns obtained under the conditions of Phase I failed to show any lines as did the Standard (Table 7-2), indicating no significant change in long-range order in the glass as a product of recrystallization. This material was not used in Phase II.

SECTION 8

CALCITE

8.1 FORMULA

$CaCO_3$.

8.2 MINERAL CLASSIFICATION

Carbonate.

8.3 SPECIMEN LOCALITY

Creel, Chihuahua, Mexico.

8.4 PROCUREMENT SOURCE

Southwest Scientific Co., Scottsdale, Arizona.

8.5 OPTICAL MICROSCOPIC ANALYSIS

This clear crystal of calcite, var. Iceland spar, is of the highest purity. No other phases are visible under the microscope (Figure 8-1). It should be noted, however, that the glide twinning characteristic of crushed calcite is quite evident in the grains studied. The ordinary index of refraction is 1.658.

8.6 THERMAL ANALYSES

8.6.1 Differential Thermal Analysis

See Figure 8-2.

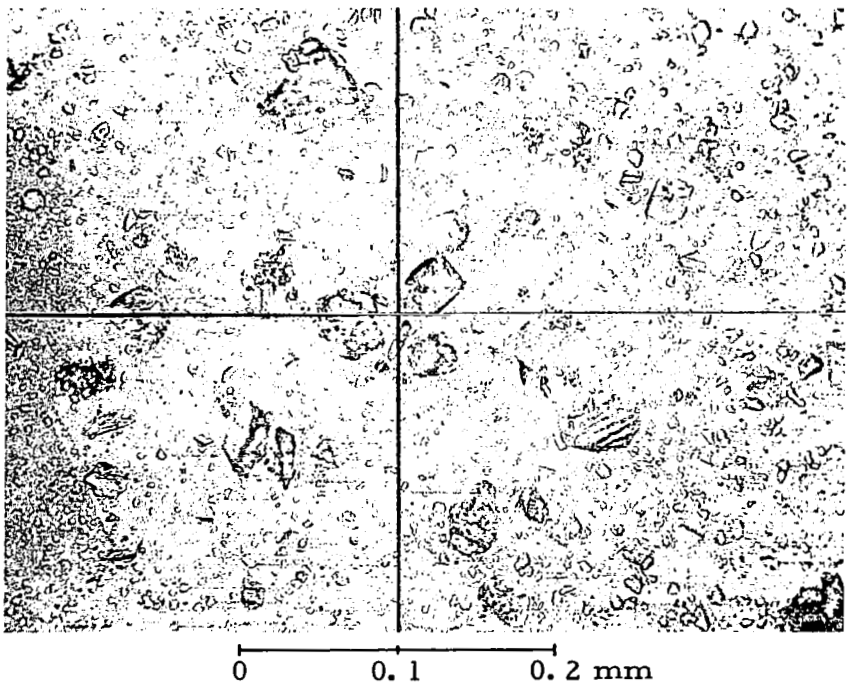

Figure 8-1 Photomicrograph of Calcite, 210X, DTA Sample in Medium Having Index of Refraction of 1. 56

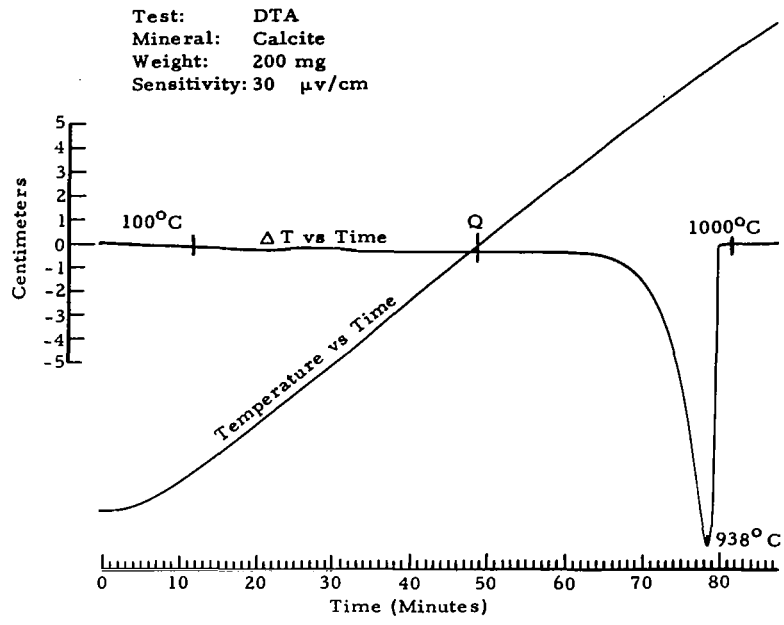

Figure 8-2 Calcite DTA

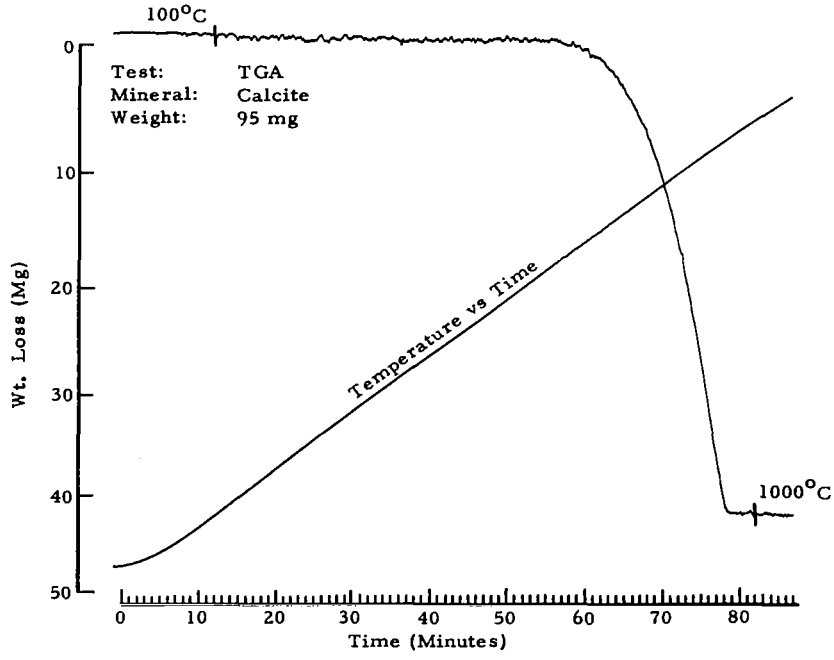

Figure 8-3 Calcite TGA

8. 6. 1. 1 Sensitivity

The sensitivity is 30 μv/cm.

8. 6. 1. 2 Peak values

These are:

250°C (+)

938°C (-) Loss of CO_2.

A small but broad exothermic peak is noted at 250°C, probably the inversion of aragonite into calcite. A more significant endothermic peak occurs at 938°C.

8. 6. 2 Thermogravimetric Analysis

A single, strong endothermic peak is shown at 938°C, nearly an ideal zero-order reaction. The TGA weight loss amounts to 44. 3% of the sample weight (Figure 8-3) and is composed essentially of CO_2. It compares favorably with the theoretical weight loss (44. 0%).

8. 6. 3 Mass Spectrometer Analyses

The calcite, while subject to a total pressure of 1×10^{-6} torr or a P_{CO_2} of approximately 10^{-9} torr, decomposes at a temperature of 323°C ±5° to yield CaO and CO_2. The electron beam in the mass spectrometer, in addition to ionizing the CO_2, possesses sufficient energy to break some of the molecular bonds of the CO_2 and produce CO, C, and O. Consequently, several mass spectrometer curves are required to monitor the volatiles (Figures 8-4 to 8-7).

It should be emphasized, however, that only one of the volatiles (CO_2) is a direct product of decomposition. Note that the temperatures at which CO, C, and O are produced closely approximate the temperature of CO_2 formation.

The mass spectrometer curve (Figure 8-4) describing the decomposition of calcite indicates a large peak beginning at 323°C. This

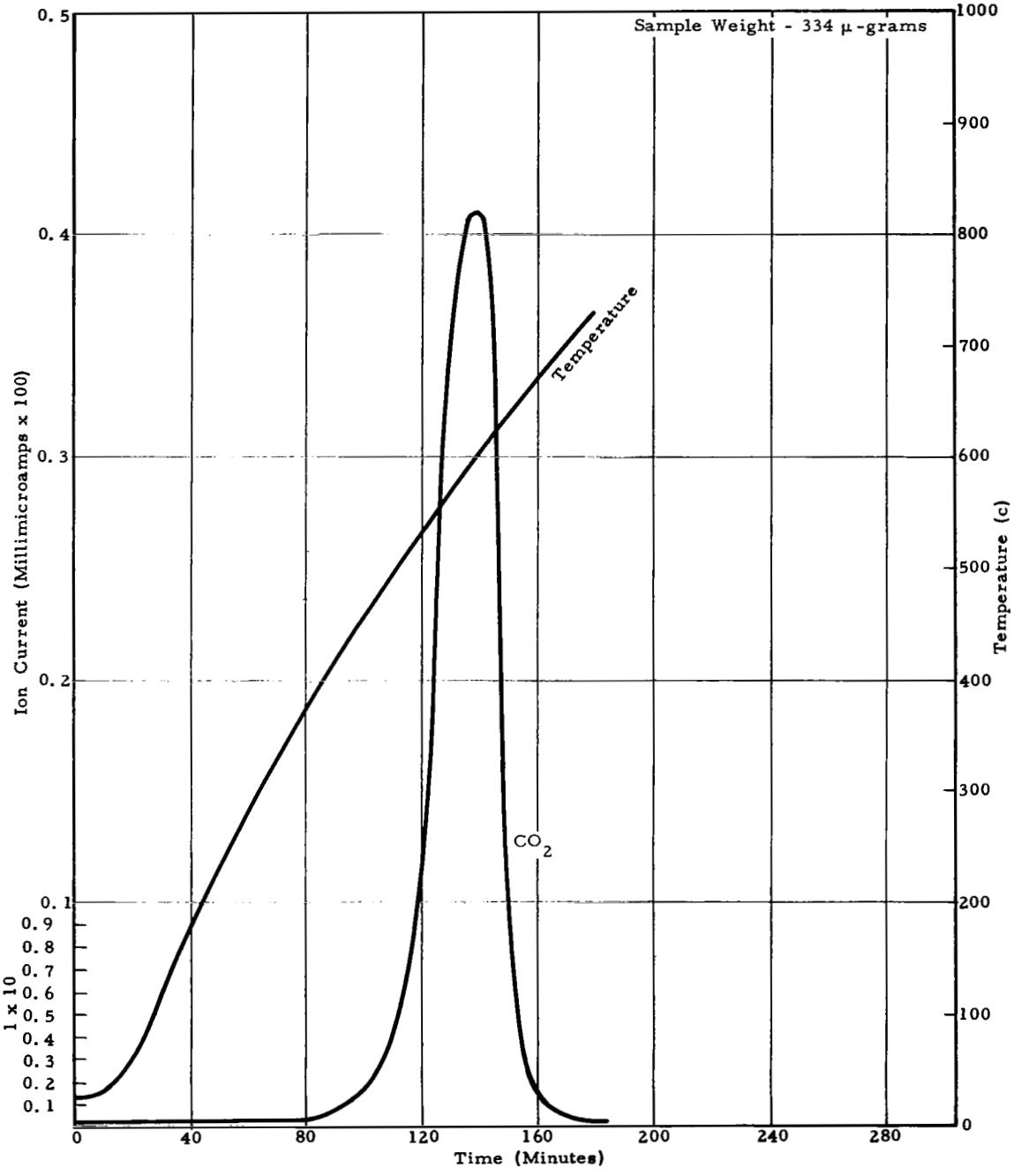

Figure 8-4 Mass Spectrometer Curve of Calcite—Scan With CO_2 Peak Plotted

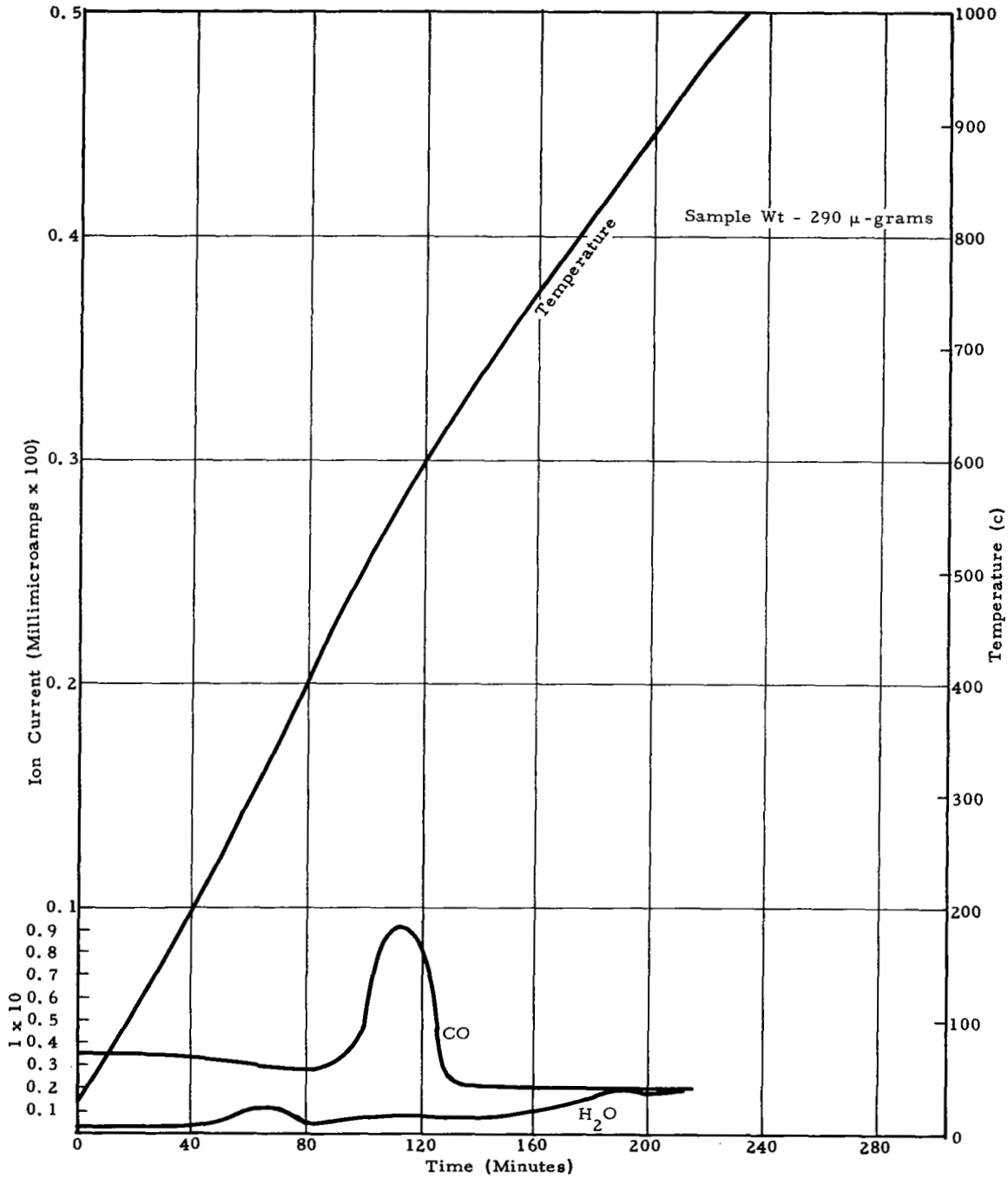

Figure 8-5 Mass Spectrometer Curve of Calcite—CO and H_2O Peaks

corresponds to the large endothermic peak at 938°C on the DTA curve. Although the loss of absorbed water is small (Figure 8-5), estimated at < 1%. it is nevertheless responsible for the slight endothermic drift in the DTA curve and the minute weight loss in the TGA curve. The evolution of C and O is shown in Figures 8-6 and 8-7.

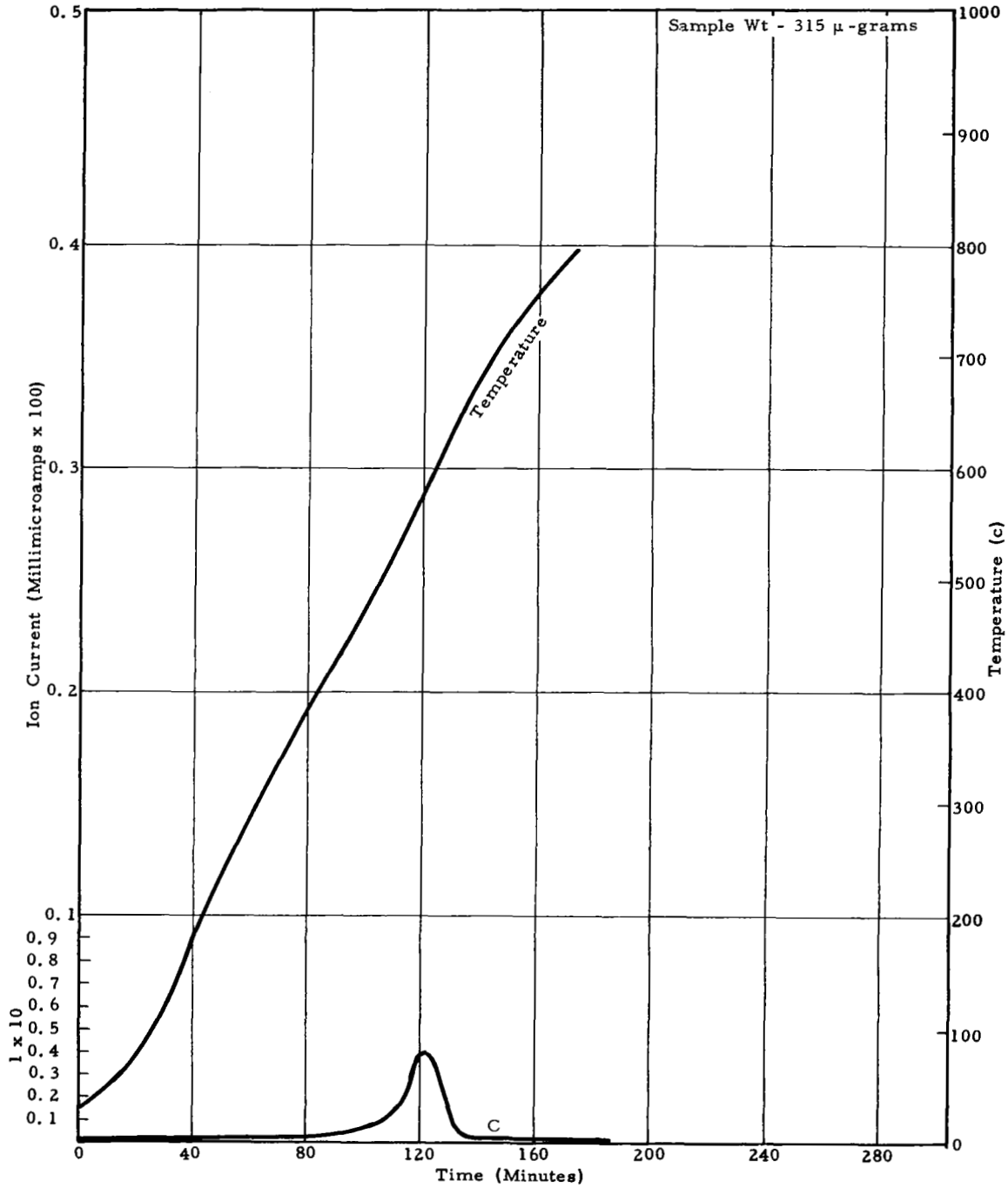

Figure 8-6 Mass Spectrometer Curve of Calcite—C Peak

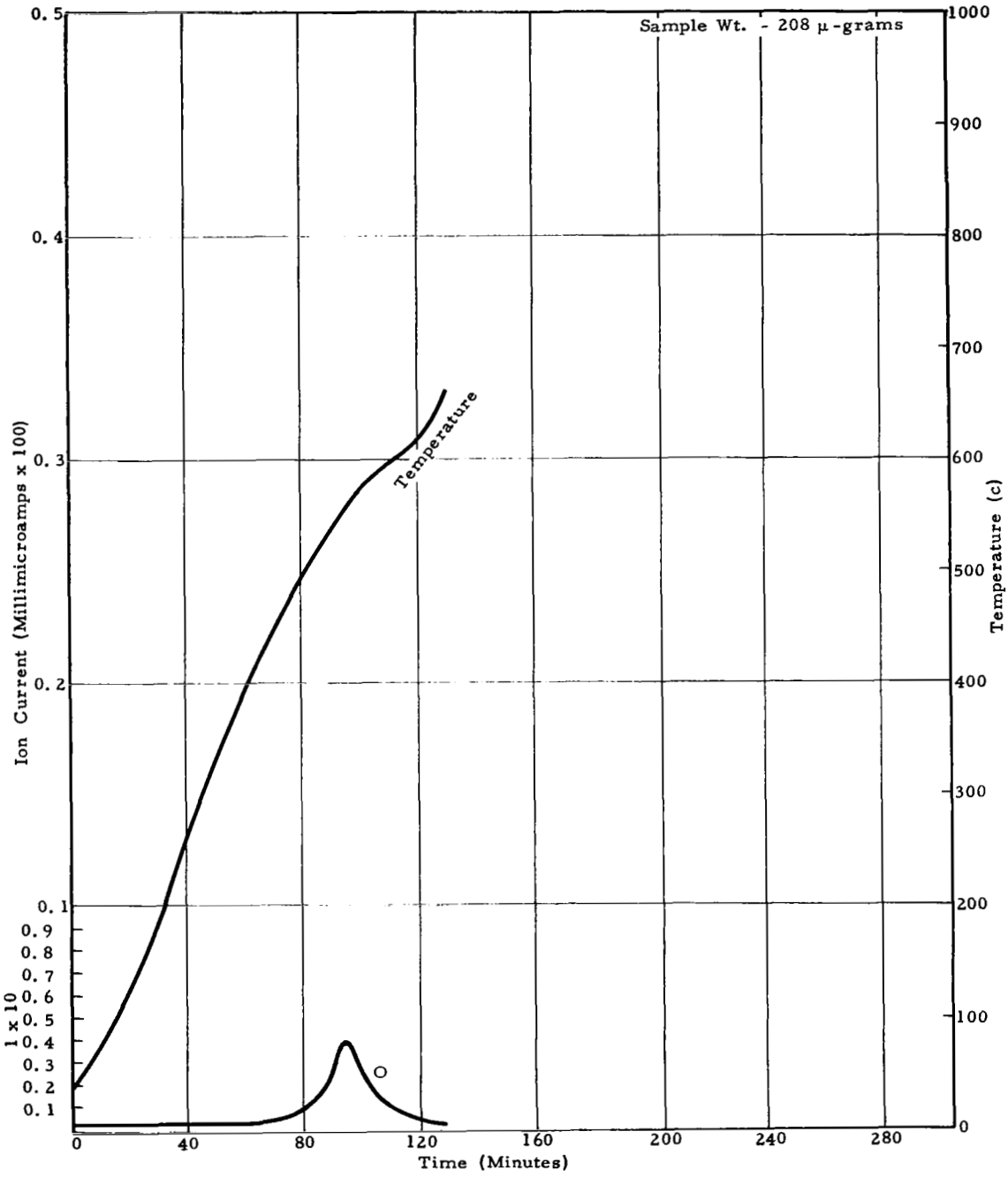

Figure 8-7 Mass Spectrometer Curve of Calcite—O Peak

8.7 X-RAY DIFFRACTION PATTERNS

8.7.1 Debye-Scherrer Standard

The calcite pattern (Figure 8-8) reveals one very weak line (D = 3.3 Å) that does not belong with the others. This line corresponds to the strongest line of aragonite (Table 8-1), a high-pressure polymorph of calcite. Since it is an established fact that calcite can be transformed into aragonite with grinding, the presence of a small amount (< 1%) of aragonite in the sample is not unexpected. Heating the sample should cause the aragonite to retransform into calcite. This inversion probably corresponds to the low exothermic peak barely detected at 250°C on the DTA curve.

TABLE 8-1

COMPARISON OF EXPERIMENTAL AND ASTM D-VALUES FOR CALCITE

Exp (Å)	ASTM (Å)	Exp (Å)	ASTM (Å)	Exp (Å)	ASTM (Å)	Exp (Å)	ASTM (Å)
3.8	3.86	1.86	1.875	1.33	1.339	1.06	1.0613
3.3	3.4 (Aragonite)	1.60	1.604	1.29	1.297	1.04	1.0473
3.0	3.035	1.52	1.525	1.24	1.247	1.03	1.0352
2.49	2.495	1.47	1.473	1.23	1.235	1.01	1.0118
2.28	2.285	1.44	1.440	1.18	1.179	0.98	0.9846
2.08	2.095	1.41	1.422	1.15	1.1538	0.96	0.9655
1.90	1.913	1.36	1.356	1.14	1.1425		

Figure 8-8 Calcite X-Ray Pattern Taken With Debye-Scherrer Camera

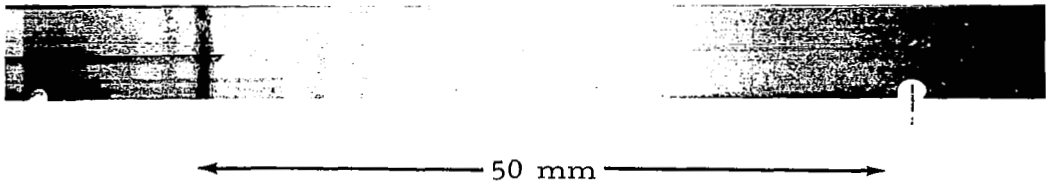

Figure 8-9 Calcite X-Ray Pattern Taken With Bendix Vacuum Camera (Magnification 2X)

8. 7. 2 Bendix Vacuum Camera Standard

There is generally good agreement (Table 8-2) between values of the Debye-Scherrer and Bendix camera standards, irrespective of the generally poorer resolution of the latter. Figure 8-9 shows the X-ray pattern taken with the Bendix Vacuum Camera.

TABLE 8-2

COMPARISON OF OBSERVED D-VALUES AND RELATIVE INTENSITY MEASUREMENTS FOR CALCITE

Debye-Scherrer Standard, CuK_α		Bendix Camera Standard, CuK_α	
d_{obs}	$\frac{i}{i_o}$	d_{obs}	$\frac{i}{i_o}$
3. 8	25	3. 7	5
3. 3	25	3. 2	40
3. 0	100	2. 8	100
3. 28	50	2. 3	20
2. 08	50	2. 1	30
1. 90	50	1. 9	30
1. 60	90	1. 7	30
1. 52	50	1. 5	10
1. 41	50	1. 4	10

8. 7. 3 Vacuum Patterns

All diffraction patterns obtained under the conditions of Phase I precisely duplicated that of the standard, using visual comparison. Therefore, as explained in Section 8. 8, no change occurred and this mineral was not included in Phase II.

8. 8 ANALYSIS OF THERMODYNAMIC AND CRYSTAL STRUCTURE DATA

The structure of calcite is analogous to that of NaCl with the Ca^{+2} ions and the $CO_3^{=}$ groups replacing the Na^{+} and Cl^{-} ions, respectively. To accommodate the large planar CO_3^{-2} groups, the unit cell is compressed along a 3-fold axis to yield a face-centered rhombohedral cell (see Figure 8-10). The arrangement of the Ca^{+2} ions approximates that of cubic closest packing. The Ca^{+2} ions are all structurally equivalent, and each is coordinated by six oxygen atoms of six different CO_3^{-2} groups. Each oxygen atom linked to two Ca atoms and a carbon atom. The strongest bonds within the structure are the C-O bonds of the CO_3^{-2} groups.

Calcite, when subjected to elevated temperatures, decomposes to a solid, CaO, and a gas, CO_2. The decomposition of calcite requires the rupturing of one of the strong C-O bonds, thus explaining its relatively high thermal stability. One of the products of decomposition, CaO, has the NaCl structure. Consequently, each ion is octahedrally coordinated by six ions of the opposite type.

Much information concerning the thermodynamics of the dissociation of calcite is available. One of the earliest attempts to determine the vapor pressure of calcite was undertaken by J. Johnston (1910). He determined the vapor pressure of calcite at temperatures between 887 and 1167°C (see Figure 8-11). From these vapor pressure data, he obtained the following relation:

$$\text{Log } P_{CO_2} = -9,340T^{-1} + 1.1 \log T - 0.0012T + 8.882.$$

In 1923, Smyth and Adams studied the system $CaO - CaCO_3 - CO_2$ over the temperature range 1500 - 830°C and obtained the equation:

$$\text{Log } P_{CO_2} \text{ (mm)} = -11,355T^{-1} - 5.388 \log T + 29.199.$$

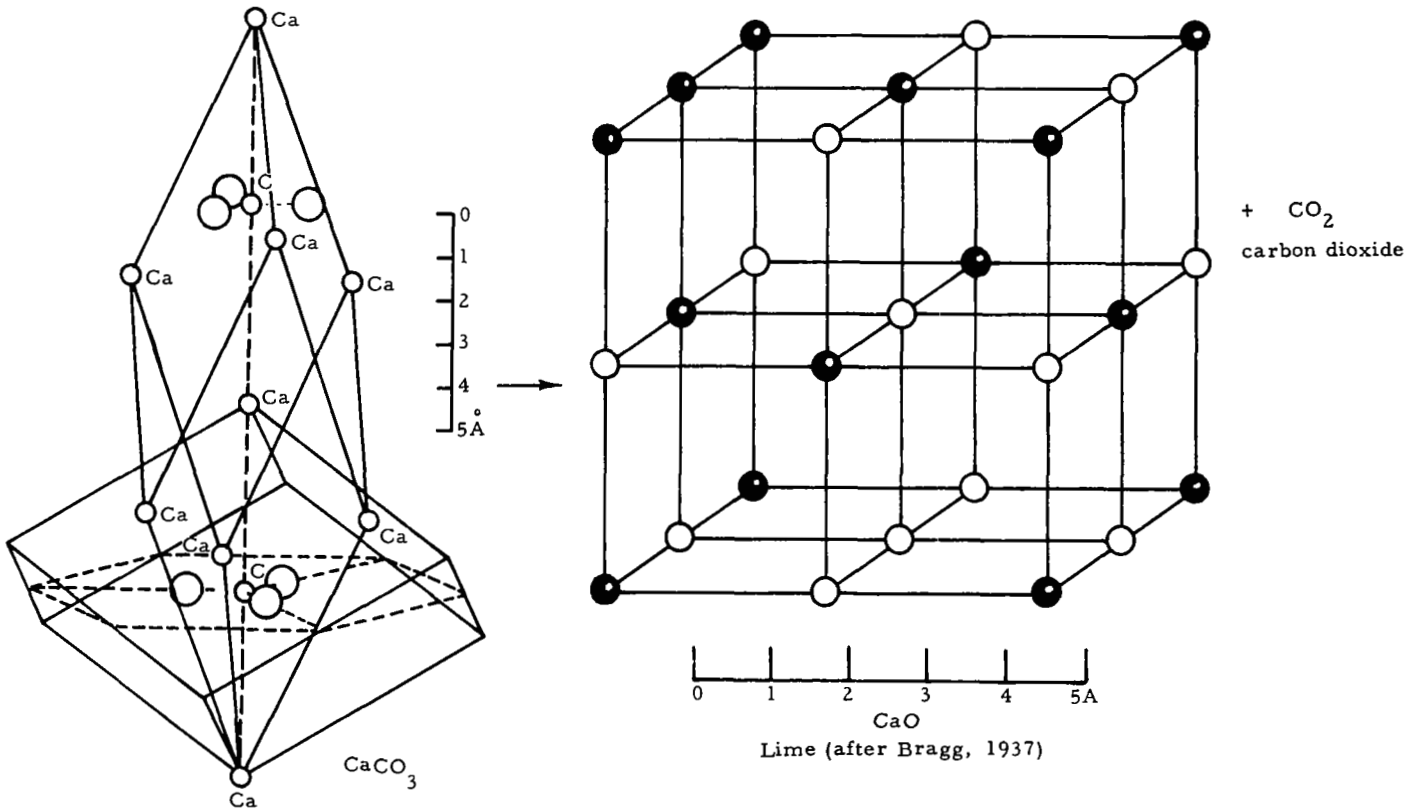

Figure 8-10 The Structure of Calcite and Lime

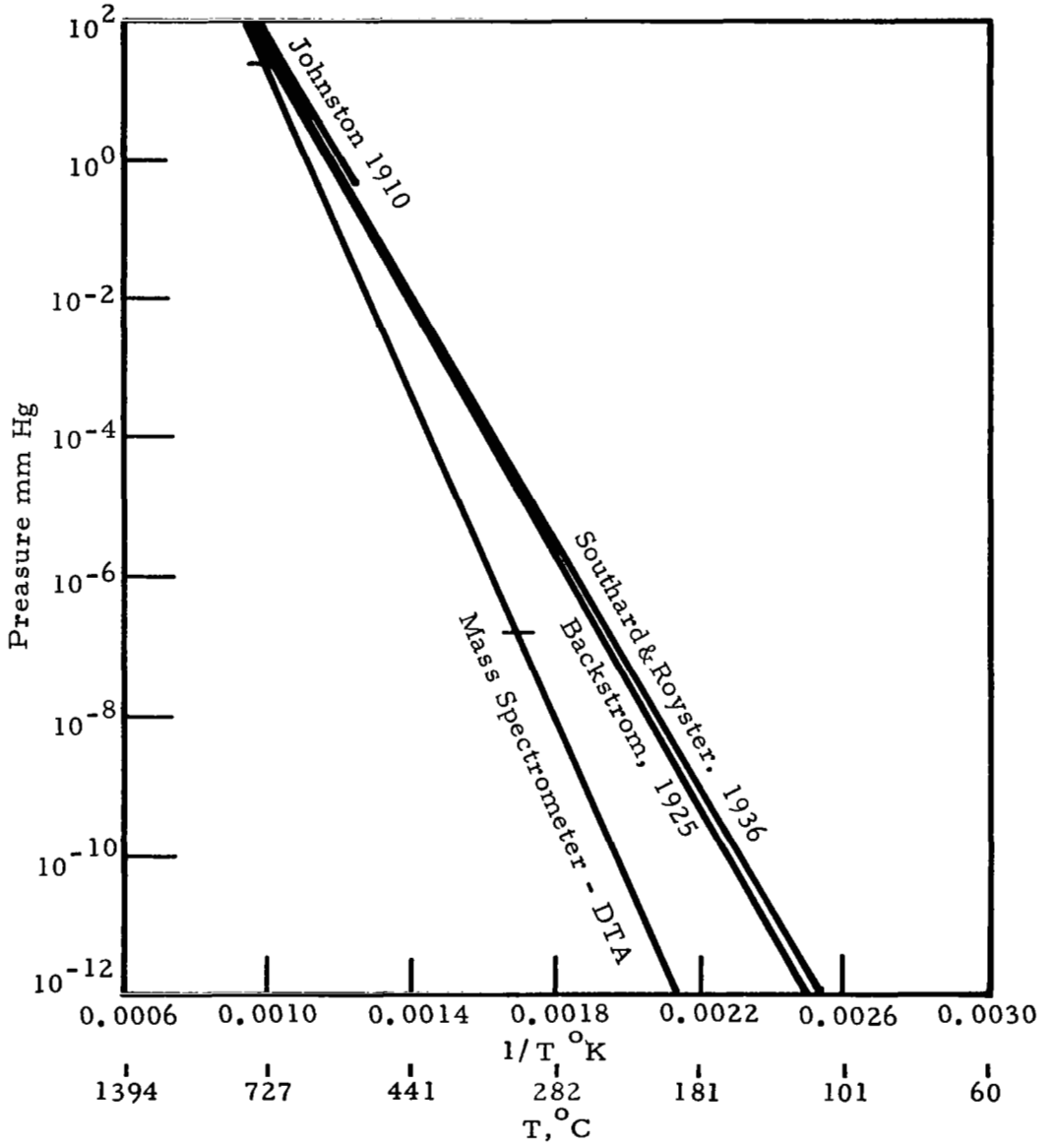

Figure 8-11 Stability Curve of Calcite

Little confidence should be placed in these equations outside of the temperature range from which they were formulated.

One of the most comprehensive studies of the stability of calcite was that of H. L. J. Backstrom (1925). Backstrom, in his calculations, applied only the most reliable of the heat capacity data available at that time. From the data of Lewis et al. (1923), he obtained a ΔCp of reaction corresponding to the equation:

$$\Delta Cp = -3.34 + 1.378 \times 10^{-2} T - 4.13 \times 10^{-6} T^2$$

which he claimed was accurate to within 1% for the temperature range 0 - 1200°C. Then letting

$$\Delta H_{298} = 42,600 \text{ cal/mole}$$

and

$$\frac{d\,\Delta H}{dT} = 3.34 - 1.378 \times 10^{-2} T + 4.13 \times 10^{-6} T^2,$$

he obtained the vapor pressure equation:

$$\text{Log } P_{mm} = -9,212.4 T^{-1} + 1.6797 \log T - 1.5048 \times 10^{-3} T + 0.1503 \times 10^{-6} T^2 + I.$$

Backstrom then applied his equation to the data of Johnston and obtained a value of I = 7.161, resulting in the equation:

$$\text{Log } P_{mm} = 9,212.4 T^{-1} + 1.6797 \log T - 1.5048 \times 10^{-3} T + 0.1503 \times 10^{-6} T^2 + 7.161.$$

Southard and Royster (1936) studied the stability of calcite. Utilizing values of P_{CO_2} obtained over a temperature range of 774-900°C and a value of Cp = 0.76 - 0.0016T, they obtained the equation:

$$\text{Log Pcm} = -9.140T^{-1} + 0.382 \log T - 0.668 \times 10^{-3}T + 9.3171.$$

A graphical representation of the vapor pressure equations of Southard and Royster (1936) and Backstrom (1925) is shown in Figure 8-11.

The results of the study of the decomposition of calcite under the pressure conditions of the mass spectrometer and DTA unit are tabulated as follows:

	P_{CO_2} mm Hg	Temperature °C
DTA	25	732 ± 20
Mass Spectrometer	1.5×10^{-7}	323 ± 5

The partial pressure of CO_2 is based upon an atmospheric content of 0.033 ± 0.001% CO_2 (Weast, 1964) and a pressure of 5×10^{-6} mm of Hg within the mass spectrometer.

Extrapolation of the data on calcite stability to lunar conditions gives:

Lunar Temperature	T°C	T°K	P_{CO_2} mm of Hg	
			Backstrom 1925	Southard & Royster 1936
Minimum nighttime	-180	93	2.1×10^{-89}	2.1×10^{-87}
Equilibrium at 1-m depth	- 55	218	4.5×10^{-32}	2.2×10^{-31}
Maximum daytime	+130	403	1.8×10^{-12}	3.2×10^{-12}

At lunar pressure (1×10^{-11} mm of Hg)		
	$T^{o}C$	$T^{o}K$
Backstrom, 1925	145	418
Southard and Royster, 1936	138	411

Based on the above data, calcite should be stable under the extremes of the lunar environment.

SECTION 9

CALCIUM MONTMORILLONITE

9.1 FORMULA

$Al_2Si_2O_5(OH)_4$.

9.2 MINERAL CLASSIFICATION AND VOLATILE

Hydrous aluminum silicate—H_2O, OH.

9.3 SPECIMEN LOCALITY

Gonzales, Texas.

9.4 PROCUREMENT SOURCE

Sample G360, Southern Clay Products.

9.5 OPTICAL MICROSCOPIC ANALYSIS

The specimen is finely divided, with the largest grains not exceeding 2μ in diameter (Figure 9-1). The only impurities evident are a few minute shards. The γ index of the calcium montmorillonite is 1.505.

9.6 THERMAL ANALYSES

9.6.1 Differential Thermal Analysis

See Figure 9-2.

9.6.1.1 Sensitivity

The sensitivity is 10μv/cm.

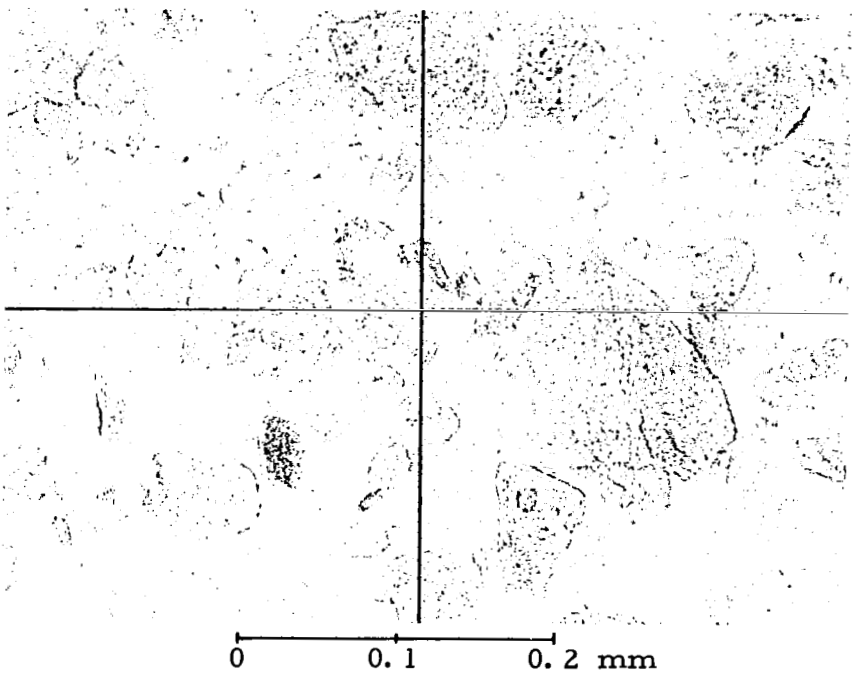

Figure 9-1 Photomicrograph of Ca-Montmorillonite, 210X; the Untreated Sample in Medium Having Index of Refraction of 1. 48

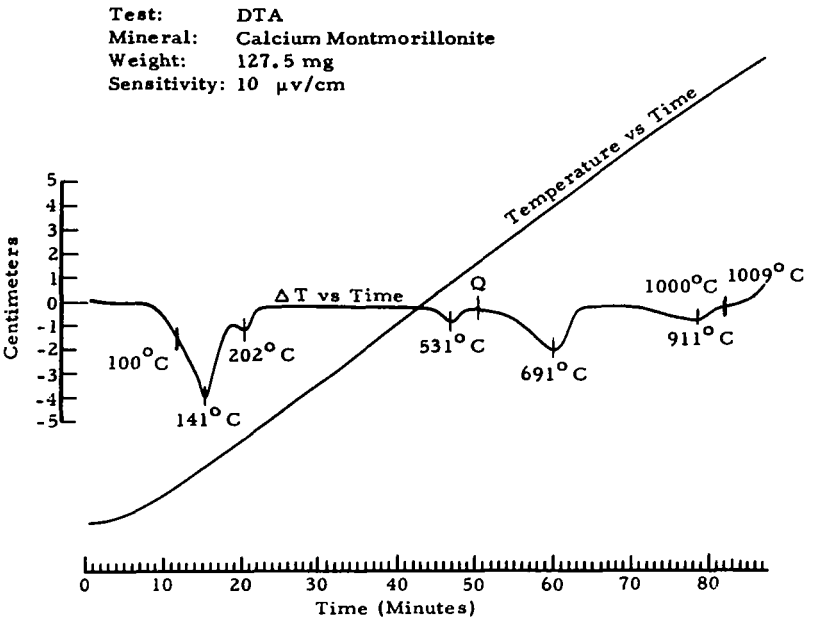

Figure 9-2 Ca-Montmorillonite DTA

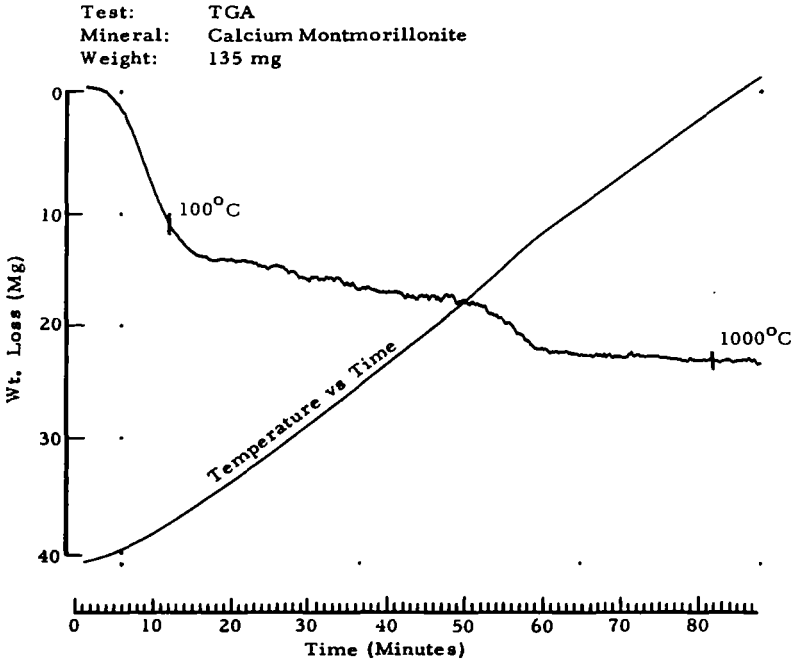

Figure 9-3 Ca-Montmorillonite TGA

9.6.1.2 Peak Values

These are:

141°C(-))	
:	Interlayer water
202°C(-))	
531°C(-)	Perhaps admixed Illite
691°C(-)	Principal loss of OH
911°C(-)	Complete breakdown of structure
above 1010°C(+)	Mullite, spinel, or gamma alumina

The double interlayer water peak is typical of calcium-montmorillonite.

9.6.2 Thermogravimetric Analysis

The TGA (Figure 9-3) indicates a 10.3% weight loss consisting of interlayer water, followed by another loss of interlayer water of 2.2%, and finally by a 3% loss of OH at the 691°C peak. No further weight reduction is recorded.

9.6.3 Mass Spectrometer Analysis

The calcium-montmorillonite sample includes a small amount of impurities, which has complicated the mass spectrometer curve (Figure 9-4). It is extremely difficult to determine precisely the temperature at which the OH volatilized.

The increase of the water content at 39°C is attributed to the volatilization of water from the impurities, while the increase at 240°C is probably derived from the OH vaporization of the calcium montmorillonite. It is evident from the size of the peaks that the sample lost all of its interlayer water in vacuum. This loss corresponds to the 141 and 202°C peaks in the DTA curve. Furthermore, the water peak at 39°C in the mass spectrometer curve corresponds to the DTA peak at 531°C. Likewise, the 240°C peak corresponds to the 691°C peak in the DTA curve.

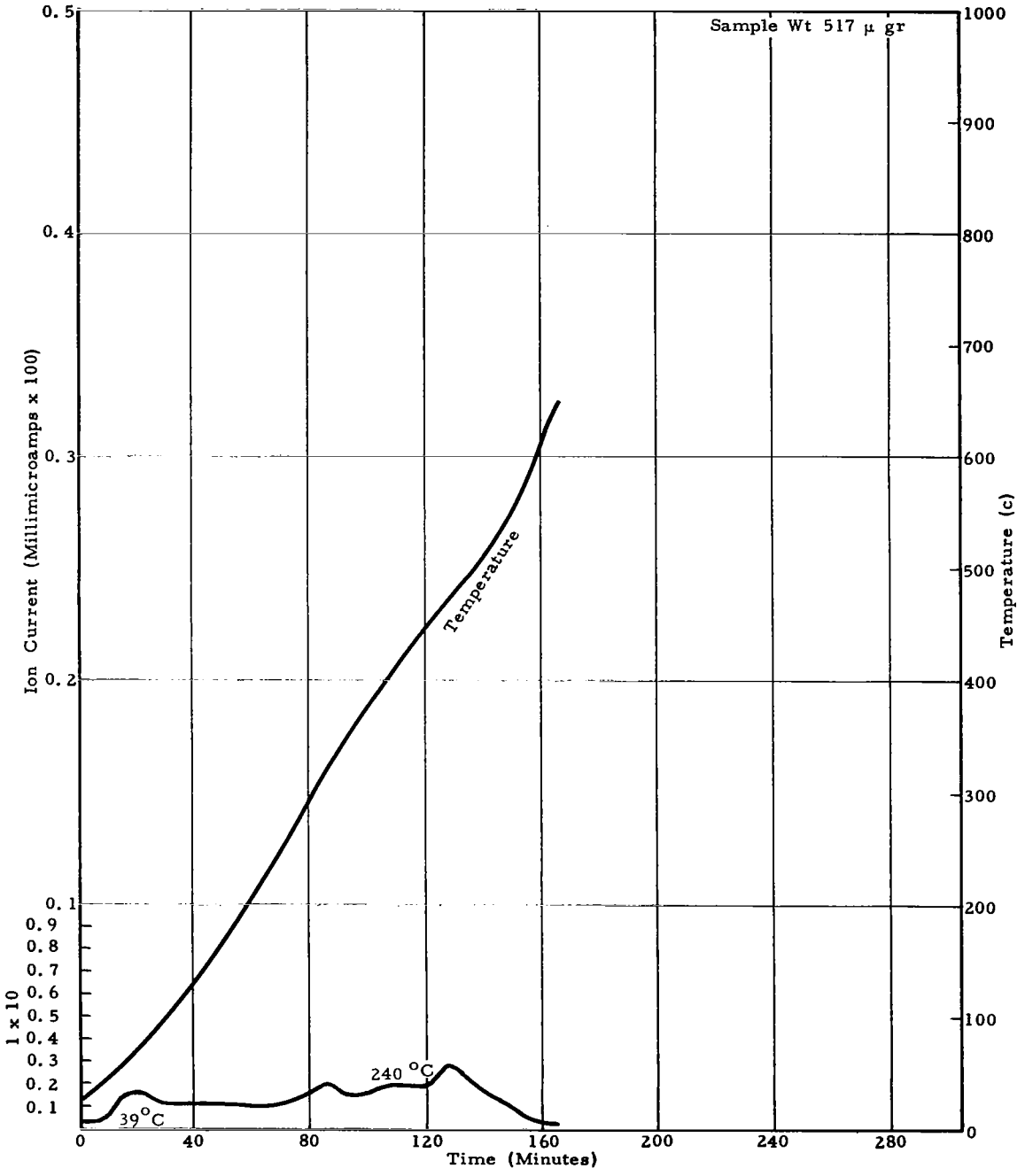

Figure 9-4 Mass Spectrometer Curve of Ca-Montmorillonite—H_2O Peak

9.7 X-RAY DIFFRACTION PATTERNS

9.7.1 Debye-Scherrer Standard

Figure 9-5 shows a calcium-montmorillonite X-ray pattern taken with the Debye-Scherrer camera. The Debye-Scherrer standard in general shows excellent correlation with ASTM values as shown in Table 9-1.

TABLE 9-1

COMPARISON OF EXPERIMENTAL AND ASTM D-VALUES FOR CA-MONTMORILLONITE

Exp (A)	ASTM (A)	Exp (A)	ASTM (A)
(4.50	4.50	1.69	1.70
Diffuse lines			
(4.05	4.05(Kerr, 1936)	1.49	1.49
3.10	3.02	1.29	1.285
2.55	(2.58	1.24	1.24
	(2.50		

9.7.2 Bendix Vacuum Camera Standard

Figure 9-6 shows a calcium-montmorillonite X-ray pattern taken with the Bendix Vacuum Camera (magnification 2x).

The correlation in values of the Debye-Scherrer and Bendix camera standards is in general good except that d-values for the Bendix camera standard are uniformly low (Table 9-2).

9.7.3 Vacuum Patterns

The diffraction patterns obtained under the conditions of Phase I duplicated those of the standard within the error of measurement. This result is surprising, however, in view of the fact that, as shown in Section 9.8, interlayer water should be lost under equilbrium conditions.

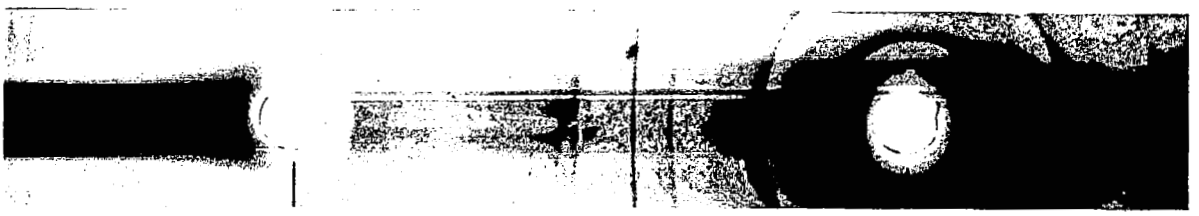

Figure 9-5 Ca-Montmorillenite X-Ray Pattern Taken With Debye-Scherrer Camera

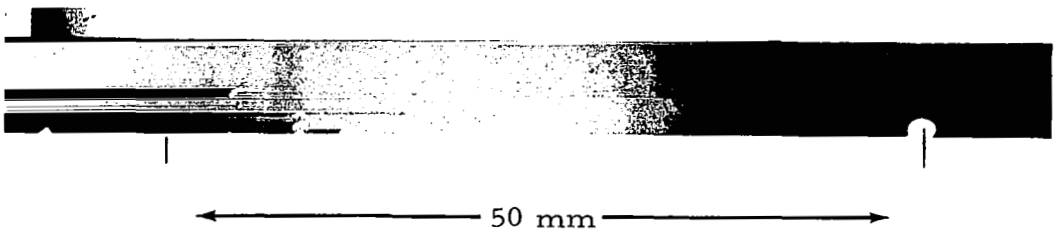

Figure 9-6 Ca-Montmorillonite X-Ray Pattern Taken With Bendix Vacuum Camera (Magnification 2X)

TABLE 9-2

COMPARISON OF OBSERVED D-VALUES AND RELATIVE INTENSITY MEASUREMENTS FOR CA-MONTMORILLONITE

Debye-Scherrer Standard, CuK_α		Bendix Camera Standard, CuK_α	
d_{obs}	$\frac{i}{i_o}$	d_{obs}	$\frac{i}{i_o}$
4.5	100	4.2	100
4.05	50	3.8	100
3.10	25	2.9	50
2.55	70	2.3	75
1.69	20	1.5	30
1.49	30	1.4	50

Since this water should volatilize readily, equilibrium with respect to it would be easily attained. The loss of interlayer water in montmorillonite is known to result in a detectable change in d-values. Montmorillonite was therefore used in Phase II.

9.7.4 Bendix Vacuum Standard, Phase II

The standard photograph of montmorillonite is reproduced in Figure 9-7. A comparison of the data obtained from the Bendix and Debye-Scherrer standards is presented in Table 9-3 and shows adequate correspondence.

9.7.5 Vacuum Patterns, Phase II

All photographs taken under conditions of high vacuum and over all temperatures duplicated that of the standard. Thus, the results of Phase I were duplicated in this respect. Since as noted above, devolatilization should occur and be readily detected by differences in X-ray patterns, these results are surprising. The only explanation at hand is

that, despite the fact specimens were packed into capillaries as loosely as possible and were of a minimum length, the dehydration of montmorillonite must be particularly sensitive to compaction. This is, in fact, the only mineral of all those studied, with the possible exception of talc, which should pack most efficiently.

TABLE 9-3

COMPARISON OF OBSERVED D-VALUES AND RELATIVE INTENSITY MEASUREMENTS OF CA-MONTMORILLONITE PHASE II

Debye-Scherrer Standard, CuK_α		Bendix Camera Standard, CuK_α	
d_{obs}	$\frac{i}{i_o}$	d_{obs}	$\frac{i}{i_o}$
4.5	100	4.5	80
4.05	50	3.9	50
3.10	25	(not observed)	
2.55	70	2.4	100
1.69	20	1.6	10
1.49	30	1.4	20

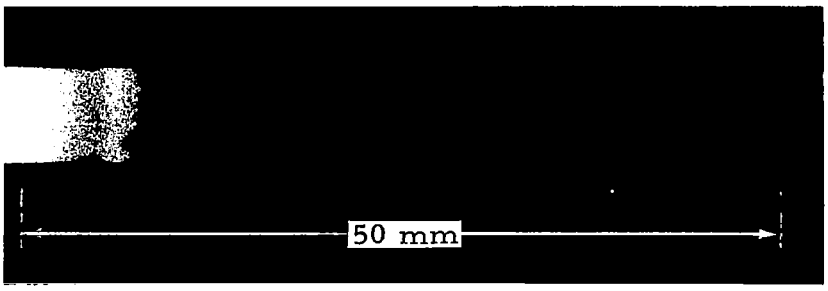

Figure 9-7 Ca-Montmorillonite Standard X-Ray Pattern Taken with Bendix Vacuum Camera, Phase II (Magnification 2x)

9.8 ANALYSIS OF THERMODYNAMIC AND CRYSTAL STRUCTURE DATA

Calcium-montmorillonite is a member of the montmorillonite group, whose general composition is $(1/2\,Ca, Na)_{0.7}(Al_{3.3}Mg_{0.7-x}Fe_x)\,Si_8O_{20}(OH)_4 \cdot nH_2O$. It is difficult to assign a 3-dimensional cell to the montmorillonites because of stacking disorder. Powder patterns of dehydrated montmorillonite are similar to those of pyrophyllite, leading many investigators to believe that the montmorillonites are isotypic with pyrophyllite. Hendricks (1942) suggested that the structure of montmorillonite is built up of composite layers, each consisting of a gibbsite ($Al_2(OH)_6$) layer sandwiched between two sheets of SiO_4 tetrahedra. In the gibbsite layer, two out of every three OH^- groups are replaced by apical oxygens of the Si_4O_{10} sheets. In montmorillonite, the charge balance of the composite sheets is upset by substitutions in both the octahedral and tetrahedral sites. Charge balance is achieved by the presence of either interlayer Na^+ or Ca^{+2} ions. Calcium-montmorillonite is the mineral in which interlayer Ca^{+2} ions predominate. However, these ions may be readily substituted by ions of similar size.

Two explanations of the montmorillonite structure have been offered. Edelman and Favejee (1940) proposed a structure similar to cristobalite (Figure 9-8). Successive Si_2O_5 sheets are joined together by the inversion of every other tetrahedron so that the inward pointing apical oxygens are linked to the $Al_2(OH)_6$ or the $Mg_2(OH)_6$ sheets. McConnell (1950) proposed that the OH^- groups can substitute for the Si-O groups in the tetrahedral layers. However, X-ray data favor the pyrophyllite type structure.

The amount of interlayer water present is a function of both the nature of the interlayer cation and the physical conditions (humidity, temperature). In the case of Ca-montmorillonite, the amount of water varies between 8 and 16 molecules of H_2O/unit cell. Midgley and Gross (1956) claim the number of stable states of montmorillonite is a function of its interlayer cation. Rowland et al. (1956) have reported that upon heating, Ca-montmorillonite passes through two stable states and that Na-montmorillonite loses water continuously and exhibits no intermediate stable states.

According to Mackenzie and Bishui (1958), the dehydration of montmorillonite occurs as the result of a combination of two neighboring OH^- ions to form one water molecule and one O^{-2} ion which is accommodated in the octahedral sheet. They note that the temperature at which

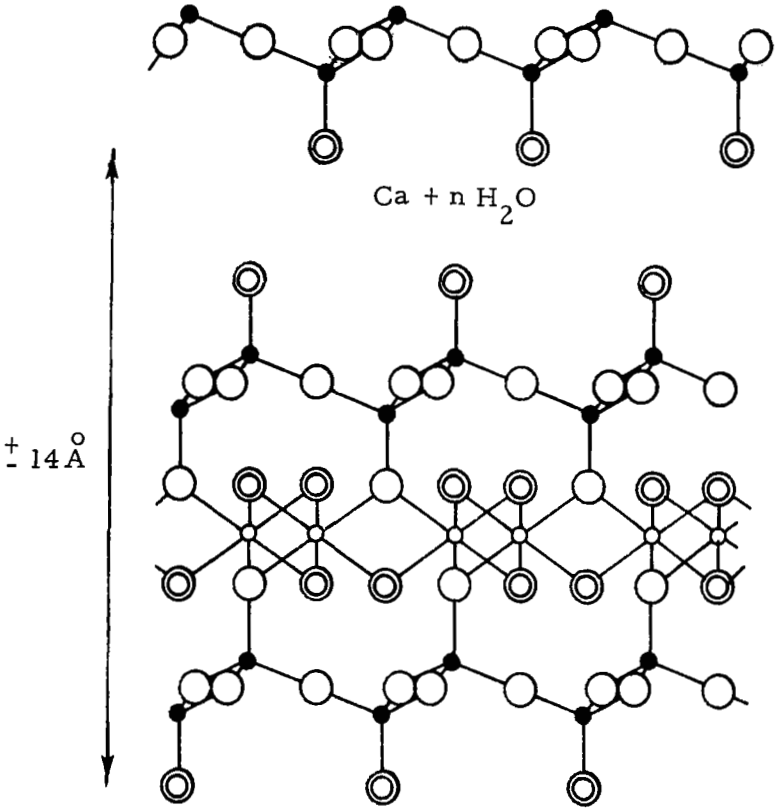

Figure 9-8 The Structure of Calcium-Montmorillonite

this occurs is a parabolic function of the cationic radius rather that cationic charge. The maximum temperature of dehydration corresponds to an interlayer cationic radius of 1.2Å. This occurs because cations of 1.2Å radius completely fill the space between the collapsed composite layers while larger ions hold the sheets apart, thus requiring less energy for the expulsion of the water molecules. In the case of smaller ions, a stronger binding of the ion to one sheet may account for easier expulsion.

Heating montmorillonite under atmospheric pressure results in the loss of interlayer water in the temperature range 100-300°C, and the loss of the OH^- in the temperature range 500-750°C. The variation in these temperatures reflects the great degree to which solid solution can take place in the montmorillonite structure. Rehydration occurs readily if the dehydration is not taken to completion (i.e., the OH^- is not lost). According to Edelman and Favejee (1940), the absorption is so strong for dried montmorillonite that it must be considered a hygroscopic material. The final breakdown of the montmorillonite structure occurs between 800-900°C. It has not yet been established whether or not there is a loss of OH^- associated with this breakdown. The final phases formed vary according to the initial composition. The most important of these products are spinel, α or β quartz or cristobalite. The maximum hydrothermal stability is a function of composition with the greatest stability occurring with the greatest substitution in the octahedral and tetrahedral sites and with the greatest resultant proportion of interlayer cations.

Noll (1936 and 1944) synthesized montmorillonite from proportions of MgO, Na_2O, CaO, Al_2O_3, H_2O, and SiO_2. Noll's results are reproduced below:

T^oC	Pressure Atm	P_{H_2O} mm of Hg
250	40.8	3.1×10^4
300	87	6.6×10^4
400	305	2.3×10^5

With the aid of these data and the Clausius-Clapeyron equation, the enthalpy of the reaction can be evaluated and the curve can be extrapolated to lower pressures and temperatures.

Fortunately, the experimental data are within the range of the ideal behavior of water vapor and consequently, little error is introduced by non-ideality. A graphical representation of the following mass spectrometer. and DTA data is also shown in Figure 9-9.

$$(1/2Ca, Na)_{0.7}(Al_{3.3}Mg_{0.7-x}Fe_x)Si_8O_{20}(OH)_4 \rightarrow (1/2Ca, Na)_{0.7}(Al_{3.3}Mg_{0.7-x}Fe_x)Si_8O_{22} + 2H_2O$$

	P_{H_2O} mm of Hg	T^oC
DTA	12.5	573 ± 20
Mass Spectrometer	5×10^{-6}	240 ± 5

It was not possible to construct a curve representing the loss of interlayer water, because it is lost at a temperature below ambient (27°C) when subjected to a P_{H_2O} of 5×10^{-6} mm of Hg.

The extrapolation of the data of Noll (1936 and 1944) to the lunar environment results in:

Lunar Temperature	T^oC	T^oK	P_{H_2O} mm of Hg
Minimum nighttime	-180	93	7.9×10^{-16}
Equilibrium at 1-m depth	- 55	218	4.0×10^{-2}
Maximum daytime	+130	403	1.7×10^{3}
At lunar pressure	-160	113	1.0×10^{-11}

Therefore, with the establishment of equilibrium on the lunar surface, Ca-montmorillonite should decompose during the lunar day and not exist in a stable phase at the equilibrium temperature associated with a depth of 1 m. Reconstitution of the montmorillonite structure during the lunar night is very unlikely, because at the lunar minimum nighttime temperature the vapor pressure of Ca-montmorillonite is greater than that of ice (5.2×10^{-19} mm of Hg). Consequently, not enough water vapor should be available for rehydration.

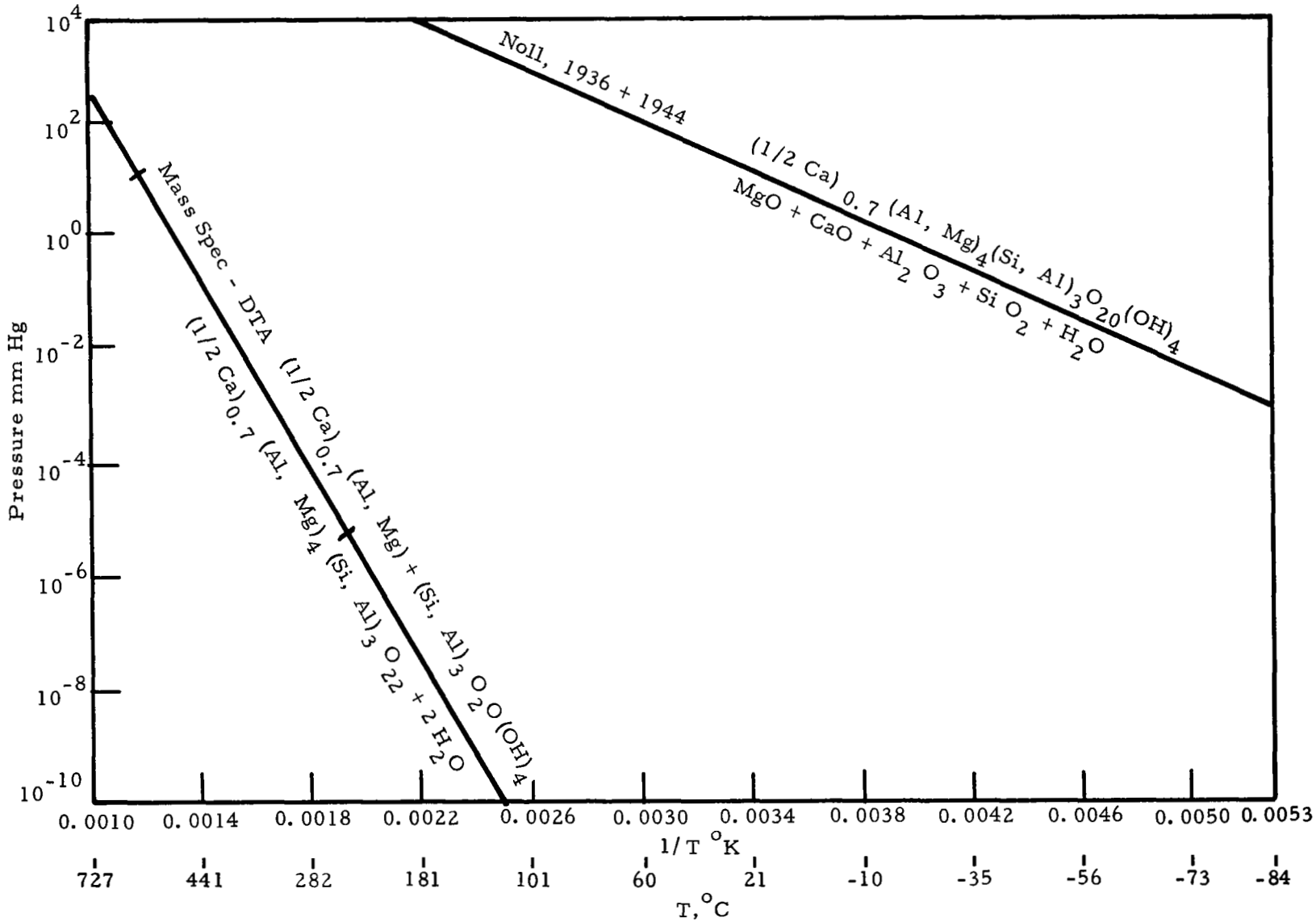

Figure 9-9 Stability Curve of Calcium-Montmorillonite

SECTION 10

GOETHITE

10.1 FORMULA

$HFeO_2$.

10.2 MINERAL CLASSIFICATION AND VOLATILE

Oxy - hydroxide.

10.3 SPECIMEN LOCALITY

Mesabi Range, Minnesota.

10.4 PROCUREMENT SOURCE

Ward's Natural Science Establishment, Inc., Rochester, New York.

10.5 OPTICAL MICROSCOPIC ANALYSIS

The deep brown-red color, the colloform structure, and parallel extinction are typical of goethite. Certain portions of the thin section (Figure 10-1) appear opaque, probably due to the perpendicular orientation of the fibers with respect to the plane of the section. No impurities are evident under the microscope.

10.6 THERMAL ANALYSES

10.6.1 Differential Thermal Analysis

See Figure 10-2.

10.6.1.1 Sensitivity

The sensitivity is 10 μv/cm.

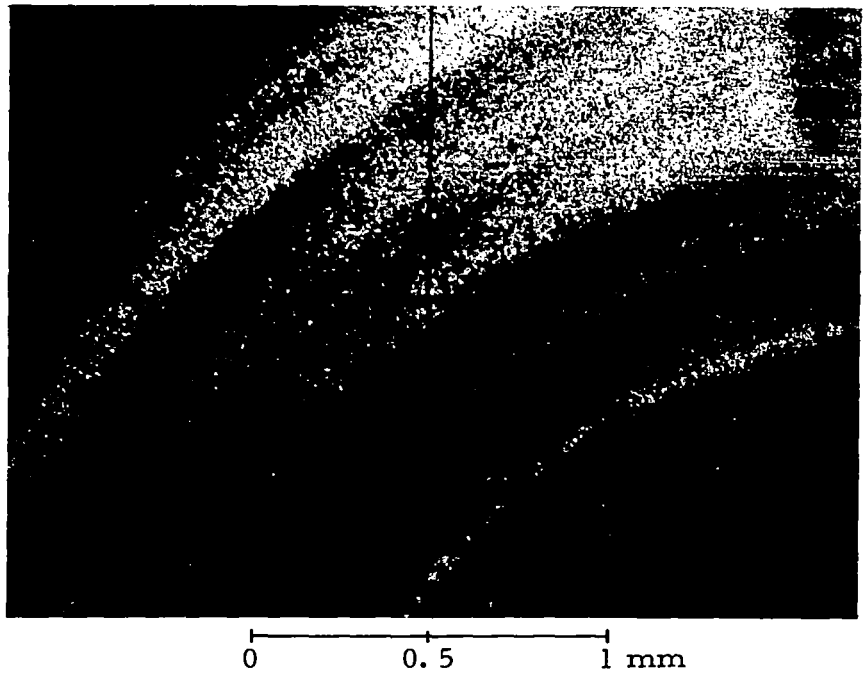

Figure 10-1 Photomicrograph of Goethite, 47X

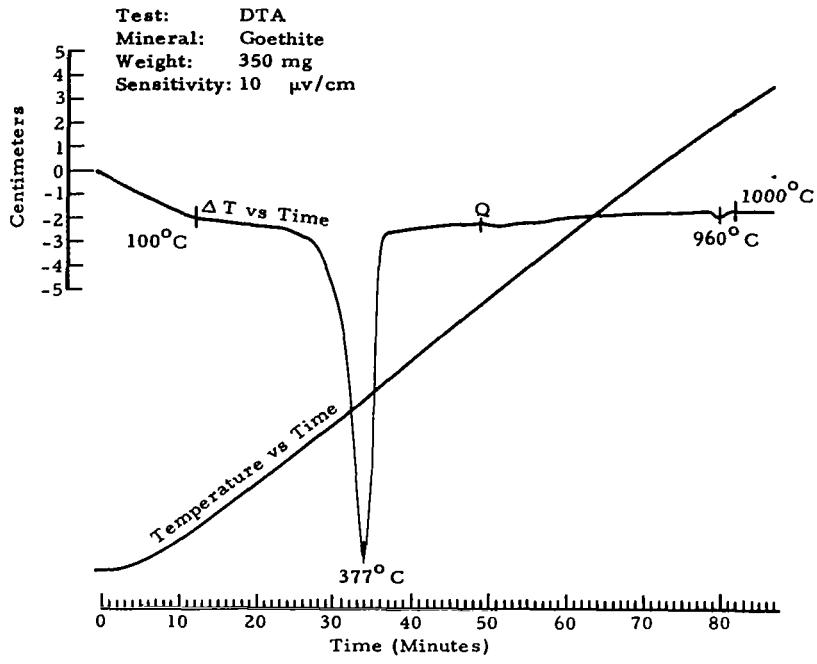

Figure 10-2 Goethite DTA

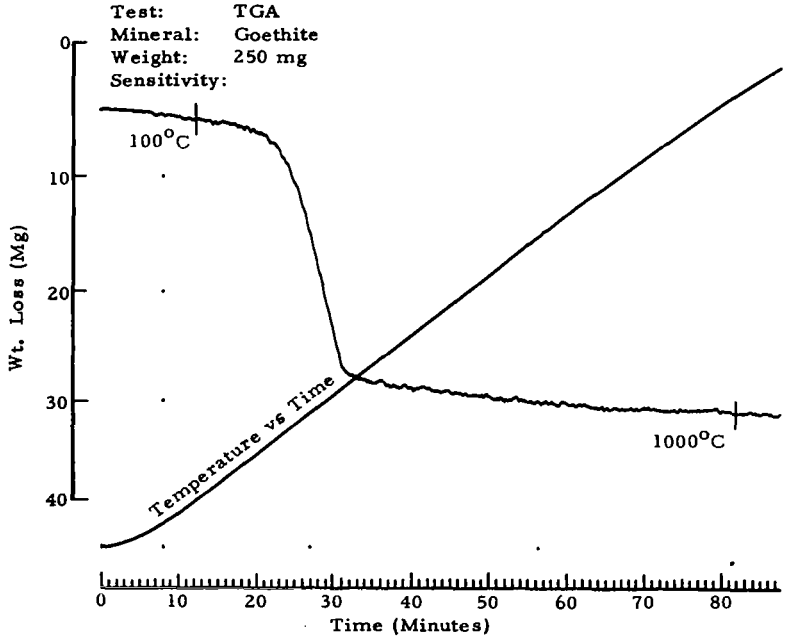

Figure 10-3 Goethite TGA

10.6.1.2 Peak Values

These are:

377°C (-) Loss of H_2O

960°C (-) Minor endothermic peak due to some impurity, perhaps calcite.

10.6.2 Thermogravimetric Analysis

The TGA weight loss amounts to 10.0% of the sample weight (Figure 10-3). It closely approximates the theoretical weight loss, which is calculated at 10.1%.

10.6.3 Mass Spectrometer Analysis

The specimen decomposes to Fe_2O_3 (hematite) and H_2O in the mass spectrometer (Figure 10-4) at 44°C ± 5° under a total pressure of 1×10^{-6} torr or a P_{H_2O} of approximately 3×10^{-7} torr. In comparison, the DTA curve shows a strong endothermic drift, culminating in a sharp endothermic peak at 377°C. This drift probably reflects the loss of absorbed water. The latter cannot be detected in the mass spectrometer (Figure 10-5), because it takes place at near ambient temperature in the vacuum.

10.7 X-RAY DIFFRACTION PATTERNS

10.7.1 Debye-Scherrer Standard

Figure 10-6 shows the goethite X-ray pattern taken with the Debye-Scherrer camera. This photograph was taken with copper radiation despite the acute fluorescence problem present with such iron-containing samples. The generally high film background is a result of this. Table 10-1 compares experimental and ASTM d-values for goethite.

10.7.2 Bendix Vacuum Camera Standard

Figure 10-7 shows the goethite X-ray pattern taken with the Bendix Vacuum Camera (magnification 2X). The vacuum camera photographs were taken with molybdenum radiation to minimize fluorescence effects. This results in a paucity of measurable data, however.

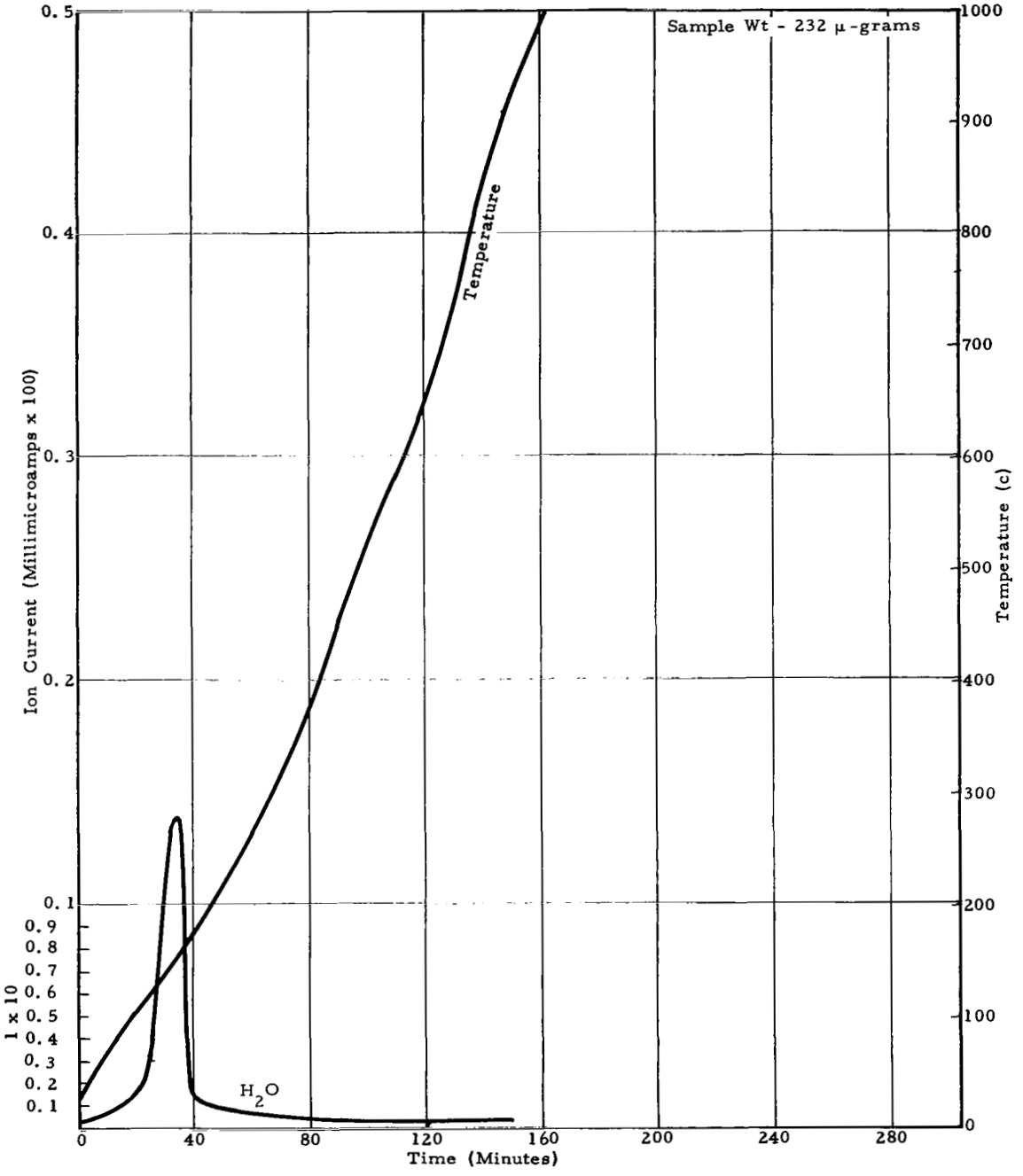

Figure 10-4 Mass Spectrometer Curve of Goethite— Scan With H_2O Peak Plotted

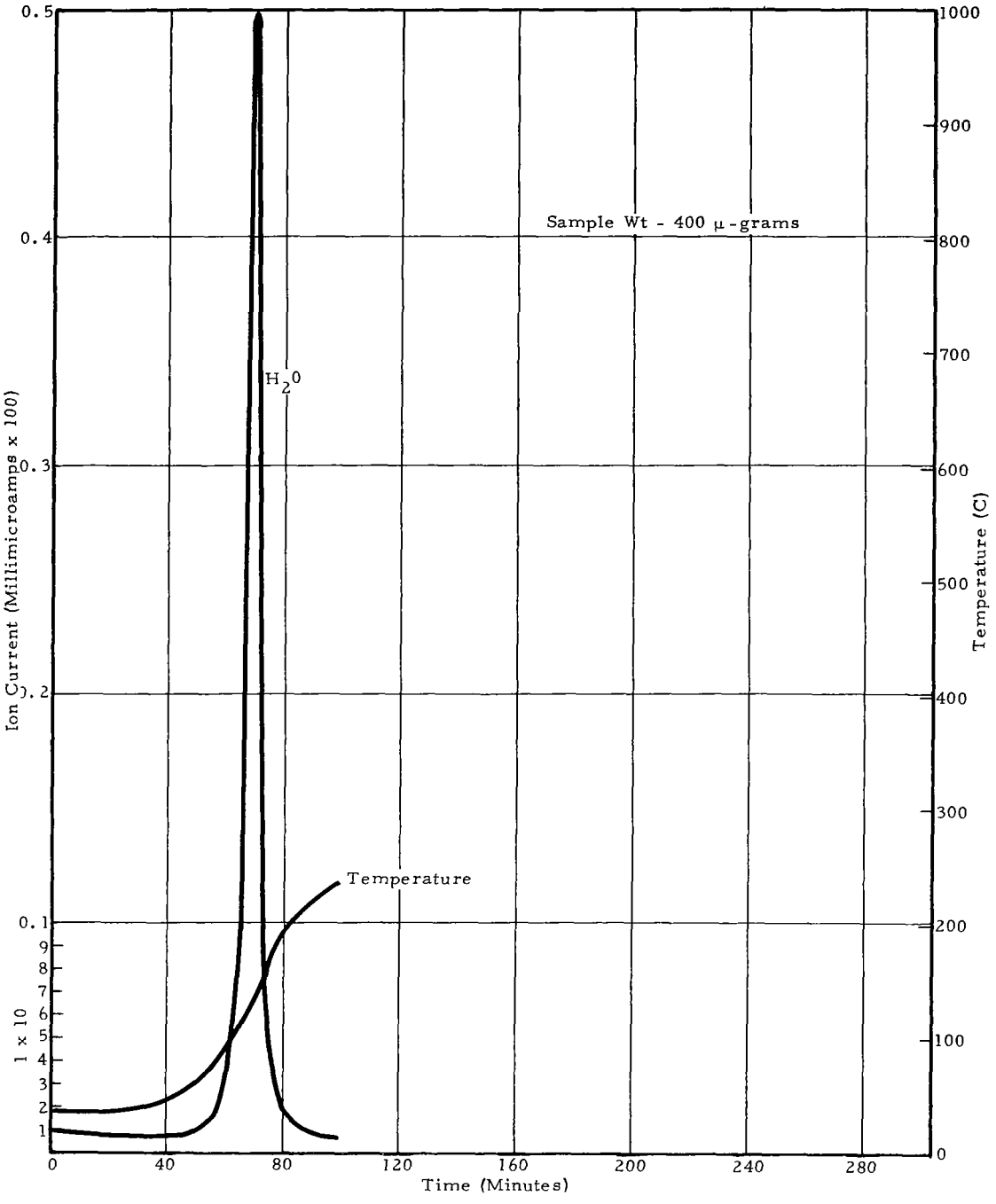

Figure 10-5 Mass Spectrometer Curve of Goethite—H_2O Peak

Figure 10-6 Goethite X-Ray Pattern Taken With Debye-Scherrer Camera

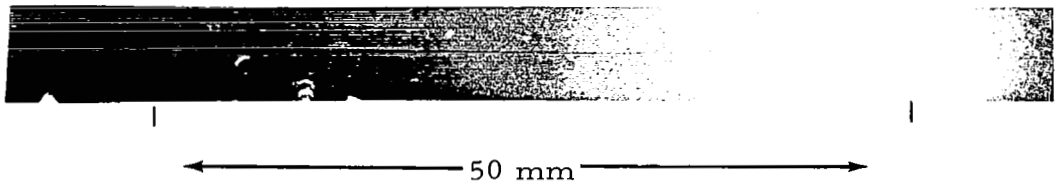

Figure 10-7 Goethite X-Ray Pattern Taken With Bendix Vacuum Camera (Magnification 2X)

TABLE 10-1

A COMPARISON OF EXPERIMENTAL AND ASTM D-VALUES FOR GOETHITE

Exp (Å)	ASTM (Å)	Exp (Å)	ASTM (Å)	Exp (Å)	ASTM (Å)	Exp (Å)	ASTM (Å)
5.0	5.0	2.00	2.00	1.45	1.456	1.15	1.151
4.2	4.21	1.92	1.92	1.42	1.42	1.14	1.141
3.38	3.37	1.80	1.80	1.39	1.392	1.125	1.125
2.70	2.69	1.72	1.719	1.35	1.347	1.065	1.071
2.58	2.57	1.69	1.689	1.32	1.318	1.050	
2.45	2.44	1.60	1.602	1.262	1.263	1.022	
2.25	2.25	1.56	1.563	1.242	1.239	1.01	
2.18	2.18	1.51	1.507	1.19	1.197	0.995	0.996

Table 10-2 compares the Debye-Scherrer Standard with the Bendix Camera Standard.

TABLE 10-2

A COMPARISON OF OBSERVED D-VALUES AND RELATIVE INTENSITY MEASUREMENTS FOR GOETHITE

Debye-Scherrer Standard, CuK_α		Bendix Camera Standard, MoK_α	
d_{obs}	$\frac{i}{i_o}$	d_{obs}	$\frac{i}{i_o}$
1.72	40	1.7	75
1.51	50	1.5	100

10. 7. 3 Vacuum Patterns

The photographs taken at high vacuum were all duplicates, but differed from that of the standard. The dehydration thus occurred at room temperature during the pumpdown stage. Refer to Figure 10-8.

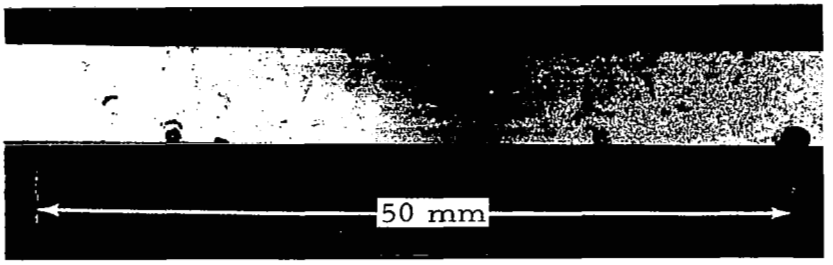

Figure 10-8 Transformed Goethite (Hematite); Photograph Obtained at 130°C and 3 x 10^{-10} Torr

TABLE 10-3

D-VALUES AND RELATIVE INTENSITIES OF THE TRANSFORMED GOETHITE (HEMATITE)

d_{obs}	$\frac{i}{i_o}$
2.02	10
1.81	100
1.57	5
1.38	10
1.09	20
0.832	20

The pattern is fogged and has spotty diffraction lines. Hence, the measured values are subject to imprecision. In addition, the use of molybdenum radiation results in both weak intensities and the occurrence of relatively small d-values in a range of the pattern where values are closely spaced. It is therefore very difficult to get a correspondence with ASTM values. However, direct visual comparison of the vacuum and standard films shows a sharp contrast in the patterns. There is no doubt,

due to the nature of the transformation, that the transformed phase is hematite. Since a transformation occurred, this mineral was used in Phase II.

It should be noted that the transformation was directly confirmed by the observation of the color of the transformed material subsequent to removal from the camera. The powder was hematite-red in color, while goethite is a characteristic yellow-brown. A diffractometer pattern of the transformed material further confirmed the identification as hematite.

10.7.4 Bendix Vacuum Standard, Phase II

All photographs of goethite obtained in Phase II of the experiment were also taken with molybdenum radiation. Intensity and d-values are given in the next section. Refer to Figure 10-9.

10.7.5 Vacuum Patterns, Phase II

Photographs taken at liquid nitrogen, liquid CO_2, and room temperature duplicated that of the standard. Photographs at 75°C, 130°C, and in the simulated spacecraft environment were duplicates of each other, but different than that of the standard, indicating that dehydration occurred between room temperature and 75°C. Relative intensity and d-values for the standard goethite and transformed goethite are listed in Table 10-4. The sample on removal from the chamber was hematite red in color, as was true in the Phase I experiment. This further verifies the dehydration to hematite as a transformation product. Figure 10-10 shows a photograph taken at 75°C and 5×10^{-10} torr.

10.8 ANALYSIS OF THERMODYNAMIC AND CRYSTAL STRUCTURE DATA

The structure of goethite is based upon a framework of hexagonally close-packed oxygen atoms (see Figure 10-11). Each Fe atom is in octahedral coordination and lies in the interstices between the close-packed layers. Each Fe provides 1/2 unit charge to each surrounding oxygen with the other 1/2 unit charge being supplied by a hydrogen atom which acts as a bridge between each pair of oxygen atoms. The bridge is considerably weaker than the other bonds in the structure.

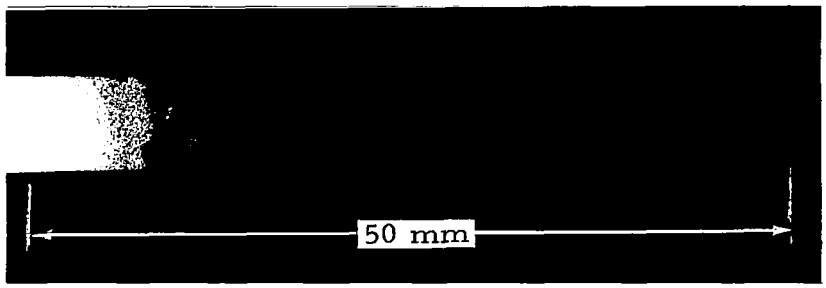

Figure 10-9 Goethite X-Ray Pattern Taken as a Standard for Phase II (Magnification 2X)

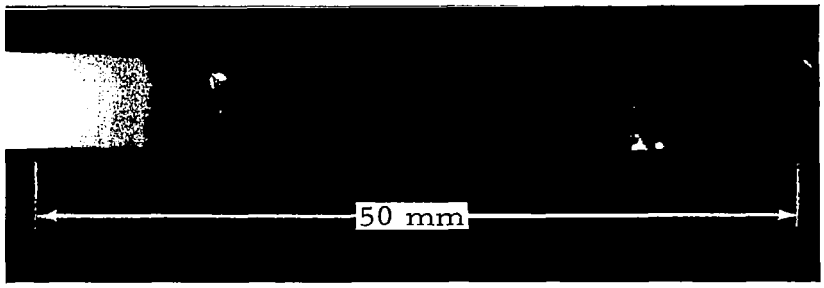

Figure 10-10 Transformed Goethite (Hematite) X-Ray Pattern Obtained at 75°C and 5 x 10^{-10} Torr

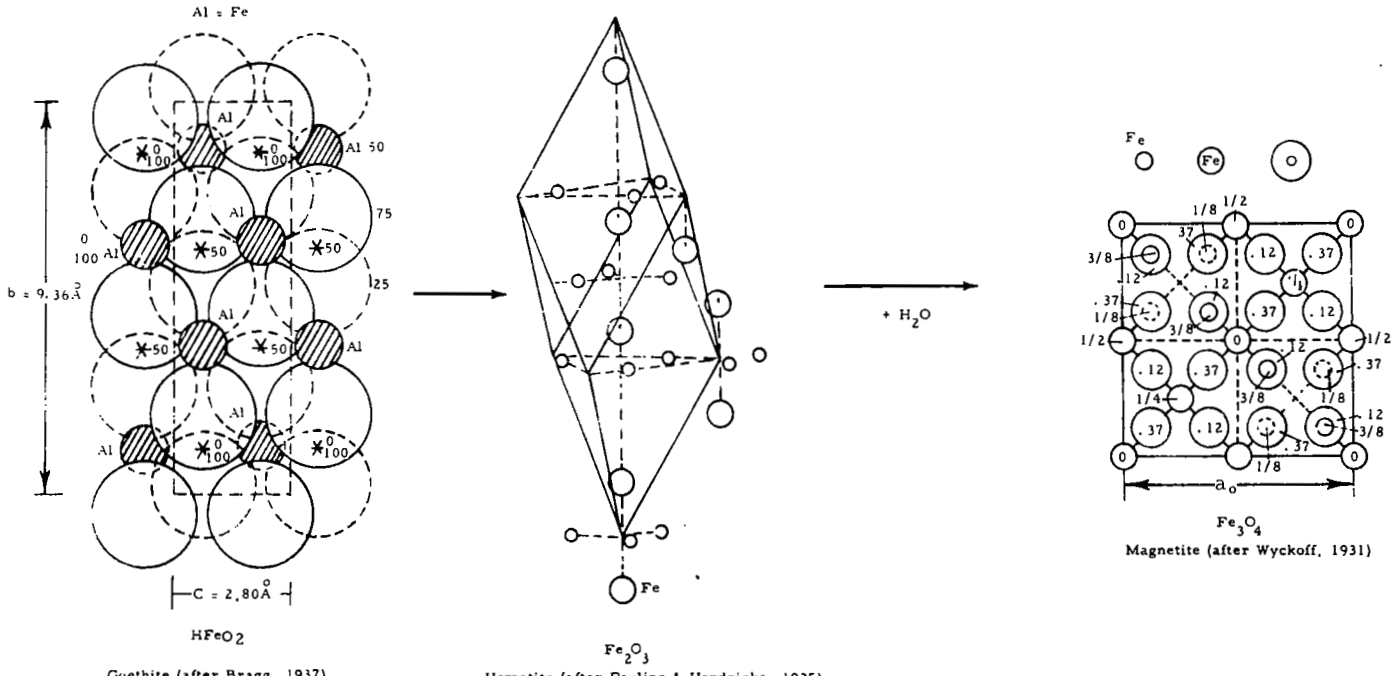

Figure 10-11 The Structures of Goethite, Hematite, and Magnetite

TABLE 10-4

D-VALUES AND RELATIVE INTENSITIES OF THE STANDARD GOETHITE AND TRANSFORMATION PRODUCT (HEMATITE)

Goethite		Hematite	
d_{obs}	$\frac{i}{i_o}$	d_{obs}	$\frac{i}{i_o}$
2.10	80	2.05	100
1.81	100	1.88	100
1.60	20	1.60	5
1.52	10	1.37	40
1.47	10	1.22	10
1.09	40	1.09	30
1.01	20	1.00	30
0.96	10	0.83	10

The dehydration of goethite results from the loss of hydrogen and one-quarter of the oxygen atoms of the closest-packed framework of oxygen atoms. The product of decomposition, hematite, also consists of a hexagonal close-packed oxygen framework (see Figure 10-11). However, in this case the Fe atoms only occupy 2/3 of the available sites due to their rearrangement during the transformation. Lima De Faria and Gay (1962) report the formation of intermediate disordered structural states, formed during the dehydration of goethite. Different intermediate states are formed by variations of the temperature and duration of the dehydration. Clearly, the intermediate states are those resulting from incomplete dehydration. However, the authors offer no information on the stabilities of the states they report.

Under conditions of sufficiently high temperature, hematite undergoes a transformation to the cubic compound magnetite (Fe_3O_4) according to the reaction:

$$6Fe_2O_3 \rightarrow 4Fe_3O_4 + O_2.$$

The unit cell of magnetite contains 32 oxygens and 24 cations. The possible cationic positions within the structure are those of 4-fold and 6-fold coordination. The distribution of the cations within the magnetite structure is $8\,Fe^{+3}$ in the tetrahedral positions and $8\,Fe^{+2}$ and $8\,Fe^{+3}$ in the octahedral positions. Layers of oxygens alternate with layers of cations perpendicular to a 3-fold axis. The layers of cations of 6-fold coordination alternate with layers in which the cations are distributed in the tetrahedral and octahedral positions in the ratio of 1:2, respectively.

Schmalz (1959) in an effort to explain the formation of ferruginous sediments, analysed the thermodynamics of the reaction:

$$2HFeO_2 \rightarrow 4\,Fe_2O_3 + H_2O\ (g).$$

Schmalz based his calculations on the data of Tunell and Posnjak (1931), which give the maximum temperature of the stability of $HFeO_2$ under a P (H_2O) of 760 mm of Hg as 130°C. He assumed that the thermal expansions of the solid phases compensated for each other and therefore arrived at a volume change of solids = +6. 8 cc/mole (hematite) for the reaction:

$$2HFeO_2 \rightarrow Fe_2O_3 + H_3O\ (g)$$

at one bar and 130°C.

Using these data in conjunction with the well-known relations $(\frac{dP}{dT}) = \frac{\Delta S'}{\Delta V'}$, he obtained a value of $\Delta S' = -37$ cal/deg mole for the reaction of 130°C. *

---

* Primed letters refer to those quantities evaluated at one bar and 130°C.

Assuming that the hematite, goethite, and water were in equilibrium at P' and T' (one bar and 130°C) and that ΔCp for the reaction is constant, he formulated the equations:

$$\Delta H = T'\Delta S' + Cp\,(T - T') = T'\,\Delta V'\,(dP/dT)' + \Delta Cp\,(T - T') \qquad (10\text{-}1)$$

$$\Delta S = \Delta S' - \Delta Cp \ln T'/T \qquad (10\text{-}2)$$

$$\Delta F = (T' - T)\left[\Delta V'\,(dP/dT)' - \Delta Cp\right] + \Delta Cp T \ln (T'/T)$$

$$\text{at } P' = P \text{ and } T' \neq T \qquad (10\text{-}3)$$

Schmalz then employed his own estimated value for the heat capacity of goethite in conjunction with those given by Rossini (1952) for H_2O and hematite and arrived at a $\Delta Cp = -5.6$ cal/deg mole (hematite) for the reaction Schmalz then introduced a variable z which is the ratio of the water vapor pressure present in a system to the vapor pressure of pure water at the same temperature. Since the free energy of a system composed of two or more solids and a vapor is a function of the vapor pressure, this ratio (z) also represents a change in the free energy. Consequently, the interaction of z and F can be represented by an equation of the form:

$$\Delta F = -RT \ln (z). \qquad (10\text{-}4)$$

By combining Equations 10-3 and 10-4, Scmalz obtained an equation defining an equilibrium state at any temperature T using P' and T' as a base:

$$-RT \ln (z) = (T' - T) \cdot \left[\Delta V'\,(dP/dT)' - \Delta Cp\right] + \Delta Cp T \ln (T'/T).$$

The variable z is proportional to the relative humidity (relative humidity = 100 z). To obtain the P_{H_2O} it is only necessary to multiply z by the vapor pressure of water at the temperature in question. The stability curve obtained from Schmalz's equation is given in Figure 10-12.

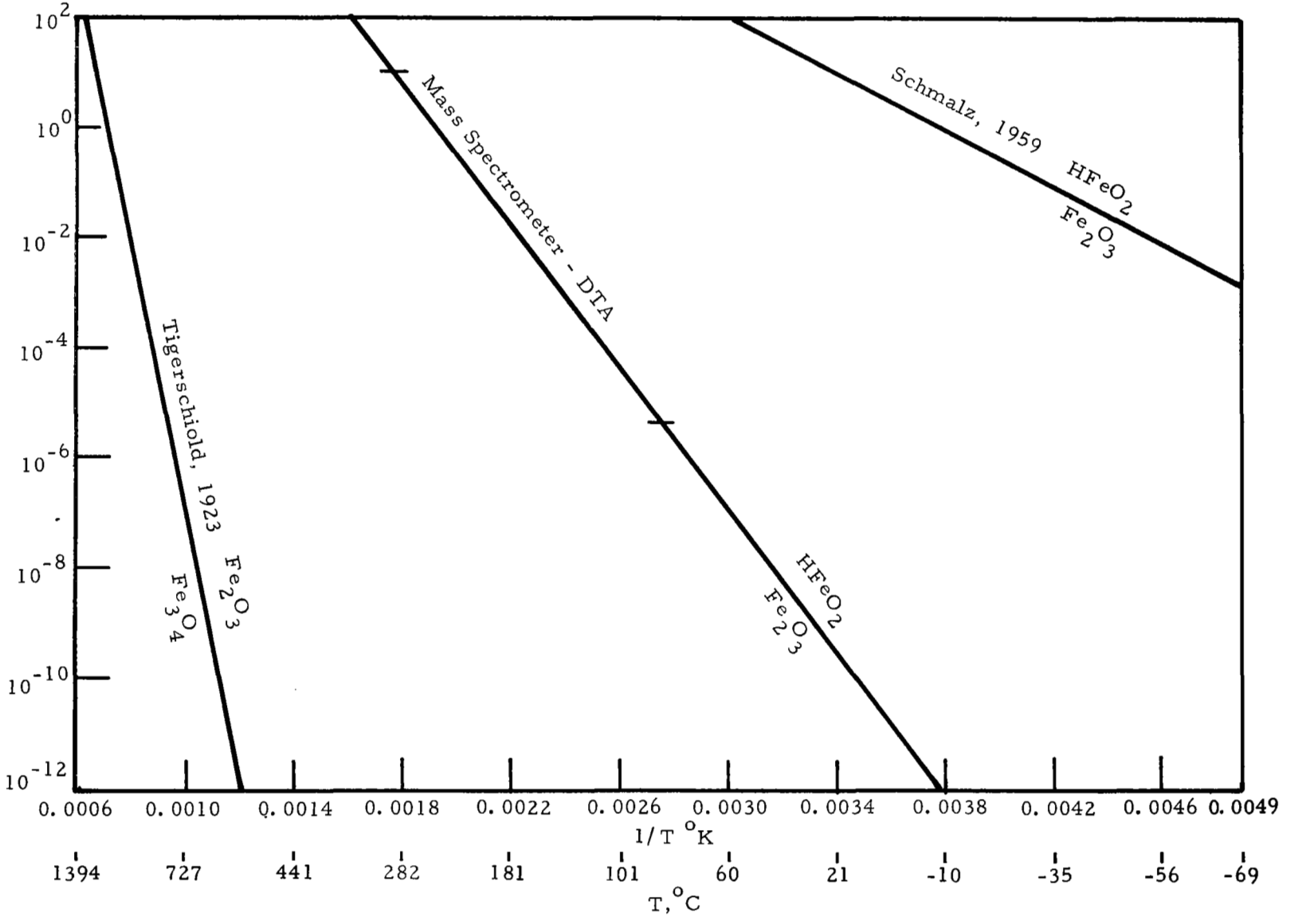

Figure 10-12 Stability Curves of Goethite and Hematite

The experimental breakdown curve as defined by the following data is also shown in Figure 10-12.

$$2\ FeO(OH) \rightarrow Fe_2O_3 + H_2O$$

	P_{H_2O} (mm of Hg)	T (^{o}C)
DTA	12.5	284 ± 20
Mass Spectrometer	5×10^{-7}	44 ± 5

Hematite, if subjected to extremely high temperatures, will transform to magnetite with the evolution of oxygen according to the following reaction:

$$6\ Fe_2O_3 \rightarrow 4\ Fe_3O_4 + H_2O$$

The thermodynamics of this reaction have been studied by several researchers. Tigerschiold (1923), using the stability and heat capacity data of Sosman and Hostetter (1916), formulated the following equation for the vapor pressure of hematite:

$$\text{Log Pmm} = -20,946/T + 3.5 \log T + 0.00011T - 0.6332.$$

The stability curve plotted from this equation is shown in Figure 10-12.

A mass spectrometer investigation was conducted on a powdered sample of pencil ore (hematite) which, as was expected, did not undergo transformation within the thermal range of the instrument. However, the hematite sample did display a rather large loss of absorbed water (1%). This phenomenon was confirmed by the general downward drift of the DTA and TGA traces. Pencil ore has a rather fibrous structure; water is probably locked in the interstices between fibers.

The stability of goethite and hematite in the lunar environment is tabulated as follows:

$$HFeO_2 \rightarrow Fe_2O_3 + H_2O$$

Lunar Temperature	$T^{\circ}C$	$T^{\circ}K$	P_{H_2O} mm of Hg
Minimum nighttime	-180	93	1.6×10^{-18}
Equilibrium at 1-m depth	- 55	218	8.5×10^{-3}
Maximum daytime	+130	403	7.7×10^{2}
At lunar pressure	-121	152	1×10^{-11}

$$6\ Fe_2O_3 \rightarrow 4\ Fe_3O_4 + O_2$$

Lunar Temperature	$T^{\circ}C$	$T^{\circ}K$	P_{H_2O} mm of Hg
Minimum nighttime	-180	93	6.3×10^{-223}
Equilibrium at 1-m depth	- 55	218	6.2×10^{-89}
Maximum daytime	+130	403	1.2×10^{-43}

Goethite is unstable under the temperature and pressure conditions of the lunar day, both at the surface and at a depth of 1 m. However, the hematite produced by the dehydration is stable under the extremes of the lunar environment. Although the thermodynamics of the dehydration indicate that goethite would be stable during the lunar night, it is very unlikely that the hematite produced during the lunar day would transform to goethite during the lunar night. This is borne out by the fact that laboratory preparations of goethite have been restricted to the oxidation of solutions of ferrous compounds or slow hydrolysis of ferric salts. Furthermore, the vapor pressure of goethite at -180°C is greater than that of ice at -180°C, and consequently there should not be enough water vapor available for rehydration.

SECTION 11

GYPSUM

11.1 FORMULA

$CaSO_4 \cdot 2 H_2O$.

11.2 MINERAL CLASSIFICATION AND VOLATILE

Sulfate - H_2O.

11.3 SPECIMEN LOCALITY

Girgenti, Sicily.

11.4 PROCUREMENT SOURCE

Southwest Scientific Co., Scottsdale, Arizona.

11.5 OPTICAL MICROSCOPIC ANALYSIS

This clear crystal of gypsum, var. selenite, has cleavage flakes which show a centered flash interference figure (Figure 11-1). The α index is 1.520. No impurities are evident under the microscope.

11.6 THERMAL ANALYSES

11.6.1 Differential Thermal Analysis

See Figure 11-2.

11.6.1.1 Sensitivity

The sensitivity is 10 μv/cm.

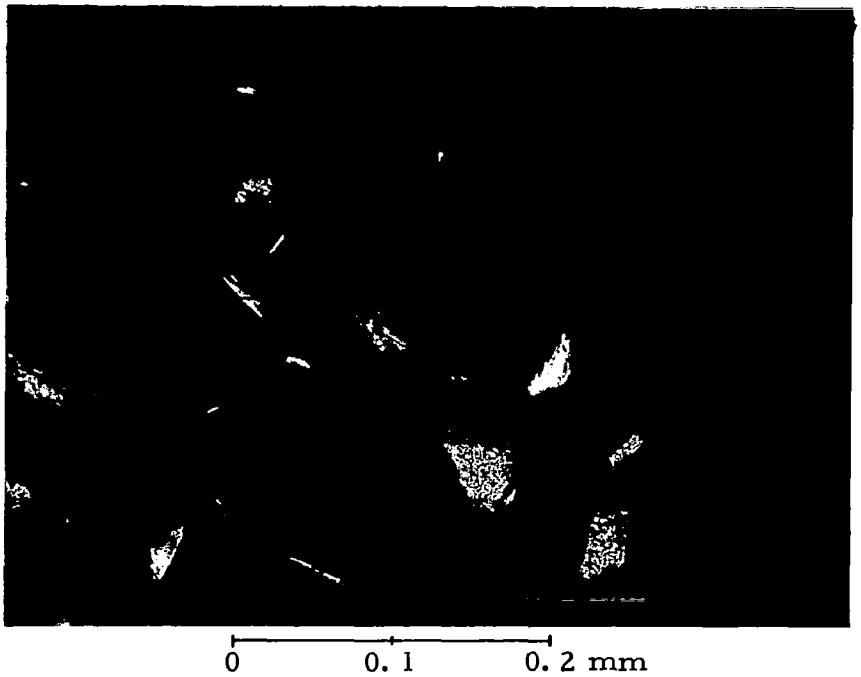

Figure 11-1 Photomicrograph of Gypsum, Crossed Polars, 210X, the DTA Sample in Liquid Having Index of Refraction of 1. 56

11.6.1.2 Peak values

These are:

168°C(-) Loss of water of crystallization to hemihydrate

203°C(-) Loss of hemihydrate water

375°C(+) Recrystallization of anhydrite from "soluble" to "insoluble" anhydrite.

11.6.2 Thermogravimetric Analysis

The TGA (Figure 11-3) reveals that the two endothermic reactions result in a weight loss of 19.8%. It represents a loss of H_2O, which agrees favorably with the theoretical weight loss of 20.9%.

11.6.3 Mass Spectrometer Analysis

The partial decomposition of gypsum to the hemihydrate cannot be observed in the mass spectrometer, because the sample is exposed to a total pressure of 1×10^{-6} torr, or a P_{H_2O} of approximately 3×10^{-7} torr, and at this pressure the change takes place at a temperature less than 27°C (room ambient). Since the equipment does not have the capability of subjecting the sample to a temperature lower than ambient, it is impossible to determine the exact temperature when the change occurs. The partial decomposition is evident, however, by the initial high water level indicated by the mass spectrometer curves (Figures 11-4 and 11-5).

The transformation from the hemihydrate form to anhydrous calcium sulfate in the mass spectrometer begins at 52°C ± 5°, as denoted by the inflection points in the first two curves of Figure 11-5. In comparison with the DTA, the hemihydrate and the soluble $CaSO_4$ transformations correspond to the two endothermic peaks in the DTA curve at 168°C and 203°C. The recrystallization of the soluble $CaSO_4$ to anhydrite corresponds to the exothermic peak in the DTA curve at 375°C. However, this reaction is not evident in the mass spectrometer.

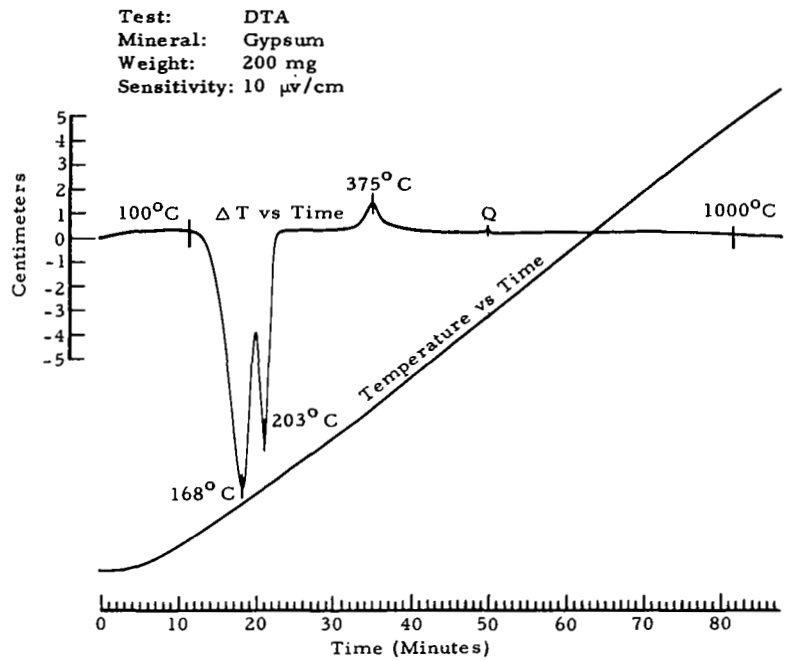

Figure 11-2 Gypsum DTA

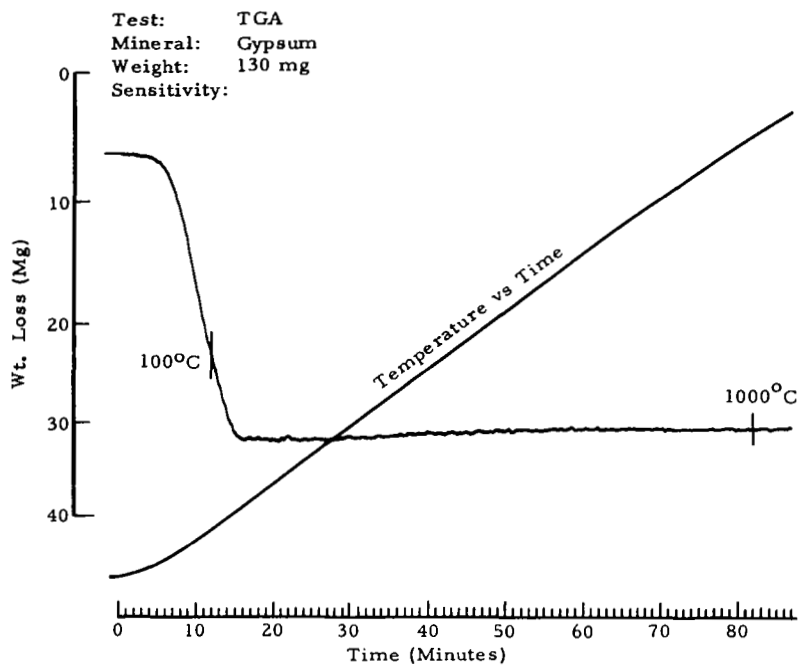

Figure 11-3 Gypsum TGA

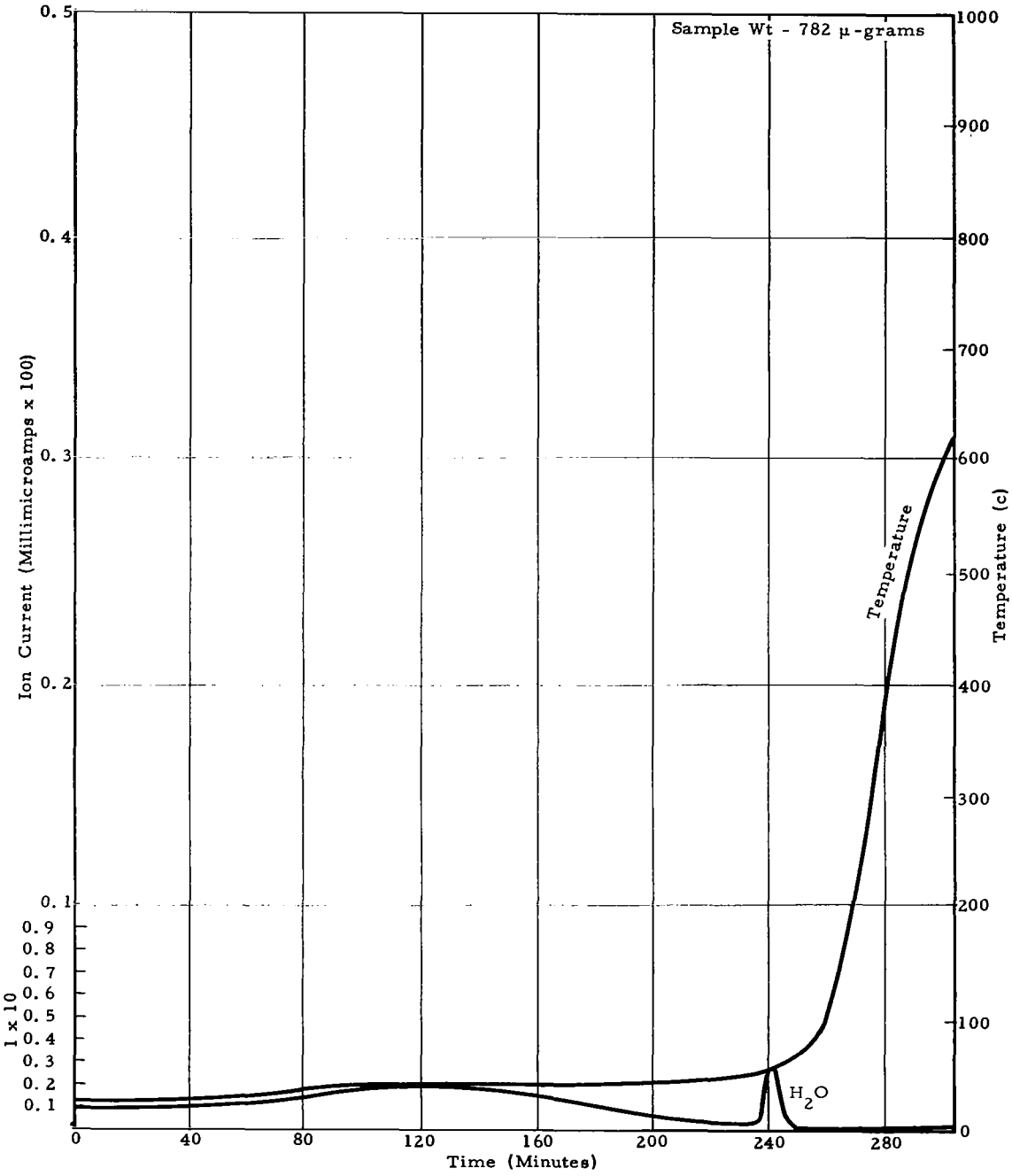

Figure 11-4 Mass Spectrometer Curve of Gypsum—H_2O Peak

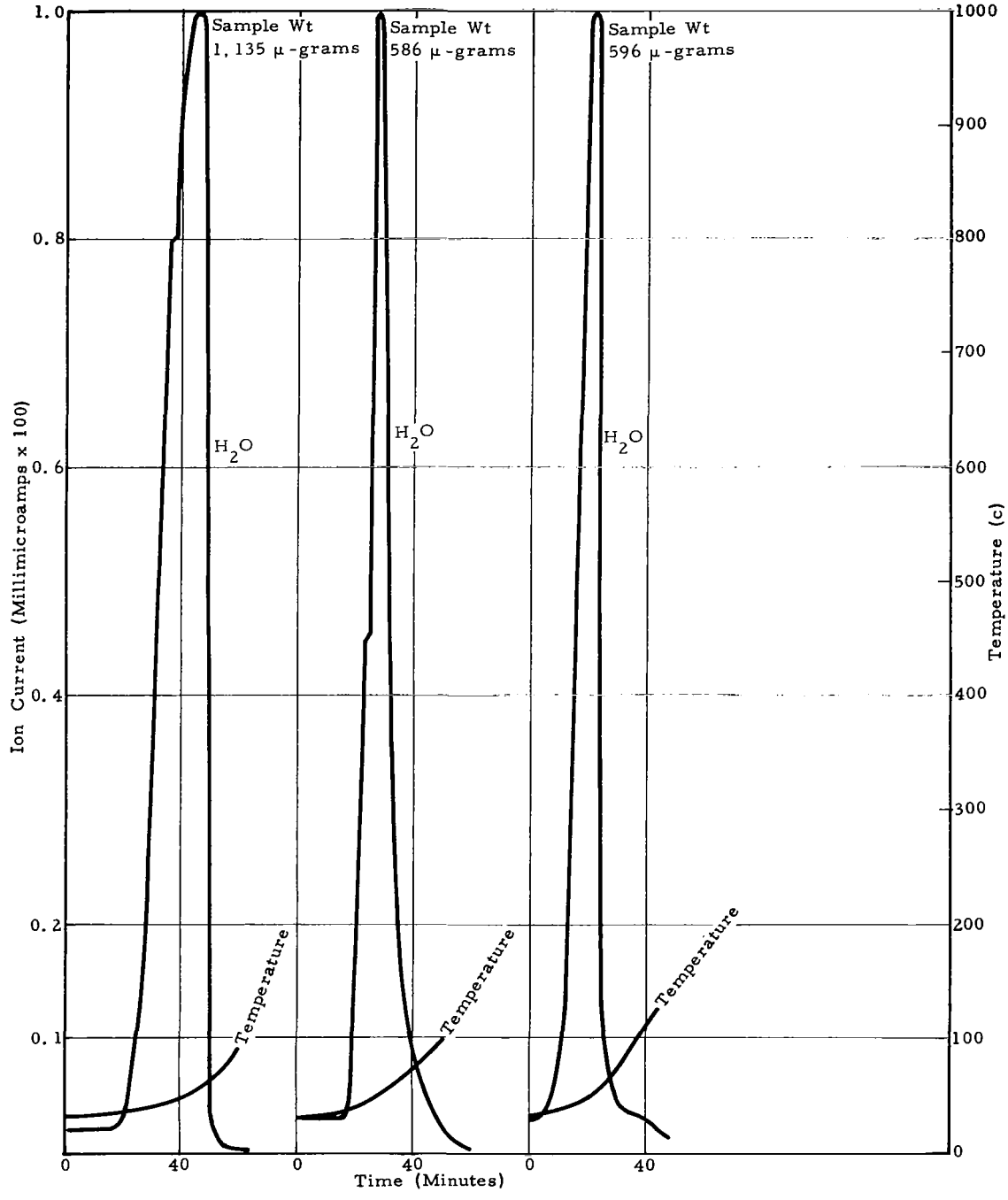

Figure 11-5 Mass Spectrometer Curve of Gypsum—H_2O Peaks

11.7 X-RAY DIFFRACTION PATTERNS

11.7.1 Debye-Scherrer Standard

Figure 11-6 shows the gypsum X-ray pattern taken with the Debye-Scherrer camera. The agreement between d-values of the Standard and the ASTM pattern is generally very satisfactory (Table 11-1).

TABLE 11-1

COMPARISON OF EXPERIMENTAL AND ASTM D-VALUES FOR GYPSUM

Exp (Å)	ASTM (Å)	Exp (Å)	ASTM (Å)	Exp (Å)	ASTM (Å)	Exp (Å)	ASTM (Å)
6.5	6.6	2.57	2.57	1.75	1.75	1.33	1.33
6.0	5.9	2.45	2.43	1.72	1.72	1.30	1.31
4.1	4.13	2.33	2.32	1.62	1.62	1.23	1.24
4.4	4.38	2.25	2.26	1.57	1.53	1.21	1.22
4.7	4.63	2.19	2.18	1.54	1.52 (Scolecite)	1.19	1.19
3.55	3.63 (Scolecite)	2.05	2.05	1.47	1.46	1.14	1.14
3.2	3.16	1.95	1.95	1.44	1.43 (Scolecite)	1.09	1.08
2.95	2.94	1.87	1.87	1.42	1.42	1.06	1.06
2.85	2.86	1.80	1.80	1.38	1.38	1.02	1.02
2.65	2.68						

11.7.2 Bendix Vacuum Camera Standard

Figure 11-7 shows the gypsum X-ray pattern taken with the Bendix vacuum camera (magnification 2X). The agreement of values for the Bendix camera standard with those for the Debye-Scherrer standard is somewhat unsatisfactory only in the low theta region where precision is relatively low (Table 11-2).

Figure 11-6 Gypsum X-Ray Pattern Taken With Debye-Scherrer Camera

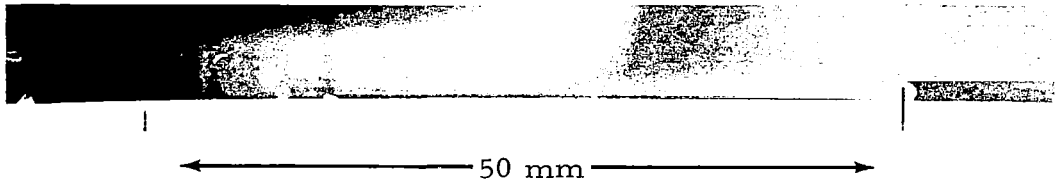

Figure 11-7 Gypsum X-Ray Pattern Taken With Bendix Vacuum Camera (Magnification 2X)

TABLE 11-2

COMPARISON OF OBSERVED D-VALUES AND RELA
INTENSITY MEASUREMENTS FOR GYPSUM

Debye-Scherrer Standard, CuK_α		Bendix Camera Standa	
d_{obs}	$\frac{i}{i_o}$	d_{obs}	$\frac{i}{i_o}$
4.3	100	4.1	10
3.75	15	3.5	
3.01	2	3.2	
2.75	7	2.8	7
2.67	60	2.6	7
2.49	60	2.5	7
2.20	25	2.2	1
2.08	50	2.0	1
1.87	50	1.9	1
1.80	80	1.8	4
1.77	70	1.7	3
1.66	70	1.6	3

11.7.3 Vacuum Patterns

Photographs of the sample of gypsum under high vacuum were all duplicates as determined by direct visual comparison, but were different than the standard photograph, indicating a change in composition and/or structure. The pattern of the transformed material was readily indexed by reference to the ASTM pattern of $CaSO_4 \cdot 1/2\ H_2O$, the hemihydrate. The photograph taken at room temperature and high vacuum, directly following pumpdown, is reproduced as Figure 11-8. Values of interplanar spacings are given in Table 11-3 and compared with the intense lines of the hemihydrate from the ASTM file.

TABLE 11-3

COMPARISON OF D-VALUES OF TRANSFORMED GYPSUM AND VALUES FROM THE ASTM PATTERN OF $CaSO_4 \cdot 1/2\ H_2O$

Transformed Gypsum		$CaSO_4 \cdot 1/2\ H_2O$	
d_{obs}	$\frac{i}{i_o}$	d_{obs}	$\frac{i}{i_o}$
3.5	10	3.48	60
3.0	100	3.01	90
2.8	100	2.80	90
2.3	10	2.33	20
2.0	10	2.00	10
1.9	10	1.91	20
1.8	70	1.85	60
1.6	50	1.69	40
1.4	10	1.39	5
1.3	5	1.35	5

As noted above, patterns obtained both at room and higher temperatures were the same, with no indication of further loss of water to anhydrite. The 2-phase decomposition is discussed in detail in Section 11.5.

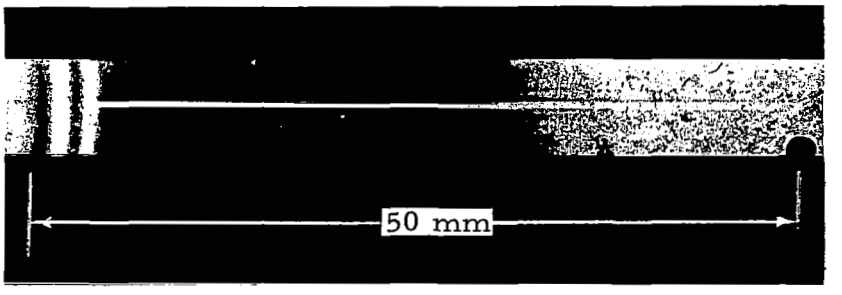

Figure 11-8 X-Ray Pattern of $CaSO_4 \cdot 1/2\ H_2O$ Obtained at Room Temperature and a Vacuum of 5×10^{-10} Torr

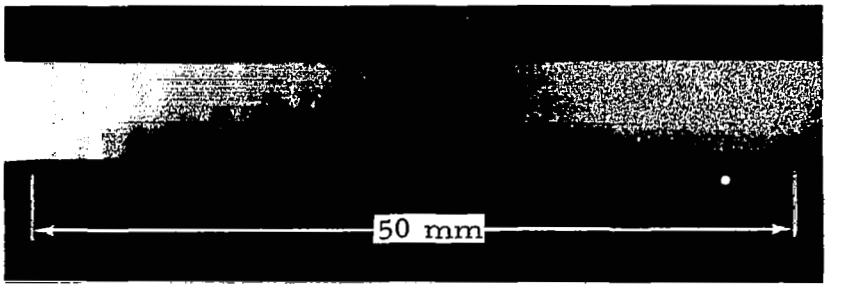

Figure 11-9 Gypsum X-Ray Pattern Taken as Standard for Phase II Experiments

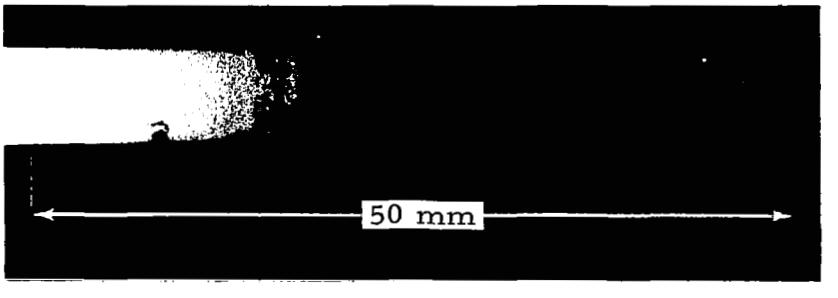

Figure 11-10 X-Ray Pattern of $CaSO_4 \cdot 1/2\ H_2O$ Obtained at 5.4×10^{-10} Torr and Liquid Nitrogen Temperature

11.7.4 Bendix Vacuum Standard, Phase II

Figure 11-9 shows the gypsum X-ray pattern taken as standard for Phase II Experiments.

Table 11-4 shows a comparison of d-values of gypsum standards for Phases I and II.

TABLE 11-4

COMPARISON OF D-VALUES OF GYPSUM STANDARDS FOR PHASES I AND II

Phase I		Phase II	
d_{obs}	$\frac{i}{i_o}$	d_{obs}	$\frac{i}{i_o}$
4.1	100	4.3	100
3.5	5	-	-
3.2	5	-	-
2.8	70	2.9	50
2.6	70	2.7	40
2.5	70	2.5	30
2.2	10	2.3	20
2.0	15	2.0	10
1.9	15	1.9	30
1.8	40	-	-
1.7	30	1.7	10
1.6	30	1.6	10

11.7.5 Vacuum Patterns, Phase II

Photographs were obtained of gypsum at various stages of the pumpdown, since there was an indication in Phase I experiments that it was the most likely phase to undergo transformation. The photograph obtained at 19-29 mm of Hg pressure duplicates the standard (Figure 11-9). However, the next photograph (Figure 11-10), taken at a pressure of about 5×10^{-10} mm, was of $CaSO_4 \cdot 1/2\ H_2O$. The pressure in the vacuum chamber was continuously monitored during pumpdown, but there was no indication of the precise pressure of dehydration.

Table 11-5 shows a comparison of d-values of transformed gypsum from Phases I and II.

TABLE 11-5

COMPARISON OF D-VALUES OF TRANSFORMED GYPSUM ($CaSO_4 \cdot 1/2\ H_2O$) FROM PHASES I AND II

Phase I		Phase II	
d_{obs}	$\frac{i}{i_o}$	d_{obs}	$\frac{i}{i_o}$
3.5	10	3.5	80
3.0	100	3.0	100
2.8	100	2.7	100
2.3	10	-	-
2.0	10	-	-
1.9	10	1.9	20
1.8	70	1.8	30
1.6	50	1.6	5
1.4	10	1.5	10
1.3	5	-	-

All other subsequent high-vacuum photographs, including that at 130°C, duplicated the one shown in Figure 11-10. Thus, the second dehydration step did not occur, as was the case in Phase I. In addition, the photograph taken in the spacecraft environment exhibited no evidence of rehydration. The dehydration sample from Phase I also showed no rehydration after subsequent lengthy exposure to the atmosphere.

11.8 ANALYSIS OF THERMODYNAMIC AND CRYSTAL STRUCTURE DATA

Gypsum, a member of the monoclinic system, has a layer-type structure (see Figure 11-11). The layers which are parallel to the (010) face consist of two sheets of $SO_4^{=}$ groups linked together by Ca^{+2} ions so as to form rigid double sheets. These double sheets alternate with sheets of water molecules. Each Ca atom is coordinated by eight oxygen atoms, six belonging to the $SO_4^{=}$ groups and two belonging to two water molecules. Each Ca^{+2} ion within a double sheet is linked to both an oxygen atom in the same double sheet and one in a neighboring sheet by a water molecule. The relative weakness of these latter bonds explains the good cleavage parallel to the (010) face.

Kelley, Southard, and Anderson (1941) report six solid phases in the $CaSO_4$ -- H_2O system with distinct thermodynamic properties: gypsum, two polymorphs of the hemihydrate (α, β), two polymorphs of soluble anhydrite (α, β), and insoluble anhydrite.

The direct dehydration of gypsum to form anhydrite occurs, but is generally not applicable to vacuum conditions.

The reaction

$$CaSO_4 \cdot 2\,H_2O \longrightarrow CaSO_4\,(\text{insol}) + 2\,H_2O$$

takes place only in the presence of water or a salt solution.

The reaction

$$CaSO_4 \cdot 2\,H_2O \longrightarrow CaSO_4\,(\text{sol}\,\alpha) + 2\,H_2O$$

according to Kelley et al. never occurs under equilibrium conditions and probably never occurs under nonequilibrium conditions.

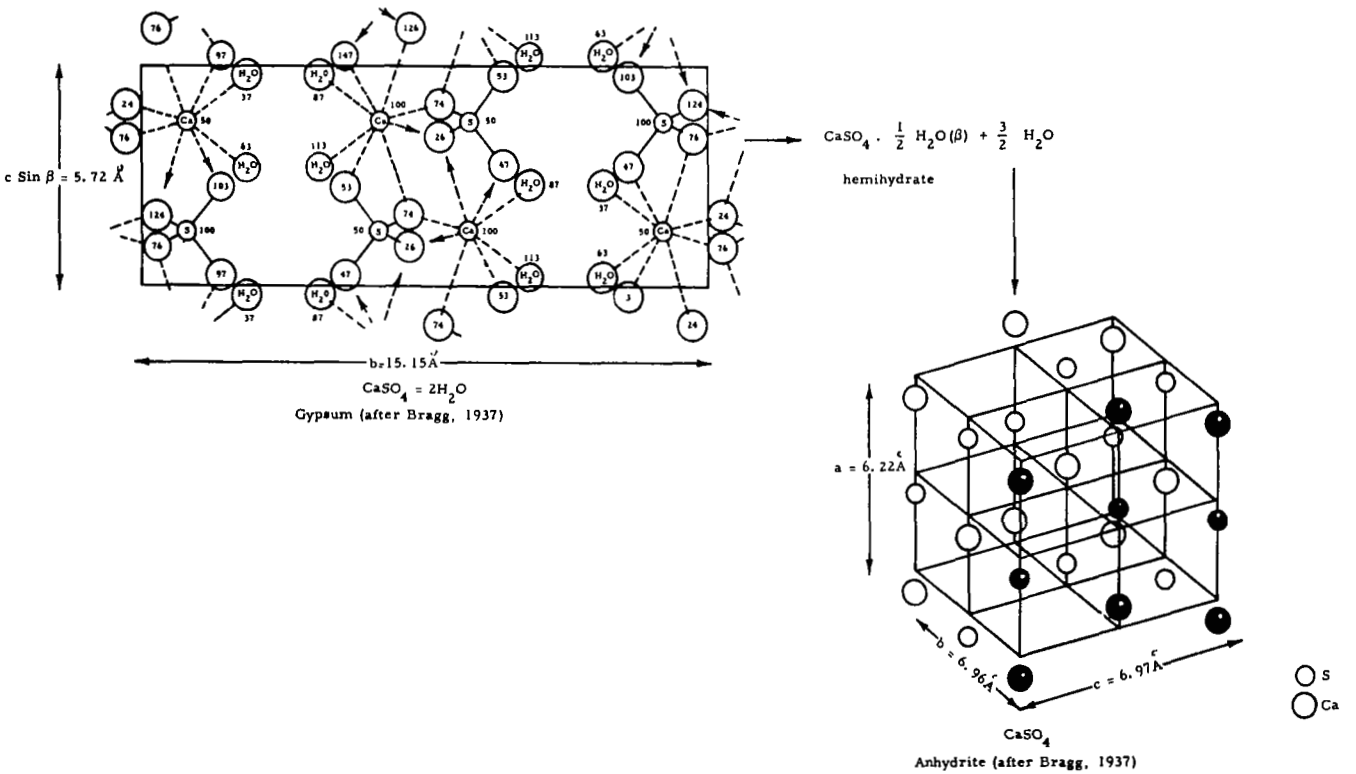

Figure 11-11 The Structure of Gypsum and Anhydrite

The reaction

$$CaSO_4 \quad 2\ H_2O \longrightarrow CaSO_4(\text{sol}\ \beta) + 2\ H_2O$$

occurs to a small extent, but it has not been established that it proceeds without the formation of the hemihydrate. The polymorph of the hemihydrate is produced when gypsum is dehydrated in a vacuum, regardless of the temperature at which this reaction occurs. The amount of water present in $CaSO_4 \cdot 1/2\ H_2O\ (\beta)$ is just equal to the theoretical amount. The other polymorphic form, $CaSO_4 \quad 1/2\ H_2O\ (\alpha)$, contains a variable amount of water and is produced when gypsum is dehydrated in an oven at atmospheric pressure.

The reaction which is most probable in the lunar environment is that which proceeds with the formation of the phase of the hemihydrate:

$$CaSO_4 \cdot 2\ H_2O \longrightarrow CaSO_4\ 1/2\ H_2O\ (\beta) + H_2O$$

The structure of the β hemihydrate is still in doubt. Some researchers believe the β hemihydrate is a definite compound whose structure differs from that of soluble anhydrite. Others maintain that there is no difference between the structures of the hemihydrate and soluble anhydrite except in their content of "zeolitic" water.

Gallitelli (1933) and Florke (1952) view the structures of the β polymorph of the hemihydrate as being open with channels through which water molecules can move. There are certain sites within this structure which are energetically more favorable and are occupied when the structure contains the stoichiometric amount of water ($n = 1/2$). From their point of view, the dehydration of gypsum is a "zeolitic"-type loss of water with a probable shrinkage of the cell parameters. The structure becomes stable again when $n = 1/2$ and all of the energetic sites are occupied. Upon heating, the remaining water is lost, causing structural deformation and changes in the cell parameters.

The final decomposition product of the dehydration of gypsum is anhydrous $CaSO_4$. Depending upon the nature of the hemihydrate from which it is produced and the temperature of dehydration, $CaSO_4$ can exist in

several polymorphic forms. The hexagonal polymorphs (α, β) are produced by the dehydration of their respective hemihydrates (α, β) in vacuum, at temperatures less than 100°C. $CaSO_4$ (α) contains 0.02-0.05% by weight of residual H_2O while $CaSO_4$ (β) contains 0.16-0.27% by weight of residual H_2O. The orthorhombic form of $CaSO_4$, commonly referred to as anhydrite, is produced by the slow dehydration of either hemihydrate above 100°C or by heating the hexagonal forms above 150°C. The structure of anhydrite (see Figure 11-11) consists of alternating planes of Ca ions and $SO_4^{=}$ groups parallel with (010) and (100) faces.

Kelley et al. (1941) conducted a comprehensive thermodynamic study of gypsum and its decomposition products. They formulated the following heat capacity equations for $CaSO_4 \cdot 2\ H_2O$, $CaSO_4 \cdot 1/2\ H_2O$ (β), $CaSO_4$ (β), and H_2O from estimated extrapolations of heat capacity curves from 0 - 300°K:

$CaSO_4 \cdot 2\ H_2O$: $Cp = 21.84 + 0.076T$ calories/mole

$CaSO_4 \cdot 1/2\ H_2O$ (β): $Cp = 11.48 + 0.061T$ calories/mole

$CaSO_4$ (β): $Cp = 14.10 + 0.33T$ calories/mole

H_2O (g): $Cp = 7.45 + 0.002T$ calories/mole

H_2O (l): $Cp = 18.02$ calories/mole

However, little error is introduced in the use of these equations in the range of 298-425°K.

Utilizing the aforementioned heat capacity equations, Kelley et al. (1941) obtained the following relations for the decomposition of gypsum to the (β) hemihydrate:

$$\Delta Cp^o = 0.82 - 0.012T$$

$$\Delta H^o = \Delta H_o^o + 0.82T - 0.006T^2 \qquad (11\text{-}1)$$

Evaluating $\Delta H_o^o = 20,640$ calories from $\Delta H_{298.1} = 20,350$ calories, Kelley et al. (1941) obtained the free-energy equation:

$$\Delta F^o = 20,640 - 1.89\,T \log T + 0.006\,T^2 + IT. \qquad (11\text{-}2)$$

By combining Equations 11-1 and 11-2 to form $\Delta S = \frac{\Delta H - \Delta F^o}{T}$, he obtained $\Delta S = 0.82 + 1.89 \log T - 0.012\,T - I$. From a value of $\Delta S_{298.1} = 53.1$ calories, $I = -51.48$ calories is calculated.

Likewise, for the reaction

$$CaSO_4 \cdot 1/2H_2O(\beta) \text{---} CaSO_4\ (\text{sol}\ \beta) + 1/2\ H_2O,$$

the relations giving the free-energy can be calculated. Employing

$$\Delta Cp = 6.34 - 0.027\,T$$

$$\Delta H^o = \Delta H_o^o + 6.34\,T - 0.0135\,T^2 \qquad (11\text{-}3)$$

with $\Delta H_o = 7170$ calories evaluated from $\Delta H_{298.1} = 2610$ calories, Kelley et al. (1941) obtained the free-energy equation:

$$\Delta F^o = 7170 - 14.60\,T \log T + 0.0135\,T^2 + IT. \qquad (11\text{-}4)$$

Utilizing the entropy equation obtained by a combination of Equations 11-3 and 11-4 and a value of $\Delta S_{298.1} = 16.36$ calories,

$$\Delta S = 6.34 + 14.60 \log T - 0.027\,T - I$$

Kelley et al. (1941) calculated a value of $I = 18.06$ calories.

Experimental data have shown that I is relatively constant over the range 273.1 - 380°K. To utilize these free-energy relations in the construction of stability diagrams (see Figure 11-12), it is necessary to combine them with the well-known relation for a reaction producing one mole of an ideal gas.

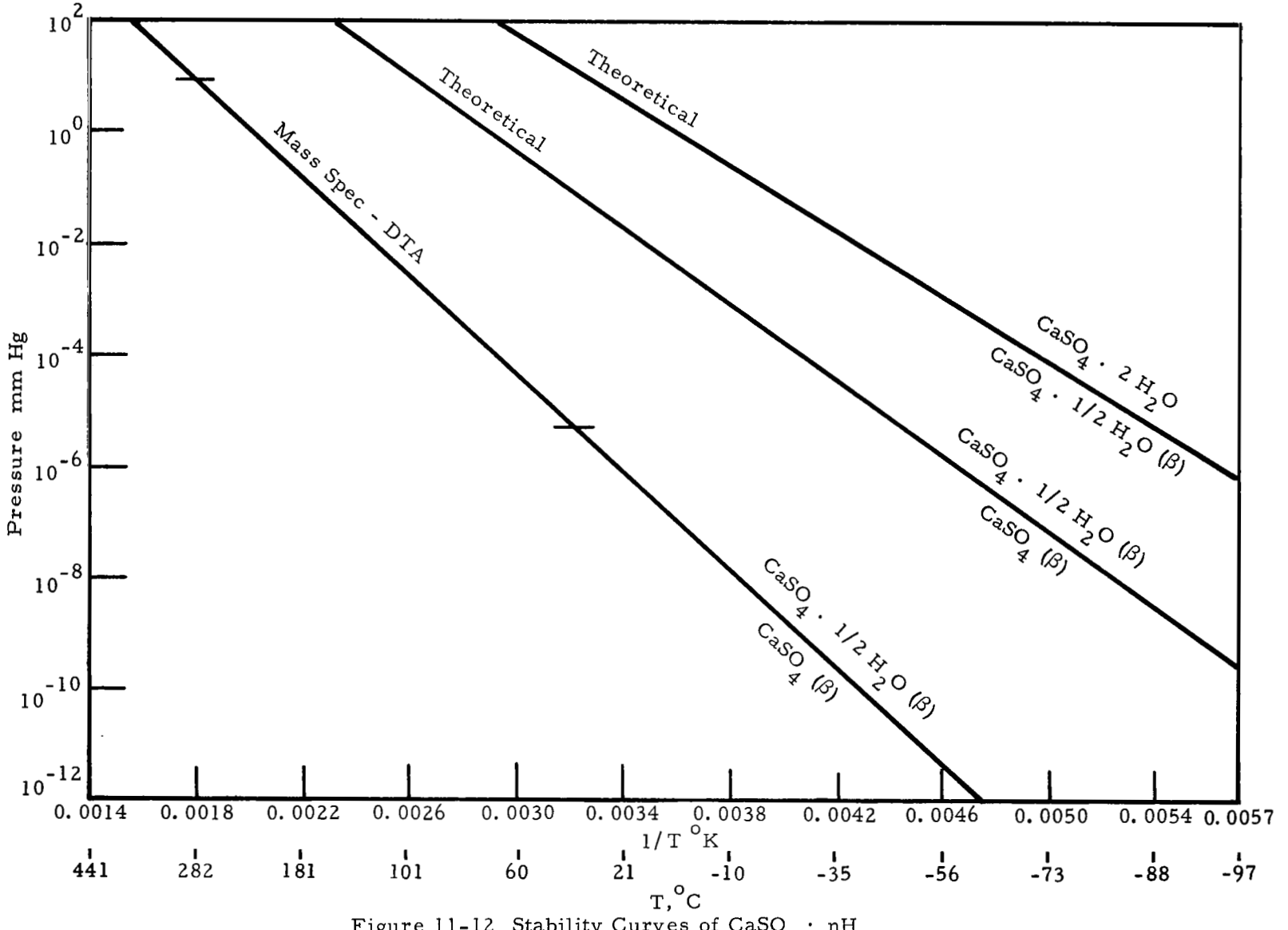

Figure 11-12 Stability Curves of $CaSO_4 \cdot nH_2$

$$\Delta F^{o} = -RT\ln P \qquad (11\text{-}5)$$

where P is the vapor pressure in atmospheres of the phase under investigation. Thus, by combining Equations 11-2 and 11-4 with 11-5, the vapor pressure equations for gypsum dehydrating to the hemihydrate and for the hemihydrate dehydrating to the soluble anhydrite are obtained:

$$\ln (P)^{3/2} = \frac{-20,640 - 1.89\,T \log T + 0.006\,T^{2} + 51.48\,T}{RT}$$

$$\ln (P)^{1/2} = \frac{-7170 - 14.60\,T \log T + 0.0135\,T^{2} + 18.06\,T}{RT}$$

which define the stability of gypsum and the hemihydrate.

It was not possible to determine the breakdown of gypsum in the mass spectrometer, because under experimental conditions at a P_{H_2O} of 5×10^{-6} mm of Hg, it decomposes at a temperature somewhat less than 27°C. However, it was possible to study the breakdown of the hemihydrate. The mass spectrometer and the DTA data are tabulated as follows:

$$CaSO_4 \cdot 2\,H_2O \longrightarrow CaSO_4 \cdot 1/2\,H_2O\,(\beta) + 3/2\,H_2O$$

	$\frac{P_{H_2O}\ \text{mm of Hg}}{12.5}$	$\frac{T^{o}C}{145}$
DTA		
Mass Spectrometer	---	---

$$CaSO_4 \cdot 1/2\,H_2O\,(\beta) \longrightarrow CaSO_4\,(\beta) + 1/2\,H_2O$$

	$\frac{P_{H_2O}\ \text{mm of Hg}}{12.5}$	$\frac{T^{o}C}{190}$
DTA		
Mass Spectrometer	5×10^{-6}	52

The curve representing the experimental breakdown of hemihydrate is shown in Figure 11-12. The thermodynamic data of Kelley et al. (1941) extrapolated to lunar conditions gives:

Gypsum ⟶ Hemihydrate (β)

Lunar Temperature	$T^{o}C$	$T^{o}K$	P mm of Hg
Minimum nighttime	-180	93	3.8×10^{-22}
Equilibrium at 1-m depth	-55	218	1.2×10^{-3}
Maximum daytime	+130	403	2.0×10^{3}
At lunar pressure	-137	136	1.0×10^{-11}

Hemihydrate (β) ⟶ Anhydrite (β)

Lunar Temperature	$T^{o}C$	$T^{o}K$	P mm of Hg
Minimum nighttime	-180	93	1.9×10^{-27}
Equilibrium at 1-m depth	-55	218	4.8×10^{-6}
Maximum daytime	+130	403	2.8×10^{1}
At lunar pressure	-110	163	1.0×10^{-11}

The thermodynamic data indicate that gypsum should dehydrate to $CaSO_4$ (β) during the lunar day and not exist in a stable phase at the equilibrium temperature associated with a depth of 1 m. Given sufficient water vapor, it should rehydrate during the lunar night. The kinetics are also favorable; $CaSO_4$ (β) rehydrates rapidly when exposed to water vapor. The other polymorph of $CaSO_4$, $CaSO_4$ (insol), which is produced by heating the soluble polymorphys above 150°C or dehydrating the hemihydrate in a vacuum above 100°C, does not readily rehydrate. Rehydration experiments on this polymorph of several months duration have generally proven to be unsuccessful. Therefore, one would expect to find $CaSO_4$ (β) below the lunar surface and a mixture of $CaSO_4$ (insol) and $CaSO_4$ (β) at the surface with possible rehydration of the (β) polymorph during the lunar night.

SECTION 12

HEMATITE

12.1 FORMULA

Fe_2O_3.

12.2 MINERAL CLASSIFICATION AND VOLATILE

Oxide-none.

12.3 SPECIMEN LOCALITY

Egremont, Cumberland, England.

12.4 PROCUREMENT SOURCE

Southwest Scientific Co., Scottsdale, Arizona.

12.5 OPTICAL MICROSCOPIC ANALYSIS

The hematite specimen, var. needle ore, is too opaque for conventional microscopic examination. Only the thinnest edges reveal a deep-red color in transmitted light. In reflected light, the hematite appears steel gray to red. Under the binocular microscope (Figure 12-1), no impurities are visible in the dense fibrous mass.

12.6 THERMAL ANALYSES

12.6.1 Differential Thermal Analysis

Figure 12-2.

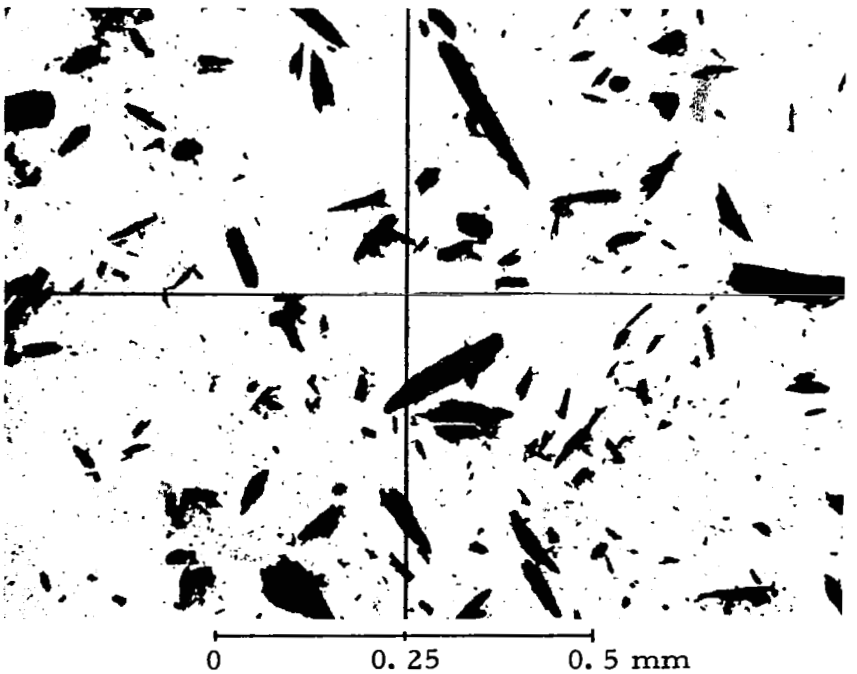

Figure 12-1 Photomicrograph of Hematite, 100X; the DTA Sample in Liquid Having Index of Refraction of 1. 68

12.6.1.1 Sensitivity

The sensitivity is 10 μv/cm.

12.6.1.2 Peak Values

These are:

350°C (+)

685°C (-)

The DTA curve indicates a general endothermic drift, with a minor exothermic peak at 350°C and a small endothermic break at 685°C produced by some unknown impurities.

12.6.2 Thermogravimetric Analysis

The TGA shows no significant weight loss (Figure 12-3). It is estimated that the weight loss amounts to less than 1% of the original sample weight and is probably due to the volatilization of adsorbed water.

12.6.3 Mass Spectrometer Analysis

The mass spectrometer curve (Figure 12-4) reveals the loss of no volatiles other than adsorbed water, which explains the endothermic drift of the DTA curve and the weight loss suggested by the TGA curve. As noted above, the amount of water loss is estimated at less than 1% and it may have originated from the water locked within the fibrous aggregate of the mineral. On the other hand, the small exothermic peak in the DTA curve at 350°C cannot be related to a corresponding loss of volatiles in the mass spectometer.

12.7 X-RAY DIFFRACTION PATTERNS

12.7.1 Debye-Sherrer Standard

Figure 12-5 shows the hematite X-ray pattern taken with the Debye-Scherrer camera.

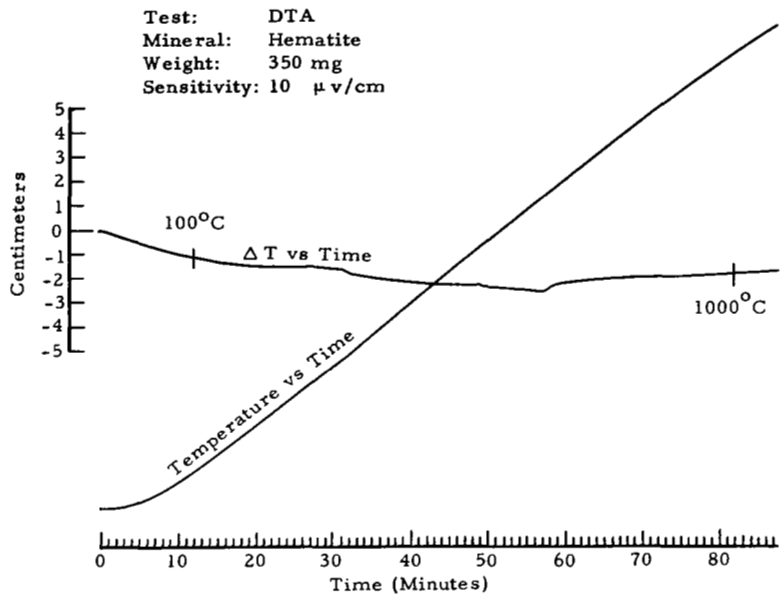

Figure 12-2 Hematite DTA

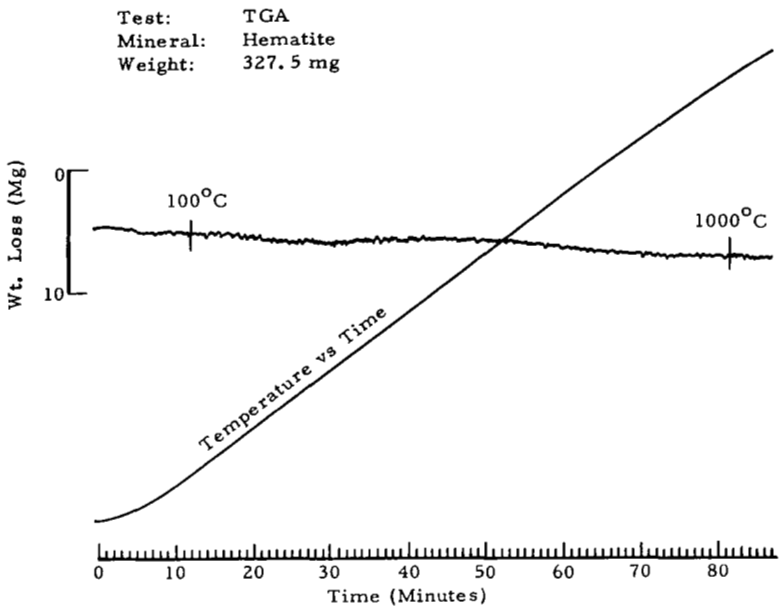

Figure 12-3 Hematite TGA

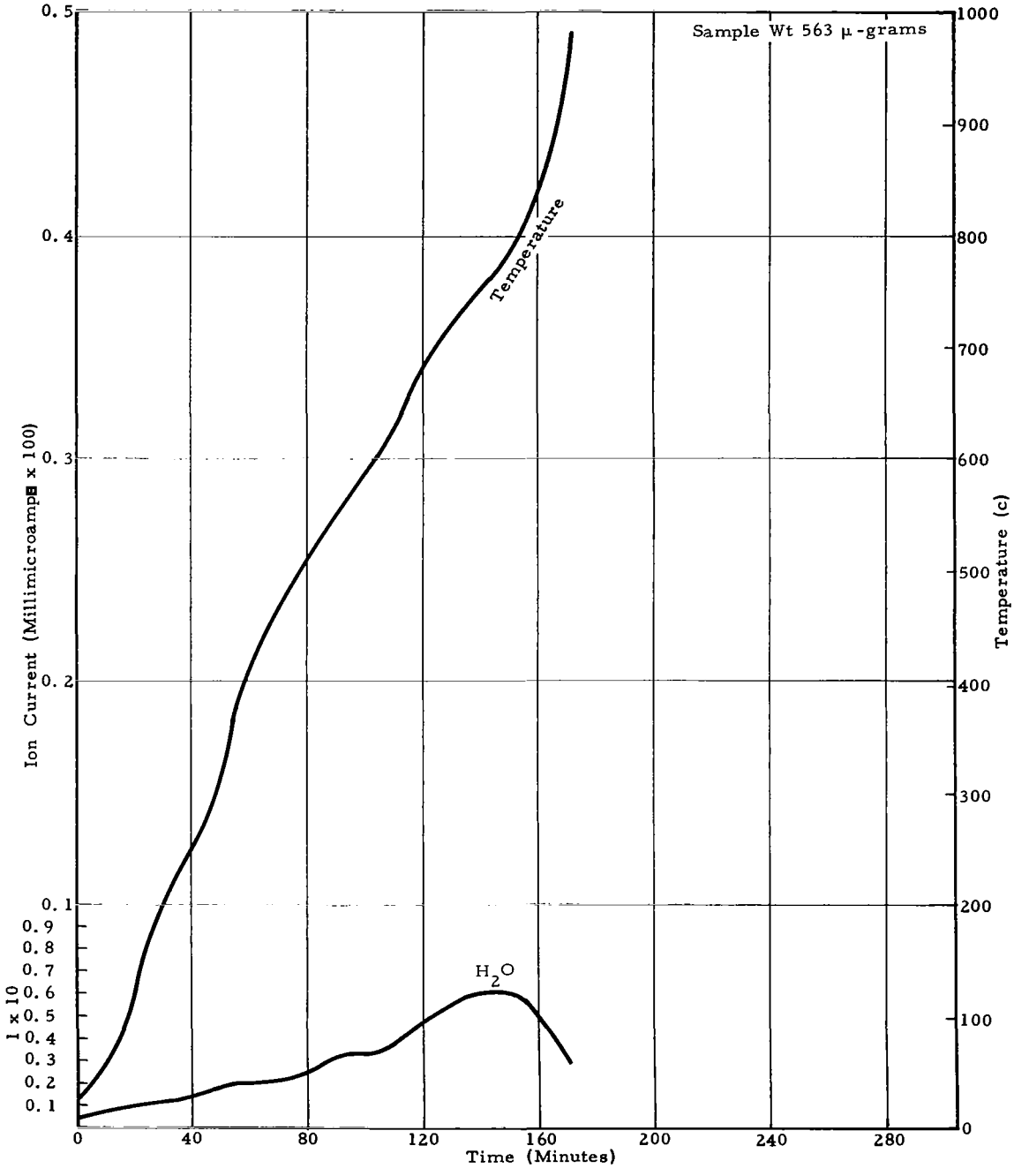

Figure 12-4 Mass Spectrometer Curve of Hematite—Scan With H_2O Peak Plotted

Table 12-1 is a comparison of experimental and ASTM d-values for hematite.

TABLE 12-1

COMPARISON OF EXPERIMENTAL AND ASTM D-VALUES FOR HEMATITE

Exp (Å)	ASTM (Å)	Exp (Å)	ASTM (Å)
3.7	3.66	1.45	1.45
2.7	2.69	1.35	1.349
2.57	2.57	1.26	1.258
2.20	2.201	1.19	1.189
1.84	1.838	1.16	1.162
1.69	1.69	1.14	1.141
1.59	1.59	1.10	1.10
1.49	1.484	1.055	1.055
		1.039	1.038

12.7.2 Bendix Vacuum Camera Standard

Figure 12-6 shows the hematite X-ray pattern taken with the Bendix vacuum camera (magnification 2X).

To obtain an X-ray pattern of this iron-containing sample with the Bendix vacuum camera, it was necessary to use molybdenum radiation. Thus, very few lines are present. In addition, one line does not correspond to a Debye-Scherrer line, since copper radiation was used for the latter. A comparison of the Debye-Scherrer Standard and the Bendix Camera Standard is presented in Table 12-2.

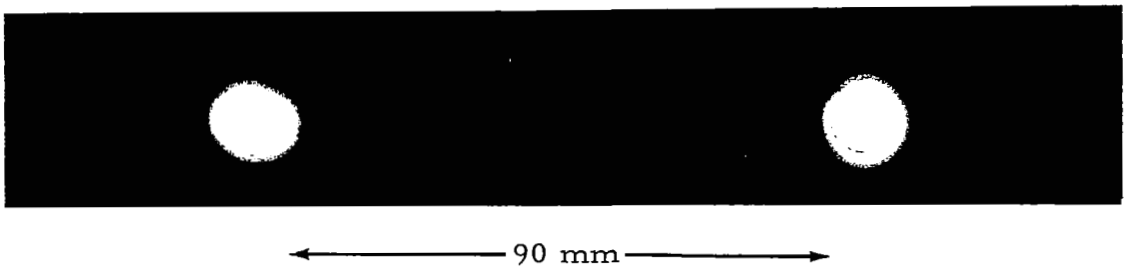

Figure 12-5 Hematite X-Ray Pattern Taken With Debye-Scherrer Camera

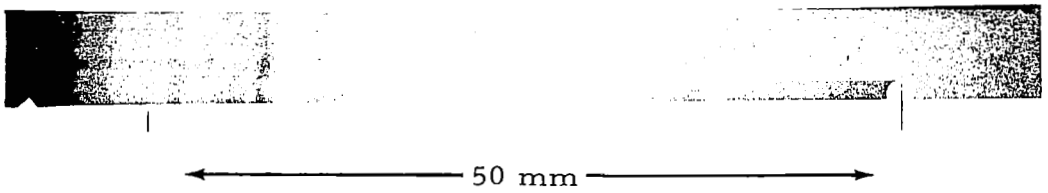

Figure 12-6 Hematite X-Ray Pattern Taken With Bendix Vacuum Camera (Magnification 2X)

TABLE 12-2

COMPARISON OF OBSERVED D-VALUES AND RELATIVE INTENSITY MEASUREMENTS FOR HEMATITE

Debye-Scherrer Standard		Bendix Camera Standard, MoK_α	
d_{obs}	$\frac{i}{i_o}$	d_{obs}	$\frac{i}{i_o}$
1.84	90	1.8	75
1.59	90	1.6	75
1.35	100	1.3	100
—	10	0.88	2

12.7.3 Vacuum Patterns

All patterns obtained under the conditions of Phase I duplicated the standard. Thus no changes occurred. However, there is no known change whose possible occurrence might be predicted to occur for this nonvolatile containing mineral.

12.8 ANALYSIS OF THERMODYNAMIC AND CRYSTAL STRUCTURE DATA

A discussion is given in the corresponding section on geothite.

SECTION 13

IRRADIATED PLAGIOCLASE

13.1 FORMULA

$Ab_{48}\ An_{52}$.

13.2 MINERAL CLASSIFICATION AND VOLATILE

Silicate, feldspar group - none.

13.3 SPECIMEN LOCALITY

Androtsy, Madagascar.

13.4 PROCUREMENT SOURCE

Southwest Scientific Co., Scottsdale, Arizona.

13.5 OPTICAL MICROSCOPIC ANALYSIS

A very coarsely crystalline labradorite is used as the test sample in this experiment. A prominent feature of the labradorite is the albite twinning, with pericline twinning present to a lesser degree. Although some cracked areas have been altered to white opaque kaolin, the material in the slide (Figure 13-1) appears clear and fresh. It is composed of 0.5% pyroxene (augite or diopside) occurring in small clusters of crystals. Some of these crystals range as large as 0.2 mm in diameter. A very small fraction of 1% consists of dark brown to black needles lying parallel to the (010) plane. Some are randomly oriented. The needles measure up to several tenths of a millimeter long and from 1 to 10 μ in diameter, and can almost certainly be identified as rutile.

With the slide on the universal stage and employing the Rittmann zone method, it is possible to determine the composition of the labradorite

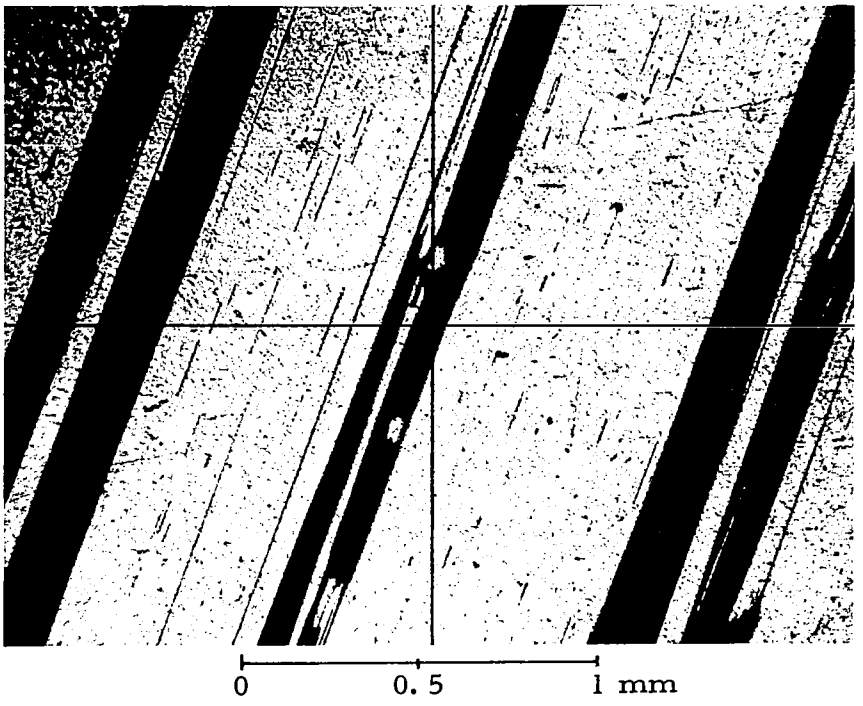

Figure 13-1 Photomicrograph of Labradorite, Crossed Polars, 47X, Showing Albite Twinning, Rutile Needles (Parallel with Twinning), and Pyroxene Crystals in Central Dark Twin Band

as Ab_{48} An_{52}. The extinction angles, measured on (010) and (001), indicate an identical composition. However, the indexes of refraction, determined on crushed fragments (α = 1.558), reveal a somewhat more calcic composition.

13.6 THERMAL ANALYSES

13.6.1 Differential Thermal Analysis

See Figure 13-2.

13.6.1.1 Sensitivity

The sensitivity is 5 μv/cm.

13.6.1.2 Peak Values

There are no peak values. The DTA curve discloses no significant change to 1050°C, but only a slight endothermic drift.

13.6.2 Thermogravimetric Analysis

The TGA curve (Figure 13-3) shows no weight loss to a temperature of 1050°C.

13.6.3 Mass Spectrometer Analysis

Analysis of the mass spectrometer curves reveals that neither the irradiated (Figure 13-4) nor the nonirradiated (Figure 13-5) plagioclase specimens had undergone chemical change in the mass spectrometer. The loss of a small amount of water is indicated, however, in both cases. Closer examination of the DTA and TGA curves confirm this water loss, namely, by the slight endothermic drift of the DTA and the negative drift of the TGA.

13.7 X-RAY DIFFRACTION PATTERNS

13.7.1 Debye-Scherrer Standard

After 30 hr of neutron exposure at the core face of The University of Michigan nuclear reactor, there is no detectable difference evident between the pattern of the irradiated plagioclase (Figure 13-6) and that of the nonirradiated plagioclase (Figure 13-7).

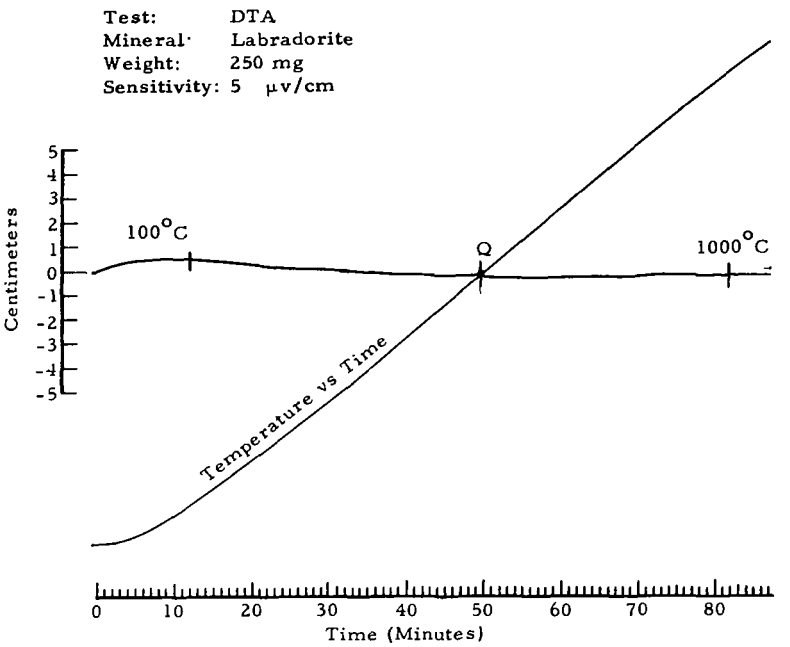

Figure 13-2 Irradiated Plagioclase DTA

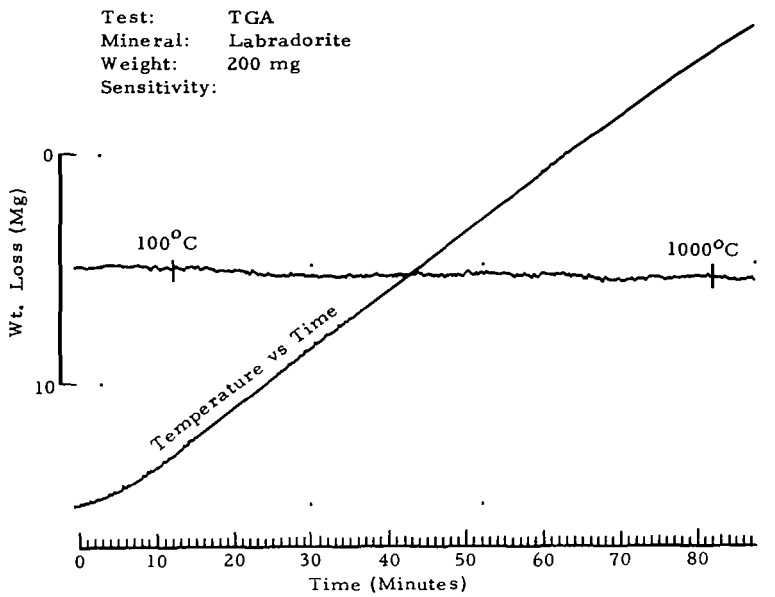

Figure 13-3 Irradiated Plagioclase TGA

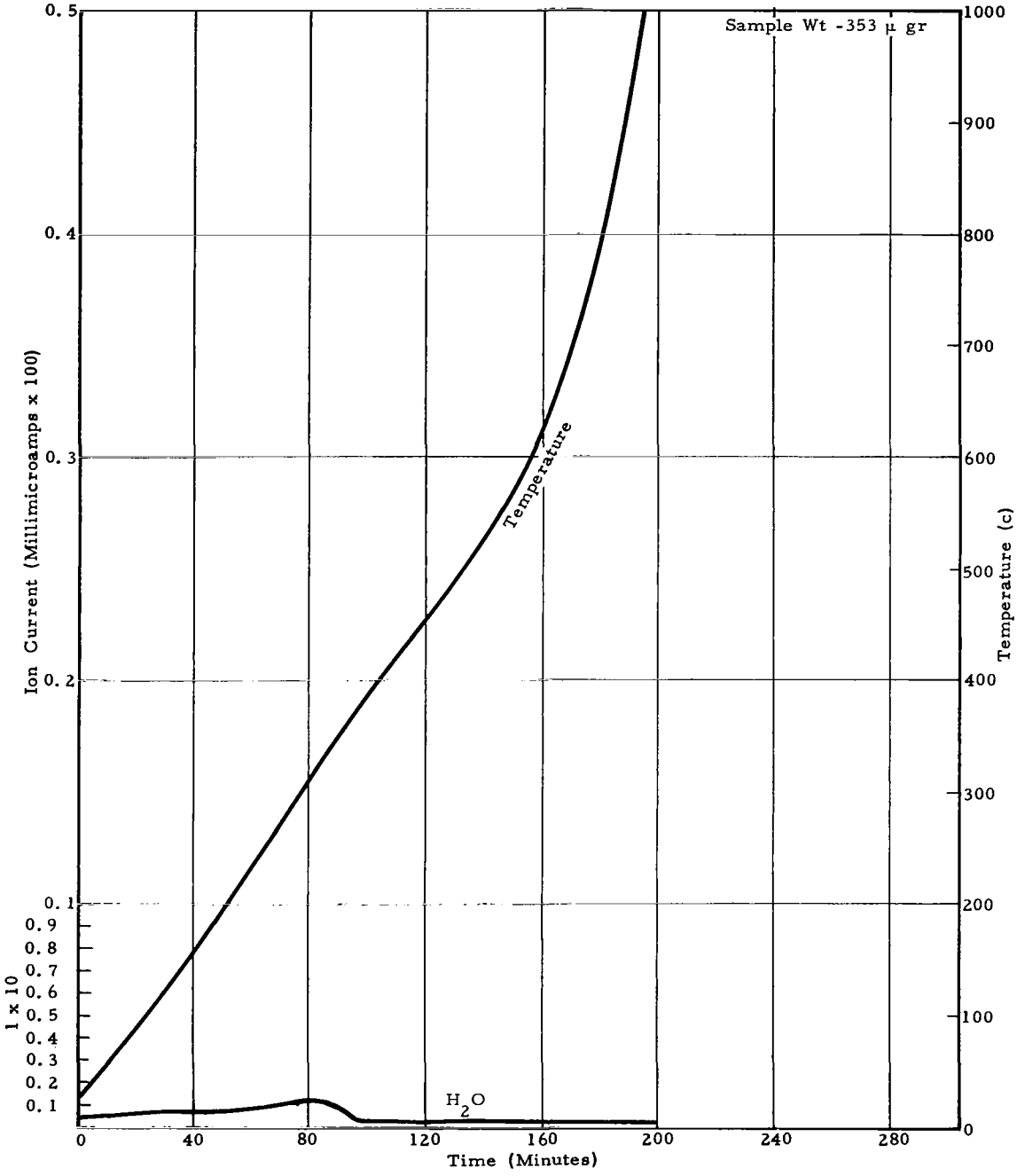

Figure 13-4 Mass Spectrometer Curve of Plagioclase (Irradiated Labradorite) - H_2O Peak

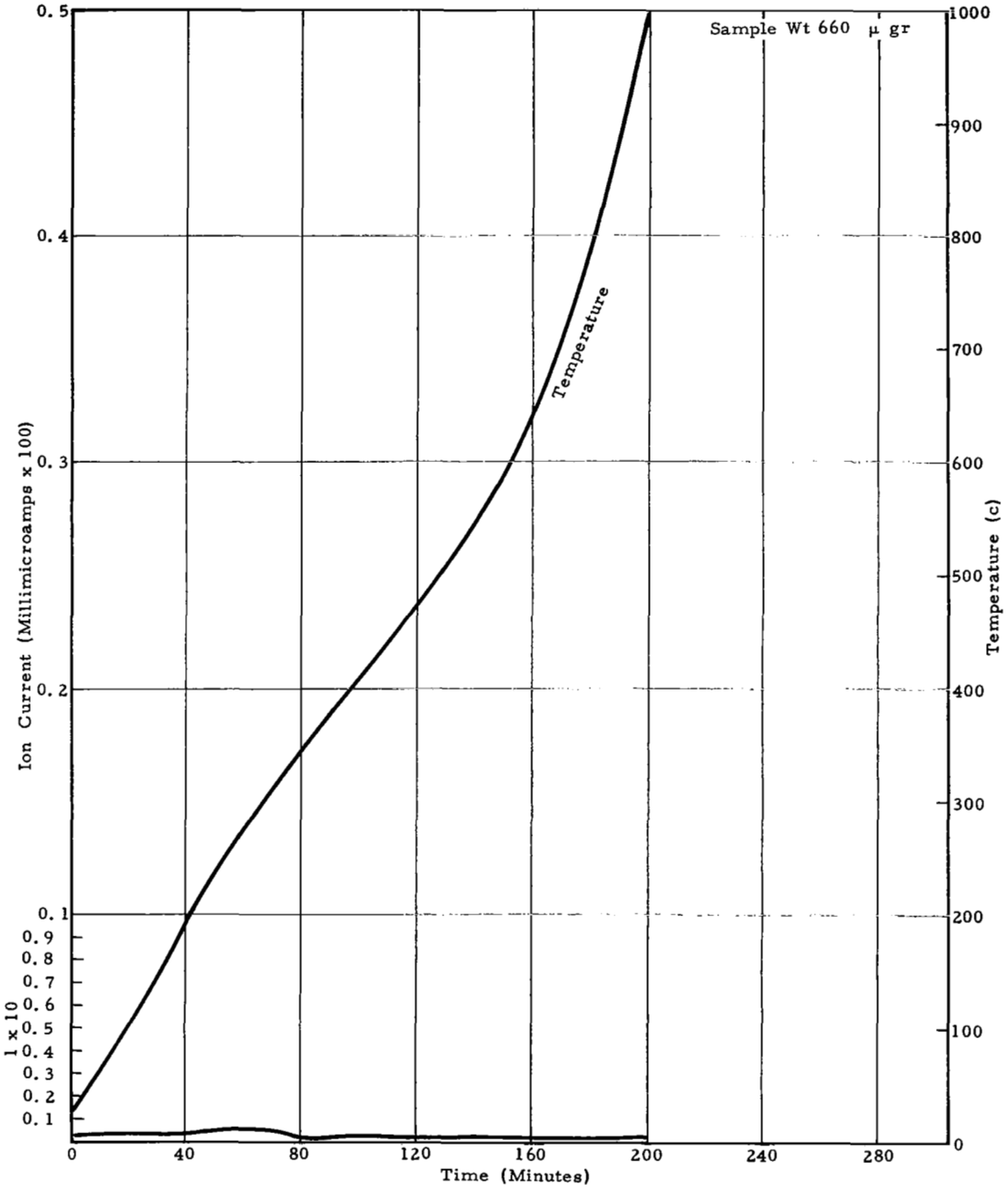

Figure 13-5 Mass Spectrometer Curve of Plagioclase (Nonirradiated Labradorite) - H_2O Peak

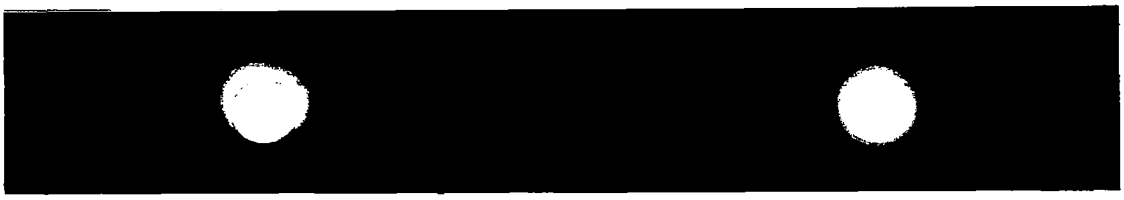

Figure 13-6 Plagioclase (Irradiated) X-Ray Pattern Taken With Debye-Scherrer Camera

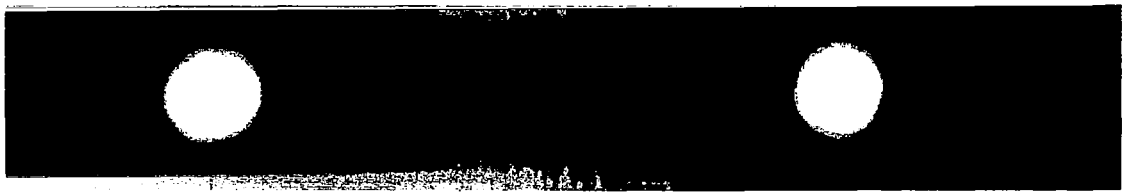

Figure 13-7 Plagioclase (Nonirradiated) X-Ray Pattern Taken With Debye-Scherrer Camera

TABLE 13-1

COMPARISON OF EXPERIMENTAL AND ASTM D-VALUES FOR PLAGIOCLASE (IRRADIATED AND NONIRRADIATED)

Exp(Å)	ASTM(Å)	Exp(Å)	ASTM(Å)	Exp(Å)	ASTM(Å)	Exp(Å)	ASTM(Å)
6.5	6.48	2.50	2.51	1.77	1.77	1.34	1.35
4.0	4.04	2.29	2.29	1.60	1.62	1.26	1.27
3.7	3.75	2.10	2.12	1.57	1.56	1.24	1.25
3.2	3.20	2.00	2.01	1.54	1.53	1.21	1.21
2.9	2.95	1.91	1.92	1.49	1.48	1.15	1.16
2.8	2.84	1.82	1.83	1.38	1.37	1.13	1.13
2.65	2.66						

13.7.2 Bendix Vacuum Camera Standard

The pattern is spotty due to a preponderance of crystallite sizes that are only slightly smaller than the 300-mesh sieve used for all test specimens. However, there is reasonable agreement with the intense lines of the Debye-Scherrer pattern.

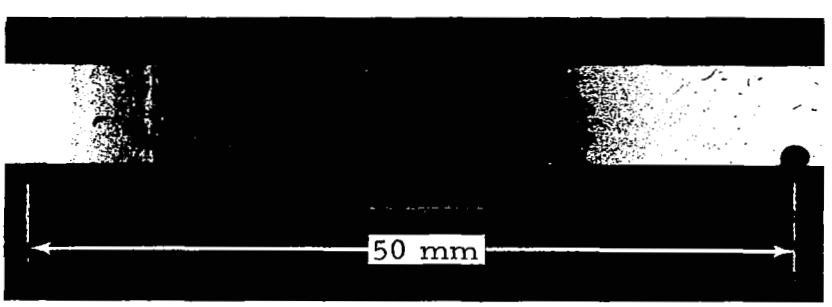

Figure 13-8 X-ray Pattern Taken With Bendix Vacuum Camera (Magnification 2x)

A comparison of d-values and relative intensity measurements obtained by the Debye-Scherrer Standard and the Bendix Camera Standard is given in Table 13-2.

TABLE 13-2

COMPARISON OF OBSERVED D-VALUES AND RELATIVE INTENSITY MEASUREMENTS FOR PLAGIOCLASE (IRRADIATED AND NONIRRADIATED)

Debye-Scherrer Standard, CuK_α		Bendix Camera Standard, CuK_α	
d_{obs}	$\frac{i}{i_o}$	d_{obs}	$\frac{i}{i_o}$
4.0	20	4.1	10
3.2	100	3.1	100
2.50	10	2.4	20
2.00	2	2.0	5
1.60	2	1.7	2

13.7.3 Vacuum Patterns

All diffraction patterns obtained under the conditions of Phase I precisely duplicated that of the standard. However, plagioclase was included only after having been irradiated in the hope that irradiation damage would be evident by structure disorder as reflected in the X-ray photographs, and that changes in the order-disorder relations might subsequently be detected, at least at the highest temperatures, in the vacuum camera. No change was evident following irradiation, however, as noted above. This mineral was therefore not included in Phase II.

13.8 ANALYSIS OF THERMODYNAMIC AND CRYSTAL STRUCTURE DATA

Since the hypothesized disorder with irradiation cannot be treated with equilibrium thermodynamics and since it did not occur, no discussion is presented here regarding it. The feldspar structure relations are discussed in Section 5 under NH_4 feldspar relations.

SECTION 14

MUSCOVITE

14.1 FORMULA

$KAl_2 (Al Si_3O_{10}) (OH)_2$.

14.2 MINERAL CLASSIFICATION AND VOLATILE

Silicate, mica group - (OH).

14.3 SPECIMEN LOCALITY

Effingham Township, Ontario, Canada.

14.4 PROCUREMENT SOURCE

Ward's Natural Science Establishment, Inc. Rochester, New York.

14.5 OPTICAL MICROSCOPIC ANALYSIS

The clear cleavage fragments include a small amount (1%) of tiny opaque specks, probably magnetite (Figure 14-1). The specimen is optically negative and has a 2V of about 40° with the indexes $\beta = \gamma = 1.590$.

14.6 THERMAL ANALYSES

14.6.1 Differential Thermal Analysis

See Figure 14-2.

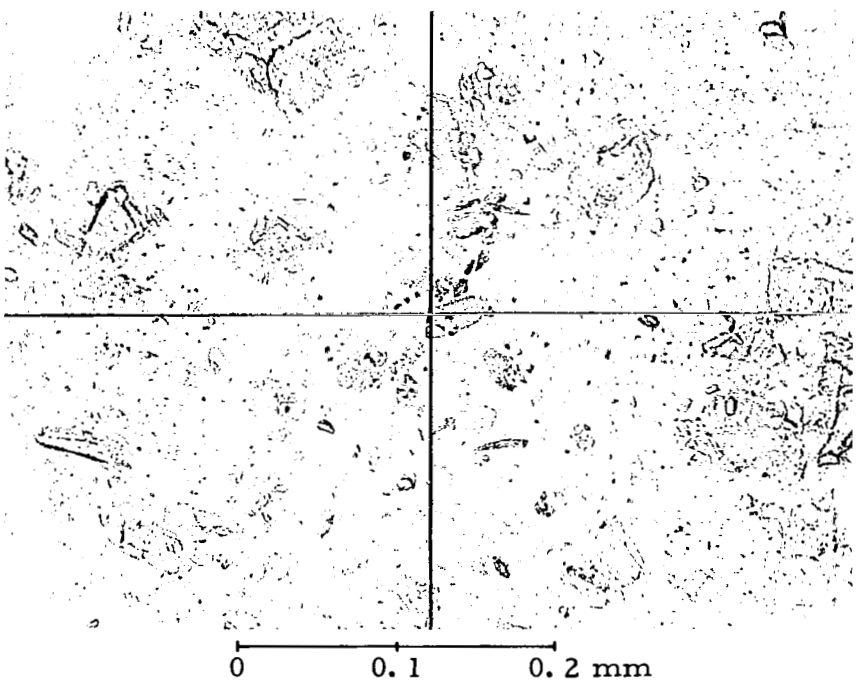

Figure 14-1 Photomicrograph of Muscovite, 210X, DTA Sample Immersed in Liquid Having Index of Refraction of 1.48

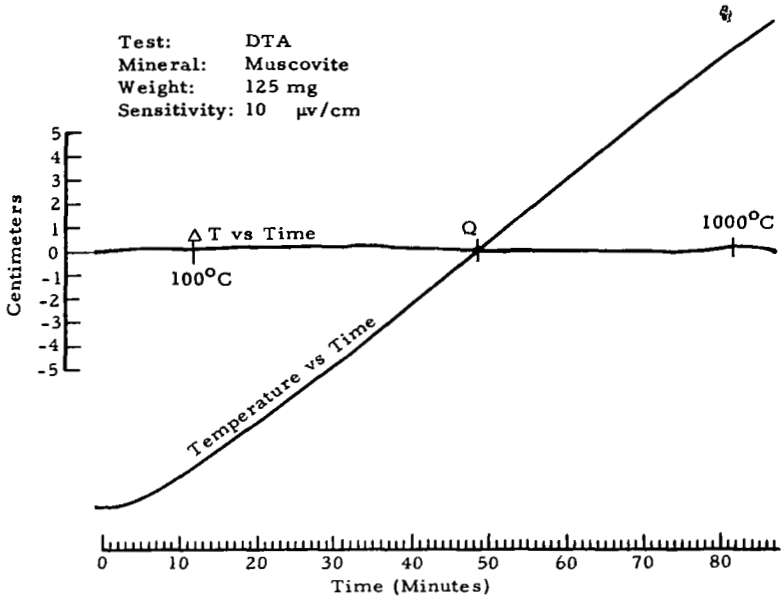

Figure 14-2 Muscovite DTA

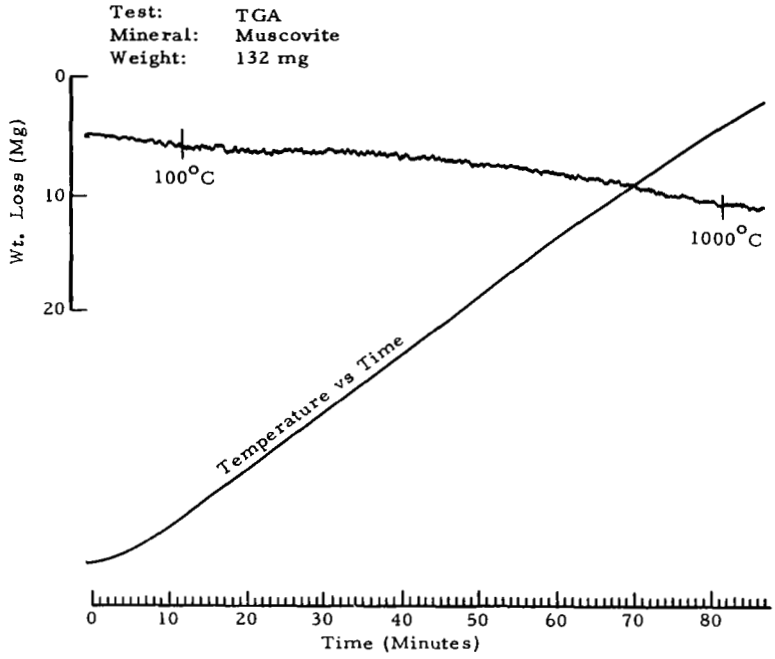

Figure 14-3 Muscovite TGA

14. 6. 1. 1 Sensitivity

The sensitivity is 10 μv/cm.

14. 6. 1. 2 Peak Values

There are no peak values.

The DTA curve shows no reaction from room temperature to 1060°C. Reference is made to similar behavior by a Goshen, Massachusetts, muscovite that had been dry ground for two hours (Mackenzie and Milne, 1953, "Effect of Grinding on Muscovite," Min. Mag., 30, 178-185).

14. 6. 2 Thermogravimetric Analysis

The TGA (Figure 14-3) indicates a very gradual weight loss, beginning at about 400°C and adding up to a total weight loss of 3%. It is doubtful whether this weight loss should be attributed to the loss of structural OH.

14. 6. 3 Mass Spectrometer Analysis

The mass spectrometer curve (Figure 14-4), as in the case of the DTA curve, discloses no compositional changes. However, in contrast to the TGA curve, which reveals a 3% weight loss, the mass spectrometer analysis indicates a water loss of less than 1%. A reasonable explanation for this discrepancy is that in all likelihood, water had been absorbed by the specimen during the grinding process. Upon exposure to vacuum in the mass spectrometer, most of this water was immediately removed from the sample.

14. 7 X-RAY DIFFRACTION PATTERNS

14. 7. 1 Debye-Scherrer Standard

Figure 14-5 shows the muscovite X-ray pattern taken with the Debye-Scherrer camera.

Excellent agreement is present between values obtained from the Debye-Scherrer standard and the ASTM file values as shown in Table 14-1.

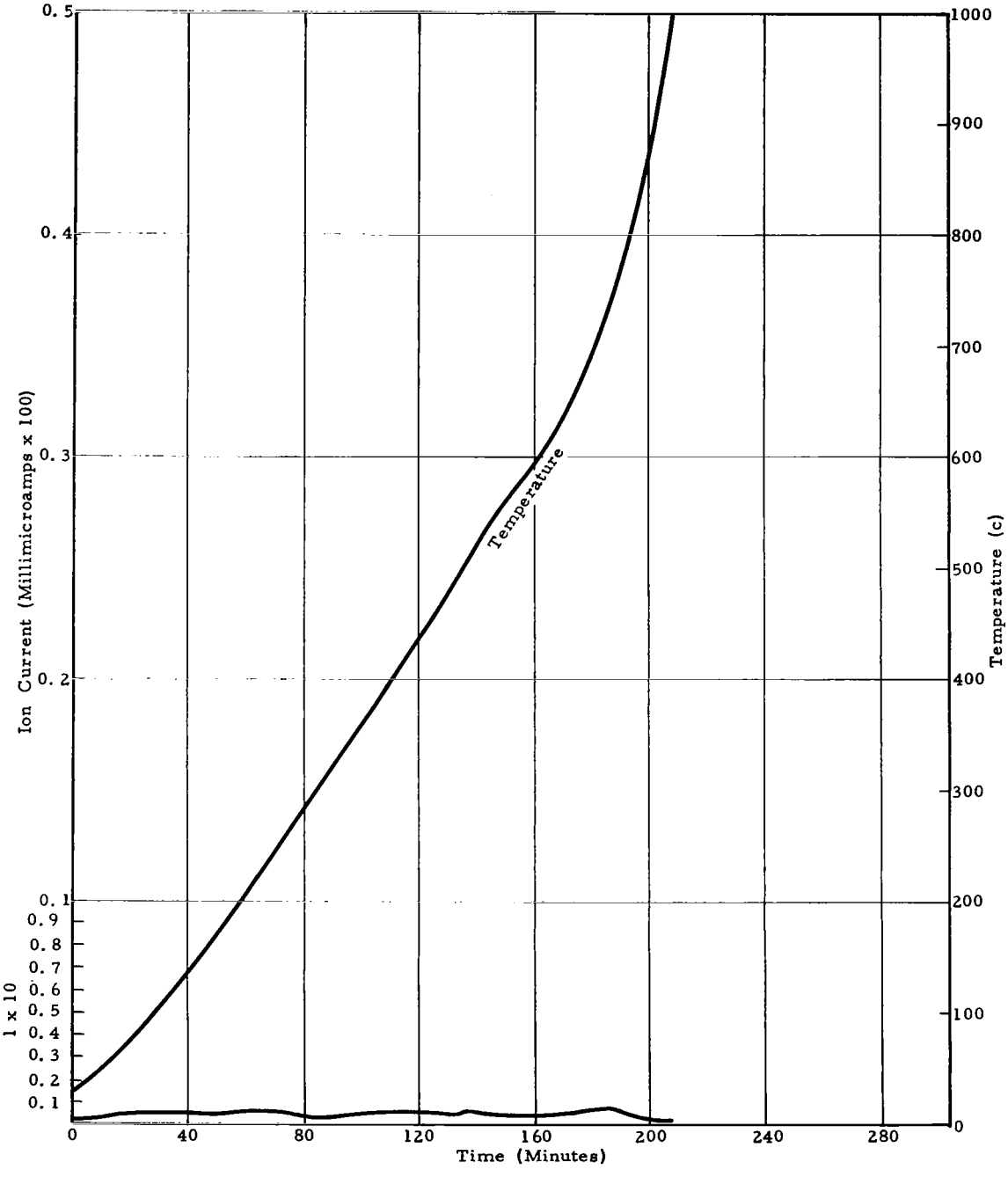

Figure 14-4 Mass Spectrometer Curve of Muscovite—H_2O Peak

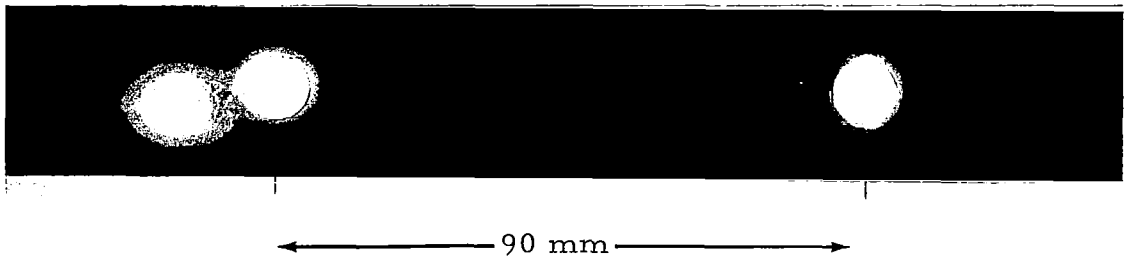

Figure 14-5 Muscovite X-Ray Pattern Taken With Debye-Scherrer Camera

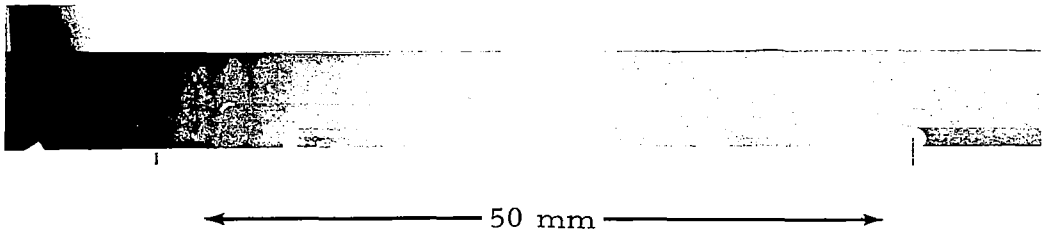

Figure 14-6 Muscovite X-Ray Pattern Taken With Bendix Vacuum Camera (Magnification 2X)

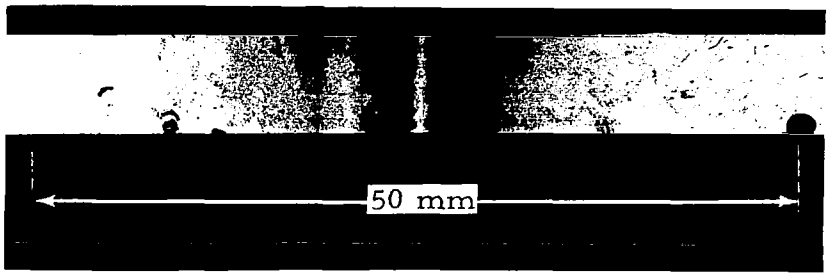

Figure 14-7 Muscovite X-Ray Pattern Taken at 180°C and a Vacuum of 8×10^{-10} Torr (Pattern Identical to that Taken at Room Temperature)

TABLE 14-1

COMPARISON OF EXPERIMENTAL AND ASTM D-VALUES FOR MUSCOVITE

Exp (Å)	ASTM(Å)	Exp (Å)	ASTM (Å)	Exp (Å)	ASTM (Å)	Exp (Å)	ASTM (Å)
9.90	9.95	2.95	2.987	2.12	2.132	1.35	1.352
4.9	4.97	2.82	2.859	1.97	1.972	1.33	1.335
4.5	4.47	2.75	2.789	1.70	1.704	1.155	1.1582
3.95	3.95	2.57	2.566	1.65 pair	1.646	1.13	1.1300
3.85	3.882	2.45	2.450	1.60	1.603	1.100	1.167
3.50	3.489	2.38	2.384	1.55	1.559	1.065	- End of List
3.30	3.32	2.25	2.254	1.50	1.504	1.047	-
3.20	3.199	2.20	2.208	1.44	1.453	-	-

14.7.2 Bendix Vacuum Camera Standard

The Bendix camera standard is also a particularly good one, in that an unusually large number of lines are resolved, and these show good correspondence with the Debye-Scherrer standard as shown in Table 14-2. This was somewhat unexpected as muscovite is particularly susceptible to preferred orientation effects in sample preparation.

14.7.3 Vacuum Patterns

The diffraction photographs of muscovite taken under all conditions from pumpdown to high vacuum, were precisely the same. In addition, more than one standard photograph had been obtained prior to pumpdown, and these also duplicated the standard reproduced in Figure 14-6. A photograph taken following pumpdown is shown in Figure 14-7; data obtained from it are given in Table 14-3.

TABLE 14-2

COMPARISON OF OBSERVED D-VALUES AND RELATIVE INTENSITY MEASUREMENTS FOR MUSCOVITE

Debye-Scherrer Standard, CuK_α		Bendix Camera Standard, CuK_α	
d_{obs}	$\frac{i}{i_o}$	d_{obs}	$\frac{i}{i_o}$
4.5 (pair)	100	4.3	70
3.85	30	3.8	20
3.20	40	3.1	40
2.82	10	2.9	5
2.75	40	2.7	40
2.38	100	2.4	100
2.25	20	2.3	5
2.12	20	2.1	5
1.97	50	2.0	10
1.70	40	1.8	5
1.55	40	1.5	2
1.35	40	1.4	30

TABLE 14-3

COMPARISON OF D-VALUES AND RELATIVE INTENSITIES FOR THE STANDARD BENDIX CAMERA PHOTOGRAPH AND THE PHOTOGRAPH OBTAINED AT ULTRAHIGH VACUUM

Bendix Standard, CuK_α		Bendix Ultrahigh Vacuum, CuK_α	
d_{obs}	$\frac{i}{i_o}$	d_{obs}	$\frac{i}{i_o}$
4.3	70	4.7	20
3.8	20	-	-
3.1	40	3.1	15
2.9	5	-	-
2.7	40	2.6	15
2.4	100	2.4	100
2.3	5	-	-
2.1	5	-	-
2.0	10	-	-
1.8	5	-	-
1.5	2	1.5	10
1.4	30	1.4	80

Although the patterns are obviously different, the photograph obtained in ultrahigh vacuum has lines which correlate well with those of the standard. This is interpreted to be due to change in orientation of muscovite crystallite plates during pumpdown, probably caused by loss of surface absorbed water, and resulting in preferred orientation. A Debye-Scherrer photograph was taken of the material in the capillary at the end of the experiment after the vacuum was broken. This duplicated the standard Debye-Scherrer photograph, further confirming that no devolatilization of muscovite had taken place. However, to substantiate these results, muscovite was again used in Phase II of the experiment.

14. 7. 4 Bendix Vacuum Standard, Phase II

The standard photograph taken for Phase II is shown in Figure 14-8; data obtained from it are compared with the standard of Phase I in Table 14-4.

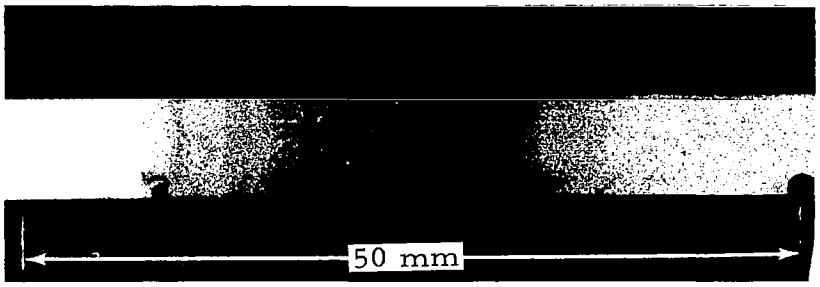

Figure 14-8 Muscovite X-Ray Pattern Taken as Standard for Phase II

The agreement between the standard photographs, as shown in Table 14-4, is generally excellent and the minor differences may be attributed to sample preferred orientation and error of measurement.

14. 7. 5 Vacuum Patterns, Phase II

All photographs taken at all temperatures under conditions of ultrahigh vacuum duplicated the standard photograph, indicating that no change occurred in the muscovite. This further confirms that the differences in the diffraction patterns noted in Phase I were a result of differing specimen preferred orientation.

TABLE 14-4

COMPARISON OF D-VALUES AND RELATIVE INTENSITIES OF THE MUSCOVITE STANDARDS IN PHASES I AND II

Standard, Phase I		Standard, Phase II	
d_{obs}	$\frac{i}{i_o}$	d_{obs}	$\frac{i}{i_o}$
4.3	70	4.5	50
3.8	20	-	-
3.1	40	-	-
2.9	5	2.9	5
2.7	40	2.7	5
2.4	100	2.5	100
2.3	5	2.3	10
2.1	5	2.1	10
2.0	10	2.0	10
1.8	5	1.8	10
1.5	2	1.5	10
1.4	30	1.4	20

14.8 ANALYSIS OF THERMODYNAMICS AND CRYSTAL STRUCTURE DATA

Muscovite has a layered structure consisting of alternating octahedral and tetrahedral sheets parallel to a-b plane. The tetrahedral sheets consist of a network of linked Si and Al tetrahedra in which three out of four of the available sites are occupied by silicon atoms with the remaining one occupied by an Al atom. If the symbol X denotes a cation, the formula of this sheet can be represented as X_2O_5.

The octahedral sheet consists of two sheets of a close-packed array of O atoms and OH^- groups and is the result of placing two tetrahedral sheets containing OH^- groups together with their vertexes pointing inward (see Figure 14-9). This combination of two tetrahedral sheets to form an octahedral sheet provides sites for Al atoms in 6-fold coordination. However, only two-thirds of the available sites are occupied with the rest remaining vacant. This arrangement allows the cross-linking of vertexes by Al atoms, thus forming a rigid layer structure.

The combination of two composite layers provides 12-fold coordination sites which are occupied by K^+ ions. The bonds between the K^+ ions and the O atoms of each layer are by far the weakest in the structure, thus explaining the perfect cleavage in this direction.

The complete decomposition of muscovite, at pressures ranging from several thousand bars to low vacuum (10^{-3} mm of Hg), proceeds with the formation of sanidine, corundum, and water vapor.[1] Occasionally, when the decomposition is carried out in the pressure range of atmospheric to low vacuum, reaction proceeds with the formation of an intermediate compound, "dehydrated" muscovite. However, dehydrated muscovite has not been thoroughly studied. Consequently, there is much conjecture concerning the mechanism of the reaction. Many researchers believe that there is no structural transformation brought about by "dehydration," while others, e.g., Roy (1949), believe that dehydration causes a marked expansion in the c-axis direction due to a warpage of the structural layers.

---

[1] See section on Ammonium Feldspar for a description of the structure of sanidine. The structure of corundum is analogous to that of hematite.

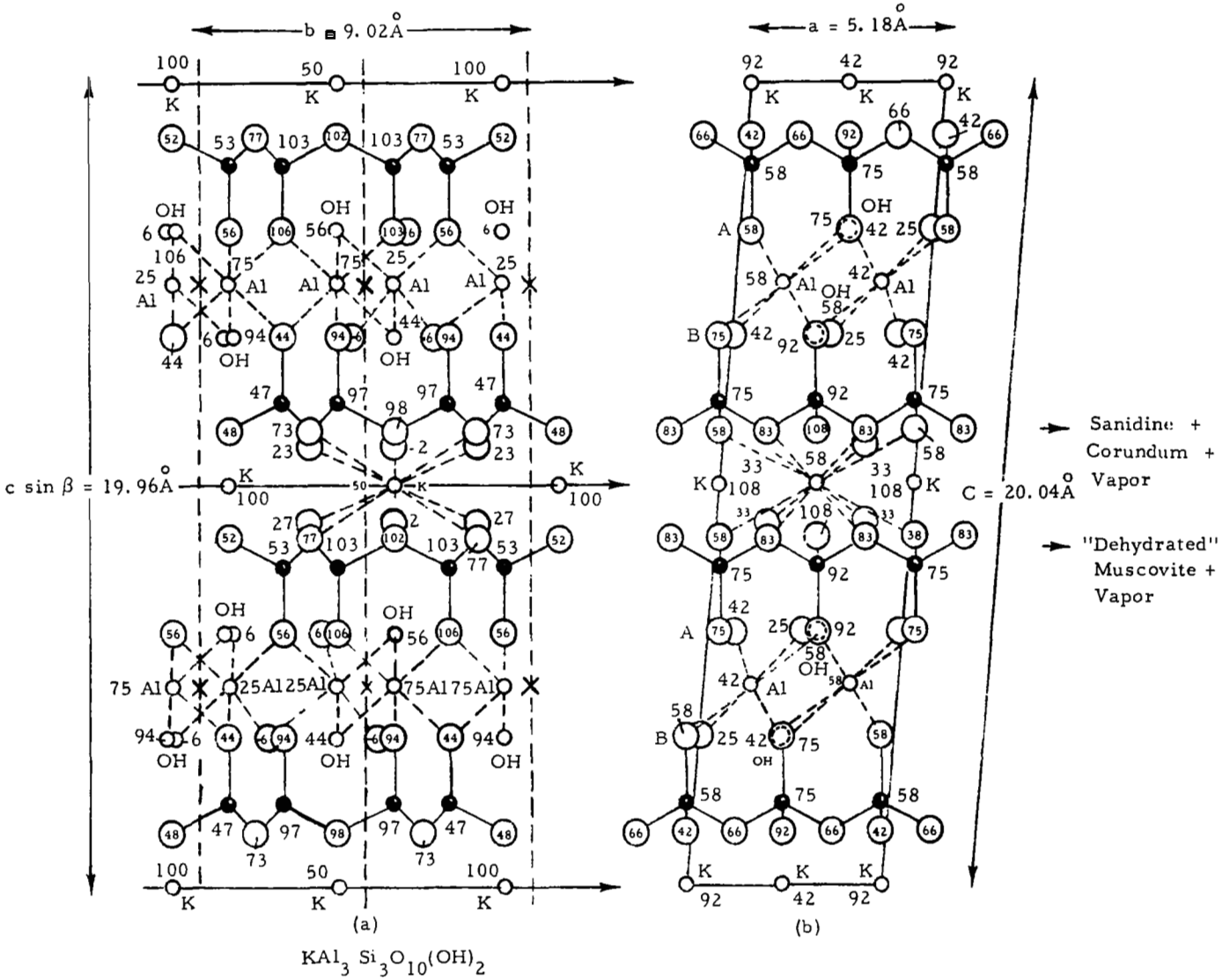

Figure 14-9 The Structure of Muscovite

The reaction muscovite → sanidine + corundum + vapor has been extensively studied under hydrothermal conditions. However, other than numerous vacuum DTA investigations, no low-pressure studies have been undertaken on this mineral. The following enthalpy equations for muscovite, "dehydrated" muscovite, sanidine, corundum, and water vapor are available from the literature:

Muscovite: Pankratz, 1964

$$H_T^o - H_{298}^o = 97.56T + 13.19 \times 10^{-3}T^2 + 25.44 \times 10^5 T^{-1} - 38,793$$

(0.2%, 298° - 1000°K)

"Dehydrated" Muscovite: Prankratz, 1964

$$H_T^o - H_{298}^o = 89.05T + 9.90 \times 10^{-3}T^2 + 24.14 \times 10^5 T^{-1} - 35,527$$

(0.1%, 298° - 1200°K)

Sanidine: Kelley, 1960

$$H_T^o - H_{298}^o = 63.83T + 6.45 \times 10^{-3}T^2 + 17.05 \times 10^5 T^{-1} - 25,323$$

(0.4%, 298° - 1400°K)

Corundum: Kelley, 1960

$$H_T^o - H_{298}^o = 27.49T + 1.41 \times 10^{-3}T^2 + 8.38 \times 10^5 T^{-1} - 11,131$$

(0.5%, 298° - 1800°K)

Water: Kelley, 1960

$$H_T^o - H_{298}^o = 7.30T + 1.23 \times 10^{-3}T - 2,285$$

(10.5%, 298° - 2500°K)

These can be used to evaluate the low-pressure equilibrium curves for the reactions:

$$KAl_3Si_3O_{10}(OH)_2 \rightarrow KAl_2Si_3O_8 + Al_2O_3 + H_2O$$

muscovite sanidine corundum water

$$KAl_3Si_3O_{10}(OH)_2 \rightarrow KAl_3Si_3O_{11} + H_2O$$

muscovite dehydrated muscovite water

Considering the reaction muscovite → sanidine + corundum + vapor, the ΔH of reaction can be calculated employing the relation $\Delta H^{\circ}_{T,\,R} = \Delta H^{\circ}_{T}$ products - ΔH°_{T}, reactants:

$$\Delta H^{\circ}_{T,\,R} = \Delta H^{\circ}_{298} + 1.06T - 4.10 \times 10^{-3}T^{2} - 0.01 \times 10^{5}T^{-1} + 51. \qquad (14\text{-}1)$$

To evaluate this equation, a value for the enthalpy of the reaction at $298^{\circ}K$ and one atmosphere is needed. This quantity can be calculated from the following enthalpies of formation ($298^{\circ}K$) from the oxides:

$KAl_3Si_3O_{10}(OH)_2$	$\Delta H^{\circ}_{298} = -55.85$ Kcal/mole	Barany 1964
$KAl_2Si_3O_8$	$H^{\circ}_{298} = -56.40$ Kcal/mole	Kracek, 1963
Al_2O_3	$H^{\circ}_{298} = 0$ Kcal/mole	
H_2O	$H^{\circ}_{(evap)} = 10.5$ Kcal/mole	Kelley, 1949
	$\Delta H^{\circ}_{298} = 9.95$ Kcal/mole	

However, it is well known that heats of formation obtained from heats of solution are not too reliable. Therefore, an alternative method will be used to check this value.

Yoder and Eugster (1955) give two values for the enthalpy of reaction at 963°K and 1500 bars, 14.2 Kcal/mole and 31.6 Kcal/mole, calculated using two different methods. They consider the first value to be the more reliable.

Substituting the value of $\Delta H^{o}_{298} = 9950$ calories into Equation 14-1 results in an equation of the form:

$$\Delta H^{o}_{T} = 1.06T - 4.10 \times 10^{-3} T^{2} - 0.01 \times 10^{5} T^{-1} + 10,001. \qquad (14\text{-}2)$$

It is now possible, using this equation, to calculate a ΔH^{o}_{963}, which is the change of enthalpy of the reaction as a function of temperature ($\Delta H^{o}_{963} = 7,221$ calories). Assuming the change of enthalpy due to the solid phases is negligible, the change of enthalpy due to the nonideality of water vapor at the pressure cited by Yoder and Eugster (1955) can now be calculated by means of the function

$$\left(\frac{\partial H}{\partial p}\right)_{T} = V - T\left(\frac{\partial V}{\partial p}\right)_{p}$$

and Kennedy's tables (1950) for the pressure-volume-temperature relations for water at elevated temperatures and pressures ($\Delta H^{1-1500}_{298} = 3205$ calories). By adding these two quantities (H^{o}_{963} and H^{1-1500}_{298}), a theoretical value for the enthalpy of reaction at 963°K and 1500 atmospheres is obtained.

$$\Delta H^{1-1500}_{963} = \Delta H^{o}_{963} + \Delta H^{1-1500}_{298}$$

$$\Delta H^{1-1500}_{963} = 7221 + 3205 = +10,426$$

This value, although approximately four Kcal lower than the value offered by Yoder and Eugster (1955), is quite reasonable and tends to confirm the probability of Yoder and Eugster's value of 31.6 Kcal being erroneous. Because of errors involved in both the calculations undertaken by the author and in the analysis of Yoder and Eugster (1955), it seems only reasonable to adopt a value which is an average of the two. This value is $\Delta H^{1-1500}_{963} = 12,313$ calories.

It is now possible to obtain a probably more reliable value for the ΔH^{o}_{298} of reaction than can be calculated from heats of solution. If

1/2 (14,200 - 10,426 calories) is added to the 7221 calories originally obtained from Equation 14-2 for ΔH^{o}_{963}, a new value of ΔH^{o}_{963} = 9108 calories is obtained. Substitution of this value for ΔH^{o}_{T}, and C for 10,001 in Equation 14-2, and solving for C results in the new equation:

$$\Delta H^{o}_{T} = 1.06T - 4.10 \times 10^{-3}T^{2} - 0.01 \times 10^{5}T^{-1} + 11,888. \quad (14\text{-}3)$$

With the aid of this equation and the Clausius-Clapeyron equation, the equilibrium pressure of water at any given temperature for the reaction muscovite → sanidine + corundum + vapor can be determined.

$$\frac{dP}{dT} = \frac{\Delta H^{o}_{T}}{T\Delta V}$$

Assuming water behaves like an ideal gas in the temperature and pressure range under study, and that the change in volume of the solid phases can be neglected, an equation of the following form is obtained:

$$\frac{dP}{P} = \frac{\Delta H^{o}_{T}}{RT^{2}}.$$

Substituting Equation 14-3 into the Clausius-Clapeyron equation and integrating results in the equation:

$$\log P = 1/R \left[1.06 \log T - 4.10 \times 10^{-3}T + 0.005 \times 10^{5}T^{-2} - 11,888T^{-1} \right] + C.$$

Due to the lack of experimental stability data at low pressures, it is necessary to evaluate the constant of integration from the high pressure-high temperature data of Yoder and Eugster, 1955 (918°K and 680 bars). The use of these values introduces error because of the nonideality of water at this pressure.

$$\log P = 1/R \left[1.06 \log T - 4.10 \times 10^{-3}T + 0.005 \times 10^{5}T^{-2} - 11,888T^{-1} \right] + 9.61 \quad (14\text{-}4)$$

This is the vapor pressure equation for the reaction muscovite → sanidine + corundum + vapor.

A similar thermodynamic analysis may be carried out for the reaction muscovite → "dehydrated" muscovite + H_2O. Coventional manipulation of the enthalpy equations again leads to an equation expressing the enthalpy of reaction as a function of temperature:

$$\Delta H^{o}_{T} = \Delta H^{o}_{298} - 1.21T - 2.06 \times 10^{-3}T^{2} - 1.30 \times 10^{5}T^{-1} + 980. \quad (14\text{-}5)$$

However, there are no literature values available for the ΔH^{o}_{298} of this reaction. Consequently, it becomes necessary to evaluate this quantity in an indirect manner.

The area under a peak on a DTA curve is proportional to the enthalpy of the corresponding reaction at that temperature. Thus, it is possible to calculate the ΔH^{o}_{T} for the dehydration of muscovite provided the DTA record contains both a peak for the dehydration and a peak for the complete structural breakdown of muscovite. Norin (1941) gives several DTA curves of muscovite, with the peak corresponding to the loss of OH^{-} at 1123°K and the peak corresponding to the breakdown of the structure at 1373°K. Unfortunately, it is not possible to determine the manner in which the enthalpies of the two reactions change with respect to one another. This restriction can best be met by utilizing a temperature midway between the two peaks (1248°K) in the following analysis. It is believed that only a small amount of error is introduced in this manner.

Employing Equation 14-3 and a temperature of 1248°K results in a value for ΔH^{o}_{1248} = 6827 calories for the reaction muscovite → sanidine + corundum + vapor. An analysis of the area under the two peaks shows that 68.8% of the total area is accounted for by the peak corresponding to the reaction muscovite → "dehydrated" muscovite + water. Therefore, the ΔH^{o}_{1248} for this reaction is (0.688) (6827 calories) or 4697 calories. Substituting this quantity into Equation 14-5 results in a value of ΔH^{o}_{298} = 8538 calories and the equation:

$$\Delta H^{o}_{T} = -1.21T - 2.06 \times 10^{-3}T^{2} - 1.30 \times 10^{5}T^{-1} + 9518. \quad (14\text{-}6)$$

Performing mathematical manipulations identical to those used in the analysis of the reaction leads to the equation:

$$\text{Log } P = 1/R \left[-1.21 \log T - 2.06 \times 10^{-3}T + 0.65 \times 10^{5}T^{-2} - 9518T^{-1} \right] + C.$$

The constant C can be evaluated from the data of Roy (1949). Roy reports two experimental temperatures at which he notes a loss of water (573°K and 723°K at one atmosphere). At 723°K, the muscovite sample lost water continuously for several hundred hours and showed marked structural expansion in the c-axis direction. At 573°K, the sample lost only a small amount of water in the first 10 hr of heating, indicating that only adsorbed water was being lost. Therefore, the true equilibrium curve for the "dehydration" may lie somewhere between the two curves calculated from these data:

723°K:

$$\log P = 1/R \left[-1.21 \log T - 2.06 \times 10^{-3} T + 0.65 \times 10^{5} T^{-2} - 9518 T^{-1} \right] + 7.28 \qquad (14\text{-}7)$$

573°K:

$$\log P = 1/R \left[-1.21 \log T - 2.06 \times 10^{-3} T + 0.65 \times 10^{5} T^{-2} - 9518 T^{-1} \right] + 8.77 \qquad (14\text{-}8)$$

The intersection of the stability curve for muscovite → sanidine + corundum + vapor with those for the reaction muscovite → "dehydrated" muscovite + water indicates that above (to higher pressure) the intersection, the equilibrium reaction is that forming sanidine, corundum, and vapor with dehydrated muscovite occurring metastably, and that below the intersection the reverse is true.

The decomposition of muscovite was not observed in the mass spectrometer; consequently, no datum is available.

A thermodynamic analysis of the reaction "dehydrated" muscovite → sanidine + corundum will not be undertaken in this report due to the theoretical difficulties involved. An equation for the ΔH°_{T} of reaction could be calculated, but the calculation of a pressure-temperature equation would be difficult because the relationship expressing the volume change for the reaction would not be a simple integrable function like the ideal gas law. Furthermore, there is not enough thermal expansion data available for such

a series of calculations. However, for most solid-solid reactions, the reaction temperature is little affected by the pressure. So, for the reaction "dehydrated" muscovite → sanidine + corundum, the stability curve can probably be closely approximated by an isothermal curve drawn through the intersection of the stability curves for the reactions: muscovite → sanidine + corundum + vapor, and muscovite → "dehydrated" muscovite + vapor. This construction can be seen in Figure 14-10.

The extrapolation of the muscovite data to the lunar environment gives:

muscovite → sanidine + corundum + vapor

Lunar Temperature	$T^{\circ}C$	$T^{\circ}K$	P_{H_2O} mm of Hg
Minimum nighttime	-180	93	2.7×10^{-51}
Equilibrium at 1-m depth	- 55	218	5.6×10^{-15}
Maximum daytime	+130	403	1.4×10^{-2}
At lunar pressure	- 28	245	1.0×10^{-11}

muscovite → "dehydrated" muscovite + vapor

Lunar Temperature	$T^{\circ}C$	$T^{\circ}K$	P_{H_2O} mm of Hg	
			Eq. 14-7	Eq. 14-8
Minimum nighttime	-180	93	3.1×10^{-39}	9.5×10^{-38}
Equilibrium at 1-m depth	- 55	218	1.4×10^{-13}	5.6×10^{-12}
Maximum daytime	+130	403	1.6×10^{-4}	7.0×10^{-3}

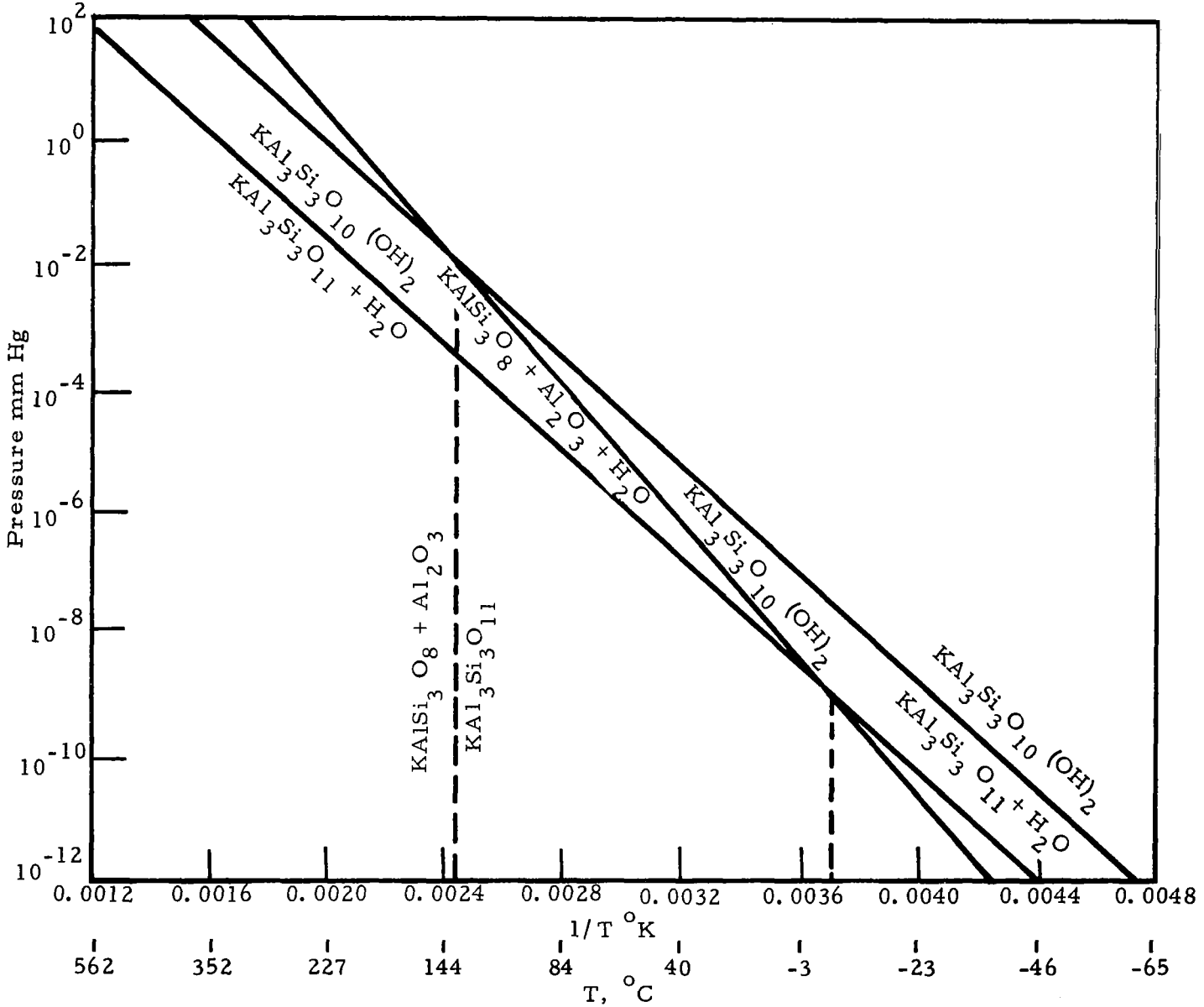

Figure 14-10 Stability Curves of Muscovite

At lunar pressure (1×10^{-11} mm of Hg)

	$T^{\circ}C$	$T^{\circ}K$
Equation 14-7	+35	238
Equation 14-8	+52	221

"dehydrated" muscovite → sanidine + corundum

At lunar pressure (1×10^{-11} mm of Hg)

	$T^{\circ}C$	$T^{\circ}K$
Equations 14-7 and 14-4	+128	401
Equations 14-8 and 14-4	- 3	270

The tabulation of the reaction characteristics in the lunar environment indicates that muscovite should completely decompose to sanidine + corundum + vapor during the lunar day but be stable at a depth of 1 m. Reconstitution of muscovite from sanidine, corundum, and vapor during the lunar night is very unlikely because of the extreme sluggishness of the reaction even at pressures of several hundred bars and temperatures of several hundred degrees.

SECTION 15

NATROLITE

15.1 FORMULA

$Na_2Al_2Si_3O_{10} \cdot 2H_2O$.

15.2 MINERAL CLASSIFICATION AND VOLATILE

Silicate, zeolite—H_2O.

15.3 SPECIMEN LOCALITY

Springfield Butte, Lane County, Oregon.

15.4 PROCUREMENT SOURCE

Ward's Natural Science Establishment, Inc., Rochester, New York.

15.5 OPTICAL MICROSCOPIC ANALYSIS

The natrolite was received from Ward's in two separate shipments with certification that both originated from the same locality. The first consists of radial aggregates of coarse cream-colored and somewhat rusty looking natrolite attached to an altered porphyritic basic rock. The practically square prisms are length slow with $\gamma = 1.490$.

Although the amount of iron oxide stain on the first batch is negligible, a second batch of natrolite specimens, similar in nature but without rust stain, was obtained from Ward's. The latter crystals appear snow white. Nevertheless, a large amount of scolecite, a zeolite similar to natrolite, is intermixed with these coarse crystals. The scolecite consists of fine fibers and is length fast. The angle $\alpha \wedge C = 18^{\circ}$.

It should be noted that the thin section (Figure 15-1) is composed of a specimen from the second batch. Although analcite, another closely associated zeolite, is a major constituent in both batches, it is readily separated from the natrolite and scolecite during sample preparation.

15.6 THERMAL ANALYSES

15.6.1 Differential Thermal Anslysis

See Figure 15-2.

15.6.1.1 Sensitivity

The sensitivity is 10 μv/cm.

15.6.1.2 Peak values

These are:

400°C(-)

435°C(-)

525°C(-)

The DTA curve depicts a gradual endothermic drift, with two shallow peaks, culminating in a major sharp endothermic peak at 400°C, followed by minor endothermic peaks at 435°C and 525°C. The heating process was terminated at 720°C to avoid melting the sample.

15.6.2 Thermogravimetric Analysis

The TGA curve (Figure 15-3) follows the DTA very closely to 400°C. Above this temperature, the loss of weight levels off but continues gradually to almost 720°C. The total weight loss amounts to 11.25% of the sample weight as compared to the ideal loss calculated at 9.5%.

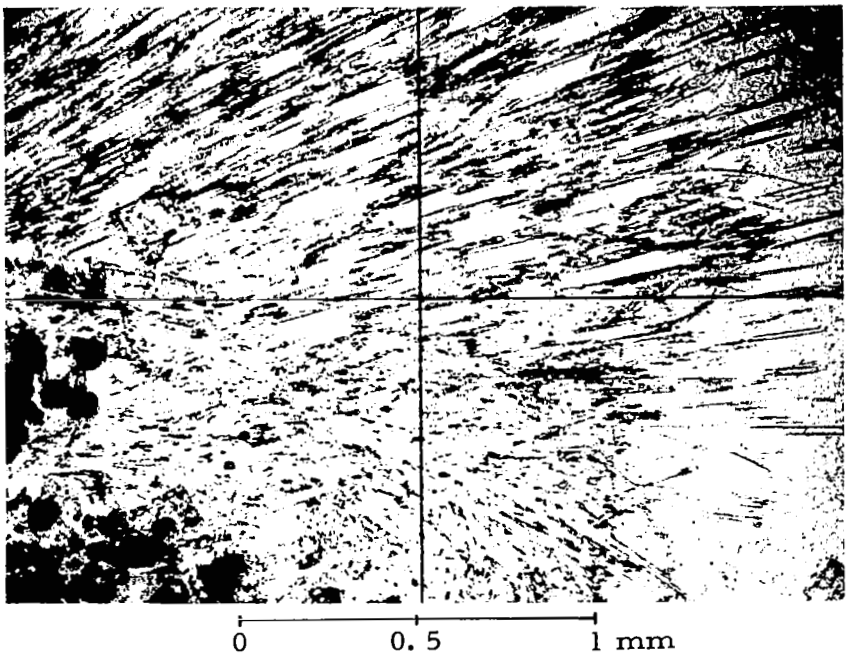

Figure 15-1 Photomicrograph of Natrolite, 47X, Coarse Needles of Natrolite and Fine Needles of Scolecite in Central Area, Analcite in Clear Right Area, Wall Rock in Lower Left Quadrant

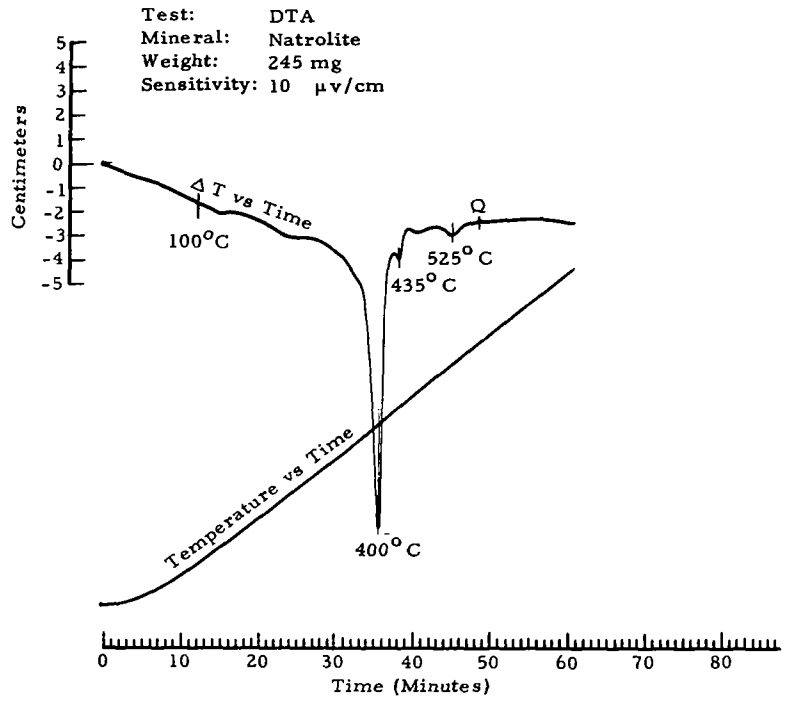

Figure 15-2 Natrolite DTA

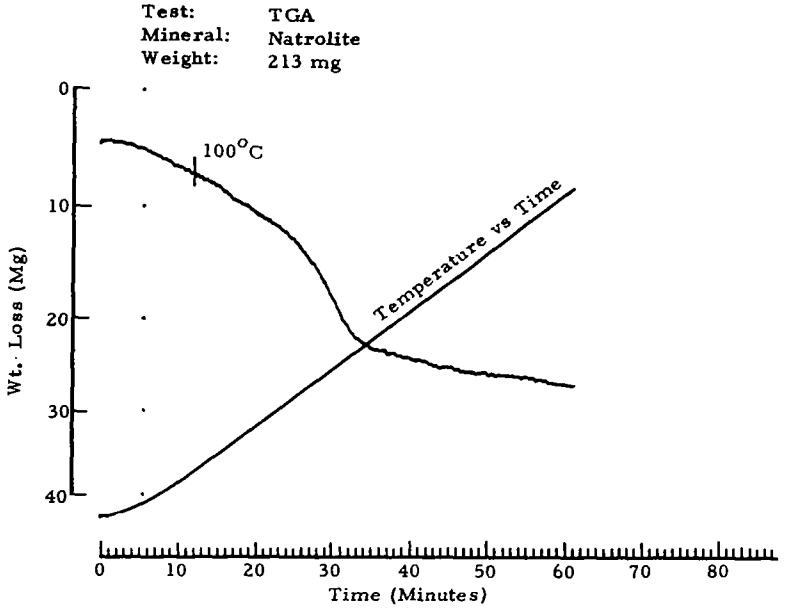

Figure 15-3 Natrolite TGA

15.6.3 Mass Spectrometer Analysis

The specimen dehydrates in the mass spectrometer at 40°C. The curve (Figure 15-4) shows a single sharp peak followed by a very small but continuous water loss. In comparison, the DTA curve reveals a large initial endothermic drift, culminating in a sharp endothermic peak at 400°C. This endothermic drift reflects the initial loss of water, either structural or absorbed. It is not evident in the mass spectrometer, since immediate volatilization in vacuum is probably responsible for the initial water loss.

15.7 X-RAY DIFFRACTION PATTERNS

15.7.1 Debye-Scherrer Standard

The natrolite pattern (Figure 15-5) discloses contamination by a second phase. Most of the lines are readily indexable with the ASTM natrolite d-values (Table 15-1), with remaining lines belonging to scolecite. This is typical of zeolites, which yield very complex powder patterns containing considerable overlap of lines of different phases. The pattern confirms the microscopic examination of the specimen. However, on the basis of relative intensities of the natrolite and scolecite lines, there is relatively little scolecite present.

TABLE 15-1

COMPARISON OF EXPERIMENTAL AND ASTM D-VALUES FOR NATROLITE

Exp (Å)	ASTM (Å)	Exp (Å)	ASTM (Å)	Exp (Å)	ASTM (Å)	Exp (Å)	ASTM (Å)
6.5	6.6	2.57	2.57	1.75	1.75	1.33	1.33
6.0	5.9	2.45	2.43	1.72	1.72	1.30	1.31
4.1	4.13	2.33	2.32	1.62	1.62	1.23	1.24
4.4	4.38	2.25	2.26	1.57	1.53	1.21	1.22
4.7	4.63	2.19	2.18	1.54	1.52 (Scolecite)	1.19	1.19
3.55	3.63 (Scolecite)	2.05	2.05	1.47	1.46	1.14	1.14
3.2	3.16	1.95	1.95	1.44	1.43 (Scolecite)	1.09	1.08
2.95	2.94	1.87	1.87	1.42	1.42	1.06	1.06
2.85	2.86	1.80	1.80	1.38	1.38	1.02	1.02
2.65	2.68						

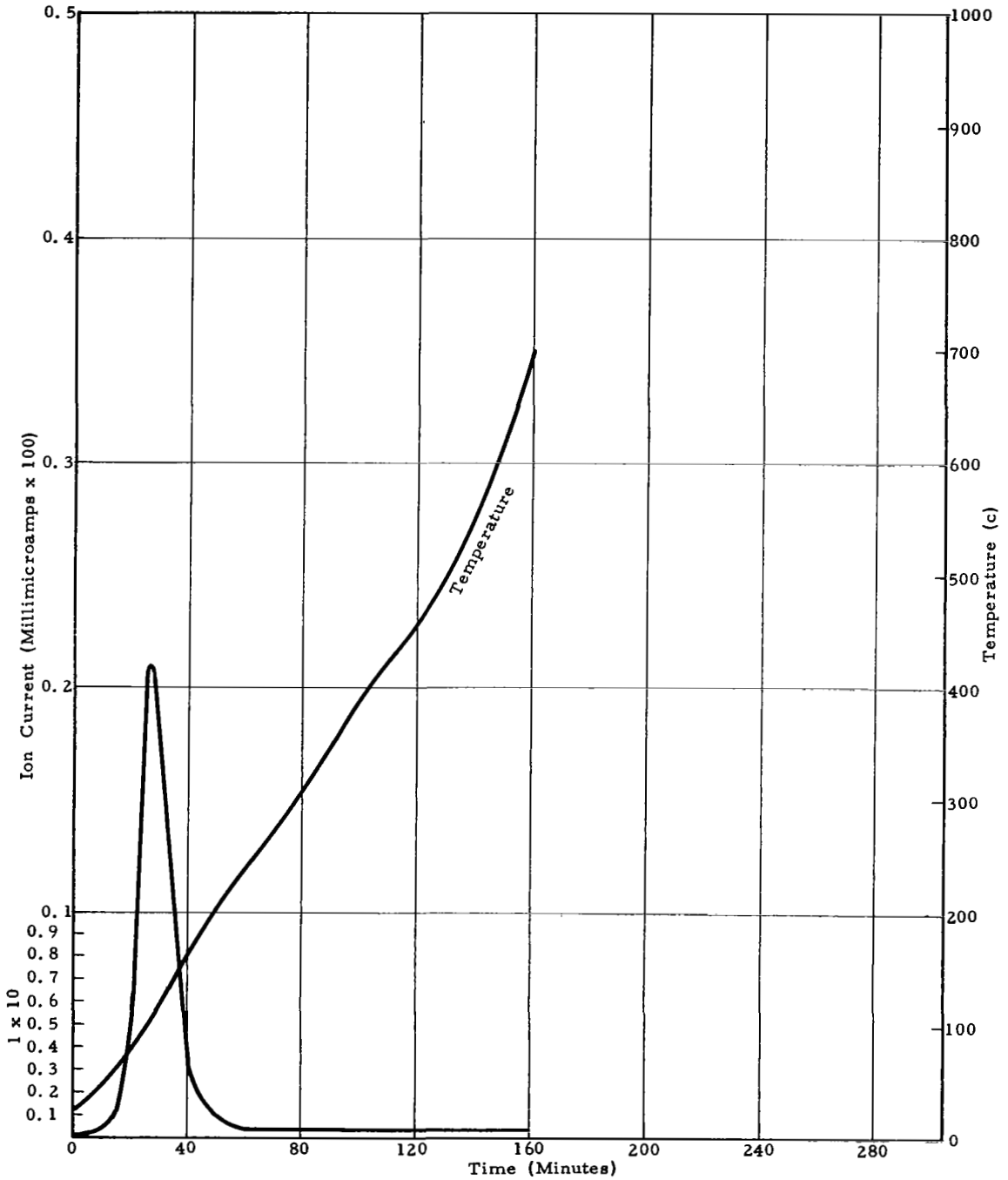

Figure 15-4 Mass Spectrometer Curve of Natrolite—H_2O Peak

15.7.2 Bendix Vacuum Camera Standard

Figure 15-6 shows the natrolite X-ray pattern taken with the Bendix Vacuum Camera (magnification 2X).

The somewhat spotty character of the diffraction lines is due to a preponderance of particle sizes not much smaller than the sieve opening of the 300-mesh screen used for all phases. Plagioclase, NH_4-feldspar, and actionlite, in addition to the natrolite, all gave this result. These are the hardest and most brittle of the phases studied, and this is obviously attributable to their similar breakage properties.

TABLE 15-2

COMPARISON OF OBSERVED D-VALUES AND RELATIVE INTENSITY MEASUREMENTS FOR NATROLITE

Debye-Scherrer Standard, CuK_α		Bendix Camera Standard, CuK_α	
d_{obs}	$\frac{i}{i_o}$	d_{obs}	$\frac{i}{i_o}$
4.1	70	3.9	50
3.55	70	3.7	50
3.20	20	3.1	20
2.85	80	2.8	90
2.57	100	2.6	100
2.19	20	2.1	20
1.91	40	1.9	30
1.80	30	1.8	10
1.57	20	1.6	30
1.42	10	1.4	10
1.38	10	1.37	5
1.31	10	1.3	5

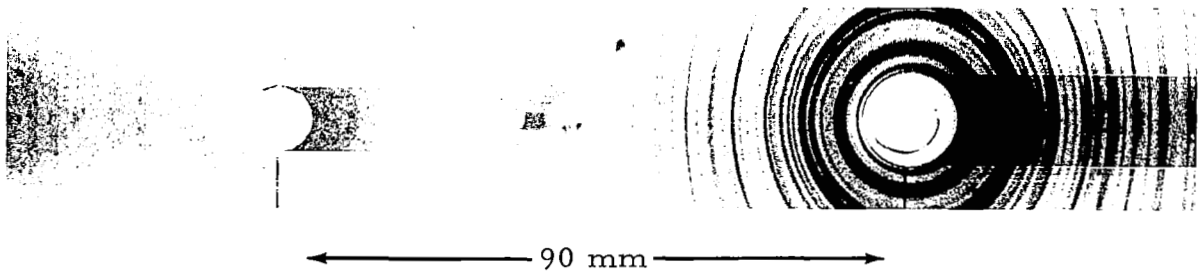

Figure 15-5 Natrolite X-Ray Pattern Taken With Debye-Scherrer Camera

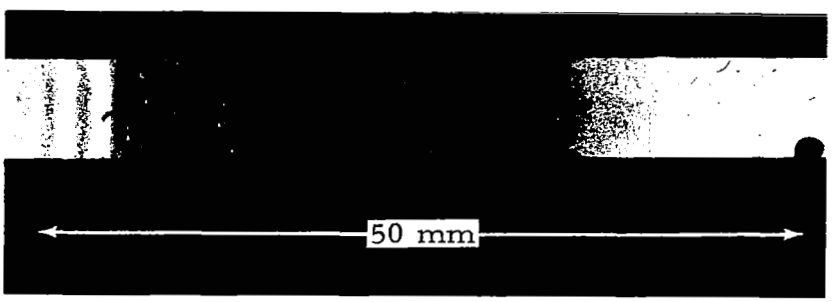

Figure 15-6 Natrolite X-Ray Pattern Taken With Bendix Vacuum Camera (Magnification 2X)

15.7.3 Vacuum Patterns

All patterns of natrolite taken at all temperatures and ultrahigh vacuum were duplicates of the standard, and in no cases could dehydration be observed from the X-ray patterns. The loss of zeolitic water from natrolite only very slightly alters the integrity of the tekosilicate framework, however, and changes in the diffraction pattern are relatively slight. The similarity in patterns was perfect enough to conclude that contrary to expectation, loss of water did not occur. Specimen packing may partially explain this result, however. This mineral was therefore included in Phase II.

15.7.4 Bendix Vacuum Standard, Phase II

This pattern was a duplicate of the standard obtained in Phase I.

15.7.5 Vacuum Patterns, Phase II

As in Phase I, all patterns were duplicates with no indication of change. This result is unexpected as noted above. The possibility cannot be discounted that so little change occurs during loss of zeolitic water that it cannot be detected.

15.8 ANALYSIS OF THERMODYNAMIC AND CRYSTAL STRUCTURE DATA

Natrolite ($Na_2Al_2Si_3O_{10} \cdot 2H_2O$) is a member of a group of minerals called zeolites. The zeolite-type structures consist of an open, wide-meshed (Si, Al)O_4 framework with the Si and the Al tetrahedra firmly held together by rigid bonds. The cavities and channels within the tetrahedral framework contain the water molecules and the cations which satisfy the negative charge of the framework. These openings are sufficiently large to permit the exchange of the cations and loss of the water of hydration without a significant structural change.

In natrolite (see Figure 15-7), the water molecules and Na^+ ions form a series of double columns which are parallel to the c-axis and pass through the channel formed by the chains of tetrahedra. The Na^+ ions occupy alternate cavities in the double columns with the others remaining vacant. Each Na atom is coordinated by six oxygen atoms, four of which are from Si-Al tetrahedra, and two of which are from the water molecules. Each water molecule, in addition to being linked to two Na atoms, is also hydrogen bonded to two oxygen atoms, one from each type of tetrahedra.

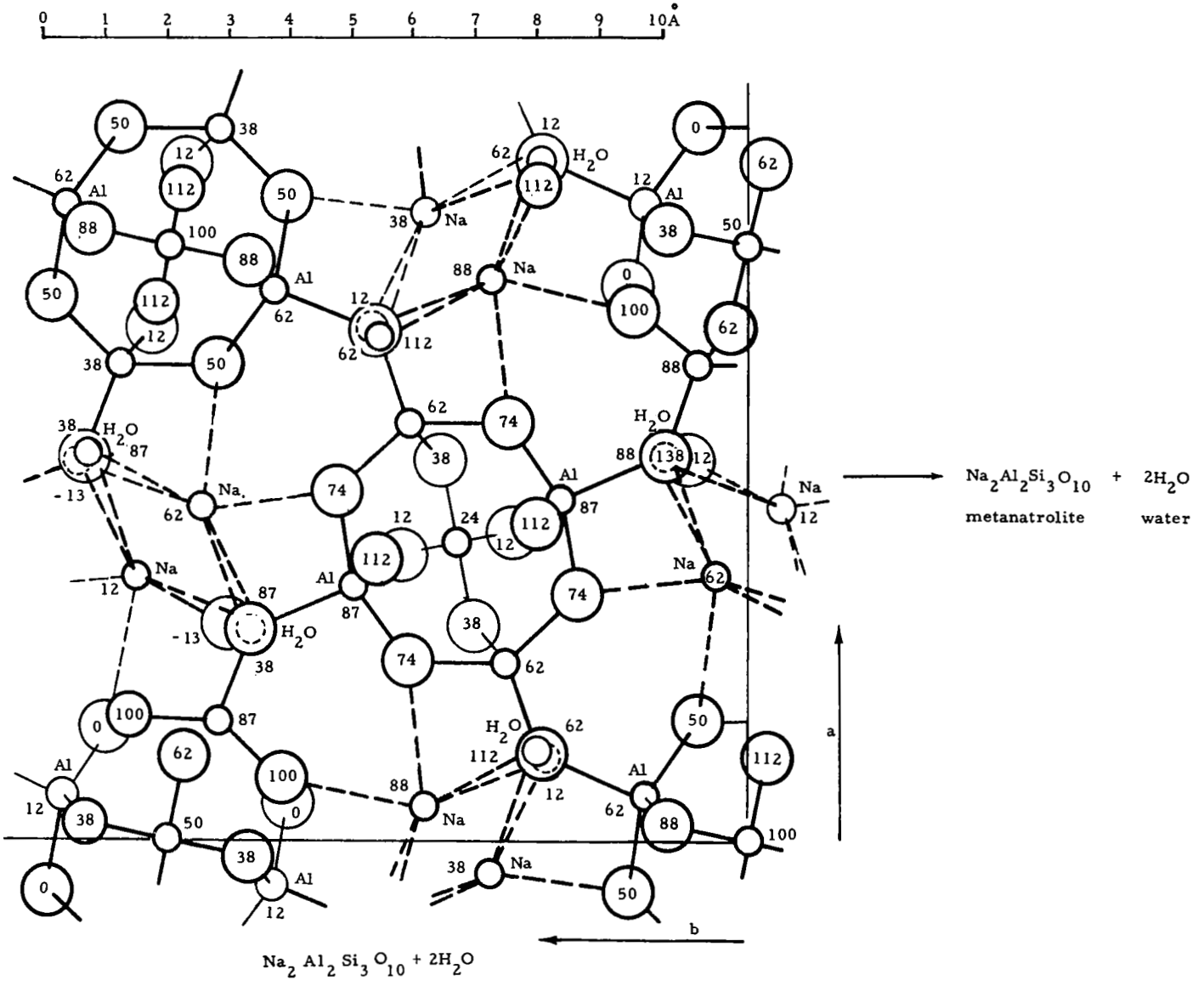

Figure 15-7 The Structure of Natrolite

There are two types of linkages which hold the tetrahedral groups together to form the natrolite chain structure. Each group consists of three SiO_4 tetrahedra and two AlO_4 tetrahedra. The first type consists of the sharing of two oxygen atoms by neighboring groups to form the chain parallel to the fiber direction. The second is the weak single oxygen linkage which holds neighboring chains together. The hydration of natrolite causes a disruption of this linkage and a serious disturbance in the local charge balance. The loss of water molecules causes the Na ions to migrate to the oxygen atom of the tetrahedra to which the water molecules were previously bound. This redistribution of charge causes a distortion of the chains and a shrinkage of the unit cell dimensions (10.7% in the a-axis and 8.3% in the b-axis). The resulting compound, metanatrolite, is monoclinic.

$$\underset{\text{Natrolite}}{Na_2Al_2Si_3O_{10}} \quad 2H_2O \rightarrow \underset{\text{Metanatrolite}}{Na_2Al_2Si_3O_{10}} + 2H_2O \quad (g)$$

Given sufficient water vapor, metanatrolite readily rehydrates to form natrolite.

From the data of Hey (1932), the stability boundary of natrolite (see Figure 15-8) may be roughly approximated. Hey determined the vapor pressure of natrolite in the temperature range 20 - 225°C with the aid of very unsophisticated instrumentation. However, this is the only information available on the stability of natrolite, other than the one temperature of dehydration determined by Fang (1963). The DTA and mass spectrometer data (see Figure 15-8) for the dehydration of natrolite are tabulated as follows:

	H_{H_2O} mm of Hg	T°C
DTA	12.5	289 ± 20
Mass Spectrometer	5×10^{-6}	40 ± 5

A curve representing these data is plotted in Figure 15-8.

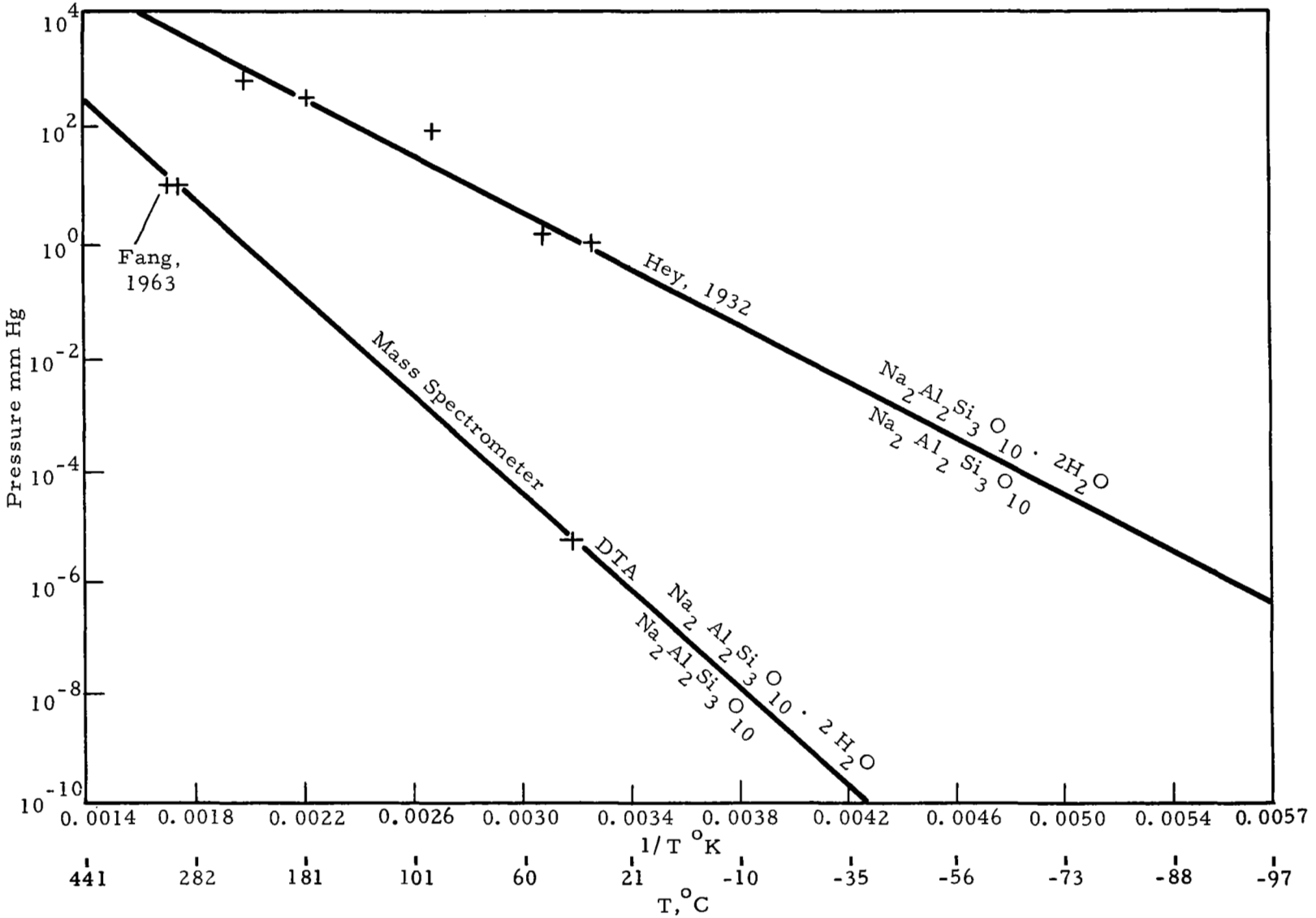

Figure 15-8 Stability Curve of Natrolite

The stability of natrolite in the lunar environment is as follows:

Lunar Temperature	$T^{\circ}C$	$T^{\circ}K$	P_{H_2O} mm of Hg
Minimum nighttime	-180	93	3.5×10^{-18}
Equilibrium at 1-m depth	-55	218	4.5×10^{-4}
Maximum daytime	+130	403	1.8×10^{-3}
At lunar pressure	-141	132	1.0×10^{-11}

The above data indicate that if equilibrium is established under conditions of lunar pressure and temperature, natrolite will dehydrate during the lunar day and also will not exist in a stable phase at the equilibrium temperature associated with a depth of 1 m. Metanatrolite readily rehydrates when exposed to water vapor. However, rehydration of metanatrolite during the lunar night is improbable, because at $-180^{\circ}C$ the vapor pressure of natrolite is greater than the sublimation pressure of ice (5.2×10^{-19} mm of Hg).

SECTION 16

TALC

16.1 FORMULA

$Mg_3 Si_4 O_{10} (OH)_2$.

16.2 MINERAL CLASSIFICATION AND VOLATILE

Silicate, mica group—(OH).

16.3 SPECIMEN LOCALITY

New Fane, Vermont.

16.4 PROCUREMENT SOURCE

The University of Michigan Mineralogical Museum.

16.5 OPTICAL MICROSCOPIC ANALYSIS

The talc specimen has a characteristic foliated massive structure. Examination of the thin section (Figure 16-1) reveals that there is no intermixture of tremolite, chlorite, or carbonates. However, some black opaque material, probably magnetite, comprises a fraction of 1%. The talc is optically negative, colorless in thin sections, shows low relief in Canada balsam, and has a measured axial angle of zero.

16.6 THERMAL ANALYSES

16.6.1 Differential Thermal Analysis

See Figure 16-2.

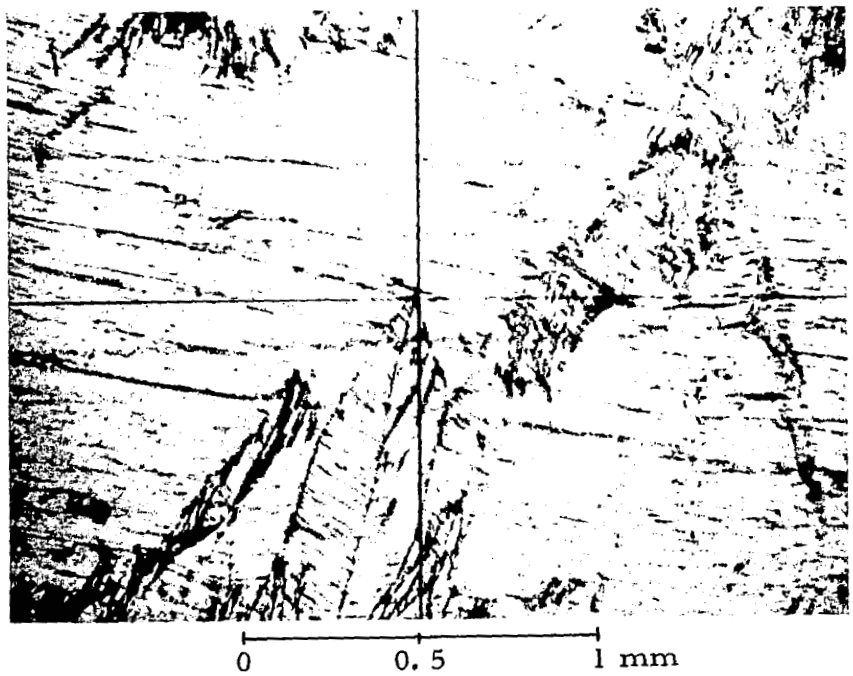

Figure 16-1 Photomicrograph of Talc, 47X

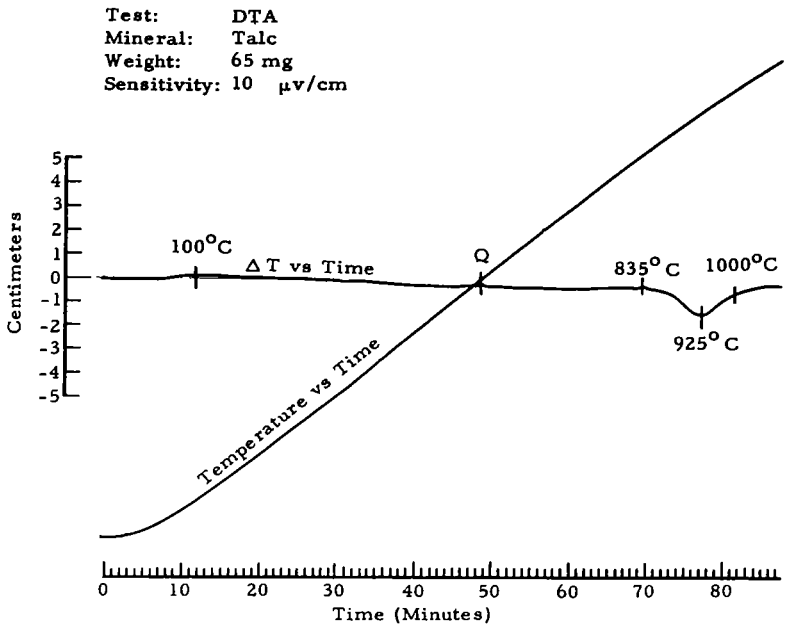

Figure 16-2 Talc DTA

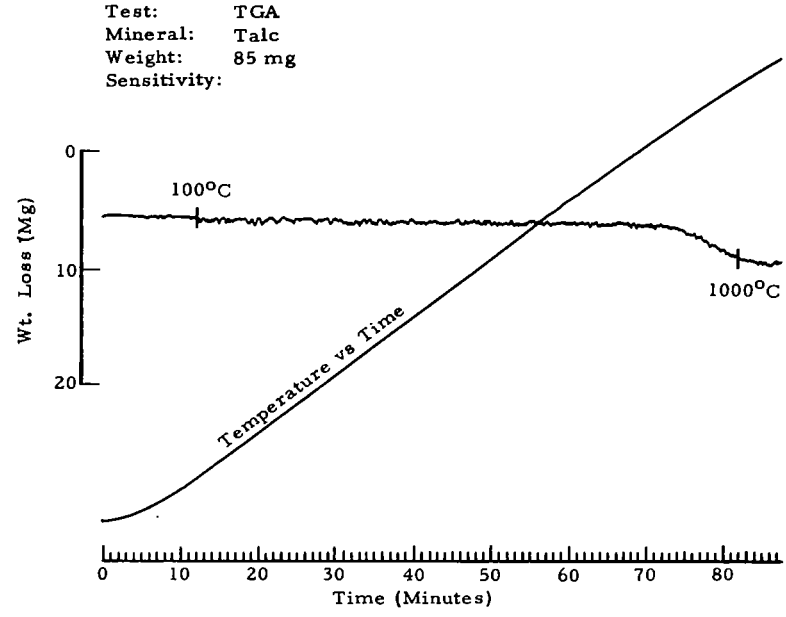

Figure 16-3 Talc TGA

16.6.1.1 Sensitivity

The sensitivity is 10 μv/cm.

16.6.1.2 Peak Values

These are:

835°C (+) Very small, probably tremolite

925°C (-) Loss of OH.

16.6.2 Thermogravimetric Analysis

The TGA curve (Figure 16-3) follows the DTA very closely and indicates a total weight loss of 5.3%. It compares favorably with the theoretical weight loss of 4.8%.

16.6.3 Mass Spectrometer Analysis

The mass spectrometer curve (Figure 16-4) shows a very small but continuous loss of absorbed water with the loss of OH taking place at 579°C. This reaction corresponds to the slight endothermic drift, culminating in an endothermic peak at 925°C, on the DTA curve.

16.7 X-RAY DIFFRACTION PATTERNS

16.7.1 Debye-Scherrer Standard

Figure 16-5 shows the talc X-ray pattern taken with the Debye-Scherrer camera.

There is generally excellent agreement between the Debye-Scherrer standard photograph and ASTM values (Table 16-1).

16.7.2 Bendix Vacuum Camera Standard

Figure 16-6 shows the talc X-ray pattern taken with the Bendix Vacuum Camera (magnification 2X).

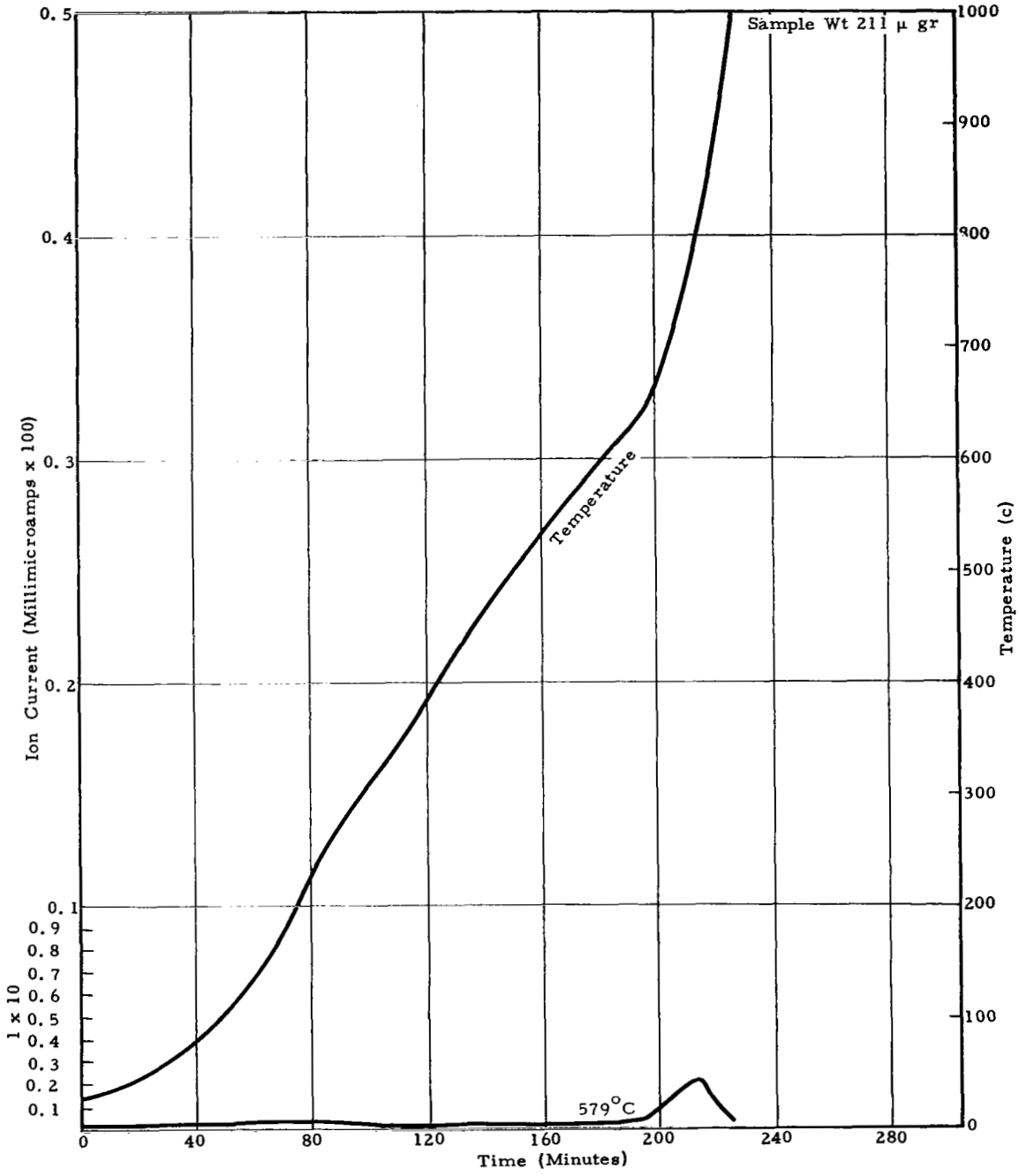

Figure 16-4 Mass Spectrometer Curve for Talc—H_2O Peak Plotted

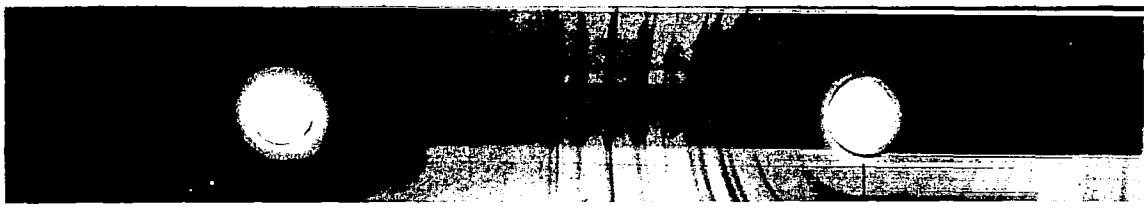

Figure 16-5 Talc X-Ray Pattern Taken With Debye-Scherrer Camera

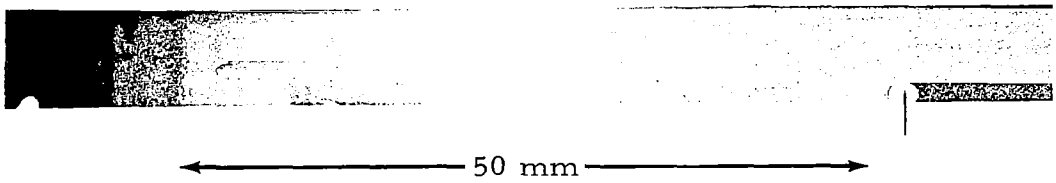

Figure 16-6 Talc X-Ray Pattern Taken With Bendix Vacuum Camera (Magnification 2X)

TABLE 16-1

COMPARISON OF EXPERIMENTAL AND ASTM D-VALUES FOR TALC

Exp (Å)	ASTM (Å)	Exp (Å)	ASTM (Å)
9.3	9.34	1.72	1.725
4.7	4.66	1.67	1.682
3.1	3.116	1.52	1.527
2.6	2.629	1.39	1.394
2.45	2.476	1.33	1.336
2.2	2.212	1.31	1.318
2.08	2.10	1.29	1.297
1.85	1.870	1.27	1.269

The agreement between values from the Debye-Scherrer standard and the Bendix camera standard (Table 16-2) is particularly good. The differences in d-values for the first line are due to the inaccuracy inherent in measuring low-theta lines.

16.7.3 Vacuum Patterns

All diffraction patterns obtained under the conditions of Phase I precisely duplicated that of the standard. Since the loss of hydroxyl ion should result in major structural changes (see Section 16.8) which would be readily evident on diffraction photographs, no devolatilization is indicated. In Section 16.8, data are presented to show that even if equilibrium were attained, devolatilization is unlikely. Therefore, this mineral was not included in Phase II.

TABLE 16-2

COMPARISON OF OBSERVED D-VALUES AND RELATIVE INTENSITY MEASUREMENTS FOR TALC

Debye-Scherrer Standard CuK_α		Bendix Camera Standard CuK_α	
d_{obs}	$\frac{i}{i_o}$	d_{obs}	$\frac{i}{i_o}$
4.7	20	4.4	30
3.1	50	2.9	60
2.45	50	2.5	20
2.20	100	2.3	100
2.08	30	2.1	20
1.85	30	1.9	10
1.72	10	1.7	2
1.52	20	1.5	10
1.39	50	1.4	50

16.8 ANALYSES OF THERMODYNAMIC AND CRYSTAL STRUCTURE DATA

Talc is a sheet silicate. It is quite similar to the micas in that it has a layered structure composed of tri-octahedral sheets sandwiched between two sheets of SiO_4 tetrahedra with none of the octahedral sites left vacant (see Figure 16-7). The full complement of Mg^{+2} ions in the octahedral sites leaves the composite sheets electrically neutral. Consequently, the composite sheets are held together by only weak Van der Waals forces. The composition of the SiO_4 sheets is Si_2O_5. The tetrahedra point inward with each apical oxygen coordinated to two Mg^{+2} ions and one OH^- group. The OH^- groups lie at the center of hexagonal rings of apical oxygens. The stacking of successive layers is similar to that of mica. The hexagonal rings of SiO_4 tetrahedra lie directly above one another, allowing many different stacking sequences based on the rotation of successive layers. This gives rise to many polymorphic forms and stacking disorder in the crystal structure.

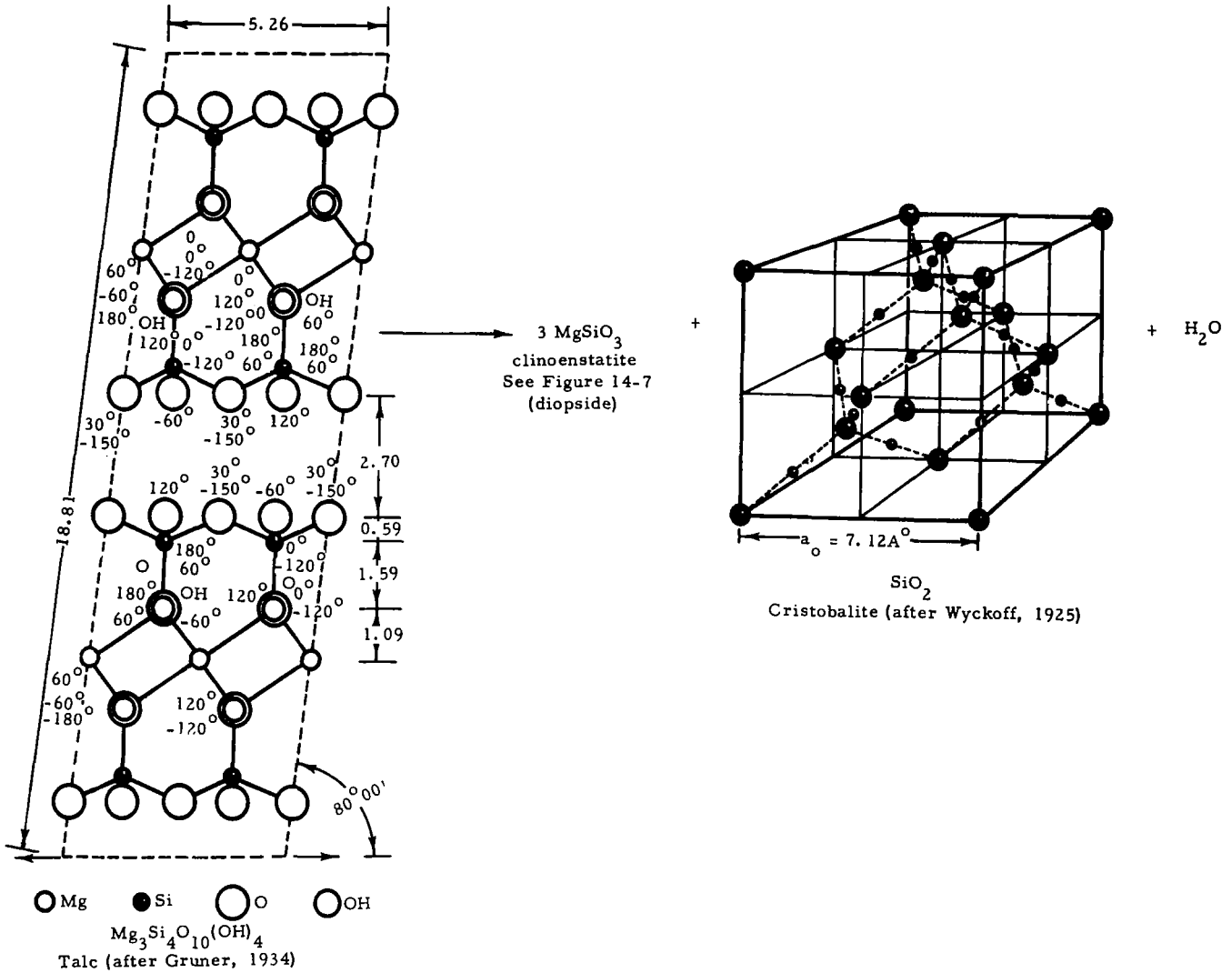

Figure 16-7 The Structures of Talc and Cristobalite

Talc shows very little variation in composition. Occasionally, small amounts of Ti or Al may substitute for Si, and small amounts of Fe or Al may substitute for Mg.

Upon heating, talc ultimately breaks down to clinoenstatite, cristobalite, and water vapor. Several investigators (Thilo, 1937; Eitel and Kedesday, 1943; Foster, 1951; and Atlas, 1952) have reported the formation of an intermediate phase which has been called meta-talc or protoenstatite. X-ray investigations have shown that this intermediate compound is one of the polymorphic forms of $MgSiO_3$. However, in this study emphasis will be placed on the reaction:

$$Mg_3Si_4O_{10}(OH)_4 \longrightarrow 3\,MgSiO_3 + SiO_2 + H_2O$$

Talc — Clinoenstatite Cristobalite

Clinoenstatite is one of the three polymorphic forms (enstatite, clinoenstatite, and protoenstatite) of $MgSiO_3$. Clinoenstatite does not occur in terrestrial rocks. Foster (1951) and Atlas (1952) have suggested that it is a metastable low-temperature form, while Morimoto (1959) believes it is a metastable high-temperature form. The structure of clinoenstatite is similar to that of diopside. However, there are some differences in the details of the pyroxene chain structure. The presence of Mg^{+2} ions requires 6-fold coordination instead of the 8-fold coordination of the Ca^{+2} ions in diopside. This difference of cation coordination results in both a shift of position and a change in shape of the chains. The shift consists of a displacement parallel to the chain length. The change in shape is caused by a rotation of the SiO_4 tetrahedra around an axis passing through the Si atom and the O atom coordinated to the Mg^{+2} ion.

The structure of cristobalite is based upon sheets of 6-membered rings of SiO_4 tetrahedra (see Figure 16-7). Ideally, the structure is cubic. However, this is not possible because it requires extremely small Si-O bond distances. Therefore cristobalite has what appears to be a tetragonal structure with successive sheets linked by Si-O-Si bonds perpendicular to (001) and with the basal oxygen atoms of successive sheets rotated 60°. This structure as compared to that of quartz is quite open and can easily accommodate foreign ions.

There are sufficient thermodynamic data available to permit calculation of the stability relation for the reactions:

$$Mg_3Si_4O_{10}(OH)_2 \rightarrow 3\,MgSiO_3 + SiO_2 + H_2O\,(g)$$

The following are the heat capacity equations and the heats of formations at 298°K for the reactants and the products:

	Cp	
$Mg_3Si_4O_{10}(OH)_2$	$84.58 + 41.68 \times 10^{-3}T - 17.96 \times 10^{5}T^{-2}$	Robie and Stout, 1963
$MgSiO_3$	$20.59 + 12.00 \times 10^{-3}T - 4.06 \times 10^{5}T^{-2}$	Kelly, 1960
SiO_2(Cristobalite)	$4.28 + 21.06 \times 10^{-3}T$	Kelly, 1960
H_2O(g)	$7.38 + 2.46 \times 10^{-3}T$	Kelly, 1960

	ΔHfm (298°K)	
$Mg_3Si_4O_{10}(OH)_2$	-43,600 ± 1500 cal/mole	Robie, 1963
$MgSiO_3$	8,690 ± 150 cal/mole	Torgeson and Sahama, 1948
SiO_2(Cristobalite)	0 cal/mole	
H_2O(g)	10,767 cal/mole	Rossini, 1952

The application of the differential form, $\frac{d(\Delta H)}{dT} = \Delta Cp$, leads to the equations:

$$d(\Delta H^\circ) = (-11.23 + 17.84 \times 10^{-3}T + 5.78 \times 10^{5}\,T^{-2})\,dT$$

$$\Delta H_T^\circ = \Delta H_o^\circ - 11.23\,T + 8.92 \times 10^{-3}T^2 - 5.78 \times 10^{5}T^{-1}$$

where ΔH_o° is the constant of integration. Evaluating ΔH_o° from $\Delta H_T^\circ = \Delta H_{298}^{\circ\,\circ} = 45,677$ (Robie, 1963), the equation

$$\Delta H_T^\circ = +50,188 - 11.23T \times 8.92 \times 10^{-3}T^2 - 5.78 \times 10^{5}T^{-1}$$

is obtained.

With a knowledge of the enthalpy of reaction as a function of temperature and the Clausius-Clapeyron equation, it is possible to calculate the vapor pressure (H_2O) of talc at any temperature:

$$\frac{dP}{dT} = \frac{\Delta H_T^{\circ}}{T \Delta V}.$$

Assuming that water vapor acts as an ideal gas in the temperature and pressure range under study and neglecting the volume of the solid phases, an equation of the form

$$\frac{dP}{P} = \frac{\Delta H_T^{\circ}}{RT^2}$$

is obtained.

Substituting the equation for the enthalpy of reaction and integrating results in the equation:

$$\text{Log } P = \frac{1}{R}\left[-50,188T^{-1} - 11.23 \log T + 8.92 \times 10^{-3}T + 2.89 \times 10^{5}T^{-2}\right] + C.$$

From the data of Robie, 1964, (P_{H_2O} = 15.2 mm of Hg at 600°C), the constant C can be evaluated

$$\log P = \frac{1}{R}\left[-50,188T^{-1} - 11.23 \log T + 8.92 \times 10^{-3}T + 2.89 \times 10^{5}T^{-2}\right] + 38.22.$$

A graphical representation of this equation is shown in Figure 16-8. This equation is valid for the temperature range 300 - 800°K. However, based on a discrepancy between the experimental values and calculated values, there is a 5% uncertainty at 200°K and a 10% uncertainty at 100°K. Therefore, there may be a significant amount of error in applying these data to the lowest lunar temperatures.

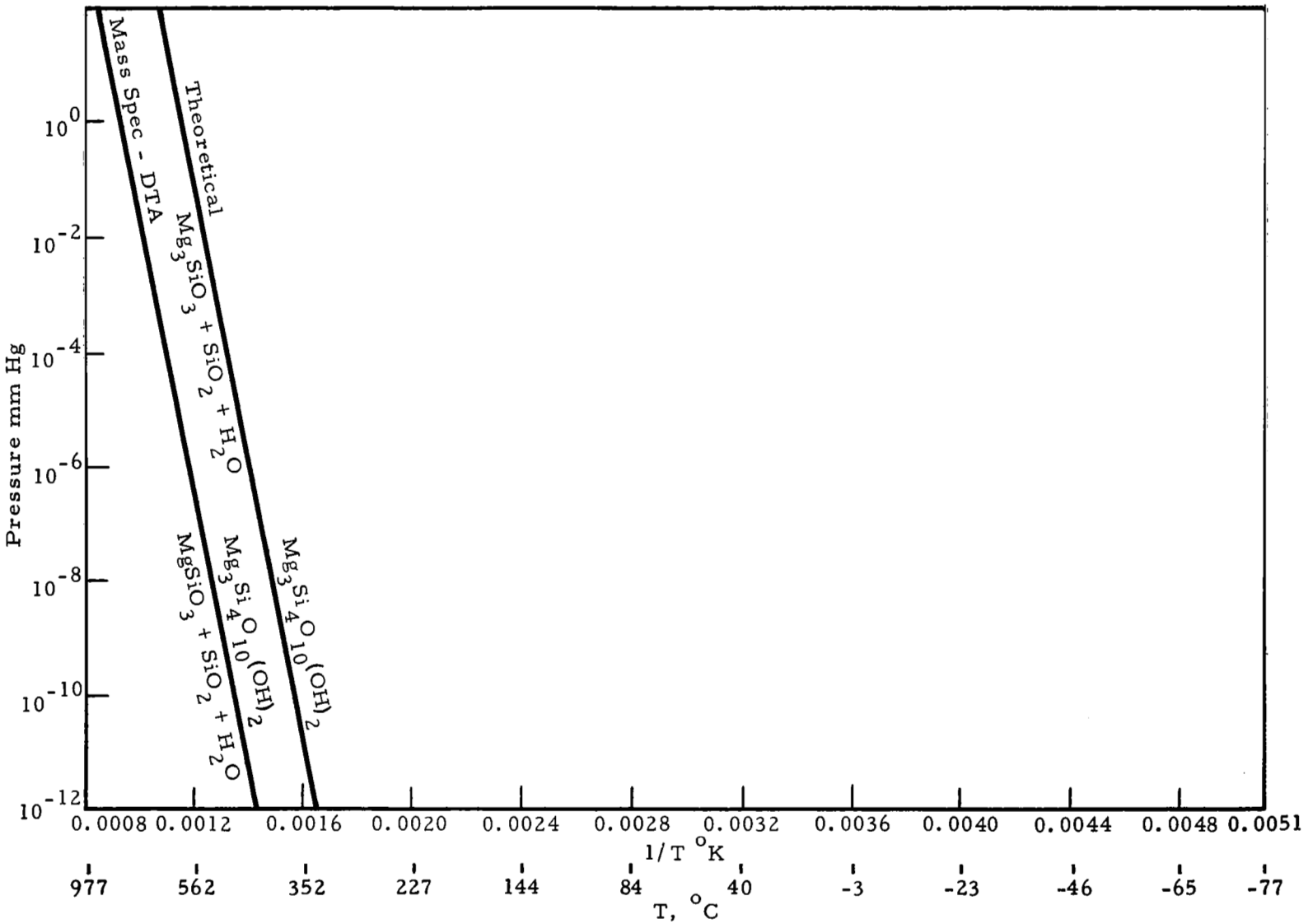

Figure 16-8 Stability Curves of Talc

The breakdown curve constructed from the following DTA and mass spectrometer data is also shown in Figure 16-8:

$$Mg_3Si_4O_{10}(OH)_2 \text{ - - - } 3MgSiO_3 + SiO_2 + H_2O(g)$$

	P_{H_2O} mm of Hg	T^oC
DTA	12.5	835 ± 20
Mass Spectrometer	5×10^{-6}	579 ± 5

Extrapolation of the previously calculated stability equation to the lunar environment gives:

Lunar Temperature	T^oC	T^oK	P_{H_2O} mm of Hg
Minimum nighttime	-180	93	1.3×10^{-235}
Equilibrium at 1-m depth	-55	218	1.3×10^{-87}
Maximum daytime	+130	403	1.0×10^{-34}
At lunar pressure	+351	624	1.0×10^{-11}

These data indicate that talc should be stable in the lunar environment.

SECTION 17

TEKTITE

17.1 FORMULA

17.2 MINERAL CLASSIFICATION AND VOLATILE

Silica glass - none.

17.3 SPECIMEN LOCALITY

Thailand.

17.4 PROCUREMENT SOURCE

Ward's Natural Science Establishment, Inc., Rochester, New York.

17.5 MICROSCOPIC ANALYSIS

The tektite specimen, var. Indochinite, presents a homogeneous glassy appearance except for small, blocky, optically isotropic inclusions which are probably lechatelierite (silica glass). In addition, a few dust-like particles are randomly distributed throughout the tektite glass (Figure 17-1). The latter's index of refraction measures 1.495. It should also be noted that the specimen does not have a flow structure.

17.6 THERMAL ANALYSES

17.6.1 Differential Thermal Analysis

See Figure 17-2.

17.6.1.1 Sensitivity

5 μv/cm.

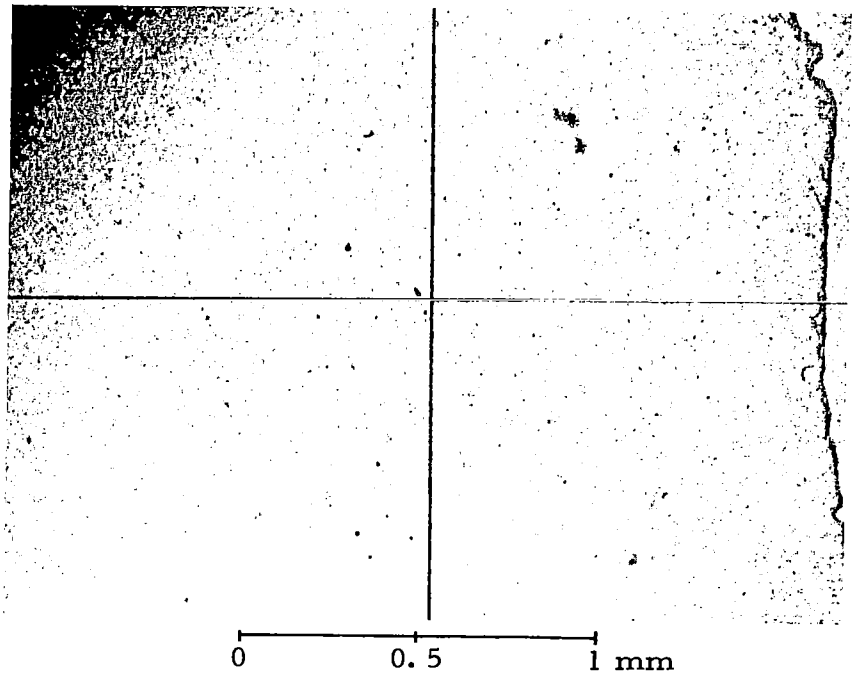

Figure 17-1 Photomicrograph of Tektite, 47X

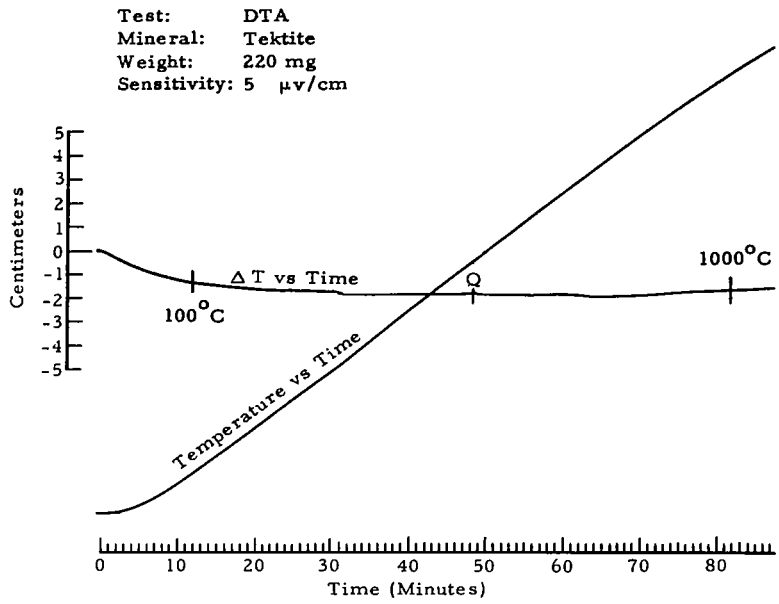

Figure 17-2 Tektite DTA

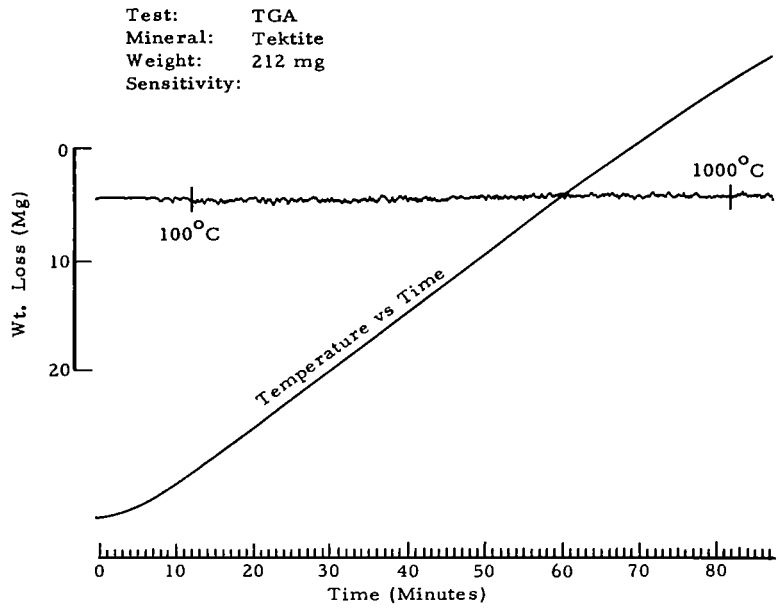

Figure 17-3 Tektite TGA

17.6.1.2 Peak values

None.

The DTA curve depicts only a small endothermic drift.

17.6.2 Thermogravimetric Analysis

No evidence of any weight loss is apparent in the TGA curve (Figure 17-3), even though the sample had been heated to a maximum temperature of 1050°C.

17.6.3 Mass Spectrometer Analysis

No changes are depicted on the mass spectrometer curve (Figure 17-4) except for the loss of some adsorbed water. This water loss is estimated at less than 1% and corresponds to the slight endothermic drift of the DTA curve.

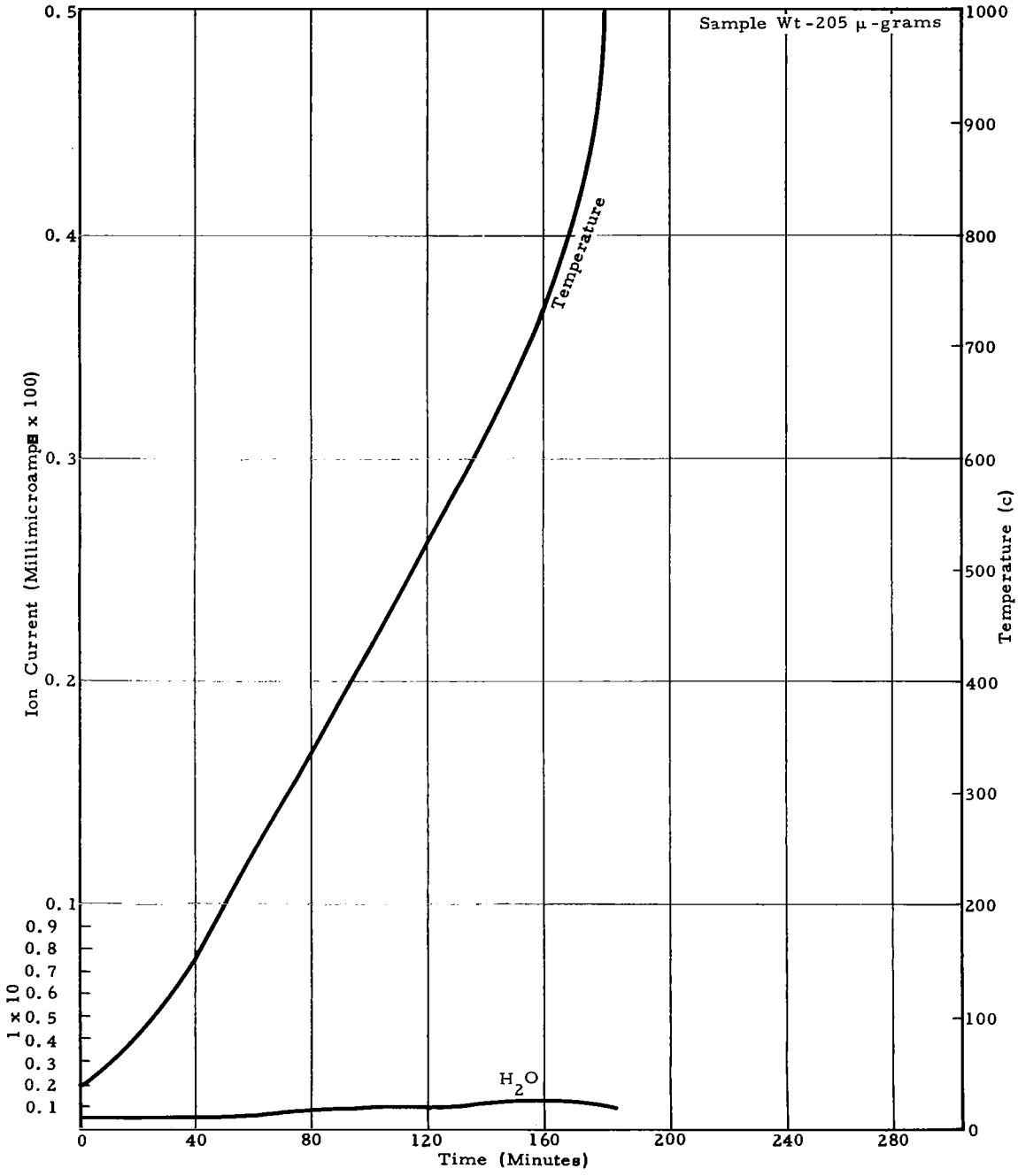

Figure 17-4 Mass Spectrometer Curve of Tektite—H_2O Peak Plotted

17.7 X-RAY DIFFRACTION PATTERNS

17.7.1 Debye-Scherrer Standard

The tektite pattern (Figure 17-5) shows no lines whatsoever, confirming its noncrystalline nature.

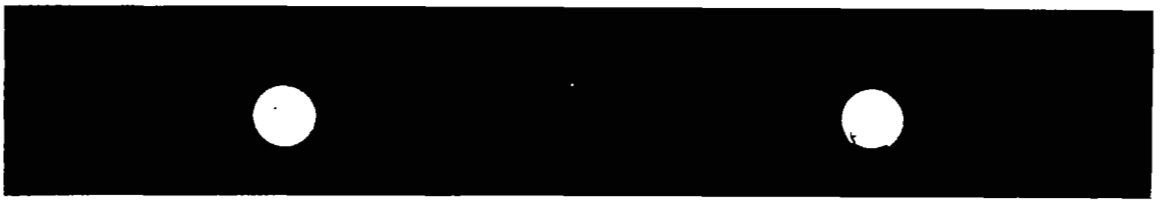

90 mm

Figure 17-5 Tektite X-Ray Pattern Taken With Debye-Scherrer Camera

17.7.2 Vacuum Patterns

All photographs, including that of the Bendix camera standard, showed no diffraction lines or even broad diffraction maxima, which are indicative of increasing long-range order in glasses as a function of time and annealing temperature. This material was therefore not included in Phase II.

17.8 ANALYSIS OF THERMODYNAMIC AND CRYSTAL STRUCTURE DATA

No analysis is included here since the nonequilibrium glass ordering process cannot be adequately and simply treated.

SECTION 18

SUMMARY AND CONCLUSIONS

18.1 TEST MINERALS

The mineral samples used in this research study were carefully chosen to represent those classes of materials most likely to undergo change in the lunar environment. These included a carbonate (calcite) which is known to decompose with the loss of CO_2, common rock-forming silicates containing volatile hydroxyl ion (e. g. , talc, muscovite), a compound with water of hydration (gypsum), a mineral with zeolitic water (natrolite), a clay mineral (montmorillonite) with interlayer water known to be easily lost or gained reversibly, a feldspar containing volatile NH_4, and an oxide with hydrogen-bonding (goethite). In addition to these phases, all of which are known to lose a volatile at high temperature or low pressure, basalt glass, a tektite, and a neutron-irradiated plagioclase were studied to determine the possible changes in disordered structures in the lunar environment. Hematite (Fe_2O_3), which is known not to undergo structural or compositional changes, was also studied.

18.2 EXPERIMENTS

The properties of the samples used were all carefully documented, and in particular, optical microscopic, DTA, TGA, and time-of-flight (TOF) mass spectrometer studies were made to determine compositional changes at elevated temperatures. Together, this research determines the composition and amount of transformation products. Since these experiments were performed with continuously changing temperature the pressure-temperature relations for decomposition are not equilibrium values. The decomposition temperatures at a given pressure are known to lag in these experiments up to a hundred degrees beyond the equilibrium values.

18.3 STABILITY CURVES

As a part of this research program, the stability curves for transformations were determined as a function of pressure and temperature. Data for the formulation of these relations were obtained from an intensive literature search. In some cases, the available data were insufficient to make more than approximate extrapolations into the low-pressure range. In others where more than one transformation was possible or where nonequilibrium transformation occurred, only qualitative approximations were made. Nevertheless, the stability relations for all predictable transformations were documented. These relations are, of course, determined only for conditions of equilibrium. The mass spectrographic and DTA results gave good agreement with the stability curves, considering of course that the latter methods yield nonequilibrium values.

18.4 THEORETICAL VS. EXPERIMENTAL RESULTS

Of the phases studied, only hematite, basalt glass, and tektite could yield a volatile during transformation which might not be detected by X-ray diffraction of the sample before and after transformation. Of the remainder, only calcite and talc were not expected to transform under all lunar pressure-temperature conditions. Furthermore, muscovite and actinolite (both silicates containing hydroxyl ion in a close-packed anion framework) were found to have relatively high stability, and it is predicted that they would be stable at a depth of one meter.

Of the remaining minerals, stability data and other experimental results indicate that NH_4 feldspar, montmorillonite, and natrolite should readily devolatilize. However, if for some reason the vapor pressure of these volatiles should again exceed the vapor pressure of the volatiles in the equivalent "revolatilized mineral", the minerals would reversibly regain the volatiles. Insofar as the dehydration of goethite to hematite is concerned, the transformation should be irreversible, due to the major changes in structure involved. In the case of the two steps of dehydration of gypsum, the first step should be reversible (published data inconclusive, however), and the second, irreversible, again as a result of the major structural changes involved.

Under all simulated conditions of the lunar environment, only two minerals showed evidence of change. Goethite and gypsum transformed during both Phases I and II of the investigation. Moreover, gypsum, which loses its water of hydration in a 2-step process involving the formation of the intermediate hemihydrate form, transformed to the hemihydrate form ($CaSO_4 \cdot 1/2\ H_2O$). The transformed gypsum hemihydrate did not lose any more H_2O however, even though this should have occurred on the basis of determined stability relations.

Montmorillonite was expected to lose its interlayer water. Since the resulting change in structure is readily detected by X-ray diffraction, it was surprising to find no change under all test conditions. It is likely that in the case of montmorillonite, the dehydration could have been at least partially inhibited by crystallite packing. The lack of dehydration of montmorillonite is surprising in that its tendency to lose water is roughly equivalent to that of gypsum, which was shown to dehydrate during the pumpdown stage of the experiment well before the final vacuum condition was achieved. The dehydration of geothite and gypsum confirmed that the surface of each open-ended capillary mount was exposed to the required environmental conditions. In addition, the dehydration of these two phases was shown to be complete throughout the entire volume of the specimens following their removal from their mounts. Thus, the only explanation for the lack of water loss from montmorillonite would appear to be in that packing of the relatively plastic montmorillonite crystallites prevented the X-rayed portion of the sample (only about 1/4 in. from the exposed surface) from being exposed to the high vacuum. The relatively larger less deformable crystallites of gypsum and goethite did not exhibit this effect. This result is significant, then, in illustrating the importance of factors relating to the physical form of each phase, such as porosity and rock fabric, upon the occurrence of dehydration.

In the cases of natrolite and NH_4 feldspar, the devolatilization is difficult to detect by diffraction. This results from the fact that both phases are tektosilicates containing H_2O and NH_4, respectively, in large cavities in a three-dimensional aluminosilicate framework, which remains almost unchanged in geometry with devolatilization. This is particularly true at the reduced levels of resolution obtained with the Bendix vacuum camera. This degradation of resolution is attributed to the beryllium window, nonrotatability of samples, and other limiting factors related to the design experiment.

It is important to note that in no phase of this experiment could true equilibrium relations be established. A determination of equilibrium devolatilization relations involves, for any one phase, the measurement of the conditions of transformation over a range of variable pressures and temperatures, with verification through reversibility. Except in the most ideal cases, equilibrium is difficult to achieve at or near room temperature, because of the lack of thermal energy to activate changes. Fortunately, such experimental determination of equilibrium stability relations was unnecessary. As noted above, the equilibrium stability relations are readily determined either with thermochemical data or with transformation experiments at high temperatures, where reactions proceed at a measurable rate. Extrapolations may then be made into the lower pressures and/or lower temperature regions. Although such relations may be only approximate at this stage, they are entirely adequate for predicting relative stability.

If a volatile-containing phase exists metastably in the stability field of the dehydrated equivalents, then the rate of transformation depends on several factors, among them temperature, time, particle size, and particle packing. With respect to gypsum and goethite, we have shown that with the special physical conditions of this experiment, transformation occurred as predicted from equilibrium stability data. The lack of transformation of montmorillonite, for example, simply means that at least one of these variables acted to inhibit the transformation to the phase known to be the equilibrium one.

The transformation of goethite to hematite is an irreversible one, due to the difference in the crystal structures of these two phases. Thus, no change should occur in the spacecraft environment. However, the transformation of gypsum to the hemihydrate is known to be reversible as discussed in Section 11. Nevertheless, no rehydration occurred in the spacecraft environment. When the specimen was exposed to the atmosphere following its removal from the vacuum chamber, again no rehydration was noted. Mention should be made of the fact that the hemihydrate has recently been reported as occurring naturally. It is therefore not surprising that rehydration of the hemihydrate was not observed in the spacecraft environment. [1]

---

[1] R. J. Moila and E. D. Glover, "Recent Anhydrite From Clayton Playa, Nevada," J. Am. Min., Vol. 50, pp. 2063-2069, 1965.

18.5 CONCLUSIONS

It is significant from this experiment that despite the fact that only two minerals transformed, the change in environment from lunar to terrestrial, even over a short time interval, was sufficient to cause major changes in some phases. It should also be emphasized that with regard to minerals found at the lunar surface and in particular their equivalence to terrestrial phases, reliable results can be expected of the predictions made from stability data. Time, temperature extremes producing stress, high energy particles striking the surface, and other variables are ancillary environmental factors that might affect the mineral stability at the lunar surface. Nevertheless, the predicted equilibrium stability relations should be the overriding factor in determining the phase occurring on the lunar surface. In comparison, the physical conditions relating to such variables as compaction and their change with depth should be the determining factors for phases below the lunar surface.

SECTION 19

BIBLIOGRAPHY

1. Ames, L. L. and Sand, L. B., 1958, "Factors Effecting Maximum Hydrothermal Stability in Montmorillonites," Am. Min., V. 43, p. 6.

2. Andrusson, L., 1957, "Thermal Dissociation of Carbonates, Part III. Temperature Dependence and Method of True Exponents. Comparisons With Evaporation," Zeit. Physik. Chem., V. 208, p. 78.

3. Aruja, E., 1944, "An X-Ray Study of the Crystal Structure of Antigorite," Min. Mag., V. 27, p. 65.

4. Atlas, L., 1952, "The Polymorphism of $MgSiO_3$ and Solid State Equilibria in the System $MgSiO_3$-$CaMgSi_2O_6$," J. Geol., V. 60, p. 125.

5. Augustinik, A. I., Tandura, P. Z., and Sverckara, L. I., 1949, "Mechanism of Reactions in Talc During Heating," Zhur, Prikl. Khim., V. 22, p. 1150.

6. Babeleowsky, T. P. J. H. and Boerbomm, A. J. H., 1961, "Mass Spectrometric Study of CaOand Ta," Advanced Mass Spectrometry, V. 2, p. 135.

7. Backstrom, H. C., 1925 "The Thermodynamic Properties of Calcite and Aragonite," J. Am. Chem. Soc., V. 56, p. 340.

8. Barany, R., 1963, "Heats of Formation of Gehlenite and Talc," US Bur. Mines Rept. Investigation, #6251.

9. Barany, R., 1964, "Heat and Free Energy of Formation of Muscovite," US Bur. Mines Rept. Investigation, #6356.

10. Barany, R. and Kelley, K. K., 1961, "Heats and Free Energies of Formation of Gibbsite, Kaolinite, Halloysite, and Dickite," US Bur. Mines Rept. Investigation, #5825.

11. Barker, D. S., 1964, "Ammonium in Alkali Feldspars," Am. Min., V. 49, p. 851.

12. Barrer, R. M., 1956, "The Hydrothermal Chemistry of the Silicates, Part VII. Synthetic K-aluminosilicates," J. Am. Chem. Soc., V. 78, p. 2882.

13. Barth, T. F. W., 1932, "The Cristobalite Structure: I. High Christobalite, II. Low Cristobalite," Am. J. Sci., Ser. 5, V. 23, p. 350; V. 24, p. 97.

14. Barth, T. F. W., 1962, Theoretical Petrology, 2nd. ed., John Wiley and Sons, Inc., New York.

15. Bech, C. W., "Differential Thermal Analysis Curves of Carbonate Minerals," Am. Min., V. 35, p. 985.

16. Belyankin, D. S. and Donskaya, E. B., 1939, "Thermo-optical Investigation of Actionolite," Bull. Acad. Sci. U. S. S. R. Ser. Geol., #1, p. 95.

17. Bernal, J. D., Dasgupta, D. R., and Makay, A. L., 1959, "The Oxides and Hydroxides of Fe and Their Structural Inter-relationships," Clay Min. Bull, V. 4, p. 15.

18. Bichowksy and Rossini, 1936, Thermochemistry of the Chemical Substances, Reinhold Pub. Corporation, N. Y.

19. Birch, F., 1942, "Handbook of Physical Constants," Geol. Soc. Am., Spec. Paper #36.

20. Bite, K. and Matsui, M., 1933, "The Thermal Dissociation of Calcium Carbonate in the Atmosphere of Carbon Dioxide IV. The Thermal Change of Precipitated Calcium Carbonate," J. Soc. Chem. Ind. (Japan), V. 36, Supplemental binding, p. 1546.

21. Bos, H.G., 1956, "A Restricted Formulation of Le Chatelier's Principle," Chem. Weekblad, V. 52, p. 601.

22. Bowen, N. L. and Anderson, Olaf, 1914, "The System $MgO-SiO_2$," Am. J. Sci., V. 37, p. 487.

23. Bowen, N. L. and Grieg, J. W., 1924, "The System $Al_2O_3-SiO_2$," J. Am. Ceram. Soc., V. 2, pp. 238, 410.

24. Bowen, N. L., and Tuttle, O. F., 1949, "The System $MgO-SiO_2-H_2O$," Geol. Soc. Am. Bull., V. 60, p. 439.

25. Boyd, F. R., 1954, "Annual Report of the Director of the Geophysical Laboratory," Carnegie Inst. of Wash. Yearbook, #53, p. 109.

26. Boyd, F. R., 1959, "Hydrothermal Investigation of Amphiboles," Researches in Geochemistry, Wiley, N. Y.

27. Bragg, W. L., 1937, Atomic Structure of Minerals, Cornell Univ. Press, Ithaca, N. Y.

28. Bragg, W. L. and Brown, G. B., 1926, "Die Struktur des Olivins," Zeit. Krist., V. 63, p. 538.

29. Brandenburger, E., Epprecht, W., and Niggli, P., 1947, "Die Serpentin-Mineralen und ihre Synthese," Helv. Chim. Acta., V. 30, p. 9.

30. Brindley, G. W. and Zussman, J., 1957, "A Structural Study of the Thermal Transformation of Serpentine Minerals to Forsterite," Am. Min., V. 42, p. 461.

31. Carlson, E. T., Peppler, R. B., and Wells, A. S., 1953, "Studies in the System Magnesia-Silica-Water at Elevated Temperatures and Pressures," J. Research Natl. Bur. Stds., V. 51, #4, p. 179.

32. Deer, W.A., Howie, R.A., and Zussman, J., 1962, Rock Forming Minerals, V. 1-5, John Wiley and Sons, Inc., N.Y.

33. Droste, J.B. and Grim, R.E., 1959, "X-Ray Investigation Using an Autoclave for Conversion of Gypsum to the Hemihydrate," Am. Min., V. 44, p. 731.

34. Dushman, S., 1962, Scientific Foundations of Vacuum Technique, 2nd ed., John Wiley and Sons, Inc., N.Y.

35. Earley, J.W., Milne, I.H., and McVeagh, W.J., 1953, "Thermal Dehydration and X-Ray Studies on Montmorillonites," Am. Min. V. 38, p. 770.

36. Edelman, C.H. and Favejee, J.Ch.L., 1940, "On the Crystal Structure of Montmorillonite," Zeit, Krist., V. 102, p. 417.

37. Eitel, W., 1954, The Physical Chemistry of the Silicates, Univ. of Chicago Press, Chicago.

38. Eitel, W. and Kedesday, H., 1943, "Die Metaphase der Entwasserung des Talks," Abh. Preuss Akad. Wiss. #5, p. 21.

39. Erd, R.C., White, D.E., Fahey, J.J., and Lee, D.E., 1964, "Buddingtonite, an Ammonium Feldspar With Zeolitic Water," Am. Min., V. 49, p. 831.

40. Evans, R.C., 1964, An Introduction to Crystal Chemistry, 2nd ed., Cambridge Univ. Press, Cambridge, England.

41. Ewell, R.H. and Insley, H. 1935, "Hydrothermal Syntheses of Kaolinite, Dickite, Beidellite, and Nontronite," J. Research Natl. Bur. Stds., V. 15, p. 173.

42. Ewing, F.J., 1935, "The Crystal Structure of Diaspore," J. Chem. Phys., V. 3, p. 203.

43. Fang, J.H., 1963, "Cell Dimensions of Dehydrated Natrolite," Am. Min., V. 48, p. 414.

44. Faust, Am. Min., 1948, V. 33, pp. 337-345.

45. Farnsworth, M., 1924, "Effects of Temperature and Pressure on Gypsum and Anhydrite," US Bur. Mines Rept. Investigations, #2654.

46. Fenner, C.N., 1913, "The Stability Relations of the Silica Minerals," Am. J. Sci., Ser. 4, V. 36, p. 331.

47. Flörke, O.W., 1952, "Kristallographische und Rontgenometrische Untersuchungen im System $CaSO_4$-$CaSO_4 \cdot 2H_2O$," Neues Jahrb. Min. Abh., V. 84, p. 189.

48. Foster, W.R., 1951, "High Temperature X-Ray Diffraction Study of the Polymorphism of $MgSiO_3$," J. Am. Ceram. Soc., V. 70, p. 234.

49. Francombe, M.H. and Rooksby, H.P., 1959, "Structure Transformations Effected by the Dehydration of Diaspore, Geothite, and Delta Ferric Oxide," Clay. Min. Bull, V. 4, p. 1.

50. Fricke, R. and Jucaitis, P., 1930, "Untersuchungen uber die Gleichgewichte in den Systemen $Al_2O_3 \cdot Na_2O \cdot H_2O$ and $Al_2O_3 \cdot K_2O \cdot H_2O$," Zeit. Anorg. Chem., V. 191, p. 129.

51. Fyfe, W.S., 1962, "On the Relative Stability of Talc, Anthophyllite, and Enstatite," Am. J. Sci., V. 260, p. 460.

52. Fyfe, W.S., 1964, Geochemistry of Solids, McGraw-Hill Co., N.Y.

53. Gallitelli, P., 1933, "Richerche Sul Solfato di Calcio Semidtato e sull' Anidrita Solubile," Periodico Min. Roma, V. 4, p. 132.

54. Garrels, R.M., 1957, "Some Free Energy Values From Geologic Relations," Am. Min., V. 42, pp. 780-791.

55. Garrels, R.M., 1960, Mineral Equilibria at Low Temperatures and Pressures, Harper and Brothers, N.Y.

56. Gatineau, L. and Mering, J., 1958, "Precisions Sur la Structura di la Muscovite," Clay, Min. Bull, V. 3, p. 238.

57. Ginzbury, D.M. and Barenova, R.I., 1955, "Thermodynamic Characteristics of Calcium and Magnesium Carbonates and Oxides," Trudy Vsesoyuz. Inst. Sodovoi Prom, V. 8, p. 106.

58. Glemser, O., 1959, "Binding of H_2O in Some Hydroxides and Hydrous Oxides," Nature, V. 183, p. 943.

59. Goldsztaub, S., 1931, "Deshydration des Hydrates Ferriques Naturels," Compt. Rend. Acad. Sci. Paris, V. 193, p. 533.

60. Gordon, A.R., 1934, "Calculation of Thermodynamic Quantities From Spectroscopic Data for Polyatomic Molecules; the Free Energy, Entropy, and Heat Capacities of Steam," J. Chem. Phys., V. 2, p. 65.

61. Graf, D.L. and Lamar, J.E., 1955, "Properties of Calcium and Magnesium Carbonates and Their Bearing on Some Uses of Carbonate Rocks," Econ. Geol. Fiftieth Aniv. Vol., 1905-1955, p. 639.

62. Gruner, J.W., 1934, "The Crystal Structure of Talc and Pyrophyllite," Zeit. Krist., V. 88, p. 412.

63. Guinier, A., "Mise En Evidence Des DeFauts Cristallins Per' Les Rayons X," Radiation Damage in Solids, ed., by D.S. Billington, Proceedings of the International School of Physics (Enrico Fermi), Academic Press, 1962.

64. Harker, R.I. and Tuttle, O.F., 1954, "Studies in the System $CaO-MgO-CO_2$," Geol. Soc. Am. Bull., V. 65, p. 1260.

65. Hendricks, S.B., 1939, "On the Crystal Structure of Talc and Pyrophyllite," Zeit. Krist., V. 99, p. 264.

66. Hendricks, S.B., 1942, "Lattice Structure of Clay Minerals and Some Properties of Clays," J. Geol., V. 50, p. 276.

67. Hey, M.H., 1932, "Studies on Zeolites, Part II. Natrolite and Metanatrolite," Min. Mag., V. 23, p. 243.

68. Hey, M.H., 1935, "Studies on Zeolites, Part VIII. A Theory of the Vapor Pressure of the Zeolites and of the Diffusion of H_2O or Gases in the Zeolitic Crystal," Min. Mag., V. 24, #150, p. 99.

69. Hey, M. H. and Bannister, F. A., 1932, "Studies on Zeolites, Part III. Natrolite and Metanatrolite," Min. Mag., V. 23, p. 243.

70. Hey, M. H. and Bannister, F. A., 1948, "A Note on the Thermal Decomposition of Chrysotile," Min. Mag. V. 28, p. 333.

71. Hill. A. E., 1937, "The Transition Temperature of Gypsum to Anhydrite," J. Am. Chem. Soc., V. 59, p. 2242.

72. Humphrey, G. L. and King, E. G., 1952, "Heats of Formation of Quartz and Cristobalite," J. Am. Chem. Soc., V. 74, p. 2041.

73. Jackson, W. W. and West, J., 1930, "The Crystal Structure of Muscovite," Zeit. Krist., V. 76 and 85, pp. 211, 160.

74. Johnson, J., 1910, "The Thermal Dissociation of Calcium Carbonate," J. Am. Chem. Soc., V. 32, p. 938.

75. Kabayashi, K., 1951, "Heat Capacities of Inorganic Substances at High Temperatures, Part III. Heat Capacity of Synthetic Calcite," Sci. Rept. Tokoku Univ., 1st. Ser., V. 35, p. 103.

76. Kelley, K. K. and Anderson, C. T., 1935, "Contributions to the Data on Theoretical Metallurgy, IV. Metal Carbonates–Correlations and Applications of Thermodynamic Properies," US Bur. Mines Bull., #383.

77. Kelley, K. K., 1949, "Contributions to the Data on Theoretical Metallurgy, X. High Temperature Heat-Content, Heat Capacity, and Entropy Data for Inorganic Compounds," US Bur. of Mines Bull., #476.

78. Kelley, K. K., 1960, "Contributions to the Data on Theoretical Metallurgy, XIII. High Temperature Heat-Content, Heat Capacity, and Entropy Data for the Elements and Inorganic Compounds," US Bur. of Mines Bull., #584.

79. Kelley, K. K., 1962, "Heats and Free Energies of Formation of Anhydrous Silicates," US Bur. of Mines Repts. of Investigation, #5901.

80. Kelley, K. K., Southard, J. C., and Anderson, C. F., 1941, "Thermodynamic Properties of Gypsum and its Dehydration Products," US Bur. of Mines Tech. Paper, #625.

81. Kelly, R. and Greene, R., 1951, "Irreversible Dehydration in Montmorillonite," Clay Min. Bull., V. 1, p. 221.

82. Kennedy, G. C., 1950, "Pressure-Volume-Temperature Relations in Water at Elevated Temperatures and Pressures," Am. J. Sci., V. 248, p. 540.

83. Kleinpaul, W., 1960, "Calculations of Activation Energies," Zeit, Physik. Chem., V. 26, p. 313.

84. Klever, E., 1930, "Calorimetric and X-Ray Investigations of the Dehydration of Hydrated Alumina," Trans. Ceram. Soc., V. 29, p. 149.

85. Kiriyoma, R., Koizumi, M., Yamad, K., and Kitagahi, R., 1957, "Hydrothermal Reactions of Zeolites," J. Min. Soc. Japan, V. 3, p. 107.

86. Koizumi, M., 1953, "The Differential Thermal Analysis Curves and Dehydration Curves of Zeolites," J. Min. Soc. Japan, V. 1, p. 36.

87. Koytun, V. F., 1959, "Dehydration and Rehydration in the System Iron Oxide and Water," Patannya Geol. Fiz.-Khim. Mineral, Sirovini Kremu, Akad. Nauk. Ukr. R. S. R. Zbrinik Disertalsunikh Prats, p. 32.

88. Kracek, F. C., 1953, "Annual Report of the Director of the Geophysical Laboratory," Carnegie Inst. of Wash. Yearbook, #52, p. 39.

89. Lewis, G. N., and Randall, M., 1923, "A Summary of the Specific Heats of Gases," J. Am. Chem. Soc., V. 34.

90. Lewis, G. N., and Randall, M., 1923, Thermodynamics and Free Energy of Chemical Substances, McGraw-Hill Co., N. Y.

91. Lima DeFaria, J., and Gay, P., 1962, "Disordered Structural States in the Dehydration of Geothite and Diaspore," Min. Mag., V. 33, p. 37.

92. McAtee, Jr., J.L., 1956, "Determination of Random Interstratification in Montmorillonites," Am. Min., V. 41, p. 627.

93. McConnell, D., 1950, "The Crystal Chemistry of Montmorillonite," Am. Min., V. 35, p. 166.

94. MacDonald, G.J.F., 1953, "Anhydrite-Gypsum Equilibrium Relations," Am. J. Sci., V. 251, p. 884.

95. MacDonald, G.J.F., 1954, A Critical Review of Geologically Important Thermochemical Data, PhD Thesis Harvard Univ.

96. Mackenzie, Milne, 1952, "Effect of Grinding Muscovite," Min Mag, 30, p. 178-185.

97. Mackenzie, R.C. and Bishui, B.M., 1958, The Montmorillonite Differential Thermal Curve, Part II. Effect of Exchangeable Cations on the Dehydration of Normal Montmorillonite," Clay Min. Bull., V. 3, p. 276.

98. Megaw, H.D., 1952, "The Structure of Arfvillite $Ca_3(SiO_3OH)_2 \cdot 2H_2$)," Acta. Cryst., V. 5, p. 477.

99. Midgley, H.G., and Gross, K.A., 1956, "Thermal Reactions of Smectites," Clay Min. Bull, V. 3, p. 79.

100. Milligan, W.O. and Weiser, H.B., 1937, "The Mechanism of Dehydration of Zeolites," J. Phys. Chem., V. 41, p. 1024.

101. Morey, G.W. and Ingerson, E., 1937, "The Pneumatolytic and Hydrothermal Alteration and Synthesis of Silicates," Econ. Geol., V. 32, p. 607.

102. Morimoto, N., 1959, "Annual Report of the Director of the Geophysical Laboratory," Carnegie Inst. of Wash. Yearbook, #58, p. 197.

103. Muyushiro, Akiho, 1960, "Thermodynamics of Reactions of Rock Forming Minerals with Silica," Japanese J. Geol. and Geography Trans. 31, p. 71.

104. Noll, W., 1932, "Synthese Von Montmorilloniten, Ein. Beitrag Zur Kenntniss Der Belchungs-Bedingungen Und Des Chemismus Von Montmorillinit," Chemie Der Erde, V. 10, pp. 129, 154.

105. Noll, W., 1936, "Hydrothermal Synthesis Des Muscovite, Ein Beitrag Zur Frage Serizitbildung in Tonschiefern," Nach. Gesell, Wiss. Gottingen Math-Physik Kl., pp. 122-134.

106. Noll, W., 1944, "New Investigations in Water-Silicate Systems," Kolloid Zeits., V. 107, p. 181.

107. Noll, W., 1950, "Synthesis in System $MgO/SiO_2/H_2O$," Zeit. Anorg. Chem., V. 261, p. 1.

108. Norin, R., 1941, "Tillampning Ar Termisk Analys Pa Leror Och Vattenlraltiga Mineral," Geol. Foren Stockh. Fork, V. 63, p. 203.

109. Pankratz, L. B., 1964, "High Temperature Heat Contents and Entropies of Muscovite and Dehydrated Muscovite," US Bur. of Mines Rept. Investigation, #6371, p. 6.

110. Pauling, L., 1930, "The Structure of Micas and Related Minerals," Proc. Nat. Acad. Sci. USA., V. 16, p. 123.

111. Pauling, L. and Hendricks, S. B., 1925, "The Crystal Structure of Hematite and Corundum," J. Am. Chem. Soc., V. 47, p. 781.

112. Pavarennykh, A., 1959, "Dehydration and Dissociation of Minerals," Trudy Mineral. Muzeya, #9, p. 99.

113. Peng, C.J., 1955, "Thermal Analysis Study of the Natrolite Group," Am. Min., V. 40, p. 834.

114. Pistanius, C. W. F T. and Sharp, W. E., 1960, "Properties of Water, Part VI. Entropy and Gibbs Free Energy of Water in the Range 10-1000°C and 1-250,000 Bars," Am. J. Sci., V. 258, p. 757.

115. Posnjak, E , 1938, "The system $CaSO_4$," US Bur. of Mines Tech. Paper, Ser. 5, V. 35-A, p. 247.

116. Posnjak, E. and Bowen, N. L., 1931, "The role of H_2O in Tremolite," Am. J. Sci., Ser. 5, V. 22, p. 203.

117. Radoslovich, E. W., 1960, "The Structure of Muscovite, $KAl_2(Si_3Al)O_{10}(OH)_2$," Acta. Cryst., V. 13, p. 919.

118. Ralston, Oliver C., 1929, "Iron Oxide Reduction Equilibria," US Bur. of Mines Bull., #296.

119. Repa, A. G., 1954, "Reactions of Silicate Formation," Zhur. Priklad. Khim, V. 27, p. 1184.

120. Robie, R. A., 1964, "Equilibrium of Talc with Enstatite and Quartz," Science, V. 143, #3610, p. 1957.

121. Robie, R. A. and Stout, J. W , 1963, "Heat Capacity from 11-350°K, Entropy and Heat of Formation of Talc and Tremolite," J. Phys. Chem., V. 67, p. 2252.

122. Ross, C. S., 1964, "Volatiles in Volcanic Glasses and their Stability Relations," Am. Min., V. 49, p. 258.

123. Rossini, F. D. et al., 1952, "Selected Values of Chemical Thermodynamic Properties," US Nat. Bur. Stds. Circ., #500, US Dept. of Commerce.

124. Rowland, R. A., Weiss, E. J., and Bradley, W. F., 1956, "Dehydration of Moroionic Montmorillonites," Proc. 4th Nat. Conf. on Clays and Clay Minerals, USA, p. 85.

125. Roy, R., 1949, "Decomposition and Resynthesis of the Micas," J. Am. Ceram. Soc., V. 32, p. 204.

126. Roy, R. and Osborn, E. F., 1954, "The System Al_2O_3-SiO_2-H_2O," Am. Min., #39, p. 853.

127. Roy, R. and Roy, D. M., 1954, "An Experimental Study of the Formation and Properties of Synthetic Serpentines and Related Layer Silicate Minerals," Am. Min., V. 39, p. 957.

128. Roy, R. and Tuttle, O. F., 1957, Physics and Chemistry of the Earth, Pergamon Press, N. Y., Ch. 6.

129. Sabatier, G., 1955, "Kinetics of the Dehydration of Several Silicates," J. Chem. Phys., V. 52, p. 60.

130. Schmalz, R. F , 1958, "Thermodynamic Calculations Relating to the Origin of Red Beds," Geol. Soc. Am. Bull., V. 69, p. 1639.

131. Schmalz, R. F., 1959, "A Note on the System $Fe_2O_3 . H_2O$," J. Geophys. Res., V. 64, p. 575.

132. Smith, F. G. and Kidd, D. J., 1949, "Hematite-Geothite Relations in Neutral and Alkaline Solutions Under Pressure," Am. Min., V. 34, p. 403.

133. Smith, J. V. and Yoder, H. S., 1956, "Theoretical and X-ray Study of the Mica Polymorphs," Min. Mag., V. 31, #234, p. 209.

134. Smyth, F. H. and Adams, L. H., 1923, "The System Calcium Oxide-Carbon Dioxide," J. Am. Chem. Soc., V. 45, p. 1167.

135. Southard, J. C. and Royster, P. H., 1936, "The Thermal Dissociation of Calcium Carbonate," J. Phys. Chem., V. 40, p. 435.

136. Steiner, L. E., 1941, Introduction to Chemical Thermodynamics, McGraw-Hill Co., N. Y.

137. Taylor, W. H., 1933 "The Structure of Sanidine and Other Feldspars," Zeit. Krist., V. 85, p. 425.

138. Thilo, E., 1939, "Chemische Untersuchungen Von Silikaten IX. Die Umwandung Von Tremolit in Diopsid Beim Erhitzen," Zeit. Krist., V. 101, p. 345.

139. Tigerschiold, Magnus, 1923, "Jarnets Oxide Fran Termodynamisk Synpunket," Avtryck Ur Jernkontorets Annaler For Ar, p. 67.

140. Torgeson, D. R. and Sahama, T. G., 1948, "A Hydrofluoric Acid Calorimeter and the Determination of the Heats of Formation of $MgSiO_4$, $MgSiO_3$, and $CaSiO_3$," J. Am. Chem. Soc., V. 70, p. 2156.

141. Tunell, G. and Posnjak, E., 1931, "The Stability Relations of Goethite and Hematite," Econ. Geol., V. 26, p. 337.

142. Turner, F. J. and Verhoogan, J., 1951, Igneous and Metamorphic Petrology, 1st. ed., McGraw-Hill Co.

143. Vermaas, F. H. S., 1952, "The Amphibole Asbestos of South Africa," Trans. Geol. Soc. South Africa, V. 55, p. 199.

144. Von Ubisch, H., 1953, "Mass Spectrometry and Mineralogy," Geologeska Foreningens Forhandlinger, #475, p. 469.

145. Warren, B. E., 1929, "The Structure of Tremolite $H_2Ca_2Mg_5(SiC_3)_8$," Zeit. Krist., V. 72, p. 42.

146. Warren, B. E. and Modell, D. I., 1930, "The Structure of Enstatite $MgSiO_3$," Zeit. Krist., V. 75, p. 1.

147. Weast, R. C., Selby, S. M., Hodgman, C. D., 1964, Handbook of Chemistry and Physics, Chemical Rubber Co., Cleveland.

148. Weeks, W. F., 1953, "Equilibria Relations During Thermal Metamorphism of Carbonate Rocks," Geol. Soc. Am. Bull., V. 64, p. 1490.

149. Weiser, H. B., Milligan, W. O., and Eckholm, W. C., 1936, "The Mechanism of the Dehydration of Calcium Sulfate Hemihydrate," J. Am. Chem. Soc., V. 58, p. 1261.

150. Weller, W. and King, E. G., 1963, "Low Temperature Heat Capacity and Entropy at 298.15°K of Muscovite," US Bur. of Mines Rept. Investigation, #6281, p. 4.

151. Wicks, C. E. and Block, F. E., 1962, "Thermodynamic Properties of o5 Elements," US Bur. of Mines Bull., #605.

152. Wittels, M., 1951, "Structural Transformations in Amphiboles at Elevated Temperatures," Am. Min., V. 36, p. 851.

153. Wittels, M., 1952, "Structural Disintegration of Some Amphiboles," Am. Min., V. 37, p. 28.

154. Wyckoff, R. W. G., 1924, The Structure of Crystals, The Chemical Catalog Co., Inc., N. Y.

155. Wyckoff, R. W. G., 1925, "Die Kristalstruktur Von Cristobalit SiO_2 (Bei Hohen Temperature Stabile Form)," Zeit, Krist., V. 62, p. 189.

156. Wyckoff, R., 1931, The Structure of Crystals, 2nd ed., Chemical Catalog Co., Inc., N. Y.

157. Wyllie, P. J. and Tuttle, O. F., 1960, "The System $CaO.CO_2.H_2O$ and the Origin of Carbonatites," J. Petrol., V. 1, p. 1.

158. Yoder, H. S., Jr., 1952, "The $MgO-Al_2O_3-SiO_2-H_2O$ System and Related Metamorphic Facies," Am. J. Sci., Bowen Volume, p. 569.

159. Yoder, H. S., 1954, "Annual Report of the Director of the Geophysical Laboratory," Carnegie Inst. of Washington Yearbook, #53, p. 95.

160. Yoder, H. S. and Eugster, H. P., 1953, "Synthesis and Stability of the Muscovites," Geol. Soc. Am. Bull., V. 64, p. 1486.

161. Yoder, H. S. and Eugster, H. P., 1954, "Phlogopite Systhesis and Stability Range," Geochim. et Cosmochim. Acta, V. 6, p. 157.

162. Yoder, H. S. and Eugster, H. P., 1955, "Synthetic and Natural Muscovites," Geochim. et Cosmochim. Acta, V. 8, p. 225.

163. Zussman, J., 1954, "Investigation of the Crystal Structure of Antigorite," Min. Mag., V. 30, p. 498.

164. Zussman, J., 1955, "The Crystal Structure of an Actinolite," Acta. Cryst., V. 8, p. 301.

165. Zwetsch, A., 1934, "Rontgenuntersuchungen Und Der Keramik," Ber. Deut. Keram. Ges., V. 14, p. 2.

APPENDIX I

CONTRACT SUMMARY

On 16 November 1964, The Bendix Corporation entered into Contract NAS 9-3734 with NASA for performance of certain tests and analyses. The following summarizes the requirements of that contract, the significant technical problems encountered, and the resulting contract revisions.

I.1 ORIGINAL CONTRACT

The contract set forth the following as its purpose and objectives:

1. Purpose - to evaluate the stability of various earth minerals in a simulated lunar environment. Changes in mineral content which were to be investigated were those due to a loss or gain of chemical constituents and those due to a structural rearrangement of ions.

2. General Objective - to determine the possible composition and crystalline form of minerals present in the lunar environment.

3. Specific Objectives - to determine what chemical and/or structural changes occur when certain earth minerals are subjected to temperature and vacuum conditions simulating those of the lunar environment, and to determine the stability of such chemical and/or structural forms when exposed to spacecraft and earth environments.

The environmental conditions referred to above were defined as:

	Temperature	Humidity	Atmosphere
Lunar	-180°C to 130°C	Nil	10^{-11} torr
Spacecraft	32°C	70%	Oxygen, 5 psia
Re-entry	60°C	70%	Oxygen, 5 psia
Earth	35°C	100%	Normal earth

The exposure durations required for each of the above environments were defined as:

1. Lunar - Stabilize pressure at or near 10^{-11} torr with temperature at 130°C and hold for seven days; reduce temperature to -180°C and hold for one day; this cycle is repeated over a period of several months within the term of contract performance.

2. Spacecraft - Expose samples to spacecraft environmental conditions set forth above simultaneously for a total of four days.

3. Re-entry - Expose to this set of conditions for a total of one hour.

4. Earth - Expose for two days.

The contract also required certain investigations regarding disordered materials which in summary are:

1. Pulverize muscovite, tektite, and basalt glass until no X-ray diffraction pattern can be obtained. Disorder plagioclase by grinding to about 1-micron size and exposing it to a radiation of a high-energy source. Observe samples of these minerals while they are subjected to the various required environmental conditions through X-ray photos to determine whether crystallization occurs. Determine hygroscopic properties of these minerals by accurate weighing before and after exposure to the test conditions.

2. Perform quantitative determinations of water vapor and other gases of each of the mineral samples.

3. Synthesize muscovite with about 1/2 of the OH^- replaced by F^- or Cl^- and synthesize feldspars with high NH_4^+ content. Determine how readily HF, HCl, and NH_3 vaporize from their respective minerals. Perform additional spectrographic measurements to determine which volatiles are produced first.

4. Analyze reaction products of all mineral samples including the synthesized minerals.

It was expected that these experiments would provide an early input to (and guide the conduct of) the long-term test plan wherein the samples were to be exposed to the various environmental conditions.

I. 2 PROBLEMS ENCOUNTERED

After considerable effort had been expended in design and fabrication of an integrated test setup in which all requirements of the long-term experiments could be accommodated, it was discovered during preliminary test runs that surface eruptions of the samples as arranged in the chamber were very likely and that they would essentially prohibit attainment of a suitable vacuum level and perhaps even result in "cross pollination" of the samples. (Prior test runs had been made with just one mineral sample. The presence of heterogenous samples produced unanticipated problems in achieving desired vacuum, as each sample reacts uniquely to increasing vacuum. Further, the fine powder samples used were found to trap air molecules as well as volatile products, which would expand rather suddenly, carrying portions of the mineral samples with them in a sort of explosion.)

As a solution, it was recommended by the contractor and agreed to by NASA that two separate chambers be used concurrently to run the long-term experiments. The previously designed chamber would be used as planned, but with only very small amounts of the mineral samples placed in capillary tubes plugged at the ends with fine fiberglass. At the same time, larger samples of the same minerals would be placed in a larger vacuum chamber, developing essentially the same vacuum and cycling temperature in the same way as in the small chamber. These larger samples would be used for subsequent chemical analyses after exposure to the planned environment.

This revised test plan was implemented, and the following additional problems ensued:

1. The samples in the small chamber could not be brought to -180°C, primarily because the cold wall design being used relied solely on radiation for heat transfer from the samples. It was mutually agreed that the temperature cycling to be used in the small chamber would be from ambient to 130°C, while the samples in the large chamber would be cycled from -180°C to 130°C.

2. The larger chamber was able to subject the sample to the -180°C temperature at an acceptable vacuum level (3×10^{-11} torr); however, when the sample temperature was raised to the 130°C mark, the

pressure rose to 10^{-6} torr and could be returned only to the 10^{-8} torr range. After trying unsuccessfully for approximately two months, it was determined that outgassing of the samples was preventing achievement of the desired vacuum level. NASA and the contractor reluctantly agreed that this test plan had to be abandoned.

3. Attempts by the contractor to secure a chemical analysis firm acceptable to NASA to analyze the samples after subjection to the test environments were not successful.

I. 3 CONTRACT MODIFICATION

In view of the above-listed problems, a contract revision which completely reoriented the work remaining to be performed was negotiated between the parties. Briefly stated, the revision required design and fabrication of a new sample holder which would enable the small chamber to subject the samples to the -180°C temperature, running of a temperature cycling of six mineral samples (NH_4 feldspar, gypsum, calcium-montmorillonite, goethite, muscovite, and natrolite) while at a stabilization pressure of 5×10^{-10} torr, then subjecting the samples to a 4-day exposure to a simulated spacecraft environment of 32°C, 5 psia oxygen, and 100% relative humidity, taking X-ray photos at -180°C, liquid CO_2 temperature, room ambient, 75°C, 130°C and after the 4-day spacecraft environment exposure, and deleting the requirement for chemical analysis by the contractor.

Specific items which the contract had previously required and which were not performed as a result of the modified program were:

1. Synthesize muscovite with F^- or Cl^- - Bendix intended to perform this synthesis after the feldspar synthesis had been completed. Because of the difficulty in producing a sufficient quantity of acceptable ammoniated feldspar, caused by several equipment failures, this synthesis had not been attempted at the time of program reorientation. It was not included in the revised plan, because it was anticipated: (1) that it would require undue time and effort, and (2) that the ammoniated feldspar synthesis had yielded sufficient data to meet contract objectives.

2. Pulverize muscovite until no X-ray diffraction pattern is obtained - Bendix attempted to do this; however, it was abandoned because no practical means were available to Bendix to perform it. The muscovite proved to be extremely difficult to crush at all, and its preparation ultimately was accomplished by cutting with a pair of scissors. The muscovite would split into thinner layers, but the layers would not tear readily into small enough pieces by the attempted crushing.

3. Determine hygroscopic properties of muscovite, basalt, tektite, and irradiated plagioclase by accurate weighing following their exposure to the full range of temperature cycling and humidity conditions required in the contract. This was not performed because the initial test program could not be completed due to equipment problems and the revised test program deleted testing of all of these minerals, with the exception of muscovite. This task was not included in the contract revision, probably because the contemplated size of the muscovite sample would be too small for this type of testing.

"The aeronautical and space activities of the United States shall be conducted so as to contribute . . . to the expansion of human knowledge of phenomena in the atmosphere and space. The Administration shall provide for the widest practicable and appropriate dissemination of information concerning its activities and the results thereof."

—NATIONAL AERONAUTICS AND SPACE ACT OF 1958

NASA SCIENTIFIC AND TECHNICAL PUBLICATIONS

TECHNICAL REPORTS: Scientific and technical information considered important, complete, and a lasting contribution to existing knowledge.

TECHNICAL NOTES: Information less broad in scope but nevertheless of importance as a contribution to existing knowledge.

TECHNICAL MEMORANDUMS: Information receiving limited distribution because of preliminary data, security classification, or other reasons.

CONTRACTOR REPORTS: Scientific and technical information generated under a NASA contract or grant and considered an important contribution to existing knowledge.

TECHNICAL TRANSLATIONS: Information published in a foreign language considered to merit NASA distribution in English.

SPECIAL PUBLICATIONS: Information derived from or of value to NASA activities. Publications include conference proceedings, monographs, data compilations, handbooks, sourcebooks, and special bibliographies.

TECHNOLOGY UTILIZATION PUBLICATIONS: Information on technology used by NASA that may be of particular interest in commercial and other non-aerospace applications. Publications include Tech Briefs, Technology Utilization Reports and Notes, and Technology Surveys.

Details on the availability of these publications may be obtained from:

SCIENTIFIC AND TECHNICAL INFORMATION DIVISION

NATIONAL AERONAUTICS AND SPACE ADMINISTRATION

Washington, D.C. 20546